Volume Integral Equation Methods for Forward and Inverse Bioelectromagnetic Approaches


Doctoral Dissertation
Doctoral Program in Electrical, Electronics, and Communications Engineering
(33^{rd} cycle)

Volume Integral Equation Methods for Forward and Inverse Bioelectromagnetic Problems

Clément Henry

* * * * * *

Supervisor
Prof. Francesco P. Andriulli

Doctoral Examination Committee:
Prof. Kristof Cools, Technische Universiteit Delft (Referee)
Prof. Marco Mussetta, Politecnico di Milano (Referee)
Prof. Giuseppe Vecchi, Politecnico di Torino
Prof. Roberto D. Graglia, Politecnico di Torino
Prof. Simon B. Adrian, Universität Rostock
Prof. Francesco P. Andriulli, Politecnico di Torino

Politecnico di Torino
June 3, 2021

Summary

This dissertation describes doctoral research activities on new computational techniques based on volume integral equations specifically tailored for bioelectromagnetic applications such as electroencephalography (EEG) source localization, microwave imaging, and inverse scattering synthesis for improved dosimetric assessment.

This thesis work began with an in-depth analysis of the conditioning properties of full-wave volume integral equations, particularly in a scenario with a low frequency electromagnetic source illuminating an inhomogeneous object with high material contrast, which corresponds to the operating regime of numerous bioelectromagnetic applications. This analysis led to the introduction of a new set of volume quasi-Helmholtz projectors that, with proper re-scaling, renders the electric flux volume integral equation (D-VIE) accurate and stable at low frequencies in lossy dielectric objects. This new method was successfully applied in EEG source localization for solving the forward problem.

In parallel, bioelectromagnetic applications requiring higher frequency modeling were investigated. For instance, the usage of the D-VIE formulation in inverse scattering scenarios required the full derivation of a new inversion algorithm based on modified gradient methods. The practical use of this new inverse solver is illustrated through its application in microwave imaging and inverse source synthesis. Regarding the former application, numerical examples show that it compares to several standard inverse scattering schemes in a canonical setting. The latter responds to the need of understanding the impact of mobile phones on brain activity. To remedy one significant limitation of the existing techniques that attempt to assess this risk with an EEG helmet, which acts as a shield for the incoming radiations of the phone, an inverse synthesis algorithm was introduced for the design of a deformation source enabling EEG recordings with a non perturbed field distribution in the head.

Acknowledgements

First and foremost, I would like to direct my gratitude to Prof. Francesco Andriulli. He was always willing to share his knowledge and insights on the topics investigated in this PhD thesis and beyond.

My gratitude also extends to my lab colleagues with whom I have learned a lot and had the pleasure of working. Thank you Tiffany, Simon, Maxime, Lyes, John Erick, Davide, Damiano, Andrea, Alexandre, Alessandro, and Adrien.

Moreover, some research activities presented in this dissertation have been conducted in collaboration with other research groups. I would like to acknowledge Prof. Joe Wiart, Prof. Christian Person, Dr. Xi Cheng, and Prof. Rajendra Mitharwal for these collaborations.

Last but not least, I would like to thank my dear family and Linda for their support during these years.

Contents

Chapter 1

Introduction

Bioelectromagnetics is an interdisciplinary field in which the interaction of electromagnetic waves and living organisms is investigated. A significant portion of bioelectromagnetics is dedicated to the study of the electromagnetic fields in the human brain. In this spectrum of applications, the fields originate either from the brain itself or from external sources. Understanding the former type of source is important for the diagnosis and treatment of several neuro-pathologies such as Parkinson's and Alzheimer's syndromes. The study of latter paves the way to better treatment (e.g. transcranial electric stimulation) and diagnosis (e.g. microwave imaging for cancer detection) of brain diseases together with better safety guidelines for the design of radiating sources (e.g. electromagnetic dosimetry). Regardless of the nature of the source, it is crucial to infer some knowledge (e.g. geometry, material) about the environment in which they radiate, that is the head and its surroundings. This can done from observations (e.g. measured field). This mapping between the observation space and the physical model is referred to as inverse problem. To solve an inverse problem, one requires a forward model, which provides the model response for some given parameters of the physical model. This response to electromagnetic sources is governed by Maxwell's equations, which are at the basis of electromagnetic field theory. They represent a set of equations relating sources, fields, and fluxes for some given dielectric and ferromagnetic parameters, thus enabling electromagnetic forward modeling.

However, there exist analytic solutions to Maxwell's equations in closed form only in few cases. For complex structures such as the brain, no analytic solution is known. This leaves two possible options: model the head in a very simplistic way and use existing analytic solutions (e.g. spherical model of the head) or reformulate the original problem into an approximated problem numerically solvable with a computational method. The increase in computer capacity in the last decades has led toward the latter option for most of real-world applications. This is especially true in electromagnetics, in which the domain of computational electromagnetics (CEM) has emerged. This field deals with the theoretical and computational

aspects required to provide stable, fast, and accurate solutions to real-world electromagnetic problems. Computational methods in CEM can be split into two classes: partial differential equations (PDEs) methods and integral equations (IEs) methods. While the former amounts to directly solve Maxwell's equations, the latter recast Maxwell's equations into integral equations in which the new unknowns are equivalent sources. In general, solving an electromagnetic problem with IEs requires less degrees of freedom than with PDEs. In both cases the unknowns (equivalent sources in IEs, fields or fluxes in PDEs) and the geometry are decomposed into unitary elements thus translating the continuous problem to a discrete one, having the form of a matrix equation that once solved gives an approximation of the unknowns of the continuous equations. Although IE methods require less unknowns than PDE methods for a given problem, they give rise to a linear system in which the matrix is dense, which is computationally expensive to solve. This drawback has been significantly attenuated with the introduction of acceleration techniques on top of the standard IE schemes. For these reasons, IE-based computational methods remain competitive in bioelectromagnetic problems and were employed in the framework of this thesis work. The main concepts about IEs are briefly introduced in chapter 2.

Depending on the nature of the bioeletromagnetic problem, IE-based solvers are generally either surfacic (SIE) or volumic (VIE). Surface formulations are efficient in the sense that they require the discretization of the surface of the object under study only while volume integral equations require the discretization of the whole object. This drawback of VIE methods allows, nevertheless, the modelization of highly inhomogeneous and anisotropic objects, which is required to get a realistic head forward modeling. The choice of the volume integral formulation depends on the requirements of the biomedical method it is applied to. When solely taking into consideration the resistive effects occurring in biological tissues, VIEs derived from Poisson equation can be used and when the capacitive and inductive effects also need to be included, full-wave solvers are employed. On the one hand, Poisson-based solvers are not valid outside the quasi-static regime and, on the other hand, full-wave solvers suffer from the low-frequency (LF) breakdown: they are unstable (i.e. ill-conditioned) and fail to converge at low frequencies. Therefore, there is a gap between low and high frequency bio-electromagnetic modeling, which prevents traditional numerical solvers to be used in some applications. This problem is treated in chapter 3 by introducing a new set of volume quasi-Helmholtz projectors that enable a proper re-scaling of the electric flux volume integral equation (D-VIE) when applied to the modeling of inhomogeneous objects. Numerical results confirm the theoretical treatment and show that this formulation can be used as a forward bioelectromagnetic solver.

Starting from an existing solver for the forward modeling, inverse scattering (IS) problems can be solved. This type of inverse problem is emphasized in chapter 4. In electromagnetics, these problems aim at retrieving the position and material

of an unknown object in the known domain. One of the main issues to tackle in IS problems is the non-linear relationship between the scattered field and the material parameters in the object. Two main categories of solvers exist: gradient based methods and Born iterative methods. The former methods enable simultaneously the minimization of the error with the measured data and the enforcement of Maxwell's equations in the object while the latter schemes alternatively perform these operations. In this chapter, a new D-VIE gradient based algorithm is introduced and compared to existing inverse scattering techniques in the two families above-mentioned.

In chapter 5 another bioelectromagnetic inverse scattering problem is presented which is motivated by the desire of evaluating the impact of radio frequency (RF) devices on brain activity. The measurement of brain activity is performed through an electroencephalography (EEG) setup which requires placing electrodes caps on the scalp of the patient. When the impact of an RF source on brain activity is investigated, the metallic caps induce a shielding of the field radiated by the source, which yields a perturbed field inside the brain. A field reconstruction antenna should thus be designed to mimic the field radiated by the source in the presence of an EEG device. This chapter introduces a new inverse synthesis algorithm for the design of a reconstruction source composed of an array of dipoles and a dielectric lens.

Finally, chapter 6 summarizes the results presented in this dissertation. Possible routes for the extension of this thesis work are provided.

Chapter 2

Background and Notations

ELECTROMAGNETIC THEORY is a powerful tool for understanding and describing various phenomena occurring in nature. This theory is governed by Maxwell's equations and, in this chapter, some basic concepts of electromagnetism are first introduced in Section 2.1. Subsequently, Section 2.2 is dedicated to the derivation of integral equations (IE) formulations, surface and volume IEs in this case, from which originates the work presented in this thesis. The discretization of these formulations is provided in Section 2.3. Last step of this chapter, Section 2.4 gives some insight on a key property of numerical solvers, that is its stability.

2.1 Maxwell's Equations in Macroscopic Media

Maxwell's equations are the fundamental equations to describe electromagnetic phenomena. At position $\boldsymbol{r}$ and at time t they are given as

$$\begin{aligned}
\boldsymbol{\nabla} \times \mathcal{H}(\boldsymbol{r},t) &= \mathcal{J}(\boldsymbol{r},t) + \frac{\partial \mathcal{D}(\boldsymbol{r},t)}{\partial t}, && \text{(Maxwell-Ampère law)} \\
\boldsymbol{\nabla} \times \mathcal{E}(\boldsymbol{r},t) &= -\frac{\partial \mathcal{B}(\boldsymbol{r},t)}{\partial t}, && \text{(Maxwell-Faraday law)} \\
\boldsymbol{\nabla} \cdot \mathcal{B}(\boldsymbol{r},t) &= 0, && \text{(Gauss' law for magnetism)} \\
\boldsymbol{\nabla} \cdot \mathcal{D}(\boldsymbol{r},t) &= \rho(\boldsymbol{r},t). && \text{(Gauss' law)}
\end{aligned} \tag{2.1}$$

where

- $\mathcal{B}$ (T) is the magnetic flux density,
- $\mathcal{D}$ ($\mathrm{C\,m^{-2}}$) is the electric flux density,
- $\mathcal{J}$ ($\mathrm{A\,m^{-2}}$) is the electric current density,
- $\mathcal{H}$ ($\mathrm{A\,m^{-1}}$) is the magnetic field,

- $\mathcal{E}$ ($\mathrm{V\,m^{-1}}$) is the electric field,
- ρ ($\mathrm{C\,m^{-3}}$) is the electric charge density.

If the electromagnetic fields are weak enough (linear medium) and in the absence of ferroelectric and ferromagnetic materials, the flux and field densities are related with the following relations

$$\mathcal{D} = \epsilon\mathcal{E}, \tag{2.2}$$
$$\mathcal{B} = \mu\mathcal{H}, \tag{2.3}$$

with ϵ ($\mathrm{F\,m^{-1}}$) and μ ($\mathrm{H\,m^{-1}}$) being the permittivity and permeability in the medium, respectively. In this chapter, the objects considered have permittivity and permeability that are stationary (time independent permittivity), possibly dispersive (frequency dependent materials), isotropic (scalar permittivity), and that depend on the position (inhomogeneous medium). Moreover, the objects studied here are assumed to be in vacuum, with permittivity ϵ_0 and permeability μ_0. The relative permittivity and permeability, defined with respect to ϵ_0 and μ_0, respectively, read

$$\epsilon_r = \epsilon/\epsilon_0, \tag{2.4}$$
$$\mu_r = \mu/\mu_0. \tag{2.5}$$

2.1.1 Time-Harmonic Fields

In most engineering problems, Maxwell's equations can be simplified by assuming time-harmonic electromagnetic fields (i.e. fields, charges, and currents oscillating at a single frequency). This assumption is adopted in this thesis. It means that all the quantities have a sinusoidal time dependence. For example, a field $\mathcal{F}(\boldsymbol{r}, t)$ can be formulated as

$$\mathcal{F}(\boldsymbol{r}, t) = \boldsymbol{F}_0(\boldsymbol{r}) \cos\left(\omega t + \beta(\boldsymbol{r})\right), \tag{2.6}$$

in which $\boldsymbol{F}_0$ is the amplitude of $\mathcal{F}(\boldsymbol{r}, t)$, ω denotes its angular frequency, and β its phase. The quantity $\mathcal{F}$ and its time derivative then read

$$\mathcal{F}(\boldsymbol{r}, t) = \mathrm{Re}\,\left(\boldsymbol{F}_0(\boldsymbol{r}) e^{j\omega t + j\beta(\boldsymbol{r})}\right), \tag{2.7}$$
$$\frac{\partial \mathcal{F}(\boldsymbol{r}, t)}{\partial t} = \mathrm{Re}\,\left(j\omega \boldsymbol{F}_0(\boldsymbol{r}) e^{j\omega t + j\beta(\boldsymbol{r})}\right). \tag{2.8}$$

Using eq. (2.7), and defining the phasor $\boldsymbol{F}(\boldsymbol{r}) = \boldsymbol{F}_0(\boldsymbol{r}) e^{j\beta(\boldsymbol{r})}$, we obtain that

$$\mathcal{F}(\boldsymbol{r}, t) = \mathrm{Re}\,\left(\boldsymbol{F}(\boldsymbol{r}, \omega) e^{j\omega t}\right). \tag{2.9}$$

Leveraging the transformations given by eq. (2.8) and eq. (2.9), we obtain Maxwell's equations for the time harmonic electromagnetic fields

$$\begin{aligned} \boldsymbol{\nabla} \times \boldsymbol{H} &= \boldsymbol{J} + j\omega \boldsymbol{D}, \\ \boldsymbol{\nabla} \times \boldsymbol{E} &= -j\omega \boldsymbol{B}, \\ \boldsymbol{\nabla} \cdot \boldsymbol{B} &= 0, \\ \boldsymbol{\nabla} \cdot \boldsymbol{D} &= \rho. \end{aligned} \tag{2.10}$$

2.1.2 Scalar and Vector Potentials in Free Space

The radiation of electromagnetic waves from current and charge distributions in an unbounded domain with homogeneous permittivity ϵ and permeability μ is discussed in the following.

First, the magnetic flux and the electric field can be decomposed with scalar and vector quantities as follows

$$\boldsymbol{E} = -\boldsymbol{\nabla}\varphi - j\omega \boldsymbol{A}, \tag{2.11}$$

$$\boldsymbol{B} = \boldsymbol{\nabla} \times \boldsymbol{A}, \tag{2.12}$$

in which φ and $\boldsymbol{A}$ are the electric scalar potential and the magnetic vector potential, respectively. The existence of these decompositions can be proven using the Helmholtz's theorem, Gauss' law, and Gauss' law for magnetism. Note that φ and $\boldsymbol{A}$ do not have a unique expression, i.e. several expressions of φ and $\boldsymbol{A}$ can lead to the same $\boldsymbol{E}$ and $\boldsymbol{B}$. This degree of freedom is called gauge invariance. Applying the operator $\boldsymbol{\nabla} \times \boldsymbol{\nabla}\times$ to eq. (2.11) gives

$$\boldsymbol{\nabla} \times \boldsymbol{\nabla} \times \boldsymbol{E} = -\boldsymbol{\nabla} \times \boldsymbol{\nabla} \times \boldsymbol{\nabla}\varphi - j\omega \boldsymbol{\nabla} \times \boldsymbol{\nabla} \times \boldsymbol{A}, \tag{2.13}$$

Since $\boldsymbol{\nabla} \times \boldsymbol{\nabla}\varphi = \boldsymbol{0}$, eq. (2.13) reduces to

$$\boldsymbol{\nabla} \times \boldsymbol{\nabla} \times \boldsymbol{A} = -\frac{1}{j\omega} \boldsymbol{\nabla} \times \boldsymbol{\nabla} \times \boldsymbol{E}. \tag{2.14}$$

Then, leveraging Maxwell-Ampère and Maxwell-Faraday equations together with eq. (2.14) gives

$$\begin{aligned} \boldsymbol{\nabla} \times \boldsymbol{\nabla} \times \boldsymbol{A} &= \mu \boldsymbol{\nabla} \times \boldsymbol{H} \\ &= \mu(\boldsymbol{J} + j\omega\epsilon \boldsymbol{E}) \\ &= \mu \boldsymbol{J} - \frac{1}{c^2} j\omega \boldsymbol{\nabla}\phi + \frac{1}{c^2}\omega^2 \boldsymbol{A}, \end{aligned} \tag{2.15}$$

in which $c = 1/\sqrt{\epsilon\mu}$ is the speed of light in the medium.

Next, using the identity $\boldsymbol{\nabla} \times \boldsymbol{\nabla} \times \boldsymbol{A} = \boldsymbol{\nabla}(\boldsymbol{\nabla} \cdot \boldsymbol{A}) - \boldsymbol{\nabla}^2 \boldsymbol{A}$ gives

$$\boldsymbol{\nabla}(\boldsymbol{\nabla} \cdot \boldsymbol{A}) - \boldsymbol{\nabla}^2 \boldsymbol{A} = \mu \boldsymbol{J} - \frac{1}{c^2} j\omega \boldsymbol{\nabla}\phi + \frac{\omega^2}{c^2} \boldsymbol{A}. \tag{2.16}$$

Recalling that the magnetic and electric fields remain invariant through gauge transformations and applying the Lorenz gauge condition ($\nabla \cdot \boldsymbol{A} + \frac{j\omega}{c^2}\phi = 0$) to eq. (2.16), we obtain

$$k^2 \boldsymbol{A} + \boldsymbol{\nabla}^2 \boldsymbol{A} = -\mu \boldsymbol{J}, \tag{2.17}$$

in which $k = \omega/c$ is the wave number of the time harmonic wave. Equation (2.17) is a vector Helmholtz equation. Under the Sommerfeld radiation condition [91], its solution, in this case the magnetic vector potential $\boldsymbol{A}$, can be written as

$$\boldsymbol{A}(\boldsymbol{r}) = \mu \int_{\Omega} G(\boldsymbol{r}, \boldsymbol{r}') \boldsymbol{J}(\boldsymbol{r}') \, \mathrm{d}v', \tag{2.18}$$

with $G(\boldsymbol{r}, \boldsymbol{r}') = e^{-jk\|\boldsymbol{r}-\boldsymbol{r}'\|}/(4\pi\|\boldsymbol{r}-\boldsymbol{r}'\|)$ being the Green's function in free space in $\mathbb{R}^3$ and $\|\cdot\|$ the Euclidean norm. Subsequently, using Maxwell's equations and the relations between the fields and the potentials (eq. (2.11) and eq. (2.12)) leads to the fields radiated by electric sources

$$\boldsymbol{E}_e(\boldsymbol{r}) = -j\omega \boldsymbol{A}(\boldsymbol{r}) + \frac{1}{j\omega\mu\epsilon} \boldsymbol{\nabla}(\boldsymbol{\nabla} \cdot \boldsymbol{A}(\boldsymbol{r})) \tag{2.19}$$

$$\boldsymbol{H}_e(\boldsymbol{r}) = \frac{1}{\mu} \boldsymbol{\nabla} \times \boldsymbol{A}(\boldsymbol{r}). \tag{2.20}$$

Similarly, the electric and magnetic fields created by a magnetic current density $\boldsymbol{M}$ can be obtained by introducing the electric vector potential

$$\boldsymbol{F}(\boldsymbol{r}) = \epsilon \int_{\Omega} G(\boldsymbol{r}, \boldsymbol{r}') \boldsymbol{M}(\boldsymbol{r}') \, \mathrm{d}v', \tag{2.21}$$

which is the solution of the following vector Helmholtz equation

$$\boldsymbol{\nabla}^2 \boldsymbol{F} + k^2 \boldsymbol{F} = -\epsilon \boldsymbol{M}. \tag{2.22}$$

Finally, the electromagnetic fields radiated by magnetic sources can be written as follows

$$\boldsymbol{E}_m(\boldsymbol{r}) = -\frac{1}{\epsilon} \boldsymbol{\nabla} \times \boldsymbol{F}(\boldsymbol{r}) \tag{2.23}$$

$$\boldsymbol{H}_m(\boldsymbol{r}) = -j\omega \boldsymbol{F}(\boldsymbol{r}) + \frac{1}{j\omega\mu\epsilon} \boldsymbol{\nabla}(\boldsymbol{\nabla} \cdot \boldsymbol{F}(\boldsymbol{r})). \tag{2.24}$$

Note that the magnetic sources are not physical and are thus not present in the standard Maxwell's equations. They are employed for the sake of symmetry when interchanging the electric and the magnetic quantities in these equations.

2.1.3 Boundary Conditions

Up to now, the electromagnetic field behavior was described in a continuous medium (unbounded domain). To solve problems in the presence of various types of scatterers, it is necessary to introduce relations between the physical quantities on both sides of the scatterer. Let $\Gamma \in \mathbb{R}^3$ be an interface between two different media with unit normal $\hat{\boldsymbol{n}}$ pointing from media $-$ to media $+$, the physical quantities must satisfy the following conditions near Γ

$$\hat{\boldsymbol{n}} \times (\boldsymbol{H}_+ - \boldsymbol{H}_-) = \boldsymbol{J}_s, \tag{2.25}$$
$$\hat{\boldsymbol{n}} \times (\boldsymbol{E}_+ - \boldsymbol{E}_-) = -\boldsymbol{M}_s, \tag{2.26}$$
$$\hat{\boldsymbol{n}} \cdot (\boldsymbol{B}_+ - \boldsymbol{B}_-) = \rho_{m,s}, \tag{2.27}$$
$$\hat{\boldsymbol{n}} \cdot (\boldsymbol{D}_+ - \boldsymbol{D}_-) = \rho_{e,s}, \tag{2.28}$$

in which $\boldsymbol{J}_s$ denotes an electric surface current density tangential to Γ that makes the tangential component of $\boldsymbol{H}$ discontinuous, $\boldsymbol{M}_s$ is a magnetic surface current density that makes the tangential component of $\boldsymbol{E}$ discontinuous, $\rho_{m,s}$ is the surface magnetic charge density on Γ that makes the normal component of $\boldsymbol{B}$ discontinuous, and $\rho_{e,s}$ is the surface electric charge density on Γ that makes the normal component of $\boldsymbol{D}$ discontinuous.

If media $-$ is a perfect electric conductor (PEC), there are no magnetic currents and surface magnetic charges on Γ, the resulting relations near Γ are

$$\hat{\boldsymbol{n}} \times (\boldsymbol{H}_+ - \boldsymbol{H}_-) = \boldsymbol{J}_s, \tag{2.29}$$
$$\hat{\boldsymbol{n}} \times (\boldsymbol{E}_+ - \boldsymbol{E}_-) = 0, \tag{2.30}$$
$$\hat{\boldsymbol{n}} \cdot (\boldsymbol{B}_+ - \boldsymbol{B}_-) = 0, \tag{2.31}$$
$$\hat{\boldsymbol{n}} \cdot (\boldsymbol{D}_+ - \boldsymbol{D}_-) = \rho_{e,s}. \tag{2.32}$$

This property will be employed later on to derive the surface electric field integral equation for modeling PEC objects.

2.2 Integral Equations

2.2.1 Equivalence Principles

Integral equation methods originate from the equivalence principles. They allow reformulating the original problem by substituting the scatterer with equivalent sources that scatter the same electromagnetic field as the one produced by the original scatterer in the presence of an incident electromagnetic wave. Note that in the following the background is supposed to be vacuum.

2.2.1.1 Surface Equivalence Principle

Let $\Omega \subset \mathbb{R}^3$ be an isotropic and homogeneous domain of permittivity ϵ and permeability μ delimited by a fictitious surface $\Gamma \subset \mathbb{R}^3$ enclosed in a homogeneous background with constant permittivity ϵ_0 and permeability μ_0 and illuminated by incident electric and magnetic fields $\boldsymbol{E}_i$ and $\boldsymbol{H}_i$. From the surface equivalence principle (SEP), it results that the total fields $\boldsymbol{E}$ and $\boldsymbol{H}$ outside Ω are uniquely determined by the incident fields and the scattered fields which are functions of the tangential parts of the $\boldsymbol{E}$ and $\boldsymbol{H}$ on Γ. From the boundary conditions given in eq. (2.25) and eq. (2.26), these tangential field components are the following equivalent surface electric and magnetic current densities

$$\boldsymbol{J}_s(\boldsymbol{r}) = \hat{\boldsymbol{n}}(\boldsymbol{r}) \times \boldsymbol{H}(\boldsymbol{r}), \tag{2.33}$$

$$\boldsymbol{M}_s(\boldsymbol{r}) = -\hat{\boldsymbol{n}}(\boldsymbol{r}) \times \boldsymbol{E}(\boldsymbol{r}), \tag{2.34}$$

in which the fields inside Ω ($\boldsymbol{E}_-$ and $\boldsymbol{H}_-$) are chosen to be zero. Then the interior of Ω can be replaced by a medium with permittivity and permeability equal to ϵ_0 and μ_0, thus creating a configuration in which the surface equivalent sources radiate in an unbounded space of permittivity ϵ_0 and permeability μ_0.

2.2.1.2 Volume Equivalence Principle

The volume equivalence principle also applies to inhomogeneous (potentially anisotropic) scatterers. Let $\Omega \subset \mathbb{R}^3$ be an isotropic and inhomogeneous object of permittivity ϵ and permeability μ enclosed in a homogeneous background with constant permittivity ϵ_0 and permeability μ_0 and illuminated by incident electric and magnetic fields $\boldsymbol{E}_i$ and $\boldsymbol{H}_i$. From the volume equivalence principle (VEP), the fields scattered by Ω can be formulated in terms of volume electric and magnetic current densities in the homogeneous background that read [57]

$$\boldsymbol{J}_v(\boldsymbol{r}) = j\omega\epsilon_0\chi(\boldsymbol{r})\boldsymbol{E}(\boldsymbol{r}), \tag{2.35}$$

$$\boldsymbol{M}_v(\boldsymbol{r}) = j\omega\mu_0\tau(\boldsymbol{r})\boldsymbol{H}(\boldsymbol{r}), \tag{2.36}$$

in which $\chi(\boldsymbol{r}) = \epsilon_r(\boldsymbol{r}) - 1$ is the electric susceptibility and $\tau(\boldsymbol{r}) = \mu_r(\boldsymbol{r}) - 1$ the magnetic susceptibility. Note that the volume equivalent currents are localized only in Ω since χ and τ are zero outside the object.

2.2.2 Field-Source Radiation

Recalling the potential operators defined in eq. (2.18) and eq. (2.21) and their relations with $\boldsymbol{E}$ and $\boldsymbol{H}$ (eq. (2.19) and eq. (2.23)), the total fields radiated by electromagnetic sources in an infinite space can be expressed as follows

$$\boldsymbol{E}(\boldsymbol{r}) = \boldsymbol{E}_i(\boldsymbol{r}) + \boldsymbol{E}_e(\boldsymbol{r}) + \boldsymbol{E}_m(\boldsymbol{r}), \tag{2.37}$$

$$\boldsymbol{H}(\boldsymbol{r}) = \boldsymbol{H}_i(\boldsymbol{r}) + \boldsymbol{H}_e(\boldsymbol{r}) + \boldsymbol{H}_m(\boldsymbol{r}), \tag{2.38}$$

in which $\boldsymbol{E}_i$ and $\boldsymbol{H}_i$ are the incident electric and magnetic fields, $\boldsymbol{E}_e$ and $\boldsymbol{H}_e$ are the electric and magnetic fields due to electric current sources and $\boldsymbol{E}_m$ and $\boldsymbol{H}_m$ are the electric and magnetic fields due to magnetic current sources introduced in section 2.1.2. Calculating $\boldsymbol{E}_e(\boldsymbol{r})$, $\boldsymbol{E}_m(\boldsymbol{r})$, $\boldsymbol{H}_e(\boldsymbol{r})$, and $\boldsymbol{H}_e(\boldsymbol{r})$ near the equivalent sources (Γ or Ω) yields a singularity. All the (volume and surface) terms behave well in this limit except for the curl of the vector potentials (eq. (2.19) and eq. (2.23)) on Γ when considering surface equivalent sources. This singularity requires introducing an additional term, which is function of the relative solid angle subtended in $\boldsymbol{r}$ by Γ [92]

$$\Omega_s(\boldsymbol{r}) = \begin{cases} 1, & r \in \Omega \\ \frac{1}{2}, & r \in \Gamma \\ 0, & \text{otherwise.} \end{cases} \tag{2.39}$$

Note that $\Omega_s(\boldsymbol{r}) = 1$ everywhere in $\mathbb{R}^3$ for volume equivalent sources. Substituting $\boldsymbol{E}_e$, $\boldsymbol{H}_e$, $\boldsymbol{E}_m$, and $\boldsymbol{H}_m$ by their expressions in eq. (2.37) and taking eq. (2.39) into account, both the surface and the volume integral equations can be written as [57, 105]

$$\Omega_s(\boldsymbol{r})\boldsymbol{E}(\boldsymbol{r}) = \boldsymbol{E}_i(\boldsymbol{r}) - j\omega\boldsymbol{A}(\boldsymbol{r}) + \frac{1}{j\omega\mu_0\epsilon_0}\boldsymbol{\nabla}(\boldsymbol{\nabla}\cdot\boldsymbol{A}(\boldsymbol{r})) - \frac{1}{\epsilon_0}\boldsymbol{\nabla}\times\boldsymbol{F}(\boldsymbol{r}), \tag{2.40}$$

$$\Omega_s(\boldsymbol{r})\boldsymbol{H}(\boldsymbol{r}) = \boldsymbol{H}_i(\boldsymbol{r}) - j\omega\boldsymbol{F}(\boldsymbol{r}) + \frac{1}{j\omega\mu_0\epsilon_0}\boldsymbol{\nabla}(\boldsymbol{\nabla}\cdot\boldsymbol{F}(\boldsymbol{r})) + \frac{1}{\mu_0}\boldsymbol{\nabla}\times\boldsymbol{A}(\boldsymbol{r}), \tag{2.41}$$

in which

$$\boldsymbol{A}(\boldsymbol{r}) = \mu_0(\boldsymbol{\mathcal{S}}_\Psi\boldsymbol{J})(\boldsymbol{r}), \tag{2.42}$$

$$\boldsymbol{F}(\boldsymbol{r}) = \epsilon_0(\boldsymbol{\mathcal{S}}_\Psi\boldsymbol{M})(\boldsymbol{r}). \tag{2.43}$$

The operator $\boldsymbol{\mathcal{S}}_\Psi$ is defined as

$$(\boldsymbol{\mathcal{S}}_\Psi\boldsymbol{J})(\boldsymbol{r}) = \int_\Psi G_0(\boldsymbol{r},\boldsymbol{r}')\boldsymbol{J}(\boldsymbol{r}')\,\mathrm{d}\psi', \tag{2.44}$$

with Ψ being the support of the equivalent sources $\boldsymbol{J}$, that is Γ for the surface equivalent sources $\boldsymbol{J_s}$ and Ω for volume equivalent sources $\boldsymbol{J_v}$. Note that $G_0(\boldsymbol{r},\boldsymbol{r}') = \exp(-jk_0\|\boldsymbol{r}-\boldsymbol{r}'\|)/(4\pi\|\boldsymbol{r}-\boldsymbol{r}'\|)$ is the 3D Green's function in vacuum and k_0 is the wave number in vacuum. Finally, the following operators, valid for both surface and volume sources, are introduced for the derivation of the formulations

$$(\boldsymbol{\mathcal{L}}_\Psi\boldsymbol{J})(\boldsymbol{r}) = \left(\boldsymbol{\nabla}\boldsymbol{\nabla}\cdot + k_0^2\right)(\boldsymbol{\mathcal{S}}_\Psi\boldsymbol{J})(\boldsymbol{r}) \tag{2.45}$$

$$(\boldsymbol{\mathcal{N}}_\Psi\boldsymbol{J})(\boldsymbol{r}) = \boldsymbol{\nabla}\times\boldsymbol{\nabla}\times(\boldsymbol{\mathcal{S}}_\Psi\boldsymbol{J})(\boldsymbol{r}) \tag{2.46}$$

$$(\boldsymbol{\mathcal{K}}_\Psi\boldsymbol{J})(\boldsymbol{r}) = \boldsymbol{\nabla}\times(\boldsymbol{\mathcal{S}}_\Psi\boldsymbol{J})(\boldsymbol{r}). \tag{2.47}$$

Note that it is common to split $\boldsymbol{\mathcal{L}}_\Psi$ into the two following operators

$$\left(\boldsymbol{\mathcal{T}}_A^\Psi \boldsymbol{J}\right)(\boldsymbol{r}) = \int_\Psi G_0(\boldsymbol{r},\boldsymbol{r}')\boldsymbol{J}(\boldsymbol{r}')\,\mathrm{d}\psi', \tag{2.48}$$

$$\left(\boldsymbol{\mathcal{T}}_\Phi^\Psi \boldsymbol{J}\right)(\boldsymbol{r}) = \boldsymbol{\nabla}\int_\Psi G_0(\boldsymbol{r},\boldsymbol{r}')\boldsymbol{\nabla}'\cdot\boldsymbol{J}(\boldsymbol{r}')\,\mathrm{d}\psi', \tag{2.49}$$

such that $\boldsymbol{\mathcal{L}}_\Psi = \boldsymbol{\mathcal{T}}_\Phi^\Psi + k_0^2\boldsymbol{\mathcal{T}}_A^\Psi$.

2.2.3 Surface Integral Equations

Surface integral equations (SIE) are employed to model piecewise homogeneous dielectric or conducting objects. Let $\Omega \subset \mathbb{R}^3$ be a simply connected object with closed boundary Γ of permittivity ϵ and permeability μ and illuminated by a time-harmonic incident electric field $\boldsymbol{E_i}$ in a background of permittivity ϵ_0 and permeability μ_0. Equations (2.40) and (2.41) can be solved for the tangential components of the fields by applying the rotated tangential trace operator $\boldsymbol{\gamma}_r$ (trace mapping $H_{\mathrm{Curl}}(\Omega)$ into $H_{\mathrm{Div}}^{-1/2}(\Gamma)$ [105]), which is defined as

$$\boldsymbol{\gamma}_r : \boldsymbol{X} \to \hat{\boldsymbol{n}}(\boldsymbol{r}) \times \boldsymbol{X}\Big|_\Gamma, \tag{2.50}$$

where $\boldsymbol{X}\Big|_\Gamma$ denotes $\boldsymbol{X}$ at the boundary Γ [19]. Note that a more rigorous definition of this operator is provided in [19]. Leveraging eq. (2.40), eq. (2.41), the operators defined in section 2.2.2, and the surface equivalence principle, the resulting electric field (surface EFIE) and magnetic field (surface MFIE) surface integral equations can be written as a 2-by-2 matrix system

$$\begin{bmatrix} \frac{\eta_0}{jk_0}\boldsymbol{\gamma}_r\boldsymbol{\mathcal{L}}_\Gamma & \frac{1}{2}\boldsymbol{\mathcal{I}} - \boldsymbol{\gamma}_r\boldsymbol{\mathcal{K}}_\Gamma \\ -\frac{1}{2}\boldsymbol{\mathcal{I}} + \boldsymbol{\gamma}_r\boldsymbol{\mathcal{K}}_\Gamma & \frac{1}{jk_0\eta_0}\boldsymbol{\gamma}_r\boldsymbol{\mathcal{L}}_\Gamma \end{bmatrix} \begin{bmatrix} \boldsymbol{J}_s \\ \boldsymbol{M}_s \end{bmatrix} = \begin{bmatrix} -\boldsymbol{\gamma}_r\boldsymbol{E}_i \\ -\boldsymbol{\gamma}_r\boldsymbol{H}_i, \end{bmatrix}, \tag{2.51}$$

in which η_0 is the impedance of vacuum and $\boldsymbol{\mathcal{I}}$ is the identity operator. In the dissertation, SIEs are employed to model open metallic objects, which can be considered as PECs, in which there are no magnetic sources. In that case, eq. (2.51) simplifies to

$$\frac{\eta_0}{jk_0}\boldsymbol{\gamma}_r\boldsymbol{\mathcal{L}}_\Gamma\boldsymbol{J}_s = -\boldsymbol{\gamma}_r\boldsymbol{E}_i, \tag{2.52}$$

which can also be written as

$$-j\eta_0 k_0\boldsymbol{\gamma}_r\boldsymbol{\mathcal{T}}_A^\Gamma\boldsymbol{J}_s + \frac{\eta_0}{jk_0}\boldsymbol{\gamma}_r\boldsymbol{\mathcal{T}}_\Phi^\Gamma\boldsymbol{J}_s = -\boldsymbol{\gamma}_r\boldsymbol{E}_i. \tag{2.53}$$

2.2.4 Volume Integral Equations

Volume integral equations (VIE) are employed to model inhomogeneous objects which can possibly be anisotropic, although they are assumed to be isotropic in

the following. Let $\Omega \subset \mathbb{R}^3$ be a dielectric object illuminated by time-harmonic incident electric and magnetic fields $\boldsymbol{E_i}$ and $\boldsymbol{H_i}$ in a background of permittivity ϵ_0 and permeability μ_0. Leveraging the volume equivalence principle (section 2.2.1.2), the scatterer can be substituted by equivalent volume current densities $\boldsymbol{J}_v$ and $\boldsymbol{M}_v$.

2.2.4.1 Current-based VIE (JM-VIE)

Leveraging eqs. (2.35), (2.36), (2.40) and (2.41), the JM-VIE reads

$$\begin{bmatrix} \boldsymbol{\mathcal{I}} - \chi\boldsymbol{\mathcal{L}}_\Omega & j\omega\epsilon_0\chi\boldsymbol{\mathcal{K}}_\Omega \\ -j\omega\mu_0\tau\boldsymbol{\mathcal{K}}_\Omega & \boldsymbol{\mathcal{I}} - \tau\boldsymbol{\mathcal{L}}_\Omega \end{bmatrix} \begin{bmatrix} \boldsymbol{J}_v \\ \boldsymbol{M}_v \end{bmatrix} = \begin{bmatrix} j\omega\epsilon_0\chi\boldsymbol{E}_i \\ j\omega\mu_0\tau\boldsymbol{H}_i \end{bmatrix}. \tag{2.54}$$

In this dissertation, non-magnetic problems are treated, so that eq. (2.54) becomes the current volume integral equation (J-VIE) and can be written as follows

$$\boldsymbol{J}_v(\boldsymbol{r}) - \chi(\boldsymbol{r})\boldsymbol{\mathcal{L}}_\Omega(\boldsymbol{J}_v(\boldsymbol{r})) = j\omega\epsilon_0\chi(\boldsymbol{r})\boldsymbol{E}_i(\boldsymbol{r}). \tag{2.55}$$

To make its discretization possible, the J-VIE is written as an equivalent form of eq. (2.55) which leverages the identity $\boldsymbol{\mathcal{L}}_\Omega(\boldsymbol{J_v}) = \boldsymbol{\mathcal{N}}_\Omega(\boldsymbol{J_v}) - \boldsymbol{J_v}$ introduced in [93]. This second version of the J-VIE reads

$$\boldsymbol{J_v}(\boldsymbol{r}) - \chi(\boldsymbol{r})\left(\boldsymbol{\mathcal{N}}_\Omega(\boldsymbol{J_v}(\boldsymbol{r})) - \boldsymbol{J_v}(\boldsymbol{r})\right) = j\omega\epsilon_0\chi(\boldsymbol{r})\boldsymbol{E}_i(\boldsymbol{r}). \tag{2.56}$$

2.2.4.2 Electric Flux VIE (DB-VIE)

Solving the VIE for the electric flux density $\boldsymbol{D}$ and the magnetic flux density $\boldsymbol{B}$ requires expressing the volume equivalent currents in terms of $\boldsymbol{D}$ and $\boldsymbol{B}$

$$\boldsymbol{J_v}(\boldsymbol{r}) = j\omega\kappa(\boldsymbol{r})\boldsymbol{D}(\boldsymbol{r}), \tag{2.57}$$
$$\boldsymbol{M_v}(\boldsymbol{r}) = j\omega\iota(\boldsymbol{r})\boldsymbol{B}(\boldsymbol{r}), \tag{2.58}$$

where $\kappa(\boldsymbol{r}) = (\epsilon_r(\boldsymbol{r})-1)/\epsilon_r(\boldsymbol{r})$ is the dielectric contrast and $\iota(\boldsymbol{r}) = (\mu_r(\boldsymbol{r})-1)/\mu_r(\boldsymbol{r})$ is the ferromagnetic contrast. The DB-VIE thus obtained reads

$$\begin{bmatrix} \epsilon^{-1}\boldsymbol{\mathcal{I}} - \boldsymbol{\mathcal{L}}_\kappa^\Omega & j\omega\mu_0\boldsymbol{\mathcal{K}}_\iota^\Omega \\ -j\omega\epsilon_0\boldsymbol{\mathcal{K}}_\kappa^\Omega & \mu^{-1}\boldsymbol{\mathcal{I}} - \boldsymbol{\mathcal{L}}_\iota^\Omega \end{bmatrix} \begin{bmatrix} \boldsymbol{D} \\ \boldsymbol{B} \end{bmatrix} = \begin{bmatrix} \boldsymbol{E}_i \\ \boldsymbol{H}_i \end{bmatrix}, \tag{2.59}$$

in which $\boldsymbol{\mathcal{A}}_c^\Omega(\boldsymbol{X}) = \boldsymbol{\mathcal{A}}_\Omega(c\boldsymbol{X})$. With non-magnetic objects, eq. (2.59) reduces to the electric flux volume integral equation (D-VIE)

$$\frac{\boldsymbol{D}(\boldsymbol{r})}{\epsilon(\boldsymbol{r})} - \left(\boldsymbol{\mathcal{L}}_\kappa^\Omega\boldsymbol{D}\right)(\boldsymbol{r}) = \boldsymbol{E}_i(\boldsymbol{r}), \tag{2.60}$$

with

$$\left(\boldsymbol{\mathcal{L}}_\kappa^\Omega\boldsymbol{D}\right)(\boldsymbol{r}) = \frac{k_0^2}{\epsilon_0}\left(\boldsymbol{\mathcal{T}}_A^{\kappa,\Omega}\boldsymbol{D}\right)(\boldsymbol{r}) + \frac{1}{\epsilon_0}\left(\boldsymbol{\mathcal{T}}_\Phi^{\kappa,\Omega}\boldsymbol{D}\right)(\boldsymbol{r}), \tag{2.61}$$

in which $\boldsymbol{\mathcal{T}}_O^{c,\Omega}(\boldsymbol{X}) = \boldsymbol{\mathcal{T}}_O^{\Omega}(c\boldsymbol{X})$. In the following, it will be also required to define an operator that maps κ to $\boldsymbol{E}_s$ for a given electric flux. This new operator $\boldsymbol{\mathcal{L}}_{\boldsymbol{D}}^{\Omega_D}$ is defined such that

$$\left(\boldsymbol{\mathcal{L}}_{\boldsymbol{D}}^{\Omega}\kappa\right)(\boldsymbol{r}) = \left(\boldsymbol{\mathcal{L}}_{\kappa}^{\Omega}\boldsymbol{D}\right)(\boldsymbol{r}). \tag{2.62}$$

2.2.5 Hybrid Volume Surface Integral Equations

An electric hybrid volume-surface integral equation (HVSIE) combines a surface integral equation and a volume integral equation to model inhomogeneous dielectric bodies together with PEC objects. Consider a composite scatterer made of a PEC object with boundary Γ (can be either open or closed) and a linear inhomogeneous dielectric object Ω illuminated by a time-harmonic incident electromagnetic wave $\boldsymbol{E}_i$ in a background medium with permittivity ϵ_0 and permeability μ_0, as shown in fig. 2.1.

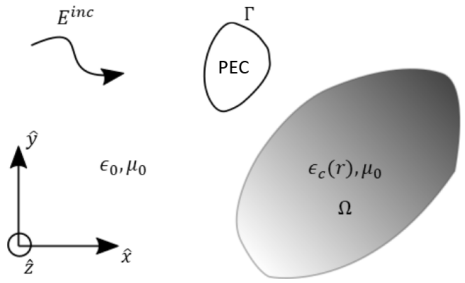

Figure 2.1: Description of the 3D scattering problem. The PEC parts are modeled by their boundary (i.e. Γ) and the dielectric parts are modeled by their volume (i.e. Ω).

Using both the volume equivalence principle (section 2.2.1.2) and the surface equivalence principle (section 2.2.1.1), the dielectric bodies can be replaced by an equivalent volume current density $\boldsymbol{J}_d$ in Ω and the conducting objects by an equivalent surface current density $\boldsymbol{J}_s$ on Γ. The volume current density is defined as

$$\boldsymbol{J}_d(\boldsymbol{r}) = j\omega\boldsymbol{D}(\boldsymbol{r}). \tag{2.63}$$

Note that the HVSIE is solved for $\boldsymbol{J}_d$ so that both the volume and surface unknowns have the dimension of a current density. The total field $\boldsymbol{E}$ can then be written as a sum of the incident field and the scattered fields

$$\boldsymbol{E}(\boldsymbol{r}) = \boldsymbol{E}_i(\boldsymbol{r}) + \boldsymbol{E}_s^v(\boldsymbol{r}) + \boldsymbol{E}_s^s(\boldsymbol{r}), \tag{2.64}$$

where $\boldsymbol{E}_s^s$ is the field scattered by $\boldsymbol{J}_s$ and $\boldsymbol{E}_s^v$ is the field scattered by $\boldsymbol{J}_d$

$$\boldsymbol{E}_s^v(\boldsymbol{r}) = -jk_0\eta_0\boldsymbol{\mathcal{T}}_A^{\kappa,\Omega}(\boldsymbol{J}_d(\boldsymbol{r}')) + \frac{\eta_0}{jk_0}\boldsymbol{\mathcal{T}}_\Phi^{\kappa,\Omega}(\boldsymbol{J}_d(\boldsymbol{r}')), \tag{2.65}$$

$$\boldsymbol{E}_s^s(\boldsymbol{r}) = -jk_0\eta_0\boldsymbol{\mathcal{T}}_A^{\Gamma}(\boldsymbol{J}_s(\boldsymbol{r}')) + \frac{\eta_0}{jk_0}\boldsymbol{\mathcal{T}}_\Phi^{\Gamma}(\boldsymbol{J}_s(\boldsymbol{r}')). \tag{2.66}$$

The resulting volume integral equation in Ω can be expressed as

$$\frac{\boldsymbol{J}_d(\boldsymbol{r})}{j\omega\epsilon(\boldsymbol{r})} - \boldsymbol{E}_s^v(\boldsymbol{J}_d(\boldsymbol{r}')) - \boldsymbol{E}_s^s(\boldsymbol{J}_s(\boldsymbol{r}')) = \boldsymbol{E}_i(\boldsymbol{r}), \quad \boldsymbol{r} \in \Omega. \tag{2.67}$$

On a PEC object, the boundary conditions require that the tangential component of the total electric field vanishes. This gives the surface integral equation on Γ

$$-\boldsymbol{\gamma}_r\boldsymbol{E}_i(\boldsymbol{r}) = \boldsymbol{\gamma}_r\boldsymbol{E}_s^v(\boldsymbol{J}_d(\boldsymbol{r}')) + \boldsymbol{\gamma}_r\boldsymbol{E}_s^s(\boldsymbol{J}_s(\boldsymbol{r}')), \quad \boldsymbol{r} \in \Gamma. \tag{2.68}$$

In the HVSIE, eq. (2.67) and eq. (2.68) should be simultaneously solved for $\boldsymbol{J}_d$ and $\boldsymbol{J}_s$.

2.3 Numerical Solutions of Integral Equations

The various formulations that were presented above provide the exact solutions to Maxwell's equations. However, there exists a known analytical solution only in few canonical cases (e.g. dielectric sphere, PEC sphere). In real-world scattering scenarios, the geometry of the scatterer is often too complicated to derive an analytic solution. This explains the need for numerical methods in electromagnetics. They allow solving complicated electromagnetic problems by approximating them. In the following, it is shown how the formulations employed in the rest of the thesis are numerically solved.

2.3.1 Method of Moments

All the numerical solutions presented in this section are obtained by applying the method of moments (MoM) [57]. It consists in transforming an integral equation (e.g. D-VIE, J-VIE) into a linear system. We start from the following integral equation

$$\boldsymbol{\mathcal{L}}x = y, \tag{2.69}$$

in which $\boldsymbol{\mathcal{L}}$ is the integral operator, x is the solution that we are looking for, and y is a known excitation term. To solve eq. (2.69) in the general case, we first assume that x can be approximated using a set of basis functions $\{f_m\}$

$$x \approx \sum_{m=1}^{N} [\boldsymbol{x}]_m f_m, \tag{2.70}$$

in which N is the number of basis functions and $[\boldsymbol{x}]_m$ is the coefficient of the discretized solution associated to the basis function f_m. Note that f_m is function of the position $\boldsymbol{r}$. Inserting eq. (2.70) into eq. (2.69) yields

$$\sum_{m=1}^{N} [\boldsymbol{x}]_m \boldsymbol{\mathcal{L}} f_m = y. \tag{2.71}$$

To be solved numerically, eq. (2.71) also needs to be discretized. This step is called the *testing* procedure. It consists in taking the inner product between eq. (2.71) and a set of testing functions $\{g_n\}$. We obtain

$$\sum_{m=1}^{N} [\boldsymbol{x}]_m \langle g_n, \boldsymbol{\mathcal{L}} f_m \rangle_\Omega = \langle g_n, y \rangle_\Omega, \quad n = 1,2,...,N, \tag{2.72}$$

where $\langle a, b \rangle_\Omega = \int_\Omega a(\boldsymbol{r}) \cdot b(\boldsymbol{r}) \, \mathrm{d}v$ is the L^2-inner product with $\boldsymbol{r} \in \Omega$ and $\Omega \subset \mathbb{R}^3$. Equation (2.72) is a system of equations which can be rewritten in a matrix form as

$$\boldsymbol{Z}\boldsymbol{x} = \boldsymbol{y}, \tag{2.73}$$

in which $\boldsymbol{Z}$ is the system matrix whose elements are defined as

$$[\boldsymbol{Z}]_{nm} = \langle g_n, \boldsymbol{\mathcal{L}} f_m \rangle_\Omega, \tag{2.74}$$

and $\boldsymbol{x}$ and $\boldsymbol{y}$ are the solution and excitation vectors, respectively. The elements of $\boldsymbol{y}$ read

$$[\boldsymbol{y}]_n = \langle g_n, y \rangle_\Omega. \tag{2.75}$$

After solving eq. (2.73) for $\boldsymbol{x}$, we finally get an approximation of the solution using eq. (2.70).

2.3.2 Surface EFIE

In this section, we provide the discretization of the surface EFIE with Rao-Wilton-Glisson basis functions [86] on a triangular discretization of Γ with N_{Tri} triangles.

2.3.2.1 Rao-Wilton-Glisson basis functions

The RWG basis functions are divergence conforming basis functions (they live in the functional space $H_{\text{Div}}^{-1/2}(\Gamma)$) and thus allow the proper discretization of the EFIE. An RWG function associated to the edge n in a triangular discretization is defined as

$$\boldsymbol{f_n}(\boldsymbol{r}) = \begin{cases} \boldsymbol{f_n^+}(\boldsymbol{r}) = \frac{\boldsymbol{r} - \boldsymbol{r}_n^+}{2A_n^+}, & \boldsymbol{r} \in T_n^+ \\ \boldsymbol{f_n^-}(\boldsymbol{r}) = -\frac{\boldsymbol{r} - \boldsymbol{r}_n^-}{2A_n^-}, & \boldsymbol{r} \in T_n^- \end{cases} \tag{2.76}$$

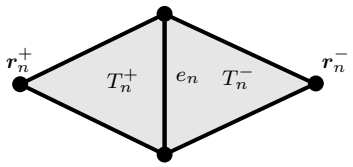

Figure 2.2: Convention used to define the RWG functions: the RWG basis function is defined on the two triangles T_n^+ and T_n^- that are formed with their common edge e_n and the vertices $\boldsymbol{r}_n^+$ and $\boldsymbol{r}_n^-$, respectively.

in which $T_n^\pm$ denotes the pair of triangles on which $\boldsymbol{f}_n^\pm$ is defined, $A_n^\pm$ is the area of $T_n^\pm$, and $\boldsymbol{r}_n^\pm$ is the vertex of $T_n^\pm$ that does not belong to e_n, the shared edge of T_n^+ and T_n^- (see fig. 2.2).

The current $\boldsymbol{J}_s$ can be approximated as a linear combination of RWG basis functions as follows

$$\boldsymbol{J}_s(\boldsymbol{r}) \approx \sum_{m=1}^{N_E} [\boldsymbol{\alpha}]_m \boldsymbol{f}_m(\boldsymbol{r}), \tag{2.77}$$

in which N_E is the number of RWG basis functions. Since the surface EFIE operators maps $H_{\text{Div}}^{-1/2}(\Gamma)$ to itself, the testing functions should belong to the dual of $H_{\text{Div}}^{-1/2}(\Gamma)$, which is $H_{\text{Curl}}^{-1/2}(\Gamma)$ [19]. The basis functions pertaining to that space are the rotated RWG functions $\{\hat{\boldsymbol{n}} \times \boldsymbol{f}_n\}$. The resulting linear system reads

$$\boldsymbol{Z}\boldsymbol{\alpha} = (\boldsymbol{Z}_{\boldsymbol{A}} + \boldsymbol{Z}_{\boldsymbol{\Phi}})\,\boldsymbol{\alpha} = \boldsymbol{v}, \tag{2.78}$$

where

$$[\boldsymbol{Z}_{\boldsymbol{A}}]_{nm} = -j\eta_0 k_0 \langle \hat{\boldsymbol{n}} \times \boldsymbol{f}_n, \boldsymbol{\gamma}_r \boldsymbol{\mathcal{T}}_A^\Gamma \boldsymbol{f}_m \rangle_\Gamma, \tag{2.79}$$

$$[\boldsymbol{Z}_{\boldsymbol{\Phi}}]_{nm} = \frac{\eta_0}{jk_0} \langle \hat{\boldsymbol{n}} \times \boldsymbol{f}_n, \boldsymbol{\gamma}_r \boldsymbol{\mathcal{T}}_\Phi^\Gamma \boldsymbol{f}_m \rangle_\Gamma, \tag{2.80}$$

$$[\boldsymbol{v}]_n = -\langle \hat{\boldsymbol{n}} \times \boldsymbol{f}_n, \boldsymbol{\gamma}_r \boldsymbol{E}_i \rangle_\Gamma. \tag{2.81}$$

2.3.3 J-VIE

In the J-VIE the inhomogeneous scatterer Ω is discretized with N_T tetrahedra with each tetrahedron having a constant permittivity. The current $\boldsymbol{J}_v$ is decomposed into its three Cartesian components ($\boldsymbol{J}_v(\boldsymbol{r}) = \boldsymbol{J}_v^x(\boldsymbol{r})\hat{\boldsymbol{x}} + \boldsymbol{J}_v^y(\boldsymbol{r})\hat{\boldsymbol{y}} + \boldsymbol{J}_v^z(\boldsymbol{r})\hat{\boldsymbol{z}}$). Each component is discretized with a piecewise constant basis function

$$\boldsymbol{J}_c^\alpha(\boldsymbol{r}) \approx \sum_{m=1}^{N_T} [\boldsymbol{a}]_m^\alpha \boldsymbol{f}_m^\alpha(\boldsymbol{r}), \tag{2.82}$$

in which $\hat{\boldsymbol{\alpha}} = \hat{\boldsymbol{x}},\ \hat{\boldsymbol{y}},\ \hat{\boldsymbol{z}}$. The basis function $\boldsymbol{f}_m^\alpha$, which lives in the functional space $L^2(\Omega)^3$, is defined as

$$\boldsymbol{f}_m^\alpha(\boldsymbol{r}) = \hat{\boldsymbol{\alpha}} P_m(\boldsymbol{r}), \tag{2.83}$$

with $P_n \in L^2(\Omega)$ being a volumetric patch with support in tetrahedron T_n. The relative permittivity in Ω is also defined using P_n

$$\epsilon_r(\boldsymbol{r}) = \sum_{m=1}^{N_T} \epsilon_r(\boldsymbol{r}_m) P_m(\boldsymbol{r}), \tag{2.84}$$

in which $\boldsymbol{r}_n$ is the center of tetrahedron T_n. Using the fact that the J-VIE operator (eq. (2.55)) maps $L^2(\Omega)^3$ to itself and that $L^2(\Omega)^3$ is its own dual [70], a Garlerkin testing procedure (same source and testing basis functions) can be applied on eq. (2.56), which results in the following linear system

$$\left([\boldsymbol{R}]^{\beta\alpha} + [\boldsymbol{R}_\chi]^{\beta\alpha} - [\boldsymbol{I}]^{\beta\alpha}\right)[\boldsymbol{a}]^{\alpha} = [\boldsymbol{v}]^{\beta}, \tag{2.85}$$

in which $[\boldsymbol{R}]^{\beta\alpha} \in \mathbb{R}^{N_T \times N_T}$, $[\boldsymbol{R}_\chi]^{\beta\alpha} \in \mathbb{R}^{N_T \times N_T}$, $[\boldsymbol{I}]^{\beta\alpha} \in \mathbb{R}^{N_T \times N_T}$, and $[\boldsymbol{v}]^{\beta} \in \mathbb{R}^{N_T \times 1}$ are defined as

$$[\boldsymbol{R}]^{\beta\alpha}_{nm} = \langle \boldsymbol{f}^{\boldsymbol{\beta}}_{\boldsymbol{n}}, \boldsymbol{f}^{\boldsymbol{\alpha}}_{\boldsymbol{m}} \rangle_\Omega, \tag{2.86}$$

$$[\boldsymbol{R}_\chi]^{\beta\alpha}_{nm} = \langle \boldsymbol{f}^{\boldsymbol{\beta}}_{\boldsymbol{n}}, \chi \boldsymbol{f}^{\boldsymbol{\alpha}}_{\boldsymbol{m}} \rangle_\Omega, \tag{2.87}$$

$$[\boldsymbol{I}]^{\beta\alpha}_{nm} = \langle \boldsymbol{f}^{\boldsymbol{\beta}}_{\boldsymbol{n}}, \chi \boldsymbol{\mathcal{N}} \boldsymbol{f}^{\boldsymbol{\alpha}}_{\boldsymbol{m}} \rangle_\Omega, \tag{2.88}$$

$$[\boldsymbol{v}]^{\beta}_{n} = j\omega\epsilon_0 \langle \boldsymbol{f}^{\boldsymbol{\beta}}_{\boldsymbol{n}}, \chi \boldsymbol{E_i} \rangle_\Omega, \tag{2.89}$$

where $\boldsymbol{\alpha}$, $\boldsymbol{\beta} = \boldsymbol{x}$, $\boldsymbol{y}$, $\boldsymbol{z}$. The procedure to numerically compute eq. (2.86), eq. (2.88), and eq. (2.89) can be found in [83].

2.3.4 D-VIE

This section presents the discretization of the D-VIE with Schaubert-Wilton-Glisson (SWG) basis functions [89] in a tetrahedral discretization of Ω with N_T tetrahedra.

2.3.4.1 Schaubert-Wilton-Glisson basis functions

The SWG basis functions are divergence conforming basis functions (they live in the functional space $H_{\text{Div}}(\Omega) \subset L^2(\Omega)^3$) and are thus suitable functions for the discretization of the D-VIE. The SWG function associated to the face n is

$$\boldsymbol{f_n}(\boldsymbol{r}) = \begin{cases} \boldsymbol{f_n^+}(\boldsymbol{r}) = \frac{1}{3V_n^+}(\boldsymbol{r} - \boldsymbol{r_n^+}), & \boldsymbol{r} \in T_n^+ \\ \boldsymbol{f_n^-}(\boldsymbol{r}) = -\frac{1}{3V_n^-}(\boldsymbol{r} - \boldsymbol{r_n^-}), & \boldsymbol{r} \in T_n^-, \end{cases} \tag{2.90}$$

in which $T_n^\pm$ denotes the pair of tetrahedra on which $\boldsymbol{f_n}$ is defined, $V_n^\pm$ is the volume of $T_n^\pm$, and $\boldsymbol{r}_n^\pm$ is the vertex of $T_n^\pm$ that does not to belong to Γ_n, the shared face of T_n^+ and T_n^- (see fig. 2.3). In the following, we will use the notation $\boldsymbol{f_n^\pm}$ to denote

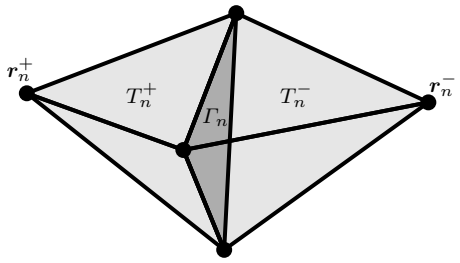

Figure 2.3: Convention used to define the SWG and the star functions: the SWG basis function is defined on the two tetrahedra T_n^+ and T_n^- that are formed with their common face Γ_n and the vertices $\boldsymbol{r}_n^+$ and $\boldsymbol{r}_n^-$, respectively. The half SWG basis functions are defined on T_n^+ only.

the part of the basis function $\boldsymbol{f_n}$ that is defined in $T_n^\pm$. The basis functions defined at the boundary of a discretized object are defined in one tetrahedron to properly model the surface charges, they are referred to as half basis functions. Note here that, by convention, the half basis function $\boldsymbol{f_m}$ is always supported by tetrahedron T_m^+. Another important property of an SWG basis function is the expression of its divergence

$$\nabla \cdot \boldsymbol{f_n}(\boldsymbol{r}) = \begin{cases} \nabla \cdot \boldsymbol{f_n^+}(\boldsymbol{r}) = \frac{1}{V_n^+}, & \boldsymbol{r} \in T_n^+ \\ \nabla \cdot \boldsymbol{f_n^-}(\boldsymbol{r}) = -\frac{1}{V_n^-}, & \boldsymbol{r} \in T_n^-. \end{cases} \tag{2.91}$$

2.3.4.2 Discretization of the D-VIE

The unknown D in Equation (2.60) must exhibit a continuous normal component through material discontinuities, it is thus discretized with SWG basis functions $\{\boldsymbol{f_m}\}$

$$\boldsymbol{D}(\boldsymbol{r}) \approx \sum_{m=1}^{N_F} [\boldsymbol{\alpha}]_m \boldsymbol{f_m}(\boldsymbol{r}). \tag{2.92}$$

in which N_F is the number of faces in the tetrahedral mesh. Since the range of the D-VIE operator lies in $H_{\text{Curl}}(\Omega)$ [70], this formulation can be properly tested with SWG basis functions which are in its dual space. Moreover, testing with the functions $\{\kappa \boldsymbol{f_n}\}$, which are SWG functions scaled with the material contrast κ [16], yields the linear system

$$\boldsymbol{Z^\kappa \alpha} = (\boldsymbol{G_\epsilon^\kappa} + \boldsymbol{Z_A^\kappa} + \boldsymbol{Z_\phi^\kappa})\, \boldsymbol{\alpha} = \boldsymbol{v^\kappa}, \tag{2.93}$$

where

$$[\boldsymbol{G}_{\boldsymbol{\epsilon}}^{\boldsymbol{\kappa}}]_{nm} = \langle \kappa \boldsymbol{f_n}, \boldsymbol{f_m}/\epsilon \rangle_\Omega \tag{2.94}$$

$$[\boldsymbol{Z}_{\boldsymbol{A}}^{\boldsymbol{\kappa}}]_{nm} = -k_0^2 {\epsilon_0}^{-1} \langle \kappa \boldsymbol{f_n}, \boldsymbol{\mathcal{T}}_A \boldsymbol{f_m} \rangle_\Omega \tag{2.95}$$

$$[\boldsymbol{Z}_{\boldsymbol{\Phi}}^{\boldsymbol{\kappa}}]_{nm} = -{\epsilon_0}^{-1} \langle \kappa \boldsymbol{f_n}, \boldsymbol{\mathcal{T}}_\Phi \boldsymbol{f_m} \rangle_\Omega \tag{2.96}$$

$$[\boldsymbol{v}^{\boldsymbol{\kappa}}]_n = \langle \kappa \boldsymbol{f_n}, \boldsymbol{E_i} \rangle_\Omega, \tag{2.97}$$

in which all the matrices are symmetric. By expanding eq. (2.94), eq. (2.95), eq. (2.96), and eq. (2.97), we get

$$[\boldsymbol{G}_{\boldsymbol{\epsilon}}^{\boldsymbol{\kappa}}]_{nm} = \int_\Omega \kappa(\boldsymbol{r}) \boldsymbol{f_n}(\boldsymbol{r}) \cdot \epsilon(\boldsymbol{r})^{-1} \boldsymbol{f_m}(\boldsymbol{r}) \, \mathrm{d}v \tag{2.98}$$

$$[\boldsymbol{Z}_{\boldsymbol{A}}^{\boldsymbol{\kappa}}]_{nm} = -\frac{k_0^2}{\epsilon_0} \int_\Omega \kappa(\boldsymbol{r}) \boldsymbol{f_n}(\boldsymbol{r}) \cdot \int_\Omega \kappa(\boldsymbol{r'}) \boldsymbol{f_m}(\boldsymbol{r'}) G_0(\boldsymbol{r}, \boldsymbol{r'}) \, \mathrm{d}v' \, \mathrm{d}v \tag{2.99}$$

$$[\boldsymbol{Z}_{\boldsymbol{\Phi}}^{\boldsymbol{\kappa}}]_{nm} = -\frac{1}{\epsilon_0} \int_\Omega \kappa(\boldsymbol{r}) \boldsymbol{f_n}(\boldsymbol{r}) \cdot \nabla \int_\Omega \nabla' \cdot (\kappa(\boldsymbol{r'}) \boldsymbol{f_m}(\boldsymbol{r'})) \, G_0(\boldsymbol{r}, \boldsymbol{r'}) \, \mathrm{d}v' \, \mathrm{d}v \tag{2.100}$$

$$[\boldsymbol{v}^{\boldsymbol{\kappa}}]_n = \int_\Omega \kappa(\boldsymbol{r}) \boldsymbol{f_n}(\boldsymbol{r}) \cdot \boldsymbol{E}_i(\boldsymbol{r}) \, \mathrm{d}v. \tag{2.101}$$

The term $[\boldsymbol{Z}_{\boldsymbol{\Phi}}^{\boldsymbol{\kappa}}]_{nm}$ in eq. (2.100) can be expanded further. Using an integration by parts, the divergence theorem, and the property of SWG basis functions, it can be shown that

$$\begin{aligned}
[\boldsymbol{Z}_{\boldsymbol{\Phi}}^{\boldsymbol{\kappa}}]_{nm} &= -\frac{1}{\epsilon_0} \int_\Omega \nabla \cdot (\kappa(\boldsymbol{r}) \boldsymbol{f_n}(\boldsymbol{r})) \int_\Omega \nabla' \cdot (\kappa(\boldsymbol{r'}) \boldsymbol{f_m}(\boldsymbol{r'})) \, G_0(\boldsymbol{r}, \boldsymbol{r'}) \, \mathrm{d}v' \, \mathrm{d}v, \\
&= -\frac{1}{\epsilon_0} \int_\Omega \kappa(\boldsymbol{r}) \nabla \cdot \boldsymbol{f_n}(\boldsymbol{r}) \int_{\Gamma_m} \delta\kappa_m \hat{\boldsymbol{n}}_m \cdot \boldsymbol{f_m}(\boldsymbol{r'}) G_0(\boldsymbol{r}, \boldsymbol{r'}) \, \mathrm{d}s' \, \mathrm{d}v \\
&+ \int_\Omega \kappa(\boldsymbol{r}) \nabla \cdot \boldsymbol{f_n}(\boldsymbol{r}) \int_\Omega \kappa(\boldsymbol{r}) \nabla \cdot \boldsymbol{f_m}(\boldsymbol{r'}) G_0(\boldsymbol{r}, \boldsymbol{r'}) \, \mathrm{d}v' \, \mathrm{d}v \\
&+ \int_{\Gamma_n} \delta\kappa_n \hat{\boldsymbol{n}}_n \cdot \boldsymbol{f_n}(\boldsymbol{r}) \int_{\Gamma_m} \delta\kappa_m \hat{\boldsymbol{n}}_m \cdot \boldsymbol{f_m}(\boldsymbol{r'}) G_0(\boldsymbol{r}, \boldsymbol{r'}) \, \mathrm{d}s' \, \mathrm{d}s \\
&+ \int_{\Gamma_n} \delta\kappa_n \hat{\boldsymbol{n}}_n \cdot \boldsymbol{f_n}(\boldsymbol{r}) \int_\Omega \kappa(\boldsymbol{r}) \nabla \cdot \boldsymbol{f_n}(\boldsymbol{r}) G_0(\boldsymbol{r}, \boldsymbol{r'}) \, \mathrm{d}v' \, \mathrm{d}s,
\end{aligned} \tag{2.102}$$

in which $\delta\kappa_n = \kappa_n^- - \kappa_n^+$ and $\hat{\boldsymbol{n}}_m$ is a unit vector normal to Γ_m oriented from T_m^+ to T_m^-. For the half basis functions $\boldsymbol{f_n}$, $\delta\kappa_n = -\kappa_n^+$.

2.3.4.3 Discretization of the D-VIE with monopolar SWG functions

In some applications, it can be convenient to extract the material dependence from the discretized operator to be able to update the full discretized operator $\boldsymbol{Z}$ by recalculating solely its material dependent part. Since the material is piecewise constant in the tetrahedra of the discretized geometry, this can be done by splitting the SWG basis function into two, a part defined on T_n^+ ($\boldsymbol{f_n^+}$) and another part

defined in T_n^- ($\boldsymbol{f}_n^-$). A similar procedure is presented in [97, 63] for RWG basis functions, it is referred to as a monopolar representation of the basis function. The monopolar matrices, which are the matrices that do not depend on the material parameters, are provided in the following. $\boldsymbol{G}_{\boldsymbol{vv}} \in \mathbb{C}^{2N_F \times 2N_F}$ is defined as follows

$$\boldsymbol{G}_{\boldsymbol{vv}} = \begin{bmatrix} \boldsymbol{G}_{\boldsymbol{vv}}^{++} & \boldsymbol{G}_{\boldsymbol{vv}}^{+-} \\ \boldsymbol{G}_{\boldsymbol{vv}}^{-+} & \boldsymbol{G}_{\boldsymbol{vv}}^{--} \end{bmatrix}, \tag{2.103}$$

in which $\boldsymbol{G}_{\boldsymbol{vv}}^{\pm\pm} \in \mathbb{C}^{N_F \times N_F}$ is defined as $[\boldsymbol{G}_{\boldsymbol{vv}}^{\pm\pm}]_{nm} = \int_\Omega \boldsymbol{f}_{\boldsymbol{n}}^{\pm}(\boldsymbol{r}) \cdot \boldsymbol{f}_{\boldsymbol{m}}^{\pm}(\boldsymbol{r})\, \mathrm{d}v$.

The monopolar matrix for the vector potential $\boldsymbol{Z}_{\boldsymbol{A}}$ reads

$$\boldsymbol{Z}_{\boldsymbol{A},\boldsymbol{vv}} = \begin{bmatrix} \boldsymbol{Z}_{\boldsymbol{A},\boldsymbol{vv}}^{++} & \boldsymbol{Z}_{\boldsymbol{A},\boldsymbol{vv}}^{+-} \\ \boldsymbol{Z}_{\boldsymbol{A},\boldsymbol{vv}}^{-+} & \boldsymbol{Z}_{\boldsymbol{A},\boldsymbol{vv}}^{--} \end{bmatrix}, \tag{2.104}$$

in which $[\boldsymbol{Z}_{\boldsymbol{A},\boldsymbol{vv}}^{\pm\pm}]_{nm} = k_0^2 \epsilon_0^{-1} \int_\Omega \boldsymbol{f}_{\boldsymbol{n}}^{\pm}(\boldsymbol{r}) \cdot \int_\Omega G_0(\boldsymbol{r}, \boldsymbol{r}') \boldsymbol{f}_{\boldsymbol{m}}^{\pm}(\boldsymbol{r}')\, \mathrm{d}v'\, \mathrm{d}v$. The scalar potential matrix $\boldsymbol{Z}_{\boldsymbol{\Phi}}$ can be subdivided into 4 monopolar matrices. $\boldsymbol{Z}_{\boldsymbol{\Phi},\boldsymbol{vv}} \in \mathbb{C}^{2N_F \times 2N_F}$ is defined as follows

$$\boldsymbol{Z}_{\boldsymbol{\Phi},\boldsymbol{vv}} = \begin{bmatrix} \boldsymbol{Z}_{\boldsymbol{\Phi},\boldsymbol{vv}}^{++} & \boldsymbol{Z}_{\boldsymbol{\Phi},\boldsymbol{vv}}^{+-} \\ \boldsymbol{Z}_{\boldsymbol{\Phi},\boldsymbol{vv}}^{-+} & \boldsymbol{Z}_{\boldsymbol{\Phi},\boldsymbol{vv}}^{--} \end{bmatrix}, \tag{2.105}$$

where $[\boldsymbol{Z}_{\boldsymbol{\Phi},\boldsymbol{vv}}^{\pm\pm}]_{nm} = \epsilon_0^{-1} \int_\Omega \nabla \cdot \boldsymbol{f}_{\boldsymbol{n}}^{\pm}(\boldsymbol{r}) \int_\Omega G_0(\boldsymbol{r}, \boldsymbol{r}') \nabla \cdot \boldsymbol{f}_{\boldsymbol{m}}^{\pm}(\boldsymbol{r}')\, \mathrm{d}v'\, \mathrm{d}v$.

The monopolar matrix $\boldsymbol{Z}_{\boldsymbol{\Phi},\boldsymbol{sv}} \in \mathbb{C}^{N_F \times 2N_F}$ include the surface terms in the testing and the volume terms in the source, it is defined as

$$\boldsymbol{Z}_{\boldsymbol{\Phi},\boldsymbol{sv}} = \begin{bmatrix} \boldsymbol{Z}_{\boldsymbol{\Phi},\boldsymbol{sv}}^{+} & \boldsymbol{Z}_{\boldsymbol{\Phi},\boldsymbol{sv}}^{-} \end{bmatrix} \tag{2.106}$$

in which $[\boldsymbol{Z}_{\boldsymbol{\Phi},\boldsymbol{sv}}^{\pm}]_{nm} = \epsilon_0^{-1} \int_{\Gamma_n} \hat{\boldsymbol{n}}_n \cdot \boldsymbol{f}_{\boldsymbol{n}}(\boldsymbol{r}) \int_\Omega G_0(\boldsymbol{r}, \boldsymbol{r}') \nabla \cdot \boldsymbol{f}_{\boldsymbol{m}}^{\pm}(\boldsymbol{r}')\, \mathrm{d}v'\, \mathrm{d}s$.

Similarly, $\boldsymbol{Z}_{\boldsymbol{\Phi},\boldsymbol{vs}} \in \mathbb{C}^{2N_F \times N_F}$,

$$\boldsymbol{Z}_{\boldsymbol{\Phi},\boldsymbol{vs}} = \boldsymbol{Z}_{\boldsymbol{\Phi},\boldsymbol{sv}}{}^{\mathrm{T}}. \tag{2.107}$$

Finally, the matrix $\boldsymbol{Z}_{\boldsymbol{\Phi},\boldsymbol{ss}} \in \mathbb{C}^{N_F \times N_F}$, that includes the surface terms in the testing and the source, reads

$$[\boldsymbol{Z}_{\boldsymbol{\Phi},\boldsymbol{ss}}]_{nm} = \epsilon_0^{-1} \int_{\Gamma_n} \hat{\boldsymbol{n}}_n \cdot \boldsymbol{f}_{\boldsymbol{n}}(\boldsymbol{r}) \int_{\Gamma_m} G_0(\boldsymbol{r}, \boldsymbol{r}') \hat{\boldsymbol{n}}_m \cdot \boldsymbol{f}_{\boldsymbol{m}}(\boldsymbol{r}')\, \mathrm{d}s'\, \mathrm{d}s \tag{2.108}$$

After building $\boldsymbol{G}_{\boldsymbol{vv}}$, $\boldsymbol{Z}_{\boldsymbol{A},\boldsymbol{vv}}$, $\boldsymbol{Z}_{\boldsymbol{\Phi},\boldsymbol{vv}}$, $\boldsymbol{Z}_{\boldsymbol{\Phi},\boldsymbol{vs}}$, $\boldsymbol{Z}_{\boldsymbol{\Phi},\boldsymbol{sv}}$, and $\boldsymbol{Z}_{\boldsymbol{\Phi},\boldsymbol{ss}}$, the next step is to obtain the matrices defined in eq. (2.94), eq. (2.95), and eq. (2.96) to define rectangular sparse matrices called mapping matrices that enable re-scaling the monopolar matrices. For volume terms, a re-scaling by $1/\epsilon_n^{\pm}$ and $\kappa_n^{\pm}$ is needed and for the surface terms $\delta\kappa_n = \kappa_n^- - \kappa_n^+$ is required. The following sparse matrices are first introduced

$$\left[\boldsymbol{\Upsilon}_{\boldsymbol{\epsilon}^{-1}}^{\pm}\right]_{nn} = \frac{1}{\epsilon_n^{\pm}} \tag{2.109}$$

$$[\boldsymbol{\Upsilon}_{\boldsymbol{\kappa}^{\pm}}]_{nn} = \kappa_n^{\pm} \tag{2.110}$$

$$[\boldsymbol{\Upsilon}_{\boldsymbol{\delta\kappa}}]_{nn} = \delta\kappa_n, \tag{2.111}$$

they all pertain to $\mathbb{C}^{N_F \times N_F}$. Next we define $\boldsymbol{\Upsilon}_{\boldsymbol{\epsilon}^{-1}}$ and $\boldsymbol{\Upsilon}_{\boldsymbol{\kappa}}$ from eq. (2.109) and eq. (2.111)

$$\boldsymbol{\Upsilon}_{\boldsymbol{\epsilon}^{-1}} = \begin{bmatrix} \boldsymbol{\Upsilon}^{+}_{\boldsymbol{\epsilon}^{-1}} & \boldsymbol{\Upsilon}^{-}_{\boldsymbol{\epsilon}^{-1}} \end{bmatrix} \tag{2.112}$$

$$\boldsymbol{\Upsilon}_{\boldsymbol{\kappa}} = \begin{bmatrix} \boldsymbol{\Upsilon}^{+}_{\boldsymbol{\kappa}} & \boldsymbol{\Upsilon}^{-}_{\boldsymbol{\kappa}} \end{bmatrix}. \tag{2.113}$$

All the matrices to build the matrices $\boldsymbol{G}^{\boldsymbol{\kappa}}_{\boldsymbol{\epsilon}}$, $\boldsymbol{Z}^{\boldsymbol{\kappa}}_{\boldsymbol{A}}$, and $\boldsymbol{Z}^{\boldsymbol{\kappa}}_{\boldsymbol{\Phi}}$ have been introduced, which yields the following definitions

$$\boldsymbol{G}^{\boldsymbol{\kappa}}_{\boldsymbol{\epsilon}} = \boldsymbol{\Upsilon}_{\boldsymbol{\kappa}} \boldsymbol{G}_{vv} \boldsymbol{\Upsilon}_{\boldsymbol{\epsilon}^{-1}}{}^{\mathrm{T}} \tag{2.114}$$

$$\boldsymbol{Z}_{\boldsymbol{A}}{}^{\boldsymbol{\kappa}} = \boldsymbol{\Upsilon}_{\boldsymbol{\kappa}} \boldsymbol{Z}_{\boldsymbol{A},vv} \boldsymbol{\Upsilon}_{\boldsymbol{\kappa}}{}^{\mathrm{T}} \tag{2.115}$$

$$\boldsymbol{Z}_{\boldsymbol{\Phi}}{}^{\boldsymbol{\kappa}} = \boldsymbol{\Upsilon}_{\boldsymbol{\kappa}} \boldsymbol{Z}_{\boldsymbol{\Phi},vv} \boldsymbol{\Upsilon}_{\boldsymbol{\kappa}}{}^{\mathrm{T}} + \boldsymbol{\Upsilon}_{\boldsymbol{\kappa}} \boldsymbol{Z}_{\boldsymbol{\Phi},vs} \boldsymbol{\Upsilon}_{\boldsymbol{\delta\kappa}}{}^{\mathrm{T}} + \boldsymbol{\Upsilon}_{\boldsymbol{\delta\kappa}} \boldsymbol{Z}_{\boldsymbol{\Phi},sv} \boldsymbol{\Upsilon}_{\boldsymbol{\kappa}}{}^{\mathrm{T}} + \boldsymbol{\Upsilon}_{\boldsymbol{\delta\kappa}} \boldsymbol{Z}_{\boldsymbol{\Phi},ss} \boldsymbol{\Upsilon}_{\boldsymbol{\delta\kappa}}{}^{\mathrm{T}}, \tag{2.116}$$

in which $\boldsymbol{Z}^{\boldsymbol{\kappa}} = \boldsymbol{G}^{\boldsymbol{\kappa}}_{\boldsymbol{\epsilon}} + \boldsymbol{Z}^{\boldsymbol{\kappa}}_{\boldsymbol{A}} + \boldsymbol{Z}^{\boldsymbol{\kappa}}_{\boldsymbol{\Phi}}$.

2.3.4.4 Numerically Solving the D-VIE for the Contrast κ

Another useful way to express the discretization of the D-VIE is to write it such that $\boldsymbol{\kappa}$, the vector containing the contrast in each tetrahedron, becomes the unknown and $\boldsymbol{\alpha}$ is the scaling of the new impedance matrix $\boldsymbol{Z}_{\boldsymbol{\alpha}}$ [73]. This matrix corresponds to the discretization of an identity operator scaled with $\boldsymbol{\alpha}$ and the scattering operator introduced in eq. (2.62). To perform this operation, the D-VIE should be tested with $\{\boldsymbol{f}_n\}$ instead of $\{\kappa \boldsymbol{f}_n\}$. In the following, this D-VIE is denoted by "non-symmetric D-VIE" while the previous discretization (eq. (2.93)) is referred to as "symmetric D-VIE". Testing by $\{\boldsymbol{f}_n\}$ yields the following linear system

$$\boldsymbol{Z}\boldsymbol{\alpha} = \left(\boldsymbol{G}_{\boldsymbol{\epsilon}} + \boldsymbol{Z}_{\boldsymbol{A}} + \boldsymbol{Z}_{\boldsymbol{\Phi}}\right)\boldsymbol{\alpha} = \boldsymbol{v}, \tag{2.117}$$

where

$$\left[\boldsymbol{G}_{\boldsymbol{\epsilon}}\right]_{nm} = \langle \boldsymbol{f}_n, \boldsymbol{f}_m/\epsilon \rangle_{\Omega} \tag{2.118}$$

$$\left[\boldsymbol{Z}_{\boldsymbol{A}}\right]_{nm} = -k_0^2 \epsilon_0{}^{-1} \langle \boldsymbol{f}_n, \boldsymbol{\mathcal{T}}_A \boldsymbol{f}_m \rangle_{\Omega} \tag{2.119}$$

$$\left[\boldsymbol{Z}_{\boldsymbol{\Phi}}\right]_{nm} = -\epsilon_0{}^{-1} \langle \boldsymbol{f}_n, \boldsymbol{\mathcal{T}}_{\Phi} \boldsymbol{f}_m \rangle_{\Omega} \tag{2.120}$$

$$\left[\boldsymbol{v}\right]_n = \langle \boldsymbol{f}_n, \boldsymbol{E}_i \rangle_{\Omega}. \tag{2.121}$$

Similarly to the symmetric D-VIE, $\boldsymbol{Z}$ can be reformulated using a monopolar representation, which yields

$$\boldsymbol{G}_{\boldsymbol{\epsilon}} = \boldsymbol{\Upsilon}_{\boldsymbol{1}} \boldsymbol{G}_{vv} \boldsymbol{\Upsilon}_{\boldsymbol{\epsilon}^{-1}}{}^{\mathrm{T}} \tag{2.122}$$

$$\boldsymbol{Z}_{\boldsymbol{A}} = \boldsymbol{\Upsilon}_{\boldsymbol{1}} \boldsymbol{Z}_{\boldsymbol{A},vv} \boldsymbol{\Upsilon}_{\boldsymbol{\kappa}}{}^{\mathrm{T}} \tag{2.123}$$

$$\boldsymbol{Z}_{\boldsymbol{\Phi}} = \boldsymbol{\Upsilon}_{\boldsymbol{1}} \boldsymbol{Z}_{\boldsymbol{\Phi},vv} \boldsymbol{\Upsilon}_{\boldsymbol{\kappa}}{}^{\mathrm{T}} + \boldsymbol{\Upsilon}_{\boldsymbol{1}} \boldsymbol{Z}_{\boldsymbol{\Phi},vs} \boldsymbol{\Upsilon}_{\boldsymbol{\delta\kappa}}{}^{\mathrm{T}} + \boldsymbol{\Upsilon}_{\boldsymbol{\delta 1}} \boldsymbol{Z}_{\boldsymbol{\Phi},sv} \boldsymbol{\Upsilon}_{\boldsymbol{\kappa}}{}^{\mathrm{T}} + \boldsymbol{\Upsilon}_{\boldsymbol{\delta 1}} \boldsymbol{Z}_{\boldsymbol{\Phi},ss} \boldsymbol{\Upsilon}_{\boldsymbol{\delta\kappa}}{}^{\mathrm{T}} \tag{2.124}$$

in which

$$\boldsymbol{\Upsilon}_1 = \begin{bmatrix} \mathbf{I} & \mathbf{I} \end{bmatrix}, \tag{2.125}$$

with $\mathbf{I}$ being an identity matrix in $\mathbb{R}^{N_F \times N_F}$ and

$$[\boldsymbol{\Upsilon}_{\delta_1}]_{nn} = \begin{cases} -1 & \text{if } \Gamma_n \in \partial\Omega \\ 0 & \text{otherwise.} \end{cases} \tag{2.126}$$

From this non-symmetric discretization (eq. (2.117)), an equivalent equation in which $\boldsymbol{\kappa}$ is the unknown can be derived

$$\boldsymbol{Z}_{\boldsymbol{\alpha}}\boldsymbol{\kappa} = \boldsymbol{Z}_{\boldsymbol{A}}^{\boldsymbol{\alpha}}\boldsymbol{\kappa} + \boldsymbol{Z}_{\boldsymbol{\Phi}}^{\boldsymbol{\alpha}}\boldsymbol{\kappa} - \frac{1}{\epsilon_0}\boldsymbol{G}_{\boldsymbol{\alpha}}\boldsymbol{\kappa} = \boldsymbol{v} - \frac{1}{\epsilon_0}\boldsymbol{G}_0\boldsymbol{\alpha}. \tag{2.127}$$

The matrices $\boldsymbol{G}_0$, $\boldsymbol{Z}_{\boldsymbol{A}}^{\boldsymbol{\alpha}}$, $\boldsymbol{Z}_{\boldsymbol{\Phi}}^{\boldsymbol{\alpha}}$, and $\boldsymbol{G}_{\boldsymbol{\alpha}}$ are provided in the following. They can be written as products of mapping matrices containing $\boldsymbol{\alpha}$ and the monopolar matrices $\boldsymbol{G}_{vv}$, $\boldsymbol{Z}_{A,vv}$, $\boldsymbol{Z}_{\Phi,vv}$, $\boldsymbol{Z}_{\Phi,vs}$, $\boldsymbol{Z}_{\Phi,sv}$, and $\boldsymbol{Z}_{\Phi,ss}$. The following mapping matrices should be defined

$$\left[\boldsymbol{\psi}_v^{\pm}\right]_{mn} = \begin{cases} [\boldsymbol{\alpha}]_n & \text{if tetrahedron } T_m \text{ is tetrahedron } T_n^{\pm} \\ 0 & \text{otherwise,} \end{cases} \tag{2.128}$$

$$[\boldsymbol{\psi}_s]_{mn} = \begin{cases} [\boldsymbol{\alpha}]_n & \text{if tetrahedron } T_m \text{ is tetrahedron } T_n^{+} \\ -[\boldsymbol{\alpha}]_n & \text{if tetrahedron } T_m \text{ is tetrahedron } T_n^{-} \\ 0 & \text{otherwise,} \end{cases} \tag{2.129}$$

in which $\boldsymbol{\psi}_v^{\pm} \in \mathbb{C}^{N_T \times N_F}$ and $\boldsymbol{\psi}_s \in \mathbb{C}^{N_T \times N_F}$.

Leveraging $\boldsymbol{\psi}_v = \begin{bmatrix} \boldsymbol{\psi}_v^{+} & \boldsymbol{\psi}_v^{-} \end{bmatrix}$ and $\boldsymbol{\psi}_s$, the matrices introduced in eq. (2.127) can be expressed as

$$\boldsymbol{Z}_{\boldsymbol{A}}^{\boldsymbol{\alpha}} = -\boldsymbol{\Upsilon}_1 \boldsymbol{Z}_{A,vv} \boldsymbol{\psi}_v{}^{\mathrm{T}} \tag{2.130}$$

$$\boldsymbol{Z}_{\boldsymbol{\Phi}}^{\boldsymbol{\alpha}} = -\boldsymbol{\Upsilon}_1 \boldsymbol{Z}_{\Phi,vv} \boldsymbol{\psi}_v{}^{\mathrm{T}} + \boldsymbol{\Upsilon}_1 \boldsymbol{Z}_{\Phi,vs} \boldsymbol{\psi}_s{}^{\mathrm{T}} + \boldsymbol{\Upsilon}_{\delta_1} \boldsymbol{Z}_{\Phi,sv} \boldsymbol{\psi}_v{}^{\mathrm{T}} + \boldsymbol{\Upsilon}_{\delta_1} \boldsymbol{Z}_{\Phi,ss} \boldsymbol{\psi}_s{}^{\mathrm{T}} \tag{2.131}$$

$$\boldsymbol{G}_{\boldsymbol{\alpha}} = \boldsymbol{\Upsilon}_1 \boldsymbol{G}_{vv} \boldsymbol{\psi}_v{}^{\mathrm{T}} \tag{2.132}$$

$$\boldsymbol{G}_0 = \boldsymbol{\Upsilon}_1 \boldsymbol{G}_{vv} \boldsymbol{\Upsilon}_1{}^{\mathrm{T}}. \tag{2.133}$$

2.3.4.5 Near Field Radiated from the Electric Flux

By solving the discretized D-VIE (eq. (2.93) or eq. (2.117)), we can obtain the electric field inside the object by evaluating eq. (2.92) at the desired location in the object. To get the scattered electric field $\boldsymbol{E}_s(\boldsymbol{r})$ at $\boldsymbol{r} \in \mathbb{R}^3$ radiated by the electric flux $\boldsymbol{D}$, the scattering operator defined in eq. (2.61) should be employed. Substituting $\boldsymbol{D}$ by its expansion with SWG basis functions in eq. (2.61) gives

$$\boldsymbol{E}_s(\boldsymbol{r}) \approx \frac{k_0^2}{\epsilon_0} \sum_{m=1}^{N_F} \alpha_m \boldsymbol{\mathcal{T}}_A(\boldsymbol{f}_m(\boldsymbol{r}')) + \frac{1}{\epsilon_0} \sum_{m=1}^{N_F} \alpha_m \boldsymbol{\mathcal{T}}_\Phi(\boldsymbol{f}_m(\boldsymbol{r}')). \tag{2.134}$$

2.3.5 Hybrid VSIE

In the HVSIE (presented in section 2.2.5), the volume dielectric current density is discretized with SWG basis functions and the surface current density with RWG basis functions, as follows

$$\boldsymbol{J}_d(\boldsymbol{r}) = j\omega \boldsymbol{D}(\boldsymbol{r}) = \sum_{m=1}^{N_F} [\boldsymbol{\alpha}_v]_m \boldsymbol{f}_{\boldsymbol{m}}^v(\boldsymbol{r}), \tag{2.135}$$

and

$$\boldsymbol{J}_s(\boldsymbol{r}) = \sum_{m=1}^{N_E} [\boldsymbol{\alpha}_s]_m \boldsymbol{f}_{\boldsymbol{m}}^s(\boldsymbol{r}), \tag{2.136}$$

in which N_F and N_E are the number of faces and edges in the tetrahedral and triangular mesh, respectively. Applying this discretization and testing the equation in a symmetric manner results in the following block matrix equation

$$\begin{bmatrix} \boldsymbol{Z}_{ss} & \boldsymbol{Z}_{vs} \\ \boldsymbol{Z}_{sv} & \boldsymbol{Z}_{vv} \end{bmatrix} \begin{bmatrix} \boldsymbol{\alpha}_s \\ \boldsymbol{\alpha}_v \end{bmatrix} = \begin{bmatrix} \boldsymbol{v}_s \\ \boldsymbol{v}_v \end{bmatrix}, \tag{2.137}$$

where

$$[\boldsymbol{Z}_{ss}]_{nm} = -jk_0\eta_0 \langle \hat{\boldsymbol{n}} \times \boldsymbol{f}_{\boldsymbol{n}}^s, \boldsymbol{\gamma}_r \boldsymbol{\mathcal{T}}_A^{\Gamma} \boldsymbol{f}_{\boldsymbol{m}}^s \rangle_{\Gamma} + \frac{\eta_0}{jk_0} \langle \hat{\boldsymbol{n}} \times \boldsymbol{f}_{\boldsymbol{n}}^s, \boldsymbol{\gamma}_r \boldsymbol{\mathcal{T}}_{\Phi}^{\Gamma} \boldsymbol{f}_{\boldsymbol{m}}^s \rangle_{\Gamma} \tag{2.138}$$

$$[\boldsymbol{Z}_{vs}]_{nm} = -jk_0\eta_0 \langle \hat{\boldsymbol{n}} \times \boldsymbol{f}_{\boldsymbol{n}}^s, \boldsymbol{\gamma}_r \boldsymbol{\mathcal{T}}_A^{\kappa,\Omega} \boldsymbol{f}_{\boldsymbol{m}}^v \rangle_{\Gamma} + \frac{\eta_0}{jk_0} \langle \hat{\boldsymbol{n}} \times \boldsymbol{f}_{\boldsymbol{n}}^s, \boldsymbol{\gamma}_r \boldsymbol{\mathcal{T}}_{\Phi}^{\kappa,\Omega} \boldsymbol{f}_{\boldsymbol{m}}^v \rangle_{\Gamma} \tag{2.139}$$

$$[\boldsymbol{Z}_{sv}]_{nm} = -jk_0\eta_0 \langle \kappa \boldsymbol{f}_{\boldsymbol{n}}^v, \boldsymbol{\mathcal{T}}_A^{\Gamma} \boldsymbol{f}_{\boldsymbol{m}}^s \rangle_{\Omega} + \frac{\eta_0}{jk_0} \langle \kappa \boldsymbol{f}_{\boldsymbol{n}}^v, \boldsymbol{\mathcal{T}}_{\Phi}^{\Gamma} \boldsymbol{f}_{\boldsymbol{m}}^s \rangle_{\Omega} \tag{2.140}$$

$$[\boldsymbol{Z}_{vv}]_{nm} = \frac{\eta_0}{jk_0} \langle \kappa \boldsymbol{f}_{\boldsymbol{n}}^v, \epsilon^{-1} \boldsymbol{f}_{\boldsymbol{m}}^v \rangle_{\Omega} + jk_0\eta_0 \langle \kappa \boldsymbol{f}_{\boldsymbol{n}}^v, \boldsymbol{\mathcal{T}}_A^{\kappa,\Omega} \boldsymbol{f}_{\boldsymbol{m}}^v \rangle_{\Omega} - \frac{\eta_0}{jk_0} \langle \kappa \boldsymbol{f}_{\boldsymbol{n}}^v, \boldsymbol{\mathcal{T}}_{\Phi}^{\kappa,\Omega} \boldsymbol{f}_{\boldsymbol{m}}^v \rangle_{\Omega} \tag{2.141}$$

$$[\boldsymbol{v}_s]_n = -\langle \hat{\boldsymbol{n}} \times \boldsymbol{f}_{\boldsymbol{n}}^s, \boldsymbol{\gamma}_r \boldsymbol{E}_i \rangle_{\Gamma} \tag{2.142}$$

$$[\boldsymbol{v}_v]_n = \langle \kappa \boldsymbol{f}_{\boldsymbol{n}}^v, \boldsymbol{E}_i \rangle_{\Omega}. \tag{2.143}$$

2.4 Iterative Solvers and Conditioning

In this section, a special focus is given to the solving of the discretized MoM equations that were derived above. Generally, the discretized system is a linear system that can be formulated as

$$\boldsymbol{Z}\boldsymbol{x} = \boldsymbol{y}, \tag{2.144}$$

in which $\boldsymbol{x}$ is the solution vector, $\boldsymbol{y}$ is the known right hand side, and $\boldsymbol{Z}$ is one of the discretized operators introduced above. Since the direct inversion of $\boldsymbol{Z}$ to

solve eq. (2.144) is very demanding computationally (cubic complexity), iterative solvers, which operate in quadratic complexity, are usually preferred for solving real-world problems, which often have a large number of degrees of freedom. When using iterative methods, the problem is generally expressed as a cost functional

$$F_n = \|\boldsymbol{Z}\boldsymbol{x_n} - \boldsymbol{y}\|^2, \tag{2.145}$$

which has to be minimized by successively updating $\boldsymbol{x_n}$ as

$$\boldsymbol{x_{n+1}} = \boldsymbol{x_n} + \alpha_n \boldsymbol{v_n}, \tag{2.146}$$

in which $\boldsymbol{x_{n+1}}$ is the solution at step $n+1$, $\boldsymbol{v_n}$ is the update direction, and α_n is a weight chosen to minimize F_n.

2.4.0.1 Convergence of the Steepest Descent Method

A fundamental property of an iterative solver is its convergence rate. This property is illustrated in the following by considering convergence in the steepest descent method [18, 90], which is one of the simplest iterative solvers. Note that $\boldsymbol{Z}$ is assumed to be a positive-definite matrix in this derivation. In this scheme, α_n and $\boldsymbol{v_n}$ can be updated at each iteration as

$$\alpha_n = \frac{\boldsymbol{r_n}^{\mathrm{T}} \boldsymbol{r_n}}{\|\boldsymbol{r_n}\|_{\boldsymbol{Z}}^2} \tag{2.147}$$

$$\boldsymbol{v_n} = \boldsymbol{r_n}, \tag{2.148}$$

in which $\boldsymbol{r_n} = \boldsymbol{Z}\boldsymbol{x_n} - \boldsymbol{y}$ is the residual and $\|\boldsymbol{x}\|_{\boldsymbol{Z}} = \left(\boldsymbol{x}^{\mathrm{T}}\boldsymbol{Z}\boldsymbol{x}\right)^{\frac{1}{2}}$ is the energy norm. In the convergence analysis, the error on the solution at step n, $\boldsymbol{e_n} = \boldsymbol{x} - \boldsymbol{x_n}$ ($\boldsymbol{x}$ being the correct solution), should be considered. It has the following relation with the residual error

$$\boldsymbol{r_n} = -\boldsymbol{Z}\boldsymbol{e_n}. \tag{2.149}$$

To analyze the convergence of the steepest descent method, $\boldsymbol{e_n}$ is first expanded as a linear combination of orthogonal eigenvectors of $\boldsymbol{Z}$ ($\boldsymbol{Z}$ being symmetric)

$$\boldsymbol{e_n} = \sum_{i=1}^{N} \xi_i \, \boldsymbol{\chi_i}, \tag{2.150}$$

in which $\boldsymbol{\chi_i}$ is the eigenvector of $\boldsymbol{Z}$ associated to the eigenvalue λ_i, ξ_i are the coefficients of the expansion, and N is the number of unknowns. To show the convergence of the algorithm, the errors $\boldsymbol{e_{n+1}}$ and $\boldsymbol{e_n}$ between two consecutive iterations should be compared. To this aim, the squared energy norm of $\boldsymbol{e_{n+1}}$ is expanded

using eq. (2.146), eq. (2.147), eq. (2.149), and the fact that $\boldsymbol{Z}$ is symmetric. This gives

$$\begin{aligned}
\|\boldsymbol{e_{n+1}}\|_{\boldsymbol{Z}}^2 &= \boldsymbol{e_{n+1}}^{\mathrm{T}} \boldsymbol{Z} \boldsymbol{e_{n+1}} \\
&= (\boldsymbol{e_n} + \alpha_n \boldsymbol{r_n})^{\mathrm{T}} \boldsymbol{Z} (\boldsymbol{e_n} + \alpha_n \boldsymbol{r_n}) \\
&= \boldsymbol{e_n}^{\mathrm{T}} \boldsymbol{Z} \boldsymbol{e_n} + 2\alpha_n \boldsymbol{r_n}^{\mathrm{T}} \boldsymbol{Z} \boldsymbol{e_n} + \alpha_n^2 \boldsymbol{r_n}^{\mathrm{T}} \boldsymbol{Z} \boldsymbol{r_n} \\
&= \|\boldsymbol{e_n}\|_{\boldsymbol{Z}}^2 - 2\frac{\boldsymbol{r_n}^{\mathrm{T}} \boldsymbol{r_n}}{\|\boldsymbol{r_n}\|_{\boldsymbol{Z}}^2} \boldsymbol{r_n}^{\mathrm{T}} \boldsymbol{r_n} + \left(\frac{\boldsymbol{r_n}^{\mathrm{T}} \boldsymbol{r_n}}{\|\boldsymbol{r_n}\|_{\boldsymbol{Z}}^2}\right)^2 \|\boldsymbol{r_n}\|_{\boldsymbol{Z}}^2 \\
&= \|\boldsymbol{e_n}\|_{\boldsymbol{Z}}^2 - \frac{\left(\boldsymbol{r_n}^{\mathrm{T}} \boldsymbol{r_n}\right)^2}{\|\boldsymbol{r_n}\|_{\boldsymbol{Z}}^2}.
\end{aligned} \tag{2.151}$$

Then, leveraging eq. (2.150) and factoring out $\|\boldsymbol{e_n}\|_{\boldsymbol{Z}}^2$ in eq. (2.151) yields

$$\begin{aligned}
\|\boldsymbol{e_{n+1}}\|_{\boldsymbol{Z}}^2 &= \|\boldsymbol{e_n}\|_{\boldsymbol{Z}}^2 \left(1 - \frac{\left(\boldsymbol{r_n}^{\mathrm{T}} \boldsymbol{r_n}\right)^2}{\left(\boldsymbol{e_n}^{\mathrm{T}} \boldsymbol{Z} \boldsymbol{e_n}\right)\left(\boldsymbol{r_n}^{\mathrm{T}} \boldsymbol{Z} \boldsymbol{r_n}\right)}\right) \\
&= \|\boldsymbol{e_n}\|_{\boldsymbol{Z}}^2 \left(1 - \frac{\left(\left(-\sum_{i=1}^N \xi_i \boldsymbol{Z} \boldsymbol{\chi_i}\right)^{\mathrm{T}} \left(-\sum_{i=1}^N \xi_i \boldsymbol{Z} \boldsymbol{\chi_i}\right)\right)^2}{\left(\left(\sum_{i=1}^N \xi_i \boldsymbol{\chi_i}\right)^{\mathrm{T}} \boldsymbol{Z} \left(\sum_{i=1}^N \xi_i \boldsymbol{\chi_i}\right)\right)\left(\left(-\sum_{i=1}^N \xi_i \boldsymbol{Z} \boldsymbol{\chi_i}\right)^{\mathrm{T}} \boldsymbol{Z} \left(-\sum_{i=1}^N \xi_i \boldsymbol{Z} \boldsymbol{\chi_i}\right)\right)}\right) \\
&= \|\boldsymbol{e_n}\|_{\boldsymbol{Z}}^2 \left(1 - \frac{\left(\sum_{i=1}^N \xi_i^2 \lambda_i^2\right)^2}{\left(\sum_{i=1}^N \xi_i^2 \lambda_i\right)\left(\sum_{i=1}^N \xi_i^2 \lambda_i^3\right)}\right) \\
&= \|\boldsymbol{e_n}\|_{\boldsymbol{Z}}^2 (1 - c^2).
\end{aligned} \tag{2.152}$$

From eq. (2.152), it results that the strict inequality $1 - c^2 < 1$ is required to reduce the error and that the convergence rate increases when c^2 gets closer to 1. To understand how c varies, we take the example of a linear system with only two unknowns ($N = 2$). In that case, $\boldsymbol{Z}$ has two eigenvalues λ_1 and λ_2 with λ_1 being the largest eigenvalue. This simplifies the expression of c^2 to

$$\begin{aligned}
c^2 &= \frac{(\xi_1^2 \lambda_1^2 + \xi_2^2 \lambda_2^2)^2}{(\xi_1^2 \lambda_1 + \xi_2^2 \lambda_2)(\xi_1^2 \lambda_1^3 + \xi_2^2 \lambda_2^3)} \\
&= \frac{(\kappa^2 + \mu^2)^2}{(\kappa + \mu^2)(\kappa^3 + \mu^2)},
\end{aligned} \tag{2.153}$$

in which $\kappa = \lambda_1/\lambda_2$ is called the condition number of $\boldsymbol{Z}$ ($\boldsymbol{Z}$ being positive-definite) and $\mu = \xi_2/\xi_1$. Next we observe by differentiating eq. (2.153) with respect to μ (for a fixed condition number) that c^2 is minimized when $\mu = \kappa$. This is the worst-case scenario for the convergence and thus it gives us a lower bound for c^2, which reads

$$c^2 \geq \frac{4\kappa^4}{\kappa^5 + 2\kappa^4 + \kappa^3} = \frac{4\kappa}{(\kappa + 1)^2}. \tag{2.154}$$

We can see in eq. (2.154) that the maximum lower bound of c^2 (fastest convergence rate) is obtained for $\kappa = 1$ (minimum condition number possible). Another observation is that when κ increases, the lower bound for c^2 decreases, so the convergence rate of the steepest descent might decrease also. Therefore, it is important to keep the condition number κ of $\boldsymbol{Z}$ as low as possible. Note that since eq. (2.154) is a lower bound, it represents the worst case scenario for the convergence rate of the iterative solver.

2.4.0.2 Condition Number

In general (not only for symmetric matrices), the condition number of an invertible matrix $\boldsymbol{Z}$ is defined as

$$\text{cond}(\boldsymbol{Z}) = \|\boldsymbol{Z}\|\|\boldsymbol{Z}^{-1}\| = \frac{s_{\max}}{s_{\min}}, \tag{2.155}$$

in which $s_{\max}$ and $s_{\min}$ are the maximum and minimum singular values of $\boldsymbol{Z}$, respectively. As we observed in the case of the steepest descent method, the conditioning of the system matrix dictates the convergence rate of the iterative solver employed. Another issue with ill-conditioned matrices is that they induce numerical instability in the problem. This originates from the fact that the exact expression of the excitation vector $\boldsymbol{y}$ and the system matrix $\boldsymbol{Z}$ cannot be used due to the finite precision used to store numbers in computers. This inaccuracy can be taken into account by adding a perturbation to $\boldsymbol{y}$ and $\boldsymbol{Z}$ [51] as follows

$$\begin{aligned} \boldsymbol{Z} &\rightarrow \boldsymbol{Z} + \epsilon \boldsymbol{Z_1} \\ \boldsymbol{y} &\rightarrow \boldsymbol{y} + \epsilon \boldsymbol{y_1}, \end{aligned}$$

in which $\epsilon \in \mathbb{R}$ and $\boldsymbol{Z_1}$ and $\boldsymbol{y_1}$ have the same dimensions as $\boldsymbol{Z}$ and $\boldsymbol{y}$, respectively. Inserting the perturbed matrix and the perturbed excitation vector in eq. (2.144), we get

$$(\boldsymbol{Z} + \epsilon \boldsymbol{Z_1})\, \tilde{\boldsymbol{x}} = \boldsymbol{y} + \epsilon \boldsymbol{y_1}, \tag{2.156}$$

in which $\tilde{\boldsymbol{x}}$ is the perturbed solution. Next, we derive an upper bound for the relative error between $\tilde{\boldsymbol{x}}$ and the exact solution $\boldsymbol{x}$. To do this, we first subtract eq. (2.144) from eq. (2.156), which after rearrangement gives

$$\tilde{\boldsymbol{x}} - \boldsymbol{x} = \epsilon \boldsymbol{Z}^{-1}(\boldsymbol{y_1} - \boldsymbol{Z_1}\boldsymbol{x} - \boldsymbol{Z_1}(\tilde{\boldsymbol{x}} - \boldsymbol{x})). \tag{2.157}$$

Then, taking the norm of eq. (2.156) yields the following inequality

$$\begin{aligned} \|\tilde{\boldsymbol{x}} - \boldsymbol{x}\| &\leq \epsilon \|\boldsymbol{Z}^{-1}\| \|\boldsymbol{y_1} - \boldsymbol{Z_1}\boldsymbol{x} - \boldsymbol{Z_1}(\tilde{\boldsymbol{x}} - \boldsymbol{x})\| \\ &\leq \epsilon \|\boldsymbol{Z}^{-1}\| \left(\|\boldsymbol{y_1}\| + \|\boldsymbol{Z_1}\|\, \|\boldsymbol{x}\| + \|\boldsymbol{Z_1}\| \|\tilde{\boldsymbol{x}} - \boldsymbol{x}\|\right). \end{aligned} \tag{2.158}$$

Assuming that $\|\boldsymbol{Z}^{-1}\|\|\boldsymbol{Z}_1\| < 1$, putting all terms in $\|\tilde{\boldsymbol{x}} - \boldsymbol{x}\|$ on the left hand side of the inequality, and dividing by $\|\boldsymbol{x}\|$, eq. (2.158) can be formulated as

$$\frac{\|\tilde{\boldsymbol{x}} - \boldsymbol{x}\|}{\|\boldsymbol{x}\|} \leq \epsilon \frac{\|\boldsymbol{Z}^{-1}\|}{1 - \|\boldsymbol{Z}^{-1}\|\|\boldsymbol{Z}_1\|} \left(\frac{\|\boldsymbol{y}_1\|}{\|\boldsymbol{x}\|} + \|\boldsymbol{Z}_1\| \right). \tag{2.159}$$

Then using the fact that $\|\boldsymbol{y}\| \leq \|\boldsymbol{Z}\|\|\boldsymbol{x}\|$ and leveraging eq. (2.155), we can write eq. (2.159) as

$$\frac{\|\tilde{\boldsymbol{x}} - \boldsymbol{x}\|}{\|\boldsymbol{x}\|} \leq \epsilon \frac{\text{cond}(\boldsymbol{Z})}{1 - \text{cond}(\boldsymbol{Z})\|\boldsymbol{Z}_1\|/\|\boldsymbol{Z}\|} \left(\frac{\|\boldsymbol{y}_1\|}{\|\boldsymbol{y}\|} + \frac{\|\boldsymbol{Z}_1\|}{\|\boldsymbol{Z}\|} \right). \tag{2.160}$$

From eq. (2.160), we observe that $\text{cond}(\boldsymbol{Z})$ plays the role of an amplifier for the relative perturbations $\|\boldsymbol{Z}_1\|/\|\boldsymbol{Z}\|$ and $\|\boldsymbol{y}_1\|/\|\boldsymbol{y}\|$ in the upper bound of the relative perturbation of the solution. Note that since this is an upper bound, it represents the worst case scenario for the relative perturbation of the solution.

Since a high condition number can yield a lower convergence rate and numerical instability, it is important to work with formulations that have a low and bounded condition number. For this reason, a preconditioner is generally employed on top of the original formulation to guarantee the well-conditioning of the system matrix.

Chapter 3

A Full-wave Volume Formulation for Neuro-imaging

THIS chapter describes research conducted on a new regularized electric flux volume integral equation (D-VIE) for modeling lossy dielectric objects in a broad frequency range. This new formulation is particularly suitable for modeling biological tissues at low frequencies, as it is required by brain epileptogenic area imaging, but also at higher ones, as it is required by several applications including, but not limited to transcranial magnetic and deep brain stimulation (TMS and DBS, respectively). When modeling at low frequency inhomogeneous objects with high complex permittivities, the traditional D-VIE is ill-conditioned and suffers from numerical instabilities, which results in slower convergences and in less accurate solutions. In this work we address these shortcomings by leveraging a new set of volume quasi-Helmholtz projectors. Their scaling makes the proposed method accurate and stable for high permittivity objects until arbitrarily low frequencies. Numerical results, canonical and realistic, corroborate the theory and confirm the stability and the accuracy of this new method both in the quasi-static regime and at higher frequencies.

3.1 Introduction

The electromagnetic modeling of human tissues has numerous applications that include brain source localization [7], dosimetry [3], deep brain stimulation (DBS) [64], transcranial magnetic stimulation (TMS) [8], electric impedance tomography [20], and hyperthermic cancer therapy [99]. All these procedures require an accurate modeling of the interactions between electromagnetic fields and the human body. Depending on the application, numerical solvers can be either full-wave solvers directly derived from Maxwell's equations or static solvers based on Poisson's equation, which are valid only in the quasi-static regime [15]. While static solvers are

sufficient to model resistive effects occurring in biological tissues, full-wave solvers are required when capacitive, inductive, and propagation effects should also be taken into consideration [15, 82]. This is the case when the source has a larger spectral content (e.g. a magnetic pulse emitted by TMS coil [30] or an electrical current injected by an electrode in neurostimulation [53]). For these applications, the modeling should be done at various frequencies and, hence, the solver used should be able to perform accurately at arbitrary frequency.

Two main families of numerical solvers are widely employed for frequency domain bio-electromagnetic modeling: integral equation (IE) and differential equation solvers. In particular, integral equation solvers can be either surfacic (SIE) or volumic (VIE) depending on the nature of the tissue to model [105]. Although these solvers give rise to dense matrices, the higher computational cost incurred can be significantly reduced using acceleration techniques such as the fast multipole method (FMM) [43] or the adaptive cross approximation (ACA) [9]. Moreover, as IE formulations automatically enforce radiation conditions, no discretization is required outside the object. Unfortunately, bio-electromagnetic modeling is a challenging task for solvers based on integral equations because of the high external permittivity contrast between the biological tissues and the background in which they are studied [37]. Indeed both a high-contrast object and/or a low operating frequency introduce a severe ill-conditioning in the discretized IE operator, which yields a slower convergence and a loss of accuracy in the solution [5]. These two phenomena are often referred to as the low-frequency (LF) and the high-contrast (HC) breakdowns respectively [85, 101, 42, 17]. In addition, the ill-scaling between the different components of the solution of the discretized system causes the latter to have fewer digits of accuracy due to finite machine precision [84].

The high-contrast breakdown in piecewise homogeneous scatterers has been cured in the case of the Poggio-Miller-Chang-Harrington-Wu-Tsai (PMCHWT) formulation [74] and in a novel single-source integral equation [42] by leveraging the Calderón identities and the low-frequency breakdown of the PMCHWT was tackled by preconditioning it with quasi-Helmholtz projectors [10]. These two methods allow for an appropriate re-scaling of the PMCHWT operator to make it stable regardless of the permittivity or of the frequency. While these stabilized surface formulations have numerous advantages, in particular the fact that they require only the boundaries of the homogeneous parts of the scatterer to be discretized, like most integral equations, they are limited to piecewise homogeneous models of biological tissues. While these stabilized surface formulations have numerous advantages, they are limited to piecewise homogeneous models of biological tissues. Volume integral equations, instead, can model objects with a high degree of inhomogeneity. Unfortunately, as their surface counterparts, they suffer from the HC breakdown [69, 70, 107, 17, 27, 98, 33] and fail to converge rapidly in applications with scatterers that have a high permittivity contrast with respect to their background. Another limitation of traditional VIE is that, even though they are

immune from the low-frequency breakdown in purely dielectric objects [23], a frequency ill-scaling between the different parts of the VIE can occur when the object under study has a complex permittivity which depends on the frequency [88]. The LF breakdown can therefore be considered as an intrinsic part of the HC breakdown in the VIE. These limitations prevent the standard volume formulations to perform well in realistic biomedical applications where the modeling of high-contrast tissues from the quasi-static regime to the microwave regime is required.

Some regularization techniques have been introduced for solving the LF and the HC problems in the electric current VIE (J-VIE), the electric field VIE (E-VIE), and the electric flux VIE (D-VIE). The LF breakdown has been cured in the J-VIE for anisotropic and inhomogeneous scatterers using a loop-star-facet decomposition for re-scaling properly the unknown [36]. However, solving this problem using a Helmholtz discretization deteriorates the dense discretization behavior of the VIE, i.e., it causes the conditioning of the system matrix to deteriorate when the average edge length h of the discretized geometry decreases [4]. The quasi-Helmholtz projectors [5] allow for the removal of the ill-scaling in the formulation while keeping its dense mesh behavior unchanged. These projectors have been adapted to the J-VIE and used for curing the HC limitation of this equation for isotropic inhomogeneous scatterers in [68]. Another approach to solve the HC problem is presented in [107], where the E-VIE is regularized using the symbol calculus and the Calderón identities. Its application to the J-VIE is discussed in [83]. While being free from the HC breakdown, the two above-mentioned methods do not consider the numerical stability of the J-VIE or the E-VIE at low frequencies when modeling lossy dielectric objects, which is an important feature for a solver operating in low-frequency biomedical applications. For the D-VIE, an effective solution to both the LF and HC breakdowns has been proposed in [41, 40] where an additional surface integral equation is used to adjust the background permittivity and lower the external dielectric contrast.

In this chapter, we introduce a new set of volume quasi-Helmholtz projectors compatible with the D-VIE to separate the solenoidal (loop) and non-solenoidal (star) parts of the discretized formulation and re-scale them appropriately, thus curing the ill-conditioning and the loss of accuracy occurring at low frequencies in lossy dielectric objects. The investigation of a new set of projectors has been necessary because the projectors proposed in [68], designed for the J-VIE, would not work for the D-VIE due to the different discretization strategies of these two equations: single cell piecewise constant basis functions for the former and Schaubert-Wilton-Glisson (SWG) basis functions [89] for the latter.

The new projectors, when combined with the appropriate re-scaling, can be used to tackle the LF breakdown. The regularized D-VIE exhibits a solution that is valid until arbitrarily low frequencies in lossy dielectric objects, unlike standard full-wave solvers. This versatility makes it an excellent formulation for biomedical applications where solvers that can operate in a broad frequency range are required.

This chapter is organized as follows: in Section 3.2 we set the background and notation, including the definition of the D-VIE along with its discrete Helmholtz decomposition. The low-frequency behavior of the D-VIE is analyzed in Section 3.4 together with the regularization we propose. Implementation details are presented in Section 3.5. Finally, Section 3.6 presents numerical examples showing the stability and accuracy of the new formulation in a broad frequency range. Some preliminary results have been presented in a conference contribution [47].

3.2 Background and Notations

Let $\Omega \subset \mathbb{R}^3$ be a simply connected object composed of a lossy dielectric and illuminated by a time-harmonic incident electric field $\boldsymbol{E}_i$ in a background of permittivity ϵ_0 and permeability μ_0. The scatterer is characterized by its complex isotropic relative permittivity $\epsilon_r(\boldsymbol{r}) = \epsilon'_r(\boldsymbol{r}) - \mathrm{j}\sigma(\boldsymbol{r})/\omega\epsilon_0$ with $\boldsymbol{r} \in \Omega$, $\epsilon'_r(\boldsymbol{r})$ the relative permittivity, $\sigma(\boldsymbol{r})$ the conductivity, and ω the angular frequency of $\boldsymbol{E}_i$. The permeability of the scatterer is further assumed to be the permeability of vacuum μ_0. Leveraging the volume equivalence principle (section 2.2.1.2), the scatterer can be substituted by a volume current density distribution

$$\boldsymbol{J}(\boldsymbol{r}) = j\omega\kappa(\boldsymbol{r})\boldsymbol{D}(\boldsymbol{r}), \tag{3.1}$$

where $\kappa(\boldsymbol{r}) = (\epsilon(\boldsymbol{r}) - \epsilon_0)/\epsilon(\boldsymbol{r})$ is the dielectric contrast and $\boldsymbol{D}$ is the electric flux density. We then recall the D-VIE introduced in section 2.2.4.2,

$$\frac{\boldsymbol{D}(\boldsymbol{r})}{\epsilon(\boldsymbol{r})} - \frac{k_0^2}{\epsilon_0}\left(\boldsymbol{\mathcal{T}}_A^{\kappa,\Omega}\boldsymbol{D}\right)(\boldsymbol{r}) - \frac{1}{\epsilon_0}\left(\boldsymbol{\mathcal{T}}_\Phi^{\kappa,\Omega}\boldsymbol{D}\right)(\boldsymbol{r}) = \boldsymbol{E_i}(\boldsymbol{r}), \quad \boldsymbol{r} \in \Omega, \tag{3.2}$$

where the vector potential $\boldsymbol{\mathcal{T}}_A^{\kappa,\Omega}$ and the scalar potential $\boldsymbol{\mathcal{T}}_\Phi^{\kappa,\Omega}$ are defined as

$$\left(\boldsymbol{\mathcal{T}}_A^{\kappa,\Omega}\boldsymbol{D}\right)(\boldsymbol{r}) = \int_\Omega G_0(\boldsymbol{r},\boldsymbol{r}')\kappa(\boldsymbol{r}')\boldsymbol{D}(\boldsymbol{r}')\,\mathrm{d}v', \tag{3.3}$$

$$\left(\boldsymbol{\mathcal{T}}_\Phi^{\kappa,\Omega}\boldsymbol{D}\right)(\boldsymbol{r}) = \nabla\int_\Omega G_0(\boldsymbol{r},\boldsymbol{r}')\nabla'\cdot(\kappa(\boldsymbol{r}')\boldsymbol{D}(\boldsymbol{r}'))\,\mathrm{d}v', \tag{3.4}$$

in which $G_0(\boldsymbol{r},\boldsymbol{r}') = \exp(-\mathrm{j}k_0\|\boldsymbol{r}-\boldsymbol{r}'\|)/\|\boldsymbol{r}-\boldsymbol{r}'\|$ is the free space 3D Green's function and $k_0 = \omega/c_0$ is the wavenumber of $\boldsymbol{E_i}$ in free space. In the context of bio-electromagnetic modeling, excitations are typically generated by plane waves and current sources. In general, the electric field radiated by an electric current distribution $\boldsymbol{J_i}$, which is commonly used to model the brain's electric activity, is

$$\boldsymbol{E_i}(\boldsymbol{r}) = \left(\boldsymbol{\mathcal{T}}'_\Phi\boldsymbol{J_i}\right)(\boldsymbol{r}) + \left(\boldsymbol{\mathcal{T}}'_A\boldsymbol{J_i}\right)(\boldsymbol{r}), \tag{3.5}$$

where $\boldsymbol{\mathcal{T}}'_A\boldsymbol{J_i} = -\mathrm{j}k_0\eta_0\int_\Omega G_0(\boldsymbol{r},\boldsymbol{r}')\boldsymbol{J_i}(\boldsymbol{r}')\,\mathrm{d}v'$ and $\boldsymbol{\mathcal{T}}'_\Phi\boldsymbol{J_i} = \eta_0/\mathrm{j}k_0\nabla\int_\Omega G_0(\boldsymbol{r},\boldsymbol{r}')\nabla'\cdot\boldsymbol{J_i}(\boldsymbol{r}')\,\mathrm{d}v'$.

Equation (3.2) can be numerically solved by expanding the unknown electric flux with SWG basis functions $\{\boldsymbol{f_m}\}$ (introduced in section 2.3.4)

$$\boldsymbol{D}(\boldsymbol{r}) \approx \sum_{m=1}^{N_F} [\boldsymbol{\alpha}]_m \boldsymbol{f_m}(\boldsymbol{r}), \tag{3.6}$$

with N_F being the number of triangular faces in the tetrahedral mesh, and then by testing the equation in a non-symmetric manner with $\{\boldsymbol{f_n}\}$, thus resulting in the non-symmetric discretized D-VIE (i.e. eq. (2.117))

$$\boldsymbol{Z\alpha} = (\boldsymbol{G_\epsilon} + \boldsymbol{Z_A} + \boldsymbol{Z_\Phi})\,\boldsymbol{\alpha} = \boldsymbol{v}, \tag{3.7}$$

in which

$$[\boldsymbol{G_\epsilon}]_{nm} = \langle \boldsymbol{f_n}, \boldsymbol{f_m}/\epsilon \rangle_\Omega \tag{3.8}$$

$$[\boldsymbol{Z_A}]_{nm} = -k_0^2 {\epsilon_0}^{-1} \langle \boldsymbol{f_n}, \boldsymbol{\mathcal{T}}_A^{\kappa,\Omega} \boldsymbol{f_m} \rangle_\Omega \tag{3.9}$$

$$[\boldsymbol{Z_\Phi}]_{nm} = -{\epsilon_0}^{-1} \langle \boldsymbol{f_n}, \boldsymbol{\mathcal{T}}_\Phi^{\kappa,\Omega} \boldsymbol{f_m} \rangle_\Omega \tag{3.10}$$

$$[\boldsymbol{v}]_n = \langle \boldsymbol{f_n}, \boldsymbol{E_i} \rangle_\Omega. \tag{3.11}$$

In the following, we review some results regarding the Helmholtz decomposition of the electric flux in the D-VIE as it is particularly useful to identify how the loop and star components of the D-VIE scale with respect to the frequency. The unknown $\boldsymbol{\alpha}$ which corresponds to the expansion coefficients of a divergence conforming quantity can be decomposed into a sum of its solenoidal and non-solenoidal components [70]

$$\boldsymbol{\alpha} = \boldsymbol{\Lambda l} + \tilde{\boldsymbol{\Sigma}} \boldsymbol{s}, \tag{3.12}$$

where $\boldsymbol{\Lambda} \in \mathbb{R}^{N_F \times N_L}$ is the loop-to-SWG transformation matrix, $\tilde{\boldsymbol{\Sigma}} \in \mathbb{R}^{N_F \times N_S}$ is the star-to-SWG transformation matrix, $\boldsymbol{l}$ are the expansion coefficients of the unknown in the solenoidal basis, and $\boldsymbol{s}$ are the expansion coefficients in the non-solenoidal basis.

The dimensions N_L and N_S are the numbers of independent loops and stars in the discretized geometry, respectively. In a tetrahedral discretization of a simply connected object, the number of stars and loops are [65, 44, 70]

$$\begin{aligned} N_S &= N_T + N_{eF} \\ N_L &= N_{iE} - N_{iV}, \end{aligned} \tag{3.13}$$

where N_T, N_{eF}, N_{iE}, and N_{iV} are the number of tetrahedra, external faces, internal edges, and internal vertices, respectively.

Volume star functions are defined on the tetrahedra of the mesh (as illustrated in fig. 3.1b) and can be defined as linear combinations of SWG basis functions. The

mapping $\boldsymbol{\Sigma_v} \in \mathbb{R}^{N_F \times N_T}$ relates the volume stars and the SWG functions as

$$[\boldsymbol{\Sigma_v}]_{mn} = \begin{cases} 1 & \text{if tetrahedron } T_n \text{ is tetrahedron } T_m^+ \\ -1 & \text{if tetrahedron } T_n \text{ is tetrahedron } T_m^- \\ 0 & \text{otherwise,} \end{cases} \tag{3.14}$$

where T_m^+ and T_m^- represent the two tetrahedra on which the basis function $\boldsymbol{f_m}$ is defined (fig. 2.3). For half basis functions, only the entries corresponding to tetrahedron T_m^+ are filled in $\boldsymbol{\Sigma_v}$. Since these specific basis functions also model surface charges at the boundary of the object, another transformation matrix $\boldsymbol{\Sigma_s} \in \mathbb{R}^{N_F \times N_{eF}}$ needs to be filled for these basis functions

$$[\boldsymbol{\Sigma_s}]_{mn} = \begin{cases} -1 & \text{if face } n \text{ is face } \Gamma_m \\ 0 & \text{otherwise.} \end{cases} \tag{3.15}$$

Note here that, by convention, the half basis function $\boldsymbol{f_m}$ is always supported by tetrahedron T_m^+. The transformation matrix from star-to-SWG is then defined as $\tilde{\boldsymbol{\Sigma}} = [\boldsymbol{\Sigma_v}\ \boldsymbol{\Sigma_s}]$.

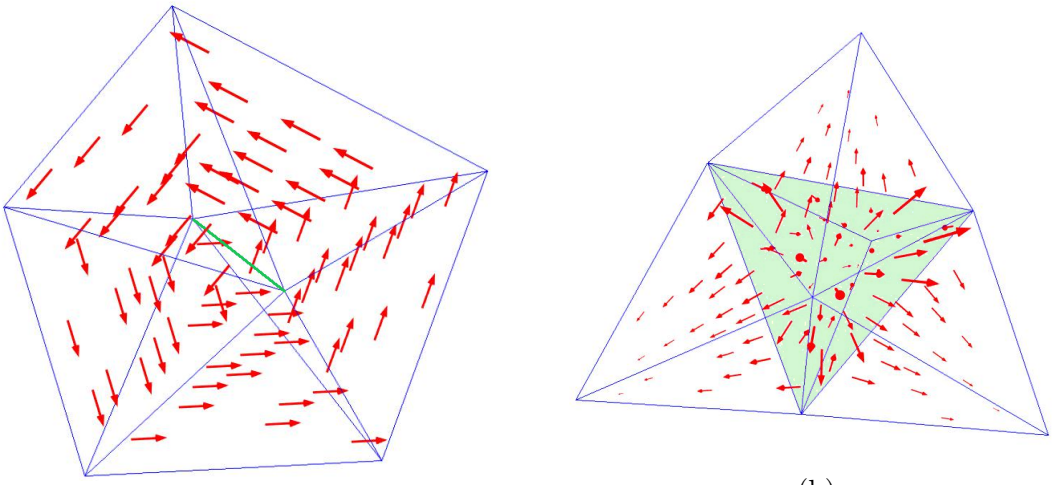

(a) (b)

Figure 3.1: (a) 3D visualization of a volume loop associated to an edge of the mesh (shown in green). (b) 3D visualization of a volume star associated to a tetrahedron of the mesh (shown in green).

The loop functions are defined on the edges of the mesh (i.e. fig. 3.1a) as linear combinations of SWG basis functions [65]. Although schemes for the creation of an independent set of loops in a tetrahedral mesh exist [65, 72], we do not build them explicitly here, they are only introduced for supporting the discussion. For

the purpose of this chapter, we will employ the properties $\boldsymbol{\Lambda}^{\mathrm{T}}\tilde{\boldsymbol{\Sigma}} = \mathbf{0}$ and $\tilde{\boldsymbol{\Sigma}}^{\mathrm{T}}\boldsymbol{\Lambda} = \mathbf{0}$, that $\boldsymbol{\Lambda}$ and $\tilde{\boldsymbol{\Sigma}}$ satisfy by construction [14].

After eliminating one column from $\tilde{\boldsymbol{\Sigma}}$ (zero total charge in Ω) yielding the mapping matrix $\boldsymbol{\Sigma}$, we obtain the full rank loop/star-to-SWG basis $\boldsymbol{B}^{\mathbf{I}}_{\boldsymbol{\Lambda\Sigma}} = [\boldsymbol{\Lambda}\ \boldsymbol{\Sigma}] \in \mathbb{R}^{N_F \times N_F}$. Applying $\boldsymbol{B}^{\mathbf{I}}_{\boldsymbol{\Lambda\Sigma}}$ to the D-VIE operator allows for separating its solenoidal and non-solenoidal parts that can be subsequently re-scaled appropriately to cure the ill-conditioning of the matrix. However, the matrix $\boldsymbol{B}^{\mathbf{I}}_{\boldsymbol{\Lambda\Sigma}}$ is ill-conditioned with a condition number that increases when the discretization of the geometry is refined.

3.3 A New Quasi-Helmholtz Decomposition of the D-VIE

In this work, we use a novel approach for performing a quasi-Helmholtz decomposition of the D-VIE without being limited by the conditioning issue of the discrete Helmholtz decomposition. We start by introducing the following loop-star decomposition of the unknown coefficients

$$\boldsymbol{\alpha} = \boldsymbol{\Lambda}\boldsymbol{l} + \boldsymbol{A}\boldsymbol{\Sigma}\boldsymbol{s}, \tag{3.16}$$

in which $\boldsymbol{A}$ is an invertible symmetric matrix. Note that it is shown in appendix A that $\boldsymbol{\Lambda}$ and $\boldsymbol{A\Sigma}$ have their column vectors linearly independent. Then, from this new decomposition, a scaled loop/star-to-SWG mapping matrix $\boldsymbol{B}^{\boldsymbol{A}^{-1}}_{\boldsymbol{\Lambda\Sigma}} = [\boldsymbol{\Lambda}\ \boldsymbol{A\Sigma}] \in \mathbb{R}^{N_F \times N_F}$ can be introduced. When $\boldsymbol{A} = \mathbf{I}$, we obtain the standard mapping matrix introduced in section 3.2 whereas using $\boldsymbol{A} = {\boldsymbol{G}_\epsilon}^{-1}$ gives a decomposition matrix that, when used to decompose the Gram matrix $\boldsymbol{G}_\epsilon$, yields the following 2-by-2 matrix

$$\begin{aligned} {\boldsymbol{B}^{\boldsymbol{G}_\epsilon}_{\boldsymbol{\Lambda\Sigma}}}^{\mathrm{T}} \boldsymbol{G}_\epsilon \boldsymbol{B}^{\boldsymbol{G}_\epsilon}_{\boldsymbol{\Lambda\Sigma}} &= \begin{bmatrix} \boldsymbol{\Lambda}^{\mathrm{T}} \\ \boldsymbol{\Sigma}^{\mathrm{T}} {\boldsymbol{G}_\epsilon}^{-1} \end{bmatrix} \boldsymbol{G}_\epsilon [\boldsymbol{\Lambda}\ {\boldsymbol{G}_\epsilon}^{-1}\boldsymbol{\Sigma}] \\ &= \begin{bmatrix} \boldsymbol{\Lambda}^{\mathrm{T}}\boldsymbol{G}_\epsilon\boldsymbol{\Lambda} & \mathbf{0} \\ \mathbf{0} & \boldsymbol{\Sigma}^{\mathrm{T}}{\boldsymbol{G}_\epsilon}^{-1}\boldsymbol{\Sigma} \end{bmatrix}, \end{aligned} \tag{3.17}$$

which shows that $\boldsymbol{G}_\epsilon$ is canceled in the off-diagonal blocks of its decomposition with $\boldsymbol{B}^{\boldsymbol{G}_\epsilon}_{\boldsymbol{\Lambda\Sigma}}$.

Besides the loop/star-to-SWG mapping matrix, a new form of volume quasi-Helmholtz projectors can be introduced from (3.16). This new set of projectors, $\boldsymbol{P}^{\boldsymbol{\Sigma}}_{\boldsymbol{A}^{-1}}$ and $\boldsymbol{P}^{\boldsymbol{\Lambda}}_{\boldsymbol{A}^{-1}}$, can respectively select the non-solenoidal and the solenoidal parts of the discretized operator without being limited by the conditioning issue of the mapping matrix $\boldsymbol{B}^{\boldsymbol{A}^{-1}}_{\boldsymbol{\Lambda\Sigma}}$. They are defined as

$$\boldsymbol{P}^{\boldsymbol{\Sigma}}_{\boldsymbol{A}^{-1}} = \boldsymbol{A\Sigma}\left(\boldsymbol{\Sigma}^{\mathrm{T}}\boldsymbol{A\Sigma}\right)^{+}\boldsymbol{\Sigma}^{\mathrm{T}} \tag{3.18}$$

$$\boldsymbol{P}^{\boldsymbol{\Lambda}}_{\boldsymbol{A}^{-1}} = \mathbf{I} - \boldsymbol{P}^{\boldsymbol{\Sigma}}_{\boldsymbol{A}^{-1}} = \boldsymbol{\Lambda}\left(\boldsymbol{\Lambda}^{\mathrm{T}}\boldsymbol{A}^{-1}\boldsymbol{\Lambda}\right)^{+}\boldsymbol{\Lambda}^{\mathrm{T}}\boldsymbol{A}^{-1}, \tag{3.19}$$

where $^+$ is the Moore-Penrose pseudo inverse. Differently from the definitions of quasi-Helmholtz projectors in previous works [5, 68], we introduce here the invertible and symmetric scaling matrix $\boldsymbol{A}$ in the projectors. Given this new definition, identity (3.19) does not follow directly from the properties of standard projectors, but its proof is provided in appendix A. These new projectors are not necessarily symmetric and their transposes are denoted by $\boldsymbol{P}_{\boldsymbol{A}^{-1}}^{\boldsymbol{\Lambda}\mathrm{T}}$ and $\boldsymbol{P}_{\boldsymbol{A}^{-1}}^{\boldsymbol{\Sigma}\mathrm{T}}$ in the following. When $\boldsymbol{A} = \mathbf{I}$, we obtain volume quasi-Helmholtz projectors, denoted by $\boldsymbol{P}_{\mathbf{I}}^{\boldsymbol{\Lambda}}$ and $\boldsymbol{P}_{\mathbf{I}}^{\boldsymbol{\Sigma}}$, that have the same form as their surface counterparts [5]. Instead, by choosing $\boldsymbol{A} = \boldsymbol{G}_{\epsilon}{}^{-1}$, we obtain the scaled projectors $\boldsymbol{P}_{\boldsymbol{G}_{\epsilon}}^{\boldsymbol{\Sigma}}$ and $\boldsymbol{P}_{\boldsymbol{G}_{\epsilon}}^{\boldsymbol{\Lambda}}$ defined as

$$\boldsymbol{P}_{\boldsymbol{G}_{\epsilon}}^{\boldsymbol{\Sigma}} = \boldsymbol{G}_{\epsilon}{}^{-1}\boldsymbol{\Sigma}\left(\boldsymbol{\Sigma}^{\mathrm{T}}\boldsymbol{G}_{\epsilon}{}^{-1}\boldsymbol{\Sigma}\right)^{+}\boldsymbol{\Sigma}^{\mathrm{T}} \tag{3.20}$$

$$\boldsymbol{P}_{\boldsymbol{G}_{\epsilon}}^{\boldsymbol{\Lambda}} = \mathbf{I} - \boldsymbol{P}_{\boldsymbol{G}_{\epsilon}}^{\boldsymbol{\Sigma}} = \boldsymbol{\Lambda}\left(\boldsymbol{\Lambda}^{\mathrm{T}}\boldsymbol{G}_{\epsilon}\boldsymbol{\Lambda}\right)^{+}\boldsymbol{\Lambda}^{\mathrm{T}}\boldsymbol{G}_{\epsilon}, \tag{3.21}$$

for which it can be easily seen that the following identities hold

$$\boldsymbol{P}_{\boldsymbol{G}_{\epsilon}}^{\boldsymbol{\Lambda}\mathrm{T}}\boldsymbol{G}_{\epsilon}\boldsymbol{P}_{\boldsymbol{G}_{\epsilon}}^{\boldsymbol{\Lambda}} = \boldsymbol{G}_{\epsilon}\boldsymbol{P}_{\boldsymbol{G}_{\epsilon}}^{\boldsymbol{\Lambda}} \tag{3.22}$$

$$\boldsymbol{P}_{\boldsymbol{G}_{\epsilon}}^{\boldsymbol{\Lambda}\mathrm{T}}\boldsymbol{G}_{\epsilon}\boldsymbol{P}_{\boldsymbol{G}_{\epsilon}}^{\boldsymbol{\Sigma}} = \mathbf{0} \tag{3.23}$$

$$\boldsymbol{P}_{\boldsymbol{G}_{\epsilon}}^{\boldsymbol{\Sigma}\mathrm{T}}\boldsymbol{G}_{\epsilon}\boldsymbol{P}_{\boldsymbol{G}_{\epsilon}}^{\boldsymbol{\Lambda}} = \mathbf{0} \tag{3.24}$$

$$\boldsymbol{P}_{\boldsymbol{G}_{\epsilon}}^{\boldsymbol{\Sigma}\mathrm{T}}\boldsymbol{G}_{\epsilon}\boldsymbol{P}_{\boldsymbol{G}_{\epsilon}}^{\boldsymbol{\Sigma}} = \boldsymbol{G}_{\epsilon}\boldsymbol{P}_{\boldsymbol{G}_{\epsilon}}^{\boldsymbol{\Sigma}}. \tag{3.25}$$

The mapping matrix $\boldsymbol{B}_{\boldsymbol{\Lambda}\boldsymbol{\Sigma}}^{\boldsymbol{A}^{-1}}$ and the associated set of scaled projectors will be further employed for the analysis and stabilization of the D-VIE, respectively.

3.4 Low-frequency Regularization of the D-VIE

We analyze here the low-frequency behavior of the D-VIE when modeling lossy dielectric objects surrounded by free space. At low frequencies, VIEs are subject to the low-frequency breakdown due to the frequency dependence of the complex permittivity of the object [88]. In the discretized D-VIE, this ill-scaling causes the ill-conditioning of the system matrix and the loss of significant digits in the solution coefficients. In this section, we first expose the low-frequency behavior of the D-VIE through a loop-star decomposition. This behavior will then be regularized using the volume quasi-Helmholtz projectors $\boldsymbol{P}_{\boldsymbol{A}^{-1}}^{\boldsymbol{\Lambda}}$ and $\boldsymbol{P}_{\boldsymbol{A}^{-1}}^{\boldsymbol{\Sigma}}$ in combination with appropriate scalings determined during the loop-star analysis to regularize the D-VIE at low frequencies without deteriorating its dense discretization behavior. To benefit from the cancellations of identity (3.17) in the loop-star decomposition of the D-VIE and (3.22) to (3.25) for its projector counterpart, the scaling matrix $\boldsymbol{A}$ could be set to $\boldsymbol{G}_{\epsilon}{}^{-1}$. However, since $\boldsymbol{G}_{\epsilon}$ is function of ω when the object is conductive (i.e. expression of the complex permittivity), it becomes singular in the static limit. For this reason, the symmetric and invertible scaling matrix $\boldsymbol{A} = \tilde{\boldsymbol{G}}_{\epsilon}{}^{-1}$

such that $\boldsymbol{G}_\epsilon = \mathrm{j}\omega\tilde{\boldsymbol{G}}_\epsilon$ is employed in the following. Another issue of this loop-star decomposition is that it could be singular due to the non-orthogonality between the column vectors of $\boldsymbol{\Lambda}$ and ${\boldsymbol{G}_\epsilon}^{-1}\boldsymbol{\Sigma}$. In appendix C, it is shown that the normalization of $\boldsymbol{\Lambda}$ and ${\tilde{\boldsymbol{G}}_\epsilon}^{-1}\boldsymbol{\Sigma}$ results in a decomposition matrix that is non-singular. The new loop/star-to-SWG decomposition matrix reads

$$\boldsymbol{B}_{\boldsymbol{\Lambda\Sigma}}^{\tilde{\boldsymbol{G}}_\epsilon} = \left[\overline{\overline{\boldsymbol{\Lambda}}},\ \overline{\overline{\boldsymbol{\Sigma}}}\right], \tag{3.26}$$

in which

$$\overline{\overline{\boldsymbol{\Lambda}}} = \boldsymbol{\Lambda}(\boldsymbol{\Lambda}^{\mathrm{T}}\boldsymbol{\Lambda})^{-\frac{1}{2}}, \tag{3.27}$$

$$\overline{\overline{\boldsymbol{\Sigma}}} = {\tilde{\boldsymbol{G}}_\epsilon}^{-1}\boldsymbol{\Sigma}(\boldsymbol{\Sigma}^{\mathrm{T}}{\tilde{\boldsymbol{G}}_\epsilon}^{-2}\boldsymbol{\Sigma})^{-\frac{1}{2}}. \tag{3.28}$$

Note that this normalized version of the loop-star decomposition matrix is only used for the purpose of the low-frequency analysis. Using $\boldsymbol{B}_{\boldsymbol{\Lambda\Sigma}}^{\tilde{\boldsymbol{G}}_\epsilon}$, the loop-star decomposition of the D-VIE can be expressed as

$${\boldsymbol{B}_{\boldsymbol{\Lambda\Sigma}}^{\tilde{\boldsymbol{G}}_\epsilon}}^{\mathrm{T}}(\boldsymbol{G}_\epsilon + \boldsymbol{Z}_{\boldsymbol{A}} + \boldsymbol{Z}_{\boldsymbol{\phi}})\boldsymbol{B}_{\boldsymbol{\Lambda\Sigma}}^{\tilde{\boldsymbol{G}}_\epsilon}\boldsymbol{\alpha}_{\boldsymbol{\Lambda\Sigma}} = {\boldsymbol{B}_{\boldsymbol{\Lambda\Sigma}}^{\tilde{\boldsymbol{G}}_\epsilon}}^{\mathrm{T}}\boldsymbol{v}, \tag{3.29}$$

where $\boldsymbol{B}_{\boldsymbol{\Lambda\Sigma}}^{\tilde{\boldsymbol{G}}_\epsilon}\boldsymbol{\alpha}_{\boldsymbol{\Lambda\Sigma}} = \boldsymbol{\alpha}$. Before pursuing with the expansion of eq. (3.29), we further decompose $\boldsymbol{Z}_{\boldsymbol{\phi}}$ as follows

$$\boldsymbol{Z}_{\boldsymbol{\phi}} = \boldsymbol{Z}_{\boldsymbol{\phi},\mathbf{11}} + \boldsymbol{Z}_{\boldsymbol{\phi},\mathbf{1\epsilon}}, \tag{3.30}$$

in which $\boldsymbol{Z}_{\boldsymbol{\phi},\mathbf{11}}$ only accounts for the volumic contributions in the object and the surfacic contributions on its boundary ($\partial\Omega$)

$$\begin{aligned}
&[\boldsymbol{Z}_{\boldsymbol{\phi},\mathbf{11}}]_{nm} = \\
&\epsilon_0^{-1}\left[\int_\Omega \nabla\cdot\boldsymbol{f}_{\boldsymbol{n}}(\boldsymbol{r})\int_\Omega G_0(\boldsymbol{r},\boldsymbol{r}')\kappa(\boldsymbol{r}')\nabla\cdot\boldsymbol{f}_{\boldsymbol{m}}(\boldsymbol{r}')\,\mathrm{d}v'\,\mathrm{d}v\right. \\
&-\int_\Omega \nabla\cdot\boldsymbol{f}_{\boldsymbol{n}}(\boldsymbol{r})\int_{\partial\Omega} G_0(\boldsymbol{r},\boldsymbol{r}')\kappa_m^+\hat{\boldsymbol{n}}_m\cdot\boldsymbol{f}_{\boldsymbol{m}}(\boldsymbol{r}')\,\mathrm{d}s'\,\mathrm{d}v \\
&-\int_{\partial\Omega} \hat{\boldsymbol{n}}_n\cdot\boldsymbol{f}_{\boldsymbol{n}}(\boldsymbol{r})\int_\Omega G_0(\boldsymbol{r},\boldsymbol{r}')\kappa(\boldsymbol{r}')\nabla\cdot\boldsymbol{f}_{\boldsymbol{m}}(\boldsymbol{r}')\,\mathrm{d}v'\,\mathrm{d}s \\
&\left.+\int_{\partial\Omega} \hat{\boldsymbol{n}}_n\cdot\boldsymbol{f}_{\boldsymbol{n}}(\boldsymbol{r})\int_{\partial\Omega} G_0(\boldsymbol{r},\boldsymbol{r}')\kappa_m^+\hat{\boldsymbol{n}}_m\cdot\boldsymbol{f}_{\boldsymbol{m}}(\boldsymbol{r}')\,\mathrm{d}s'\,\mathrm{d}s\right],
\end{aligned} \tag{3.31}$$

with κ_m^+ being the dielectric contrast in tetrahedron T_m^+ and $\hat{\boldsymbol{n}}_m$ the outward unit normal of the triangle of T_m^+ which pertains to $\partial\Omega$ and $\boldsymbol{Z}_{\boldsymbol{\phi},\mathbf{1\epsilon}}$ includes the purely surfacic contributions internal to the object (at the interface Γ_m between two tetrahedra T_m^- and T_m^+ of different material contrasts κ_m^- and κ_m^+)

$$\begin{aligned}
&[\boldsymbol{Z}_{\boldsymbol{\phi},\mathbf{1\epsilon}}]_{nm} = \epsilon_0^{-1}\cdot \\
&\left[\int_\Omega \nabla\cdot\boldsymbol{f}_{\boldsymbol{n}}(\boldsymbol{r})\int_{\Gamma_m} G_0(\boldsymbol{r},\boldsymbol{r}')\delta\kappa_m\hat{\boldsymbol{n}}_m\cdot\boldsymbol{f}_{\boldsymbol{m}}(\boldsymbol{r}')\,\mathrm{d}s'\,\mathrm{d}v\right. \\
&\left.-\int_{\partial\Omega} \hat{\boldsymbol{n}}_n\cdot\boldsymbol{f}_{\boldsymbol{n}}(\boldsymbol{r})\int_{\Gamma_m} G_0(\boldsymbol{r},\boldsymbol{r}')\delta\kappa_m\hat{\boldsymbol{n}}_m\cdot\boldsymbol{f}_{\boldsymbol{m}}(\boldsymbol{r}')\,\mathrm{d}s'\,\mathrm{d}s\right].
\end{aligned} \tag{3.32}$$

in which $\delta\kappa_m = \kappa_m^- - \kappa_m^+$ and $\hat{\boldsymbol{n}}_m$ is a unit vector normal to Γ_m oriented from T_m^+ to T_m^-. The following cancellations can be shown to arise when applying $\overline{\overline{\boldsymbol{\Lambda}}}^{\mathrm{T}}$ and $\overline{\overline{\boldsymbol{\Lambda}}}$ to the scalar potential

$$\overline{\overline{\boldsymbol{\Lambda}}}^{\mathrm{T}} \boldsymbol{Z}_{\boldsymbol{\phi},\mathbf{11}} = \mathbf{0}, \;\; \overline{\overline{\boldsymbol{\Lambda}}}^{\mathrm{T}} \boldsymbol{Z}_{\boldsymbol{\phi},\mathbf{1\epsilon}} = \mathbf{0}, \;\; \boldsymbol{Z}_{\boldsymbol{\phi},\mathbf{11}} \overline{\overline{\boldsymbol{\Lambda}}} = \mathbf{0}. \tag{3.33}$$

The fact that $\boldsymbol{\Lambda}$ (and thus $\overline{\overline{\boldsymbol{\Lambda}}}$) cancels the surface terms defined on $\partial\Omega$ in $\boldsymbol{Z}_{\boldsymbol{\phi},\mathbf{11}}$ and $\boldsymbol{Z}_{\boldsymbol{\phi},\mathbf{1\epsilon}}$ results from the absence of loops functions on $\partial\Omega$. This property is proven in appendix B.

We then represent $\boldsymbol{Z}_{\boldsymbol{\Lambda\Sigma}}$ from (3.29) as a 2-by-2 block matrix

$$\begin{aligned} \boldsymbol{Z}_{\boldsymbol{\Lambda\Sigma}} &= \boldsymbol{B}_{\boldsymbol{\Lambda\Sigma}}^{\tilde{\boldsymbol{G}}_\epsilon}{}^{\mathrm{T}} \boldsymbol{Z} \boldsymbol{B}_{\boldsymbol{\Lambda\Sigma}}^{\tilde{\boldsymbol{G}}_\epsilon} \\ &= \begin{bmatrix} \overline{\overline{\boldsymbol{\Lambda}}}^{\mathrm{T}} \boldsymbol{Z} \overline{\overline{\boldsymbol{\Lambda}}} & \overline{\overline{\boldsymbol{\Lambda}}}^{\mathrm{T}} \boldsymbol{Z} \overline{\overline{\boldsymbol{\Sigma}}} \\ \overline{\overline{\boldsymbol{\Sigma}}}^{\mathrm{T}} \boldsymbol{Z} \overline{\overline{\boldsymbol{\Lambda}}} & \overline{\overline{\boldsymbol{\Sigma}}}^{\mathrm{T}} \boldsymbol{Z} \overline{\overline{\boldsymbol{\Sigma}}} \end{bmatrix}, \end{aligned} \tag{3.34}$$

in which

$$\overline{\overline{\boldsymbol{\Lambda}}}^{\mathrm{T}} \boldsymbol{Z} \overline{\overline{\boldsymbol{\Lambda}}} = \overline{\overline{\boldsymbol{\Lambda}}}^{\mathrm{T}} (\boldsymbol{G}_\epsilon + \boldsymbol{Z}_{\boldsymbol{A}}) \overline{\overline{\boldsymbol{\Lambda}}} \tag{3.35}$$

$$\overline{\overline{\boldsymbol{\Lambda}}}^{\mathrm{T}} \boldsymbol{Z} \overline{\overline{\boldsymbol{\Sigma}}} = \overline{\overline{\boldsymbol{\Lambda}}}^{\mathrm{T}} \boldsymbol{Z}_{\boldsymbol{A}} \overline{\overline{\boldsymbol{\Sigma}}} \tag{3.36}$$

$$\overline{\overline{\boldsymbol{\Sigma}}}^{\mathrm{T}} \boldsymbol{Z} \overline{\overline{\boldsymbol{\Lambda}}} = \overline{\overline{\boldsymbol{\Sigma}}}^{\mathrm{T}} (\boldsymbol{Z}_{\boldsymbol{A}} + \boldsymbol{Z}_{\boldsymbol{\phi},\mathbf{1\epsilon}}) \overline{\overline{\boldsymbol{\Lambda}}} \tag{3.37}$$

$$\overline{\overline{\boldsymbol{\Sigma}}}^{\mathrm{T}} \boldsymbol{Z} \overline{\overline{\boldsymbol{\Sigma}}} = \overline{\overline{\boldsymbol{\Sigma}}}^{\mathrm{T}} (\boldsymbol{G}_\epsilon + \boldsymbol{Z}_{\boldsymbol{A}} + \boldsymbol{Z}_{\boldsymbol{\phi}}) \overline{\overline{\boldsymbol{\Sigma}}}. \tag{3.38}$$

We have the following frequency scalings for the real and imaginary parts of the terms in the decomposition of $\boldsymbol{Z}_{\boldsymbol{\Lambda\Sigma}}$ ((3.35), (3.36), (3.37), and (3.38))

$$\mathrm{Re}\,(\boldsymbol{G}_\epsilon) \underset{\omega\to 0}{=} \mathcal{O}(\omega^2), \;\; \mathrm{Im}\,(\boldsymbol{G}_\epsilon) \underset{\omega\to 0}{=} \mathcal{O}(\omega), \tag{3.39}$$

$$\mathrm{Re}\,(\boldsymbol{Z}_{\boldsymbol{A}}) \underset{\omega\to 0}{=} \mathcal{O}(\omega^2), \;\; \mathrm{Im}\,(\boldsymbol{Z}_{\boldsymbol{A}}) \underset{\omega\to 0}{=} \mathcal{O}(\omega^3), \tag{3.40}$$

$$\mathrm{Re}\,(\boldsymbol{Z}_{\boldsymbol{\phi},\mathbf{11}}) \underset{\omega\to 0}{=} \mathcal{O}(1), \;\; \mathrm{Im}\,(\boldsymbol{Z}_{\boldsymbol{\phi},\mathbf{11}}) \underset{\omega\to 0}{=} \mathcal{O}(\omega), \tag{3.41}$$

$$\mathrm{Re}\,(\boldsymbol{Z}_{\boldsymbol{\phi},\mathbf{1\epsilon}}) \underset{\omega\to 0}{=} \mathcal{O}(\omega^2), \;\; \mathrm{Im}\,(\boldsymbol{Z}_{\boldsymbol{\phi},\mathbf{1\epsilon}}) \underset{\omega\to 0}{=} \mathcal{O}(\omega). \tag{3.42}$$

Using (3.39) to (3.42), we deduce the scalings for $\boldsymbol{Z}_{\boldsymbol{\Lambda\Sigma}}$ at low frequencies

$$\mathrm{Re}\;(\boldsymbol{Z}_{\boldsymbol{\Lambda\Sigma}}) \underset{\omega\to 0}{=} \begin{bmatrix} \mathcal{O}(\omega^2) & \mathcal{O}(\omega^2) \\ \mathcal{O}(\omega^2) & \mathcal{O}(1) \end{bmatrix}, \tag{3.43}$$

$$\mathrm{Im}\;(\boldsymbol{Z}_{\boldsymbol{\Lambda\Sigma}}) \underset{\omega\to 0}{=} \begin{bmatrix} \mathcal{O}(\omega) & \mathcal{O}(\omega^3) \\ \mathcal{O}(\omega) & \mathcal{O}(\omega) \end{bmatrix}, \tag{3.44}$$

which, according to the Gershgorin circle theorem, confirm that $\boldsymbol{Z}_{\boldsymbol{\Lambda\Sigma}}$ is ill-conditioned. Besides the conditioning of the impedance matrix, it is also important to determine

whether or not the solution coefficients and the right hand side vectors are preserved in the static limit. We first provide the scalings of the right hand side for plane wave and dipole excitations, which are frequently employed in bioelectromagnetic applications. For a plane wave excitation, the right hand side of (3.29) has the following scalings when $\omega \to 0$

$$\mathrm{Re}\left(\boldsymbol{B}_{\boldsymbol{\Lambda\Sigma}}^{\tilde{\boldsymbol{G}}_\epsilon\,\mathrm{T}}\boldsymbol{v}_{\mathrm{PW}}\right) \underset{\omega\to 0}{=} \begin{bmatrix}\mathcal{O}(\omega^2)\\ \mathcal{O}(1)\end{bmatrix}; \mathrm{Im}\left(\boldsymbol{B}_{\boldsymbol{\Lambda\Sigma}}^{\tilde{\boldsymbol{G}}_\epsilon\,\mathrm{T}}\boldsymbol{v}_{\mathrm{PW}}\right) \underset{\omega\to 0}{=} \begin{bmatrix}\mathcal{O}(\omega)\\ \mathcal{O}(\omega)\end{bmatrix}, \tag{3.45}$$

in which $[\boldsymbol{v}_{\mathrm{PW}}]_n = \int_\Omega \boldsymbol{f_n}(\boldsymbol{r}) \cdot \boldsymbol{E}_0 \exp\left(-\mathrm{j}\boldsymbol{k}\cdot\boldsymbol{r}\right) \mathrm{d}v$ with $\boldsymbol{E}_0$ being the polarization of the plane wave and $\boldsymbol{k}$ its wave vector. It can be noted that the right hand side for a plane wave excitation scales similarly in the D-VIE and in the surface electric field integral equation [84]. To derive the frequency dependence of the loop-star decomposition of a dipole excitation, we start from the expression of the field it radiates (3.5) in which $\boldsymbol{J}_i(\boldsymbol{r},\boldsymbol{r}_0) = \mathrm{j}\omega\delta(\boldsymbol{r}-\boldsymbol{r}_0)\boldsymbol{p}$ is the current dipole with δ, $\boldsymbol{p}$, and $\boldsymbol{r_0}$ being the Dirac delta function, the dipole moment, and the dipole position, respectively. We then test (3.5) with $\{\boldsymbol{f_n}\}$ to obtain the discretized right hand side

$$\begin{aligned}[\boldsymbol{v}_{\mathrm{dip}}]_n &= [\boldsymbol{v}_{\mathrm{A}}]_n + [\boldsymbol{v}_{\Phi}]_n\\ &= \frac{k_0^2}{\epsilon_0}\boldsymbol{p}\cdot\int_\Omega \boldsymbol{f_n}(\boldsymbol{r})G_0(\boldsymbol{r},\boldsymbol{r}_0)\,\mathrm{d}v\\ &- \frac{1}{\epsilon_0}\int_\Omega \nabla\cdot\boldsymbol{f_n}(\boldsymbol{r})\boldsymbol{p}\cdot\nabla G_0(\boldsymbol{r},\boldsymbol{r}_0)\,\mathrm{d}v.\end{aligned} \tag{3.46}$$

From the Taylor expansion of G_0 and its gradient, we obtain that $\mathrm{Re}\,(G_0(\boldsymbol{r},\boldsymbol{r}_0)) = \mathcal{O}(1)$, $\mathrm{Im}\,(G_0(\boldsymbol{r},\boldsymbol{r}_0)) = \mathcal{O}(\omega)$, $\mathrm{Re}\,(\nabla G_0(\boldsymbol{r},\boldsymbol{r}_0)) = \mathcal{O}(1)$, and $\mathrm{Im}\,(\nabla G_0(\boldsymbol{r},\boldsymbol{r}_0)) = \mathcal{O}(\omega^3)$ at low frequencies. This yields the following frequency dependencies for the real and imaginary parts of the loop-star decomposition of $\boldsymbol{v}_{\mathrm{A}}$ and $\boldsymbol{v}_{\Phi}$

$$\mathrm{Re}\,(\overline{\overline{\boldsymbol{\Lambda}}}^{\mathrm{T}}\boldsymbol{v}_{\mathrm{A}}) \underset{\omega\to 0}{=} \mathcal{O}(\omega^2),\ \mathrm{Im}\,(\overline{\overline{\boldsymbol{\Lambda}}}^{\mathrm{T}}\boldsymbol{v}_{\mathrm{A}}) \underset{\omega\to 0}{=} \mathcal{O}(\omega^5) \tag{3.47}$$

$$\mathrm{Re}\,(\overline{\overline{\boldsymbol{\Sigma}}}^{\mathrm{T}}\boldsymbol{v}_{\mathrm{A}}) \underset{\omega\to 0}{=} \mathcal{O}(\omega^2),\ \mathrm{Im}\,(\overline{\overline{\boldsymbol{\Sigma}}}^{\mathrm{T}}\boldsymbol{v}_{\mathrm{A}}) \underset{\omega\to 0}{=} \mathcal{O}(\omega^3) \tag{3.48}$$

$$\mathrm{Re}\,(\overline{\overline{\boldsymbol{\Lambda}}}^{\mathrm{T}}\boldsymbol{v}_{\Phi}) \underset{\omega\to 0}{=} 0,\ \mathrm{Im}\,(\overline{\overline{\boldsymbol{\Lambda}}}^{\mathrm{T}}\boldsymbol{v}_{\Phi}) \underset{\omega\to 0}{=} 0 \tag{3.49}$$

$$\mathrm{Re}\,(\overline{\overline{\boldsymbol{\Sigma}}}^{\mathrm{T}}\boldsymbol{v}_{\Phi}) \underset{\omega\to 0}{=} \mathcal{O}(1),\ \mathrm{Im}\,(\overline{\overline{\boldsymbol{\Sigma}}}^{\mathrm{T}}\boldsymbol{v}_{\Phi}) \underset{\omega\to 0}{=} \mathcal{O}(\omega), \tag{3.50}$$

from which we obtain the scalings of $\boldsymbol{v}_{\mathrm{dip}}$ at low frequencies

$$\mathrm{Re}\left(\boldsymbol{B}_{\boldsymbol{\Lambda\Sigma}}^{\tilde{\boldsymbol{G}}_\epsilon\,\mathrm{T}}\boldsymbol{v}_{\mathrm{dip}}\right) \underset{\omega\to 0}{=} \begin{bmatrix}\mathcal{O}(\omega^2)\\ \mathcal{O}(1)\end{bmatrix}; \mathrm{Im}\left(\boldsymbol{B}_{\boldsymbol{\Lambda\Sigma}}^{\tilde{\boldsymbol{G}}_\epsilon\,\mathrm{T}}\boldsymbol{v}_{\mathrm{dip}}\right) \underset{\omega\to 0}{=} \begin{bmatrix}\mathcal{O}(\omega^5)\\ \mathcal{O}(\omega)\end{bmatrix}. \tag{3.51}$$

This concludes the scaling analysis of the right hand side for plane wave and dipole excitations. The scalings obtained are summarized in Table 3.1a, in which $\boldsymbol{v}_{\boldsymbol{\Lambda}}$

denotes the loop part of the right hand side and $\boldsymbol{\nu}_{\boldsymbol{\Sigma}}$ its star part. The terms recovered correspond to the terms for which the real (or imaginary) part of the loop and star components have the same frequency scaling. All the other terms are lost due to finite precision arithmetic. To identify the impact of this loss on the solution coefficients, we subsequently retrieve the scalings of $\boldsymbol{\alpha}_{\boldsymbol{\Lambda\Sigma}}$ for plane wave and dipole excitations. This requires the knowledge of the frequency scalings of the inverse of $\boldsymbol{Z}_{\boldsymbol{\Lambda\Sigma}}$, which are derived by inverting (3.34) using Schur complement formulas [46]

$$\mathrm{Re}\left(\boldsymbol{Z}_{\boldsymbol{\Lambda\Sigma}}{}^{-1}\right) \underset{\omega\to 0}{=} \begin{bmatrix} \mathcal{O}(1) & \mathcal{O}(\omega^2) \\ \mathcal{O}(1) & \mathcal{O}(1) \end{bmatrix} \tag{3.52}$$

$$\mathrm{Im}\left(\boldsymbol{Z}_{\boldsymbol{\Lambda\Sigma}}{}^{-1}\right) \underset{\omega\to 0}{=} \begin{bmatrix} \mathcal{O}(1/\omega) & \mathcal{O}(\omega) \\ \mathcal{O}(\omega) & \mathcal{O}(\omega) \end{bmatrix}. \tag{3.53}$$

Finally by multiplying the scaling matrix of $\boldsymbol{Z}_{\boldsymbol{\Lambda\Sigma}}{}^{-1}$ ((3.52) and (3.53)) and the scaling vector of $\boldsymbol{B}_{\boldsymbol{\Lambda\Sigma}}^{\tilde{\mathbf{G}}_\epsilon\,\mathrm{T}}\boldsymbol{\nu}$ ((3.45) for the plane wave or (3.51) for the dipole), we obtain the following scalings of $\boldsymbol{\alpha}_{\boldsymbol{\Lambda\Sigma}}$ for plane wave excitations

$$\mathrm{Re}\left(\boldsymbol{\alpha}_{\boldsymbol{\Lambda\Sigma}}^{\mathrm{PW}}\right) \underset{\omega\to 0}{=} \begin{bmatrix} \mathcal{O}(1) \\ \mathcal{O}(1) \end{bmatrix}; \mathrm{Im}\left(\boldsymbol{\alpha}_{\boldsymbol{\Lambda\Sigma}}^{\mathrm{PW}}\right) \underset{\omega\to 0}{=} \begin{bmatrix} \mathcal{O}(\omega) \\ \mathcal{O}(\omega) \end{bmatrix}, \tag{3.54}$$

and

$$\mathrm{Re}\left(\boldsymbol{\alpha}_{\boldsymbol{\Lambda\Sigma}}^{\mathrm{dip}}\right) \underset{\omega\to 0}{=} \begin{bmatrix} \mathcal{O}(\omega^2) \\ \mathcal{O}(1) \end{bmatrix}; \mathrm{Im}\left(\boldsymbol{\alpha}_{\boldsymbol{\Lambda\Sigma}}^{\mathrm{dip}}\right) \underset{\omega\to 0}{=} \begin{bmatrix} \mathcal{O}(\omega) \\ \mathcal{O}(\omega) \end{bmatrix}, \tag{3.55}$$

for dipole excitations. These scalings are summarized in table 3.1b.

The dominant terms in table 3.1b represent the real (or imaginary) components of the solution coefficients that are preserved at low frequencies, the remaining components are lost. For example, the real part of the loop component of the solution vector for the dipole excitation is lost at low frequencies. In the scope of this chapter, the D-VIE is applied in scenarios where the electric field inside the object is required. Since there is a simple scalar relation between the unknown of the D-VIE (i.e. electric flux) and the electric field, there is no re-amplification of a lost (loop or star) part possible, and thus it is not required to preserve the components of the solution lost due to finite precision at low frequencies.

Nevertheless, a loss of accuracy in the solution occurs when a term of the right hand side, which is lost at low frequencies, contributes to one of the dominant terms of the solution. In fact, it is possible that the inverse matrix $\boldsymbol{Z}_{\boldsymbol{\Lambda\Sigma}}{}^{-1}$ amplifies some vanishing terms in the right hand side vector and make them non-negligible in the solution. In table 3.1a, the terms contributing to the solution for both types of excitation are provided. For the dipole and the plane wave, it can be observed that the real part of the loop component of the right hand side is lost due to finite precision while it is supposed to contribute to the solution. For this reason, there

Table 3.1: Frequency scalings of the real and imaginary parts of $\boldsymbol{\nu}$, $\boldsymbol{\alpha}_{\Lambda\Sigma}$, and $\tilde{\boldsymbol{\nu}}$.

(a) Right hand side $\boldsymbol{\nu}$

Source	(Re , Im) $(\boldsymbol{\nu}_{\Lambda})$	(Re , Im) $(\boldsymbol{\nu}_{\Sigma})$	Terms recovered	Terms required for a correct solution
Plane Wave	(ω^2, ω)	$(1, \omega)$	Re $(\boldsymbol{\nu}_{\Sigma})$ Im $(\boldsymbol{\nu}_{\Lambda})$, Im $(\boldsymbol{\nu}_{\Sigma})$	Re $(\boldsymbol{\nu}_{\Lambda})$, Re $(\boldsymbol{\nu}_{\Sigma})$ Im $(\boldsymbol{\nu}_{\Lambda})$, Im $(\boldsymbol{\nu}_{\Sigma})$
Dipole	(ω^2, ω^5)	$(1, \omega)$	Im $(\boldsymbol{\nu}_{\Lambda})$, Im $(\boldsymbol{\nu}_{\Sigma})$	Re $(\boldsymbol{\nu}_{\Lambda})$ Im $(\boldsymbol{\nu}_{\Lambda})$, Im $(\boldsymbol{\nu}_{\Sigma})$

(b) Solution $\boldsymbol{\alpha}_{\Lambda\Sigma}$

Source	(Re , Im) $(\boldsymbol{\alpha}_{\Lambda})$	(Re , Im) $(\boldsymbol{\alpha}_{\Sigma})$	Terms recovered
Plane Wave	$(1, \omega)$	$(1, \omega)$	Re $(\boldsymbol{\alpha}_{\Lambda})$, Re $(\boldsymbol{\alpha}_{\Sigma})$ Im $(\boldsymbol{\alpha}_{\Lambda})$, Im $(\boldsymbol{\alpha}_{\Sigma})$
Dipole	(ω^2, ω)	$(1, \omega)$	Re $(\boldsymbol{\alpha}_{\Sigma})$ Im $(\boldsymbol{\alpha}_{\Lambda})$, Im $(\boldsymbol{\alpha}_{\Sigma})$

(c) Scaled right hand side $\tilde{\boldsymbol{\nu}}$

Source	(Re , Im) $(\tilde{\boldsymbol{\nu}}_{\Lambda})$	(Re , Im) $(\tilde{\boldsymbol{\nu}}_{\Sigma})$	Terms recovered	Terms required for a correct solution
Plane Wave	$(1, \omega)$	$(1, \omega)$	Re $(\tilde{\boldsymbol{\nu}}_{\Lambda})$, Re $(\tilde{\boldsymbol{\nu}}_{\Sigma})$ Im $(\tilde{\boldsymbol{\nu}}_{\Lambda})$, Im $(\tilde{\boldsymbol{\nu}}_{\Sigma})$	Re $(\tilde{\boldsymbol{\nu}}_{\Lambda})$, Re $(\tilde{\boldsymbol{\nu}}_{\Sigma})$ Im $(\tilde{\boldsymbol{\nu}}_{\Lambda})$, Im $(\tilde{\boldsymbol{\nu}}_{\Sigma})$
Dipole	(ω^4, ω)	$(1, \omega)$	Re $(\tilde{\boldsymbol{\nu}}_{\Sigma})$ Im $(\tilde{\boldsymbol{\nu}}_{\Lambda})$, Im $(\tilde{\boldsymbol{\nu}}_{\Sigma})$	Re $(\tilde{\boldsymbol{\nu}}_{\Sigma})$ Im $(\tilde{\boldsymbol{\nu}}_{\Lambda})$, Im $(\tilde{\boldsymbol{\nu}}_{\Sigma})$

is a loss of accuracy in the solution at low frequencies with plane wave and dipole excitations.

To solve the two above-mentioned issues, we regularize (3.29) by re-scaling appropriately the loop/star-to-SWG transformation matrices, resulting in the following loop-star D-VIE

$$\begin{bmatrix} C_1 \overline{\overline{\boldsymbol{\Lambda}}}^{\mathrm{T}} \\ C_2 \overline{\overline{\boldsymbol{\Sigma}}}^{\mathrm{T}} \end{bmatrix} (\boldsymbol{G}_{\epsilon} + \boldsymbol{Z}_{\boldsymbol{A}} + \boldsymbol{Z}_{\boldsymbol{\Phi}}) [C_3 \overline{\overline{\boldsymbol{\Lambda}}},\ C_4 \overline{\overline{\boldsymbol{\Sigma}}}] \tilde{\boldsymbol{\alpha}}_{\Lambda\Sigma} = \begin{bmatrix} C_1 \overline{\overline{\boldsymbol{\Lambda}}}^{\mathrm{T}} \\ C_2 \overline{\overline{\boldsymbol{\Sigma}}}^{\mathrm{T}} \end{bmatrix} \boldsymbol{\nu}, \tag{3.56}$$

in which the coefficients C_1, C_2, C_3 and C_4 have to be determined to make the loop and star parts of the preconditioned matrix ($\tilde{\boldsymbol{Z}}_{\Lambda\Sigma}$), its right hand side ($\tilde{\boldsymbol{\nu}}$), and its re-scaled solution ($\tilde{\boldsymbol{\alpha}}_{\Lambda\Sigma}$) free from ill-conditioning and loss of accuracy. Since the numerical loss comes from the right hand side and not from the solution directly, we can set C_3 and C_4 to 1 and attempt to leverage the two remaining coefficients

to regularize the rest of the equation, which gives $\boldsymbol{\alpha}_{\Lambda\Sigma} = \tilde{\boldsymbol{\alpha}}_{\Lambda\Sigma}$. Therefore, we now need to determine C_1 and C_2 for $\tilde{\boldsymbol{Z}}_{\Lambda\Sigma}$ to be well-conditioned and to avoid numerical loss. By choosing $C_1 = 1/(\mathrm{j}\omega\epsilon_0)$ and $C_2 = 1$, the matrix becomes well-conditioned and the right hand side is no longer subject to numerical loss of accuracy for both plane wave and dipole excitations. The resulting loop-star matrix $\tilde{\boldsymbol{Z}}_{\Lambda\Sigma} = \tilde{\boldsymbol{B}}_{\Lambda\Sigma}^{\tilde{\boldsymbol{G}}_\epsilon\,\mathrm{T}}(\boldsymbol{G}_\epsilon + \boldsymbol{Z}_{\boldsymbol{A}} + \boldsymbol{Z}_{\boldsymbol{\Phi}})\boldsymbol{B}_{\Lambda\Sigma}^{\tilde{\boldsymbol{G}}_\epsilon}$ has the following frequency scalings

$$\mathrm{Re}\left(\tilde{\boldsymbol{Z}}_{\Lambda\Sigma}\right) \underset{\omega\to 0}{=} \begin{bmatrix} \mathcal{O}(1) & \mathcal{O}(\omega^2) \\ \mathcal{O}(\omega^2) & \mathcal{O}(1) \end{bmatrix} \tag{3.57}$$

$$\mathrm{Im}\left(\tilde{\boldsymbol{Z}}_{\Lambda\Sigma}\right) \underset{\omega\to 0}{=} \begin{bmatrix} \mathcal{O}(\omega) & \mathcal{O}(\omega) \\ \mathcal{O}(\omega) & \mathcal{O}(\omega) \end{bmatrix}, \tag{3.58}$$

where $\tilde{\boldsymbol{B}}_{\Lambda\Sigma}^{\tilde{\boldsymbol{G}}_\epsilon} = [C_1\overline{\overline{\boldsymbol{\Lambda}}},\ C_2\overline{\overline{\boldsymbol{\Sigma}}}]$. While the diagonal blocks of (3.57) scale as $\mathcal{O}(1)$, all the other blocks get to zero at low frequencies, thus it results that $\tilde{\boldsymbol{Z}}_{\Lambda\Sigma}$ is well-conditioned. Note that leveraging the standard loop-star decomposition (eq. (3.12)) instead would have led to an upper triangular block matrix, of which the proper conditioning would have been cumbersome to prove ($\boldsymbol{Z}$ being non-symmetric). The preconditioned right hand side then scales as

$$\mathrm{Re}\left(\tilde{\boldsymbol{B}}_{\Lambda\Sigma}^{\tilde{\boldsymbol{G}}_\epsilon\,\mathrm{T}}\boldsymbol{v}_{\mathrm{PW}}\right) \underset{\omega\to 0}{=} \begin{bmatrix}\mathcal{O}(1)\\ \mathcal{O}(1)\end{bmatrix}; \mathrm{Im}\left(\tilde{\boldsymbol{B}}_{\Lambda\Sigma}^{\tilde{\boldsymbol{G}}_\epsilon\,\mathrm{T}}\boldsymbol{v}_{\mathrm{PW}}\right) \underset{\omega\to 0}{=} \begin{bmatrix}\mathcal{O}(\omega)\\ \mathcal{O}(\omega)\end{bmatrix}, \tag{3.59}$$

for the plane wave and

$$\mathrm{Re}\left(\tilde{\boldsymbol{B}}_{\Lambda\Sigma}^{\tilde{\boldsymbol{G}}_\epsilon\,\mathrm{T}}\boldsymbol{v}_{\mathrm{dip}}\right) \underset{\omega\to 0}{=} \begin{bmatrix}\mathcal{O}(\omega^4)\\ \mathcal{O}(1)\end{bmatrix}; \mathrm{Im}\left(\tilde{\boldsymbol{B}}_{\Lambda\Sigma}^{\tilde{\boldsymbol{G}}_\epsilon\,\mathrm{T}}\boldsymbol{v}_{\mathrm{dip}}\right) \underset{\omega\to 0}{=} \begin{bmatrix}\mathcal{O}(\omega)\\ \mathcal{O}(\omega)\end{bmatrix}, \tag{3.60}$$

for the dipole. From table 3.1c, it results that all the coefficients contributing to the solution are preserved at low frequencies. Therefore, the coefficients C_1, C_2, C_3, and C_4 together with the loop-star decomposition have successfully cured the ill-scaling in the matrix and the right hand side. The final equation in the normalized loop-star D-VIE reads

$$\tilde{\boldsymbol{B}}_{\Lambda\Sigma}^{\tilde{\boldsymbol{G}}_\epsilon\,\mathrm{T}}\boldsymbol{Z}\boldsymbol{B}_{\Lambda\Sigma}^{\tilde{\boldsymbol{G}}_\epsilon}\boldsymbol{\alpha}_{\Lambda\Sigma} = \tilde{\boldsymbol{B}}_{\Lambda\Sigma}^{\tilde{\boldsymbol{G}}_\epsilon\,\mathrm{T}}\boldsymbol{v}. \tag{3.61}$$

We note that, since the computation of the square roots present in the definition of the normalized loop/star-to-SWG matrix is not efficient, the non-normalized version of this mapping matrix should be employed in a numerical implementation of the loop-star D-VIE.

Subsequently, we can logically relate the above-mentioned coefficients and the quasi-Helmholtz projectors defined in (3.18) and (3.19) with $\boldsymbol{A} = \tilde{\boldsymbol{G}}_\epsilon^{-1}$ to build a preconditioned equation that does not suffer from the dense discretization breakdown. We obtain the following left and right preconditioners

$$\boldsymbol{L} = C_1\boldsymbol{P}_{\tilde{\boldsymbol{G}}_\epsilon}^{\Lambda\mathrm{T}} + C_2\boldsymbol{P}_{\tilde{\boldsymbol{G}}_\epsilon}^{\Sigma\mathrm{T}} \tag{3.62}$$

$$\boldsymbol{R} = C_3\boldsymbol{P}_{\tilde{\boldsymbol{G}}_\epsilon}^{\Lambda} + C_4\boldsymbol{P}_{\tilde{\boldsymbol{G}}_\epsilon}^{\Sigma}. \tag{3.63}$$

Since $C_3 = C_4 = 1$, we have $\boldsymbol{R} = \mathbf{I}$, and the resulting preconditioned equation to be solved reads

$$\boldsymbol{L}\boldsymbol{Z}\boldsymbol{\alpha} = \boldsymbol{L}\boldsymbol{v}, \tag{3.64}$$

in which

$$\begin{aligned}\boldsymbol{L} &= C_1\gamma_\Lambda \boldsymbol{P}_{\tilde{\boldsymbol{G}}_\epsilon}^{\boldsymbol{\Lambda}\mathrm{T}} + C_2\gamma_\Sigma \boldsymbol{P}_{\tilde{\boldsymbol{G}}_\epsilon}^{\boldsymbol{\Sigma}\mathrm{T}} \\ &= \frac{\gamma_\Lambda}{\mathrm{j}\omega\epsilon_0}\boldsymbol{P}_{\tilde{\boldsymbol{G}}_\epsilon}^{\boldsymbol{\Lambda}\mathrm{T}} + \gamma_\Sigma \boldsymbol{P}_{\tilde{\boldsymbol{G}}_\epsilon}^{\boldsymbol{\Sigma}\mathrm{T}}.\end{aligned} \tag{3.65}$$

Note that the frequency-independent coefficients γ_Λ and γ_Σ were added in (3.65) to make the norms of $(\gamma_\Lambda/(\mathrm{j}\omega\epsilon_0))\,\boldsymbol{P}_{\tilde{\boldsymbol{G}}_\epsilon}^{\boldsymbol{\Lambda}\mathrm{T}}\boldsymbol{Z}\boldsymbol{P}_{\tilde{\boldsymbol{G}}_\epsilon}^{\boldsymbol{\Lambda}}$ and of $\gamma_\Sigma \boldsymbol{P}_{\tilde{\boldsymbol{G}}_\epsilon}^{\boldsymbol{\Sigma}\mathrm{T}}\boldsymbol{Z}\boldsymbol{P}_{\tilde{\boldsymbol{G}}_\epsilon}^{\boldsymbol{\Sigma}}$ of order $\mathcal{O}(1)$ regardless of the geometry. They are defined as

$$\gamma_\Lambda = (\|\epsilon_0^{-1}\boldsymbol{G}\boldsymbol{P}_{\tilde{\boldsymbol{G}}_\epsilon}^{\boldsymbol{\Lambda}}\|)^{-1} \tag{3.66}$$

$$\gamma_\Sigma = (\|\boldsymbol{P}_{\tilde{\boldsymbol{G}}_\epsilon}^{\boldsymbol{\Sigma}\mathrm{T}}\boldsymbol{Z}_{\boldsymbol{\phi}}\boldsymbol{P}_{\tilde{\boldsymbol{G}}_\epsilon}^{\boldsymbol{\Sigma}}\|)^{-1}, \tag{3.67}$$

with $\|\cdot\|$ denoting the L^2-norm and $[\boldsymbol{G}]_{nm} = \langle \boldsymbol{f}_n, \boldsymbol{f}_m \rangle_\Omega$ being the SWG-SWG Gram matrix.

Also, note that the coefficients in front of $\boldsymbol{P}_{\tilde{\boldsymbol{G}}_\epsilon}^{\boldsymbol{\Lambda}\mathrm{T}}$ and $\boldsymbol{P}_{\tilde{\boldsymbol{G}}_\epsilon}^{\boldsymbol{\Sigma}\mathrm{T}}$ in $\boldsymbol{L}$ (eq. (3.65)) are suitable only at low frequencies ($f < 1\,\mathrm{MHz}$). Above this frequency, they should be set to 1, which is equivalent to using the standard D-VIE, that has a reasonably low condition number at high frequencies.

3.5 Implementation Related Details

This section presents the details related to the implementation of the proposed preconditioner. Starting from an existing D-VIE, the quasi-Helmholtz projectors must be computed in quasi-linear complexity not to deteriorate the overall complexity of the solver. In the case of the surface EFIE, the construction of the projectors requires inverting the graph Laplacian matrix $\boldsymbol{\Sigma}_{\boldsymbol{RWG}}{}^{\mathrm{T}}\boldsymbol{\Sigma}_{\boldsymbol{RWG}}$ in which $\boldsymbol{\Sigma}_{\boldsymbol{RWG}}$ denotes the surface star-to-RWG transformation matrix [5]. This operation can be performed in linear complexity by leveraging the algebraic multigrid (AMG) method as preconditioner [4] together with an iterative solver. However, to solve the low-frequency problem in the D-VIE we use scaled projectors, which involve the inversion of the weighted graph Laplacian $\boldsymbol{\Sigma}^{\mathrm{T}}\tilde{\boldsymbol{G}}_{\boldsymbol{\epsilon}}{}^{-1}\boldsymbol{\Sigma}$. Since the scatterer is inhomogeneous, $\tilde{\boldsymbol{G}}_{\boldsymbol{\epsilon}}$ is ill-conditioned and its inverse cannot always be computed efficiently. Instead, we observed numerically that using the real part of the diagonal of $\tilde{\boldsymbol{G}}_{\boldsymbol{\epsilon}}$ to weight the graph Laplacian matrix also makes the formulation stable. The new set of projectors is defined as follows

$$\boldsymbol{P}_{\boldsymbol{D}}^{\boldsymbol{\Sigma}} = \boldsymbol{D}^{-1}\boldsymbol{\Sigma}(\boldsymbol{\Sigma}^{\mathrm{T}}\boldsymbol{D}^{-1}\boldsymbol{\Sigma})^{+}\boldsymbol{\Sigma}^{\mathrm{T}} \tag{3.68}$$

$$\boldsymbol{P}_{\boldsymbol{D}}^{\boldsymbol{\Lambda}} = \mathbf{I} - \boldsymbol{P}_{\boldsymbol{D}}^{\boldsymbol{\Sigma}} = \boldsymbol{\Lambda}(\boldsymbol{\Lambda}^{\mathrm{T}}\boldsymbol{D}\boldsymbol{\Lambda})^{+}\boldsymbol{\Lambda}^{\mathrm{T}}\boldsymbol{D}, \tag{3.69}$$

where $\boldsymbol{D} = \mathrm{Re}\ (\boldsymbol{D_G})$ with $\boldsymbol{D_G} \in \mathbb{R}^{N_F \times N_F}$ being filled with the diagonal of $\tilde{\boldsymbol{G}}_{\boldsymbol{\epsilon}}$. Following the same approach employed for the determination of C_1 and C_2 in (3.65), the preconditioned D-VIE with $\boldsymbol{P}_D^{\boldsymbol{\Sigma}}$ and $\boldsymbol{P}_D^{\boldsymbol{\Lambda}}$ reads

$$\boldsymbol{L}_D \boldsymbol{Z} \boldsymbol{\alpha} = \boldsymbol{L}_D \boldsymbol{v}, \tag{3.70}$$

in which

$$\boldsymbol{L}_D = 1/(\mathrm{j}\omega\epsilon_0 \| \epsilon_0^{-1} \boldsymbol{P}_D^{\boldsymbol{\Lambda}\mathrm{T}} \boldsymbol{G} \boldsymbol{P}_D^{\boldsymbol{\Lambda}} \|) \boldsymbol{P}_D^{\boldsymbol{\Lambda}\mathrm{T}} + 1/\| \boldsymbol{P}_D^{\boldsymbol{\Sigma}\mathrm{T}} \boldsymbol{Z}_{\boldsymbol{\Phi}} \boldsymbol{P}_D^{\boldsymbol{\Sigma}} \| \boldsymbol{P}_D^{\boldsymbol{\Sigma}\mathrm{T}}. \tag{3.71}$$

This new preconditioner has been numerically verified to be stable in a broad frequency range, as illustrated in the next section. Moreover the weighted graph Laplacian matrix $\boldsymbol{\Sigma}^{\mathrm{T}} \boldsymbol{D}^{-1} \boldsymbol{\Sigma}$ can be inverted efficiently using an aggregation-based AMG method from [76, 77] together with a conjugate gradient (CG) algorithm.

3.6 Numerical Results

To demonstrate the proper behavior of the formulations introduced in this chapter, we compared them to the traditional D-VIE in various settings. The numerical results are provided for the D-VIE regularized with the two above-mentioned sets of scaled quasi-Helmholtz projectors: the preconditioned D-VIE leveraging projectors scaled with the Gram matrix and scaled with the diagonal matrix $\boldsymbol{D}$ are referred to as the "Regularized D-VIE $\tilde{\boldsymbol{G}}_{\boldsymbol{\epsilon}}$" (i.e. (3.64)) and "Regularized D-VIE $\boldsymbol{D}$" (i.e. (3.70)), respectively. In the experiments related to the low-frequency and the dense discretization behaviors of the D-VIE, we also compared the regularized formulations to the non-normalized loop-star D-VIE. In addition to its behavior, the correctness of the new D-VIE is validated against reference solutions which are either obtained from Mie series or finite element method (FEM) with quadratic elements. Note that the results regarding the accuracy of the solver will be provided only for the "Regularized D-VIE $\boldsymbol{D}$" for the sake of clarity.

The geometry used for the first numerical examples is composed of 3 homogeneous concentric spheres (i.e. three-layer head model) with radii 87 mm, 92 mm, and 100 mm and respective normalized conductivities $\sigma_1 = 1$, $\sigma_2 = 1/15$, and $\sigma_3 = 1$, which represent the conductivities of brain, skull, and scalp in the quasi-static regime [78]. First, we verify the conditioning of the system matrices of the regularized D-VIE, the loop-star D-VIE, and the standard D-VIE as a function of the frequency (Figure 3.2). The condition number of the standard D-VIE grows as the frequency decreases while the condition number of the two regularized D-VIE and the loop-star D-VIE remains constant until very low frequencies, which confirms the curative effects of our preconditioners.

The dense discretization conditioning of the new D-VIE is verified by increasing the discretization of a geometry composed of 3 homogeneous concentric spheres with radii 0.4 m, 0.7 m, and 1 m and respective normalized conductivities $\sigma_1 = 1$,

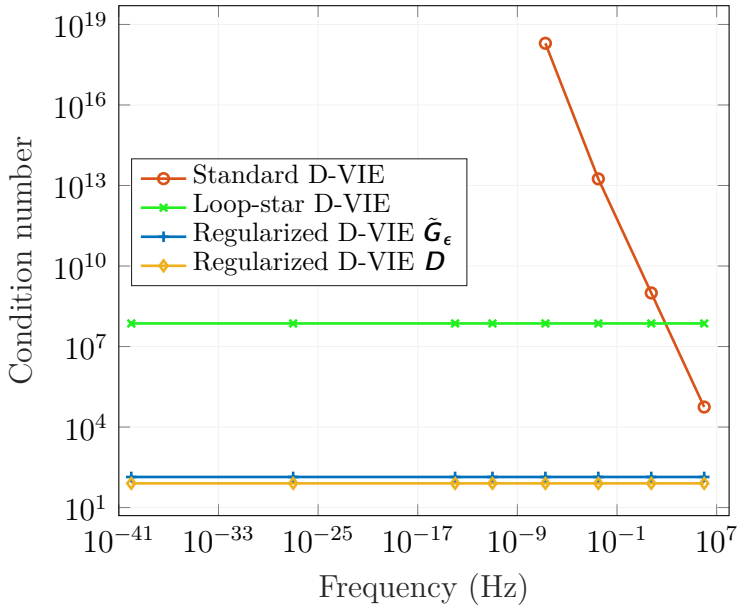

Figure 3.2: Low frequency conditioning of the standard D-VIE, the loop-star D-VIE, and the proposed D-VIE computed on a 3-layer conductive sphere with radii 87 mm, 92 mm, and 100 mm and respective conductivities $\sigma_1 = 1$, $\sigma_2 = 1/15$, and $\sigma_3 = 1$.

$\sigma_2 = 1/5$, and $\sigma_3 = 1$ (Figure 3.3). Both the traditional and the regularized D-VIE do not experience a dense mesh instability, which shows that our preconditioners do not introduce a new breakdown, unlike the D-VIE preconditioned with a standard loop-star decomposition, which has its condition number that grows unbounded when the discretization of the geometry is refined.

To complement our stability experiments we verify the correctness of the new formulation against references in the quasi-static regime and at higher frequencies. First, we establish the correctness of the formulation in an electroencephalography (EEG) setting by comparing the potential radiated by an electric point dipole on the surface of a conductive object since they are considered good models for focal brain activity [31]. The electric point dipole source has a moment of $\begin{bmatrix}0 & 0 & 1\end{bmatrix}$ and an eccentricity of 43 % in a 3-layer sphere with the aforementioned conductivities (Figure 3.4). The frequency used in the simulation is 10^{-40}Hz, although neurons operate at a frequency between 0.1 Hz and 100 Hz. The reason behind this choice is to show that the formulation does not suffer from a loss of significant digits at very low frequencies unlike standard full-wave solvers. The potential obtained in the tetrahedra of the mesh with the new formulation and the loop-star D-VIE shows a good agreement with the well-established reference solution and confirms the applicability of the new D-VIE in a typical biomedical setting.

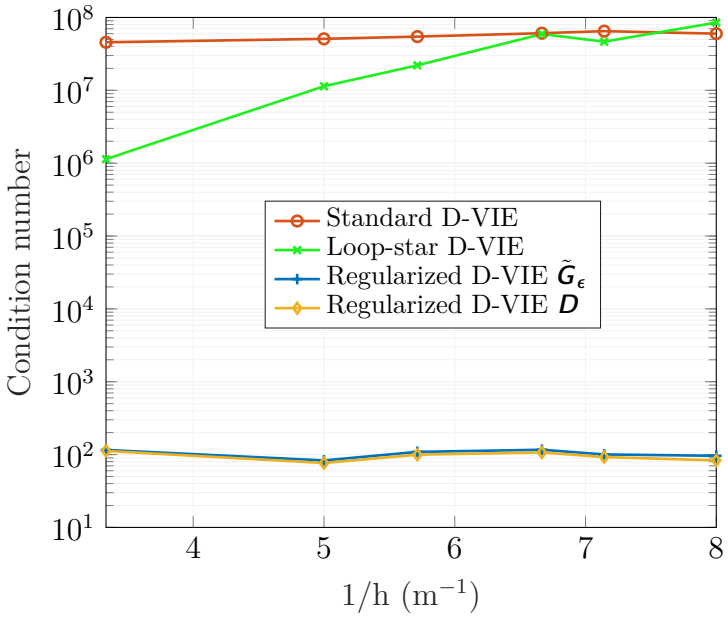

Figure 3.3: Dense discretization behavior of the standard D-VIE, the loop-star D-VIE, and the proposed D-VIE computed on a 3-layer conductive sphere with radii 0.4 m, 0.7 m, and 1 m and respective conductivities $\sigma_1 = 1$, $\sigma_2 = 1/5$, and $\sigma_3 = 1$ at $f = 1$ kHz.

At higher frequencies, we use the previous 3-layer sphere with the relative permittivities $\epsilon_{r,1} = 70$, $\epsilon_{r,2} = 15$, and $\epsilon_{r,3} = 65$ and conductivities $\sigma_1 = 0.55$, $\sigma_2 = 0.75$, and $\sigma_3 = 1.42$. These values match the relative permittivities and conductivities of the brain, skull, and skin at $f = 100$ MHz [37]. The excitation is a plane wave and the reference solution is obtained analytically from the Mie series. Once again, the solution obtained with the proposed D-VIE shows a good agreement with the reference solution (Figure 3.5).

Now that the correctness and stability of the proposed formulation have been verified in canonical settings, we verify its applicability to challenging, realistic bio-electromagnetic compatible scenarios. To assess the low- and high-frequency versatility of the new formulation we study its applicability to the bio-electromagnetic modeling of the human head. The head geometry used for these simulations has been obtained from the segmentation of an MRI image of $256 \times 256 \times 256$ voxels in FieldTrip [79], subsequently discretized into 44 733 tetrahedra.

At low frequencies, the formulation is applied to the problem of brain source localization which aims at retrieving the neural activity from the potential recordings on the scalp measured by EEG. This inverse problem has numerous applications ranging from epilepsy diagnosis [25] to brain computer interface [24]. Solving the

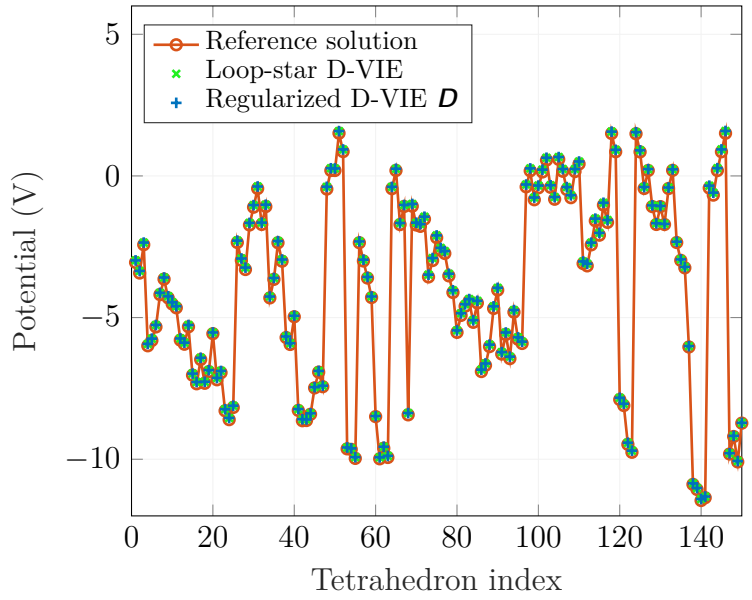

Figure 3.4: Potential obtained at the surface (in the tetrahedra of the mesh) of a 3-layer conductive sphere with the corresponding conductivities $\sigma_1 = 1$, $\sigma_2 = 1/15$, and $\sigma_3 = 1$. The excitation is an electric point dipole radiating at $f = 10^{-40}$Hz.

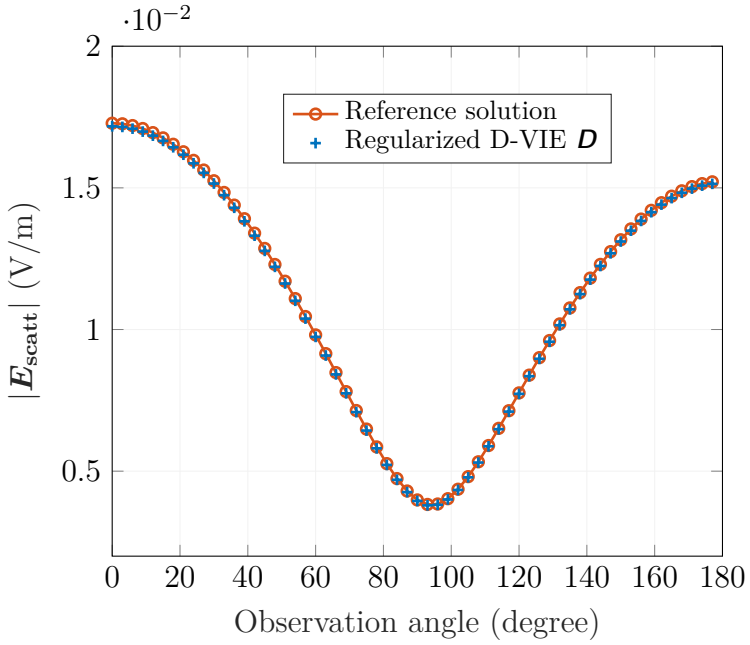

Figure 3.5: Magnitude of the field scattered by a 3-layer sphere with corresponding relative permittivities $\epsilon_{r,2} = 70$, $\epsilon_{r,2} = 15$, and $\epsilon_{r,3} = 65$ and conductivities $\sigma_1 = 0.55$, $\sigma_2 = 0.75$, and $\sigma_3 = 1.42$ illuminated by a plane wave at $f = 100\,\mathrm{MHz}$.

inverse problem – the mapping from EEG scalp measurement to the current distribution inside the head – requires solving the forward problem multiple times, which is the mapping from individual current sources to scalp potentials. In the distributed approach, the individual current sources are placed on a grid covering the parts of interest in the brain. In Figure 3.6, we show the potential radiated on the scalp by a single intracranial current source oscillating at $f = 1\,\text{Hz}$. The conductivities of the different homogeneous layers – the scalp, the skull, and the brain – are $\sigma_{\text{scalp}} = 1$, $\sigma_{\text{skull}} = 1/15$, and $\sigma_{\text{brain}} = 1$ [24]. The scalp potential, measured at 65 electrodes, is compared to a reference solution obtained from a FEM solver. The relative error obtained at each electrode remains below 4 % (Figure 3.6), which confirms the use of the regularized D-VIE in the EEG source reconstruction (Figure 3.7).

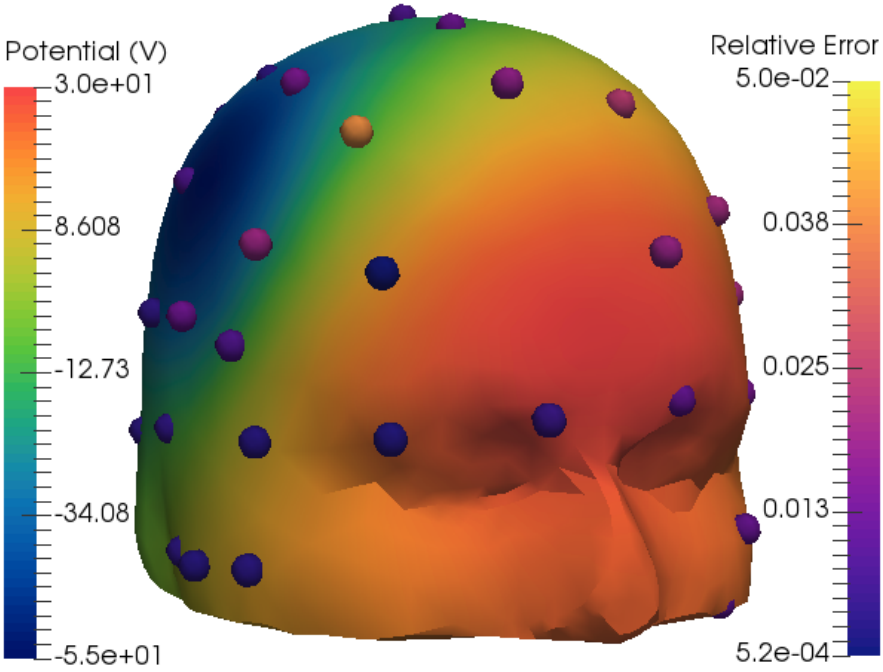

Figure 3.6: 3D visualization of the potential radiated from a current dipole oscillating at 1 Hz in the brain obtained on the scalp of the head (left color bar). The colored dots represent the 65 EEG electrodes with the corresponding relative error (right color bar).

At higher frequencies, the new formulation can be applied in the field of radiation dosimetry in the brain. It consists in the quantification of the specific absorption rate (SAR) radiated by a given source in human tissues [75]. In this scenario, we use the same head geometry as for the EEG source localization with $\epsilon_{r,\text{scalp}} = 70$, $\epsilon_{r,\text{skull}} = 15$, and $\epsilon_{r,\text{brain}} = 65$ for the relative permittivities and $\sigma_{\text{scalp}} = 0.55$, $\sigma_{\text{skull}} = 0.75$, and $\sigma_{\text{brain}} = 1.42$ for the conductivities. The head is illuminated

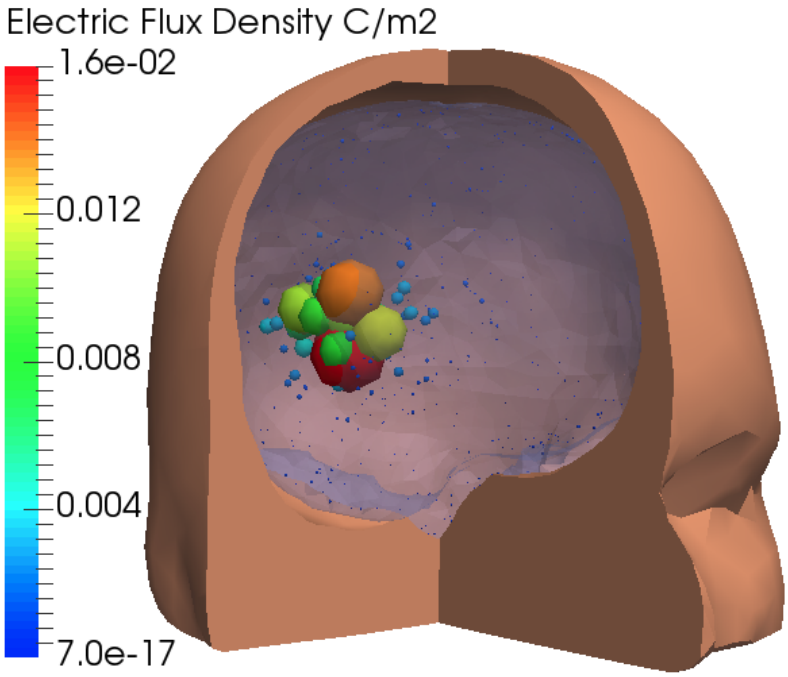

Figure 3.7: Localization of the epileptogenic area via source reconstruction.

by an electric dipole placed at 10 cm from its right side, with dipole moment of $\begin{bmatrix}0 & 0 & 1\end{bmatrix}$, and oscillating at $f = 100\,\mathrm{MHz}$. The brain is divided into voxels of side length 3 cm. The SAR is computed in each voxel n as $\sigma_n|\boldsymbol{E_n}|^2/2\rho_n$, where $|\boldsymbol{E_n}|$ is the norm of the electric field averaged over the voxel n and ρ_n its mass density in $\mathrm{kg\,m^{-3}}$. The SAR obtained with the proposed D-VIE is consistent with the reference solution, which is obtained with a FEM solver (Figure 3.9). Figure 3.8 shows the magnitude of the electric field obtained at the surface of the tetrahedral discretization of the brain.

3.7 Conclusion and Future Work

We introduced a novel volume integral equation for modeling lossy dielectric objects in a broad frequency range. The new D-VIE scheme leverages scaled volume quasi-Helmholtz projectors to cure both its low-frequency ill-conditioning without deteriorating its dense discretization behavior. Numerical examples illustrate the stability and accuracy of this new method. The preconditioned D-VIE shows good accuracy in the biomedical applications presented in this chapter, both in the quasi-static regime and at higher frequencies. A possible improvement of this method is to make it well-conditioned also in scenarios in which the internal contrast in the object under study is significant.

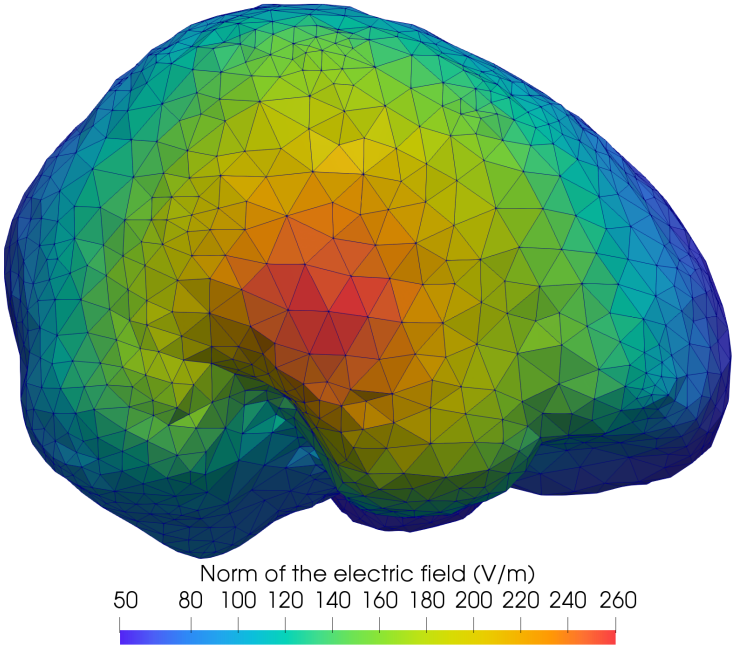

Figure 3.8: Norm of the electric field radiated by a dipole source oscillating at 100 MHz located at 10 cm from the head.

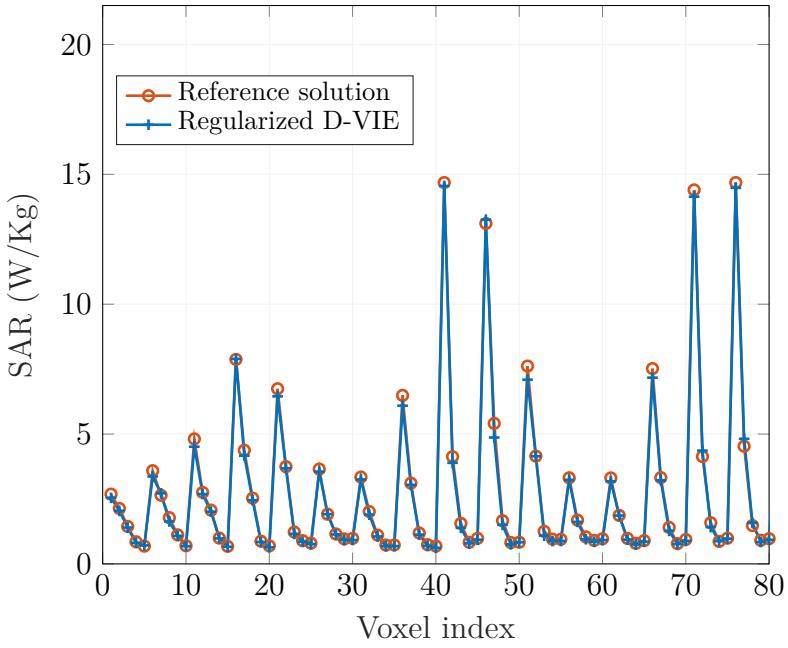

Figure 3.9: Comparison of the SAR obtained in a cubic voxel subdivision of the brain at 100 MHz.

Chapter 4

A D-VIE Based Inverse Scattering Scheme for Microwave Imaging

MICROWAVE IMAGING (MWI) is a research field in which techniques for probing unknown domains using electromagnetic waves in the microwave regime are developed. Besides the research conducted on the hardware part, it is also crucial to create performing inverse scattering solvers that provide accurate images of the domain under study from collected measurements. This chapter presents a new inverse scattering scheme based on the electric flux volume integral equation formulation. Numerical results show that this new method can reconstruct three-dimensional permittivity profiles.

4.1 Introduction

Inverse scattering (IS) consists in retrieving the shape, the location, or the material parameters of an object from measurements of scattered waves (e.g. acoustic wave, electromagnetic wave) from this object. It has numerous applications such as non destructive testing [104, 96], biomedical imaging [6, 2], and occupancy estimation [32].

Scattering problems can be of different nature including electromagnetic, acoustic, and thermal. In the framework of this chapter, electromagnetic inverse scattering is considered. In this type of problems, the data collected can be the electric or the magnetic field in the vicinity of the object under study. The goal is to reconstruct the object's relative permittivity, conductivity (lossy materials), or permeability from this measured data. Note that the location of an object can be obtained from the knowledge of the material parameters of both the object and of the background in which it is immersed.

While only the knowledge of the material parameters is useful in many applications, an inverse scattering problem generally consists of two unknowns: the total

electric (magnetic) field in a domain and the permittivity (permeability) in that domain. Due to the specific relation between these two unknowns, inverse scattering problems are more complex than standard inverse source problems (e.g. inverse problem described in the numerical results of chapter 3). While in classical inverse source problems the relation between the measured data and the unknown currents is linear, the inverse scattering problem is non-linear. This comes from the fact that there are high-order interactions in the object (multiple scattering phenomena).

An inverse scattering problem is generally composed of a data and a state equation. The data equation relates the unknown quantities in the object to the scattered field at the measurement locations. The state equation can be viewed as the forward problem in an inverse source algorithm. Its role is to enforce Maxwell's equations in the object under study and it hence acts as a regularizer for the data equation. The goal of an IS scheme is to minimize the sum of the norms of the residual errors of these two equations, referred to as cost functional, leveraging an iterative solver. The non-linearity of IS problems translates into the existence of local minima in the cost functional. Some ways to remedy this problem are to linearize it (Born approximation) or to use a priori information on some parameters of the object.

Besides being non-linear, an inverse scattering problem is often ill-posed due to the lack of information. Ill-posed problems can be subdivided into two groups: ill-defined problems and ill-conditioned problems. An ill-defined problem has an non-existing solution if over-determined and non-unique solution if under-determined [26]. Note that the latter is more frequent in inverse scattering. The conditioning properties of a system were already discussed in chapter 2 and chapter 3.

There exists two main families of algorithms to solve inverse scattering problems: Born iterative methods (BIM) and gradient based methods. In Born iterative methods, a forward problem needs to be solved at each iteration to enforce the state equation. In the gradient based algorithms, the state and data equations are simultaneously solved, and the state equation can be seen as a regularizer of the problem. In that sense, Born iterative methods are more similar to standard inverse source problems since they require solving explicitly the state equation at each iteration (i.e. forward problem). Gradient methods do not require this and for these reasons, gradient approaches are generally more efficient than Born iterative methods [39] in inverse scattering problems.

Up to now, the methods introduced from this family are the contrast source inversion [100, 12, 1] (CSI) and the modified gradient method [59, 60] (MGM). Due to its ease of implementation and performance, the CSI method is frequently employed in microwave imaging. It has been been combined with various computational methods: IE [100], FEM [106], and the finite-difference method (FDM) [35]. The advantage of integral equation formulations is that the background of the scatterer (if known) does not need to be discretized. Here we introduce an electric flux based inverse scattering scheme, which required the full derivation of a gradient

based algorithm combined with the D-VIE formulation. The D-VIE is discretized with SWG basis functions, which naturally enforce the divergence conformity of the electric flux during the inversion.

The chapter is divided as follows: a general framework for inverse scattering problems is introduced in Section 4.2 together with some standard inverse scattering schemes. Then, Section 4.3 presents the new electric flux based inversion scheme. Finally the new IS method is compared to standard IS methods to evaluate its performance in Section 4.4.

4.2 Background and Notations

In this section, some basic concepts about inverse scattering problems are introduced. Moreover, the derivations of the standard IS algorithms that are compared to the electric flux inversion method in the numerical results section are provided.

4.2.1 Notations

Let $\Omega_D \subset \mathbb{R}^3$ and $\Gamma_S \subset \mathbb{R}^3$ be the domain to image and the measurement surface, respectively. The derivation of the inverse scattering algorithms further described can be facilitated by introducing the following notations. The L^2-inner product between two vectors $\boldsymbol{u}$ and $\boldsymbol{v}$ defined on Ω_D or Γ_S is expressed as

$$\langle \boldsymbol{u}, \boldsymbol{v} \rangle_{\{\Omega_D, \Gamma_S\}} = \int_{\{\Omega_D, \Gamma_S\}} \boldsymbol{u}(\boldsymbol{r}) \cdot \bar{\boldsymbol{v}}(\boldsymbol{r}) \, \mathrm{d}\psi(\boldsymbol{r}), \quad \boldsymbol{r} \in \{\Omega_D, \Gamma_S\} \tag{4.1}$$

in which $\bar{\boldsymbol{v}}$ denotes the complex conjugate of $\boldsymbol{v}$ and the curly bracket notation $\{A, B\}$ means that it is defined either on A or B. The L^2-norm of $\boldsymbol{u}$ is then defined as

$$\|\boldsymbol{u}\|_{\{\Omega_D, \Gamma_S\}} = \langle \boldsymbol{u}, \boldsymbol{u} \rangle^{\frac{1}{2}}_{\{\Omega_D, \Gamma_S\}}. \tag{4.2}$$

It is also useful to introduce the adjoint operator $\boldsymbol{\mathcal{G}}^\star$ of $\boldsymbol{\mathcal{G}}$, which follows the relation

$$\langle \boldsymbol{v}, \boldsymbol{\mathcal{G}} \boldsymbol{u} \rangle_{\Gamma_S} = \langle \boldsymbol{\mathcal{G}}^\star \boldsymbol{v}, \boldsymbol{u} \rangle_{\Omega_D}. \tag{4.3}$$

with $\boldsymbol{\mathcal{G}}$ being an operator mapping Ω_D to Γ_S.

Another necessary mathematical tool in the following is the Fréchet derivative [34]. Let U be a Banach space. For a Fréchet differentiable functional $F : U \to \mathbb{R}$, the Fréchet derivative at $\boldsymbol{x} \in U$ is defined as

$$\frac{\partial F(\boldsymbol{x})}{\partial \boldsymbol{x}} = \lim_{\epsilon \to 0} \frac{F(\boldsymbol{x} + \epsilon \boldsymbol{h}) - F(\boldsymbol{x})}{\epsilon}, \tag{4.4}$$

for every $\boldsymbol{h} \in U$. In this chapter, U and F correspond to $L^2(\Omega_D)^3$ and $\|\cdot\|^2_{\{\Omega_D, \Gamma_S\}}$, respectively. In that case, the Fréchet derivation gives the variation of $\|\boldsymbol{x}\|^2_{\{\Omega_D, \Gamma_S\}}$

for a small variation ϵ along the direction $\boldsymbol{h}$ with respect to $\boldsymbol{x}$. Equation (4.4) can be expanded as

$$\begin{aligned}\frac{\partial\|\boldsymbol{x}\|^2_{\{\Omega_D,\Gamma_S\}}}{\partial\boldsymbol{x}} &= \lim_{\epsilon\to 0}\frac{\|\boldsymbol{x}+\epsilon\boldsymbol{h}\|^2_{\{\Omega_D,\Gamma_S\}}-\|\boldsymbol{x}\|^2_{\{\Omega_D,\Gamma_S\}}}{\epsilon}\\ &= \lim_{\epsilon\to 0}\frac{\langle\boldsymbol{x}+\epsilon\boldsymbol{h},\boldsymbol{x}+\epsilon\boldsymbol{h}\rangle_{\{\Omega_D,\Gamma_S\}}-\langle\boldsymbol{x},\boldsymbol{x}\rangle_{\{\Omega_D,\Gamma_S\}}}{\epsilon}\\ &= \langle\boldsymbol{x},\boldsymbol{h}\rangle_{\{\Omega_D,\Gamma_S\}}+\langle\boldsymbol{h},\boldsymbol{x}\rangle_{\{\Omega_D,\Gamma_S\}}\\ &= 2\mathrm{Re}\left(\langle\boldsymbol{x},\boldsymbol{h}\rangle_{\{\Omega_D,\Gamma_S\}}\right),\end{aligned} \tag{4.5}$$

in which the polarization identity was employed in the last step of the expansion. It can be observed from eq. (4.5) that the variation of $\|\boldsymbol{x}\|^2_{\{\Omega_D,\Gamma_S\}}$ (Fréchet derivative) is maximized when the direction $\boldsymbol{h}$ is equal to the left hand side of the inner product, which is $\boldsymbol{x}$ here. Note that this particular direction with maximum variation corresponds to the gradient of $\|\boldsymbol{x}\|^2_{\{\Omega_D,\Gamma_S\}}$ with respect to $\boldsymbol{x}$, which is required in the following to derive update directions in the gradient based algorithms.

4.2.2 Inverse Scattering Problems

Before treating inverse scattering problems, inverse source problems in general are first briefly discussed. An inverse source problem can be defined as a mapping from a scattered field $\boldsymbol{E}_s$ measured on Γ_S to a source current distribution $\boldsymbol{J}$ in Ω_D, as illustrated in fig. 4.1a. This type of problem is governed by the following equation

$$\boldsymbol{E}_s(\boldsymbol{r}) = \boldsymbol{\mathcal{G}_S}\boldsymbol{J} \quad \boldsymbol{r}\in\Gamma_S, \tag{4.6}$$

in which $\boldsymbol{\mathcal{G}_S}$ is a scattering operator from Ω_D to Γ_S. In inverse scattering problems, the unknown (dielectric) source current is replaced by two unknowns: the field and material contrast in Ω_D. The goal of an inverse scattering problem is to retrieve these unknowns from a scattered field $\boldsymbol{E}_s$ on a measurement surface $\Gamma_S \in \mathbb{R}^3$, generally outside Ω_D. In general, inverse scattering problems are described by the following system of equations

$$\boldsymbol{E}(\boldsymbol{r}) = \boldsymbol{E}_i(\boldsymbol{r}) + \boldsymbol{\mathcal{G}_D}(C)\boldsymbol{E} \quad \boldsymbol{r}\in\Omega_D, \tag{4.7}$$

$$\boldsymbol{E}_s(\boldsymbol{r}) = \boldsymbol{\mathcal{G}_S}(C)\boldsymbol{E} \quad \boldsymbol{r}\in\Gamma_S, \tag{4.8}$$

in which $\boldsymbol{\mathcal{G}_D}$ is a scattering operator from Ω_D to Ω_D and $\boldsymbol{E}$ is the total field in Ω_D. In this chapter, the contrast C is a function of the permittivity ϵ in the object (non-magnetic objects are considered). Moreover, the background is assumed to be vacuum and hence the material contrast is always defined with respect to ϵ_0. In the inverse scattering formulations presented in the following, the contrast can either be the dielectric contrast $C(\boldsymbol{r}) = \kappa(\boldsymbol{r})$ or the dielectric susceptibility $C(\boldsymbol{r}) = \chi(\boldsymbol{r})$ depending on the VIE formulation employed (defined in section 2.2.1.2). The field

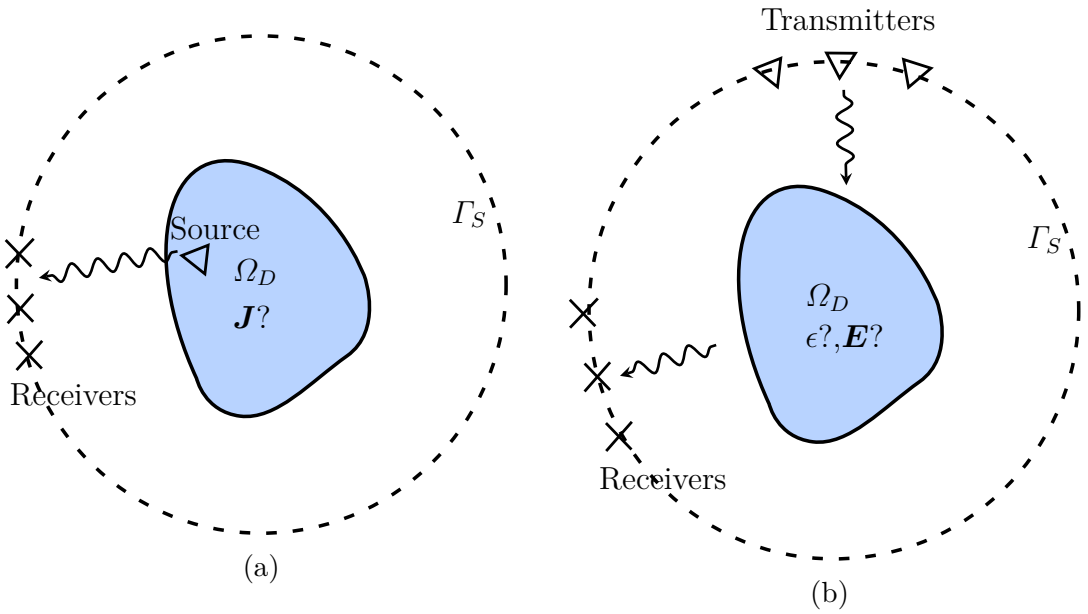

Figure 4.1: (a) Definition of an inverse source problem. It consists in retrieving the distribution of the source currents $\boldsymbol{J}$ in Ω_D from measurements of the field at the receivers positions on Γ_S. (b) Definition of the inverse scattering problem. The goal is to determine $\boldsymbol{E}$ and ϵ in Ω_D from the knowledge of the field measured by the receivers on Γ_S. The incident field is usually emitted on Γ_S also.

unknowns associated to χ and κ are $\boldsymbol{J} = \chi\boldsymbol{E}$ and $\boldsymbol{D}$, respectively. The incident field $\boldsymbol{E}_i$ is the field produced by the transmitting antennas placed on Γ_S. Each transmitting antenna induces a different scattered field $\boldsymbol{E}_s$ which is measured by the receiving antennas. Note that the same set of antennas can be used for transmitting and receiving and that in practice, the total field is measured at the antennas and the scattering field is deduced from the knowledge of both the total and the incident field. The following derivations of the IS algorithms are provided for single illumination to make the notation lighter, however the results for multi-illumination remain unchanged.

Equation (4.7) can be further simplified by introducing the operator $\boldsymbol{\mathcal{L}}$ defined as

$$\boldsymbol{\mathcal{L}}(C) = \boldsymbol{\mathcal{I}} - \boldsymbol{\mathcal{G}}_{\boldsymbol{\mathcal{D}}}(C), \tag{4.9}$$

in which $\boldsymbol{\mathcal{I}}$ is the identity operator. With this definition, eq. (4.7) can be rewritten as

$$\boldsymbol{E}_i(\boldsymbol{r}) = \boldsymbol{\mathcal{L}}(C)\boldsymbol{E} \quad \boldsymbol{r} \in \Omega_D. \tag{4.10}$$

The goal of an inverse scattering problem is to minimize the following cost functional

$$\begin{aligned} F(C,\boldsymbol{E}) &= F_{\text{data}}(C,\boldsymbol{E}) + F_{\text{state}}(C,\boldsymbol{E}) \\ &= \frac{\|\boldsymbol{\rho}\|^2_{\Gamma_S}}{\|\boldsymbol{E}_s\|^2_{\Gamma_S}} + \frac{\|\boldsymbol{f}\|^2_{\Omega_D}}{\|\boldsymbol{E}_i\|^2_{\Omega_D}} \\ &= \frac{\|\boldsymbol{E}_s - \boldsymbol{\mathcal{G}_S}(C)\boldsymbol{E}\|^2_{\Gamma_S}}{\|\boldsymbol{E}_s\|^2_{\Gamma_S}} + \frac{\|\boldsymbol{E}_i - \boldsymbol{\mathcal{L}}(C)\boldsymbol{E}\|^2_{\Omega_D}}{\|\boldsymbol{E}_i\|^2_{\Omega_D}}, \end{aligned} \tag{4.11}$$

in which $\boldsymbol{f}$ and $\boldsymbol{\rho}$ are the residual errors of the state and data equations, respectively. Due the inherent non-linearity of inverse scattering problems, the minimization of F has to be performed iteratively. At step n, the contrast and the field at step $n-1$ (C_{n-1} and $\boldsymbol{E_{n-1}}$) are updated with δ_C and $\boldsymbol{\delta_E}$ as follows

$$C_n = C_{n-1} + \delta_C, \tag{4.12}$$

$$\boldsymbol{E_n} = \boldsymbol{E_{n-1}} + \boldsymbol{\delta_E}, \tag{4.13}$$

and the residuals at step n can be written as

$$\boldsymbol{\rho_n} = \boldsymbol{E}_s - \boldsymbol{\mathcal{G}_S}(C_n)\boldsymbol{E_n}, \tag{4.14}$$

$$\boldsymbol{f_n} = \boldsymbol{E}_i - \boldsymbol{\mathcal{L}}(C_n)\boldsymbol{E_n}. \tag{4.15}$$

Thus the cost functional at step n reads

$$F_n = \frac{\|\boldsymbol{\rho_n}\|^2_{\Gamma_S}}{\|\boldsymbol{E}_s\|^2_{\Gamma_S}} + \frac{\|\boldsymbol{f_n}\|^2_{\Omega_D}}{\|\boldsymbol{E}_i\|^2_{\Omega_D}}. \tag{4.16}$$

The goal at each iteration is to determine $\boldsymbol{\delta_E}$ and δ_C to minimize F_n. Different strategies exist in inverse scattering to determine δ_C and $\boldsymbol{\delta_E}$, Born iterative methods and gradient based methods. While Born iterative methods require inserting the solution of the state equation (eq. (4.7)) into the data equation (eq. (4.8)) at each iteration, gradient based methods minimize both equations simultaneously. Algorithms from both families are presented next.

4.2.3 Born Approximation and Non-Linearity in Inverse Scattering

In this section, the non-linearity of inverse scattering problems is highlighted. This can be done by inserting the state equation (eq. (4.10)) into the data equation (eq. (4.8)) so that a single equation describing the whole inverse scattering problem is obtained

$$\begin{aligned} \boldsymbol{E}_s &= \boldsymbol{\mathcal{G}_S}(C)\boldsymbol{\mathcal{L}}(C)^{-1}\boldsymbol{E}_i \\ &= \boldsymbol{\mathcal{G}_S}(C)(\boldsymbol{\mathcal{I}} - \boldsymbol{\mathcal{G}_D}(C))^{-1}\boldsymbol{E}_i. \end{aligned} \tag{4.17}$$

As long as $\|\boldsymbol{\mathcal{G}}_{\boldsymbol{\mathcal{D}}}(C)\|_{\Omega_D} < 1$, $\boldsymbol{\mathcal{L}}^{-1}$ can be expanded in Neumann series as follows

$$(\boldsymbol{\mathcal{I}} - \boldsymbol{\mathcal{G}}_{\boldsymbol{\mathcal{D}}}(C))^{-1} = \boldsymbol{\mathcal{I}} + \sum_{j=1}^{\infty} (\boldsymbol{\mathcal{G}}_{\boldsymbol{\mathcal{D}}}(C))^j \,. \tag{4.18}$$

In that case, the scattered field can be expanded as

$$\boldsymbol{E}_s = \boldsymbol{\mathcal{G}}_{\boldsymbol{\mathcal{S}}}(C) \left(\boldsymbol{\mathcal{I}} + \sum_{j=1}^{\infty} (\boldsymbol{\mathcal{G}}_{\boldsymbol{\mathcal{D}}}(C))^j \right) \boldsymbol{E}_i. \tag{4.19}$$

Equation (4.19) clearly illustrates the non-linearity of inverse scattering problems, i.e., the lack of proportionality between $\boldsymbol{E}_s$ and C. The degree of non-linearity is determined by $\|\boldsymbol{\mathcal{G}}_{\boldsymbol{\mathcal{D}}}(C)\|_{\Omega_D}$. If the object is a weak scatterer, then $\|\boldsymbol{\mathcal{G}}_{\boldsymbol{\mathcal{D}}}(C)\|_{\Omega_D} \ll 1$, eq. (4.19) can thus be approximated as

$$\boldsymbol{E}_s \approx \boldsymbol{\mathcal{G}}_{\boldsymbol{\mathcal{S}}}(C) \boldsymbol{E}_i. \tag{4.20}$$

With this approximation, the relation between the contrast C and the scattered field becomes linear. This approximation is called Born approximation [13], it amounts to considering that $\boldsymbol{E} \approx \boldsymbol{E}_i$.

4.2.4 Regularization

Besides being non-linear, inverse scattering problems suffer from ill-posedness because of the ill-conditioning of the system and the lack of data available (underdetermined problems). Here some regularization techniques that help in determining the correct (physical) solution from an infinite set of possible solutions and that reduce the impact of the noise content of data on the accuracy of the solution are briefly summarized.

The regularization of an inverse scattering problem is generally done by adding (sometimes multiplying) one or several regularization terms to the original cost functional (eq. (4.11)). The regularized cost functional $\tilde{F}$ then reads

$$\tilde{F}(C, \boldsymbol{E}) = F_{\text{data}}(C, \boldsymbol{E}) + F_{\text{state}}(C, \boldsymbol{E}) + \alpha F_{\text{reg}}(C), \tag{4.21}$$

in which $\alpha \in \mathbb{R}^+$ is the regularization parameter and F_{reg} is the regularization penalty. The regularization parameter is usually determined through numerical experiments. When it is too high the penalty is correctly enforced but the resulting solution could not be physical and when it is too low it does not impact the solution of the original system [39].

In the Tikhonov regularization [45, 95],

$$F_{\text{reg}}^{\text{Tik}} = \|C(\boldsymbol{r})\|_{\Omega_D}^2, \quad \boldsymbol{r} \in \Omega_D \,, \tag{4.22}$$

which enforces the minimization of the L_2-norm of the contrast. It is particularly useful when the data is noisy. However, the solution C is very sensible to the choice of α.

Another common regularization technique is the total variation (TV) method [12] in which the penalty has the form

$$F_{\text{reg}}^{\text{TV}} = \int_{\Omega_D} \|\nabla C(\boldsymbol{r})\| \, \mathrm{d}v(\boldsymbol{r}), \quad \boldsymbol{r} \in \Omega_D. \tag{4.23}$$

This regularizer penalizes the cost functional for large contrast variation in the object. It thus enforces smooth permittivity profiles even in the presence of noisy data. However, as for the Tikhonov regularization, the parameter α should be chosen experimentally [67]. An interesting property of the TV regularization is that it can be used as a multiplicative regularizer, in which case the choice of a regularization parameter α is not required anymore.

Note the original inverse scattering problem admits the state equation as an intrinsic regularizer [1]. This regularizer is sometimes referred to as Maxwell's regularizer [1]. While the regularizers presented previously are mathematical artifacts, the state equation is directly based on physical properties of the object.

4.2.5 Born Iterative Method

The Born iterative method (BIM) was introduced in [103]. It attempts to solve the non-linear system presented in eq. (4.7) and eq. (4.8) by successively solving the forward problem (eq. (4.7)) for the field inside the object and then solve the data equation (eq. (4.8)) for the contrast given that field. At the beginning of the algorithm (iteration $n = 0$), the Born approximation is employed (eq. (4.20)) to initialize the field. If the contrast C_0 is not close to zero, the Born approximation does not apply and it is better to use a-priori knowledge on the contrast. In that case, the first initialization step can be replaced by a minimization of the state equation (4.7) for the initial field $\boldsymbol{E_0}$ with the estimated contrast (forward problem).

The contrast C_n at iteration n is updated as

$$C_n = \underset{C_n \in \mathbb{C}}{\arg\min} \frac{\|\boldsymbol{E}_s - \boldsymbol{\mathcal{G}_S}(C_n)\boldsymbol{E_{n-1}}\|_{\Gamma_S}^2}{\|\boldsymbol{E}_s\|_{\Gamma_S}^2}, \tag{4.24}$$

in which $\arg\min$ is the argument of the minimum and $\boldsymbol{E_{n-1}}$ is determined by solving the state equation (eq. (4.10)) assuming that the contrast C_{n-1} is known. The overall algorithm is delineated in Algorithm 1.

4.2.5.1 Implementation and Discretization of the D-VIE based BIM

For the numerical implementation of this algorithm, we opted for the D-VIE formulation. Recalling the operators defined in section 2.2.4.2, we have the following

correspondence between the unknowns and operators used in the general inverse scattering problem introduced in section 4.2.2 and the unknowns and operators of this problem

$$C \longleftrightarrow \kappa\,, \tag{4.25}$$
$$\boldsymbol{E} \longleftrightarrow \boldsymbol{D}/\epsilon\,, \tag{4.26}$$
$$\boldsymbol{\mathcal{G}_{\mathcal{D}}} \longleftrightarrow \boldsymbol{\mathcal{L}}_{\kappa}^{\Omega_D}\,, \tag{4.27}$$
$$\boldsymbol{\mathcal{G}_{\mathcal{S}}} \longleftrightarrow \boldsymbol{\mathcal{L}}_{\boldsymbol{D}}^{\Omega_D}\,. \tag{4.28}$$

With these operators, the state and data equations as a function of the electric flux $\boldsymbol{D}$ and κ read

$$\boldsymbol{E_i}(\boldsymbol{r}) + \boldsymbol{\mathcal{L}}_{\kappa}^{\Omega_D}(\boldsymbol{D}) = \frac{1-\kappa(\boldsymbol{r})}{\epsilon_0}\boldsymbol{D}(\boldsymbol{r}) \quad \boldsymbol{r} \in \Omega_D \tag{4.29}$$
$$\boldsymbol{E_s}(\boldsymbol{r}) = \boldsymbol{\mathcal{L}}_{\boldsymbol{D}}^{\Omega_D}(\boldsymbol{\kappa}) \quad \boldsymbol{r} \in \Gamma_S\,. \tag{4.30}$$

In the D-VIE-based BIM, the forward problem consists in retrieving the electric flux $\boldsymbol{D}$ from the knowledge of the contrast κ using eq. (4.29) while the inverse problem aims at retrieving the κ from $\boldsymbol{E}_s$ using eq. (4.30).

The unknown electric flux $\boldsymbol{D}$ is discretized with SWG basis functions following the procedure explained in section 2.3.4. In eq. (4.29), the discretization of $\boldsymbol{\mathcal{L}}_{\kappa}^{\Omega_D}$ follows the approach given in section 2.3.4.3 in which only the sparse matrices containing κ need to be updated at each iteration while in eq. (4.30), $\boldsymbol{\mathcal{L}}_{\boldsymbol{D}}^{\Omega_D}$ is discretized according to section 2.3.4.4 where the procedure to update the electric flux $\boldsymbol{D}$ in the discretized D-VIE is provided. In both cases, the non-symmetric D-VIE is employed.

4.2.6 Newton-Kantorovich Method

This method was introduced in [87] and is equivalent to the distorted Born iterative method (DBIM) [22, 67]. It allows for a larger variation of the contrast since it accounts for the terms of order $\mathcal{O}(\delta_C)$ in the Taylor expansion of $\boldsymbol{\mathcal{L}}(C_{n-1} + \delta_C)^{-1}$ for δ_C near zero. The data and state residual errors (eq. (4.14) and eq. (4.15)) at step n can be first rewritten in the following symbolic form

$$\boldsymbol{f_n} = \boldsymbol{E}_i - \boldsymbol{\mathcal{L}}(C_n)\boldsymbol{E_n} = \boldsymbol{E}_i - \boldsymbol{E_n} + \boldsymbol{\mathcal{G}_{\mathcal{D}}}(C_n)\boldsymbol{E_n} \tag{4.31}$$
$$\boldsymbol{\rho_n} = \boldsymbol{E}_s - \boldsymbol{\mathcal{G}_{\mathcal{S}}}(C_n)\boldsymbol{E_n}. \tag{4.32}$$

Then, the inverse of the state operator can be expanded as

$$\begin{aligned}\boldsymbol{\mathcal{L}}(C_n)^{-1} = (\boldsymbol{\mathcal{I}} - \boldsymbol{\mathcal{G}}_{\boldsymbol{\mathcal{D}}}(C_n))^{-1} &= (\boldsymbol{\mathcal{L}}(C_{n-1}) - \boldsymbol{\mathcal{G}}_{\boldsymbol{\mathcal{D}}}(\delta_C))^{-1} \\ &= \left(\boldsymbol{\mathcal{L}}(C_{n-1})\left(\boldsymbol{\mathcal{I}} - \boldsymbol{\mathcal{L}}(C_{n-1})^{-1}\boldsymbol{\mathcal{G}}_{\boldsymbol{\mathcal{D}}}(\delta_C)\right)\right)^{-1} \\ &= \left(\boldsymbol{\mathcal{I}} + \boldsymbol{\mathcal{L}}(C_{n-1})^{-1}\sum_{j=1}^{\infty}\boldsymbol{\mathcal{G}}_{\boldsymbol{\mathcal{D}}}(\delta_C^j)\right)\boldsymbol{\mathcal{L}}(C_{n-1})^{-1} \\ &= \left(\boldsymbol{\mathcal{I}} + \boldsymbol{\mathcal{L}}(C_{n-1})^{-1}\boldsymbol{\mathcal{G}}_{\boldsymbol{\mathcal{D}}}(\delta_C)\right)\boldsymbol{\mathcal{L}}(C_{n-1})^{-1} + \mathcal{O}(\delta_C^2),\end{aligned} \tag{4.33}$$

in which a Taylor expansion of $(\boldsymbol{\mathcal{I}} - \boldsymbol{\mathcal{L}}(C_{n-1})^{-1}\boldsymbol{\mathcal{G}}_{\boldsymbol{\mathcal{D}}}(\delta_C))^{-1}$ for δ_C near zero was performed. The terms of order $\mathcal{O}(\delta_C)$ are kept here, neglecting them corresponds to the Born iterative method presented in section 4.2.5. Then $\boldsymbol{E_n}$ is substituted by $\boldsymbol{\mathcal{L}}(C_n)^{-1}\boldsymbol{E}_i$ in the residual of the data equation (eq. (4.32)), which gives

$$\begin{aligned}\boldsymbol{\rho_n} &= \boldsymbol{E}_s - \boldsymbol{\mathcal{G}}_{\boldsymbol{\mathcal{S}}}(C_n)\boldsymbol{E_n} \\ &= \boldsymbol{E}_s - \boldsymbol{\mathcal{G}}_{\boldsymbol{\mathcal{S}}}(C_n)\boldsymbol{\mathcal{L}}(C_n)^{-1}\boldsymbol{E}_i \\ &= \boldsymbol{E}_s - \boldsymbol{\mathcal{G}}_{\boldsymbol{\mathcal{S}}}(C_{n-1}+\delta_C)\left(\boldsymbol{\mathcal{I}} + \boldsymbol{\mathcal{L}}(C_{n-1})^{-1}\boldsymbol{\mathcal{G}}_{\boldsymbol{\mathcal{D}}}(\delta_C)\right)\boldsymbol{\mathcal{L}}(C_{n-1})^{-1}\boldsymbol{E}_i + \mathcal{O}(\delta_C^2) \\ &= \tilde{\boldsymbol{E}}_{\boldsymbol{s,n-1}} - \boldsymbol{\mathcal{G}}_{\boldsymbol{\mathcal{S}}}(\delta_C)\boldsymbol{E_{n-1}} - \boldsymbol{\mathcal{G}}_{\boldsymbol{\mathcal{S}}}(C_{n-1})\boldsymbol{\mathcal{L}}(C_{n-1})^{-1}\boldsymbol{\mathcal{G}}_{\boldsymbol{\mathcal{D}}}(\delta_C)\boldsymbol{E_{n-1}} + \mathcal{O}(\delta_C^2),\end{aligned} \tag{4.34}$$

in which

$$\tilde{\boldsymbol{E}}_{\boldsymbol{s,n-1}} = \boldsymbol{E}_s - \boldsymbol{\mathcal{G}}_{\boldsymbol{\mathcal{S}}}(C_{n-1})\boldsymbol{E_{n-1}}. \tag{4.35}$$

The contrast update should be calculated to minimize the residual obtained in eq. (4.34). The update for the electric field remains the same as in the BIM. The resulting norms to minimize for obtaining δ_C is

$$\delta_C = \underset{\delta_C \in \mathbb{C}}{\arg\min} \frac{\|\tilde{\boldsymbol{E}}_{\boldsymbol{s,n}} - \boldsymbol{\mathcal{G}}_{\boldsymbol{\mathcal{S}}}(C_{n-1})\boldsymbol{\mathcal{L}}(C_{n-1})^{-1}\boldsymbol{\mathcal{G}}_{\boldsymbol{\mathcal{D}}}(\delta_C)\boldsymbol{E_{n-1}}\|^2_{\Gamma_S}}{\|\tilde{\boldsymbol{E}}_{\boldsymbol{s,n}}\|^2_{\Gamma_S}}. \tag{4.36}$$

in which $\boldsymbol{E_{n-1}}$ is determined by solving the state equation (eq. (4.10)) assuming that the contrast C_{n-1} is known. Note that the initialization step ($n = 0$) is the same as in the Born iterative method (section 4.2.5). The overall algorithm is delineated in Algorithm 2.

4.2.6.1 Discretization and Implementation of the D-VIE based NKM

The discretization procedure presented in section 4.2.5.1 applies also to this algorithm.

Algorithm 1: Born Iterative Method

Assume that the contrast C_0 is small enough to have $\boldsymbol{E_0} \approx \boldsymbol{E}_i\,, \boldsymbol{r} \in \Omega_D$;
$n = 1$;
Solve eq. (4.24) for C_1 using $\boldsymbol{E_0}$;
Determine the total field $\boldsymbol{E_1}$ (forward problem) using C_1 and eq. (4.10);
Update F_1 using (4.16);
while $F_n >$ *tolerance* **do**
    n=n+1;
    Determine the new contrast C_n using $\boldsymbol{E_{n-1}}$ and eq. (4.24);
    Determine the total field $\boldsymbol{E_n}$ (forward problem) using C_n and eq. (4.10);
    Update F_n using (4.16);
end

Algorithm 2: Newton-Kantorovich Method

Assume that the unknown contrast C_0 is small enough so that $\boldsymbol{E_0} \approx \boldsymbol{E}_i$ for $\boldsymbol{r} \in \Omega_D$;
n=1;
Solve eq. (4.36) for C_1 using $\boldsymbol{E_0}$ and C_0;
Use C_1 together with eq. (4.10) to obtain $\boldsymbol{E_1}$ (forward problem);
Update F_1 using eq. (4.16);
while $F_n >$ *tolerance* **do**
    n=n+1;
    Use C_{n-1}, $\boldsymbol{E_{n-1}}$, and eq. (4.36) to obtain δ_C ;
    Update C_n with the new δ_C following eq. (4.12) ;
    Use C_n together with eq. (4.10) (forward problem) to obtain $\boldsymbol{E_n}$;
    Update F_n using eq. (4.16);
end

4.2.7 Contrast Source Inversion

The contrast source inversion (CSI) method was introduced in [100]. Unlike the methods presented until now, CSI is a gradient based method. Since the derivation of the update sequence for this kind of method depends on the type of formulation used, the general notation previously used (C and $\boldsymbol{E}$) is not employed in the following. The two unknowns in this algorithm are the susceptibility $\chi(\boldsymbol{r}) = \epsilon_r(\boldsymbol{r}) - 1$ ($C \longleftrightarrow \chi$) and the contrast source defined as $\boldsymbol{w}(\boldsymbol{r}) = \chi(\boldsymbol{r})\boldsymbol{E}$ ($\boldsymbol{E} \longleftrightarrow \chi\boldsymbol{E}$).

4.2.7.1 Data and State Equations

In CSI, the state and the data equations read

$$\chi(\boldsymbol{r})\boldsymbol{E}_i(\boldsymbol{r}) + \chi(\boldsymbol{r})\boldsymbol{\mathcal{L}}_{\Omega_D}(\boldsymbol{w}) = \boldsymbol{w}(\boldsymbol{r}) \quad \boldsymbol{r} \in \Omega_D, \tag{4.37}$$

$$\boldsymbol{E}_s(\boldsymbol{r}) = \boldsymbol{\mathcal{L}}_{\Omega_D}(\boldsymbol{w}) \quad \boldsymbol{r} \in \Gamma_S, \tag{4.38}$$

in which $\boldsymbol{\mathcal{L}}_{\Omega_D}$ is defined in section 2.2.4.1 (with $\boldsymbol{J}_v(\boldsymbol{r}) = j\omega\epsilon_0\boldsymbol{w}(\boldsymbol{r})$). To simplify the notations, the integral representations of the state and data equations (eq. (4.37) and eq. (4.38)) are symbolically written as

$$\chi\boldsymbol{E}_i + \chi\boldsymbol{\mathcal{L}}_{\Omega_D}\boldsymbol{w} = \boldsymbol{w} \quad \boldsymbol{r} \in \Omega_D, \tag{4.39}$$

$$\boldsymbol{E}_s = \boldsymbol{\mathcal{L}}_{\Omega_D}\boldsymbol{w} \quad \boldsymbol{r} \in \Gamma_S. \tag{4.40}$$

4.2.7.2 Residuals and Cost Functional

Then, the following residual errors should be defined to quantify the errors of the state equation (eq. (4.39)) and data equation (eq. (4.40))

$$\boldsymbol{\rho} = \boldsymbol{E}_s - \boldsymbol{\mathcal{L}}_{\Omega_D}\boldsymbol{w}, \tag{4.41}$$

$$\boldsymbol{f} = \chi\boldsymbol{E}_i - \boldsymbol{w} + \chi\boldsymbol{\mathcal{L}}_{\Omega_D}\boldsymbol{w}. \tag{4.42}$$

Using these errors, the normalized cost functional to be minimized can be written as

$$\begin{aligned} F(\chi, \boldsymbol{w}) &= F_{\text{data}}(\boldsymbol{w}) + F_{\text{state}}(\chi, \boldsymbol{w}) \\ &= \eta_S \|\boldsymbol{\rho}\|^2_{\Gamma_S} + \eta_D \|\boldsymbol{f}\|^2_{\Omega_D} \\ &= \eta_S \|\boldsymbol{E}_s - \boldsymbol{\mathcal{L}}_{\Omega_D}\boldsymbol{w}\|^2_{\Gamma_S} + \eta_D \|\chi\boldsymbol{E}_i - \boldsymbol{w} + \chi\boldsymbol{\mathcal{L}}_{\Omega_D}\boldsymbol{w}\|^2_{\Omega_D}, \end{aligned} \tag{4.43}$$

in which $\eta_S = 1/\|\boldsymbol{E}_s\|^2_{\Gamma_S}$ and $\eta_D = 1/\|\chi\boldsymbol{E}_i\|^2_{\Omega_D}$. These two coefficients are used to balance the minimization of the F, i.e., F_{data} and F_{state} should have similar magnitudes.

To minimize F in eq. (4.43), the two unknowns are updated iteratively as follows

$$\boldsymbol{w_n} = \boldsymbol{w_{n-1}} + \alpha^w \boldsymbol{v_n}, \tag{4.44}$$

$$\chi_n = \chi_{n-1} + \alpha^\chi d_n, \tag{4.45}$$

in which $\boldsymbol{v_n}$ and d_n are the update directions obtained from the gradients of the cost functional with respect to $\boldsymbol{w}$ and χ at step n, respectively, and α^w and α^χ are coefficients obtained through line minimization of F along the update directions given by $\boldsymbol{v_n}$ and d_n. At each iteration $\boldsymbol{v_n}$, d_n, α^w, and α^χ should be determined. The cost functional at step n can then be defined as

$$F_n(\chi_n, \boldsymbol{w_n}) = \eta_S \|\boldsymbol{E}_s - \boldsymbol{\mathcal{L}}_{\Omega_D} \boldsymbol{w_n}\|^2_{\Gamma_S} + \eta_{D,n-1} \|\chi_n \boldsymbol{E}_i - \boldsymbol{w_n} + \chi_n \boldsymbol{\mathcal{L}}_{\Omega_D} \boldsymbol{w_n}\|^2_{\Omega_D}, \quad (4.46)$$

in which $\eta_{D,n-1} = 1/\|\chi_{n-1} \boldsymbol{E}_i\|^2_{\Omega_D}$.

4.2.7.3 Gradient of the cost functional with respect to $\boldsymbol{w}$

The update directions at step n can be obtained by deriving the gradient of the cost functional with respect to the unknowns at step $n-1$. To determine the gradient of the cost functional F with respect to the contrast current $\boldsymbol{w}$ at step $n-1$, the following Fréchet derivative should be first computed using eq. (4.4)

$$\frac{\partial F_{n-1}(\chi_{n-1}, \boldsymbol{w_{n-1}})}{\partial \boldsymbol{w_{n-1}}} = \lim_{\epsilon \to 0} \frac{F(\chi_{n-1}, \boldsymbol{w_{n-1}} + \epsilon \boldsymbol{v_n}) - F(\chi_{n-1}, \boldsymbol{w_{n-1}})}{\epsilon}, \quad (4.47)$$

in which χ_{n-1} is kept constant. We start from $\partial F_{\text{data},n-1}$, which has the following Fréchet derivative with respect to $\boldsymbol{w}$

$$\begin{aligned}
&\partial F_{\text{data},n-1}(\boldsymbol{w_{n-1}})/\partial \boldsymbol{w_{n-1}} \\
&= \lim_{\epsilon \to 0} \left[F_{\text{data}}(\boldsymbol{w_{n-1}} + \epsilon \boldsymbol{v_n}) - F_{\text{data}}(\boldsymbol{w_{n-1}})\right]/\epsilon \\
&= \lim_{\epsilon \to 0} \frac{\eta_S}{\epsilon} \left[\|\boldsymbol{E}_s - \boldsymbol{\mathcal{L}}_{\Omega_D} \boldsymbol{w_{n-1}} - \epsilon \boldsymbol{\mathcal{L}}_{\Omega_D} \boldsymbol{v_n}\|^2_{\Gamma_S} - \|\boldsymbol{E}_s - \boldsymbol{\mathcal{L}}_{\Omega_D} \boldsymbol{w_{n-1}}\|^2_{\Gamma_S}\right] \\
&= \lim_{\epsilon \to 0} \frac{\eta_S}{\epsilon} \left[-\epsilon \langle \boldsymbol{E}_s, \boldsymbol{\mathcal{L}}_{\Omega_D} \boldsymbol{v_n} \rangle_{\Gamma_S} - \epsilon \langle \boldsymbol{\mathcal{L}}_{\Omega_D} \boldsymbol{v_n}, \boldsymbol{E}_s \rangle_{\Gamma_S} + \epsilon^2 \|\boldsymbol{\mathcal{L}}_{\Omega_D} \boldsymbol{v_n}\|_{\Gamma_S}\right. \\
&\left. + \epsilon \langle \boldsymbol{\mathcal{L}}_{\Omega_D} \boldsymbol{w_{n-1}}, \boldsymbol{\mathcal{L}}_{\Omega_D} \boldsymbol{v_n} \rangle_{\Gamma_S} + \epsilon \langle \boldsymbol{\mathcal{L}}_{\Omega_D} \boldsymbol{v_n}, \boldsymbol{\mathcal{L}}_{\Omega_D} \boldsymbol{w_{n-1}} \rangle_{\Gamma_S}\right] \\
&= \eta_S \left[-\langle \boldsymbol{E}_s, \boldsymbol{\mathcal{L}}_{\Omega_D} \boldsymbol{v_n} \rangle_{\Gamma_S} - \langle \boldsymbol{\mathcal{L}}_{\Omega_D} \boldsymbol{v_n}, \boldsymbol{E}_s \rangle_{\Gamma_S}\right. \\
&\left. + \langle \boldsymbol{\mathcal{L}}_{\Omega_D} \boldsymbol{w_{n-1}}, \boldsymbol{\mathcal{L}}_{\Omega_D} \boldsymbol{v_n} \rangle_{\Gamma_S} + \langle \boldsymbol{\mathcal{L}}_{\Omega_D} \boldsymbol{v_n}, \boldsymbol{\mathcal{L}}_{\Omega_D} \boldsymbol{w_{n-1}} \rangle_{\Gamma_S}\right]
\end{aligned} \quad (4.48)$$

To simplify eq. (4.48) further, we introduce the adjoint operator $\boldsymbol{\mathcal{L}}^\star_{\Omega_D}$ of $\boldsymbol{\mathcal{L}}_{\Omega_D}$ which follows the relation

$$\langle \boldsymbol{v}, \boldsymbol{\mathcal{L}}_{\Omega_D} \boldsymbol{u} \rangle_{\Gamma_S} = \langle \boldsymbol{\mathcal{L}}^\star_{\Omega_D} \boldsymbol{v}, \boldsymbol{u} \rangle_{\Omega_D}. \quad (4.49)$$

Then from eq. (4.49) and using the fact that $\langle \boldsymbol{u}, \boldsymbol{v} \rangle + \langle \boldsymbol{u}, \boldsymbol{v} \rangle = 2\text{Re}\,(\langle \boldsymbol{u}, \boldsymbol{v} \rangle)$, eq. (4.48) can be written as

$$\begin{aligned}
&\partial F_{\text{data},n-1}(\boldsymbol{w_{n-1}})/\partial \boldsymbol{w_{n-1}} \\
&= -\eta_S \langle \boldsymbol{\mathcal{L}}^\star_{\Omega_D} \boldsymbol{\rho_{n-1}}, \boldsymbol{v_n} \rangle_{\Omega_D} - \eta_S \langle \boldsymbol{v_n}, \boldsymbol{\mathcal{L}}^\star_{\Omega_D} \boldsymbol{\rho_{n-1}} \rangle_{\Omega_D} \\
&= -2\eta_S \text{Re}\, \langle \boldsymbol{\mathcal{L}}^\star_{\Omega_D} \boldsymbol{\rho_{n-1}}, \boldsymbol{v_n} \rangle_{\Omega_D}.
\end{aligned} \quad (4.50)$$

Next the same approach is employed to obtain the Fréchet derivative of the cost functional $F_{\text{state},n-1}$ with respect to $\boldsymbol{w}$

$$\begin{aligned}
&\partial F_{\text{state},n-1}(\boldsymbol{w_{n-1}})/\partial \boldsymbol{w_{n-1}} \\
&= \lim_{\epsilon\to 0} \left[F_{\text{state}}(\boldsymbol{w_{n-1}} + \epsilon \boldsymbol{v_n}) - F_{\text{state}}(\boldsymbol{w_{n-1}})\right]/\epsilon \\
&= \lim_{\epsilon\to 0} \frac{\eta_{D,n-1}}{\epsilon} \Big[\|\chi \boldsymbol{E}_i - \boldsymbol{w_{n-1}} - \epsilon \boldsymbol{v_n} + \chi \boldsymbol{\mathcal{L}}_{\Omega_D} \boldsymbol{w_n} + \epsilon \chi \boldsymbol{\mathcal{L}}_{\Omega_D} \boldsymbol{v_n}\|^2_{\Omega_D} \\
&- \|\chi \boldsymbol{E}_i - \boldsymbol{w_n} + \chi \boldsymbol{\mathcal{L}}_{\Omega_D} \boldsymbol{w_n}\|^2_{\Omega_D}\Big] \\
&= -\eta_{D,n-1} \langle \boldsymbol{f_{n-1}}, \boldsymbol{v_n}\rangle_{\Omega_D} + \eta_{D,n-1} \langle \boldsymbol{\mathcal{L}}^\star_{\Omega_D} \bar{\chi}_{n-1} \boldsymbol{f_{n-1}}, \boldsymbol{v_n}\rangle_{\Omega_D} \\
&- \eta_{D,n-1} \langle \boldsymbol{v_n}, \boldsymbol{f_{n-1}}\rangle_{\Omega_D} + \eta_{D,n-1} \langle \boldsymbol{v_n}, \boldsymbol{\mathcal{L}}^\star_{\Omega_D} \bar{\chi}_{n-1} \boldsymbol{f_{n-1}}\rangle_{\Omega_D} \\
&= -2\eta_{D,n-1} \left[\langle \boldsymbol{f_{n-1}}, \boldsymbol{v_n}\rangle_{\Omega_D} - \langle \boldsymbol{\mathcal{L}}^\star_{\Omega_D} \bar{\chi}_{n-1} \boldsymbol{f_{n-1}}, \boldsymbol{v_n}\rangle_{\Omega_D}\right].
\end{aligned} \tag{4.51}$$

From eq. (4.48), eq. (4.51), and leveraging the fact that the gradient is the update direction that maximizes the Fréchet derivative (section 4.2.1), the resulting gradient of the cost functional with respect to $\boldsymbol{w}$ at step n reads

$$\boldsymbol{g}^{\boldsymbol{w}}_{\boldsymbol{n}} = \eta_S \boldsymbol{\mathcal{L}}^\star_{\Omega_D} \boldsymbol{\rho_{n-1}} + \eta_{D,n-1} (\boldsymbol{f_{n-1}} - \boldsymbol{\mathcal{L}}^\star_{\Omega_D} \bar{\chi}_{n-1} \boldsymbol{f_{n-1}}). \tag{4.52}$$

Note that the signs of the gradient terms in eq. (4.52) are opposite to the signs in eq. (4.48) and eq. (4.51), this originates from the fact that the cost functional should be minimized and thus the gradient should make the cost functional decrease.

4.2.7.4 Gradient of the cost functional with respect to χ

The susceptibility is only present in the state equation so only F_{state} needs to be considered in the following derivations. We can repeat the expansion of eq. (4.51) for $\partial F_{\text{state}}/\partial \chi$. To simplify the following derivation, the residual at step n of the state equation can be recast as

$$\boldsymbol{f'_n} = \chi_n \boldsymbol{E_n} - \boldsymbol{w_n}. \tag{4.53}$$

The Fréchet derivative of $F_{\text{state},n-1}$ with respect to χ_{n-1} then reads

$$\partial F_{\text{state},n-1}(\chi_{n-1}, \boldsymbol{w_{n-1}})/\partial \chi_{n-1} = -2\eta_{D,n-1} \text{Re}\, \langle \bar{\boldsymbol{E}}_{\boldsymbol{n-1}} \cdot \boldsymbol{f'_{n-1}}, d_n\rangle_{\Omega_D}. \tag{4.54}$$

in which $(\cdot)$ denotes the dot product between two vector functions. Note that the change of the gradient due to the variation of χ in η_D is neglected here [67]. The gradient of F with respect to κ at step n finally reads

$$\boldsymbol{g}^{\boldsymbol{\chi}}_{\boldsymbol{n}} = \eta_{D,n-1} \bar{\boldsymbol{E}}_{\boldsymbol{n-1}} \cdot \boldsymbol{f'_{n-1}}. \tag{4.55}$$

4.2.7.5 Polak-Ribière update

To improve the update directions given by the gradients $\boldsymbol{g_n^w}$ and $\boldsymbol{g_n^\chi}$, the Polak-Ribière conjugate directions can be used [61]. They allow restarting the update process when the solution is not improving sufficiently ($\boldsymbol{g_n^w} \approx \boldsymbol{g_{n-1}^w}$ or $g_n^\chi \approx g_{n-1}^\chi$). The new update direction d_n for the susceptibility can be expressed as

$$d_1 = g_1^\chi, \quad n = 1 \tag{4.56}$$

$$d_n = g_n^\chi + \gamma_n^\chi d_{n-1}, \quad n \geq 2 \tag{4.57}$$

in which

$$\gamma_n^\chi = \frac{\langle g_n^\chi, g_{n-1}^\chi \rangle_{\Omega_D}}{\|g_{n-1}^\chi\|_{\Omega_D}^2}. \tag{4.58}$$

The update direction for the contrast source reads

$$\boldsymbol{v_1} = \boldsymbol{g_1^w}, \quad n = 1 \tag{4.59}$$

$$\boldsymbol{v_n} = \boldsymbol{g_n^w} + \gamma_n^w \boldsymbol{v_{n-1}}, \quad n \geq 2 \tag{4.60}$$

in which

$$\gamma_n^w = \frac{\langle \boldsymbol{g_n^w}, \boldsymbol{g_{n-1}^w} \rangle_{\Omega_D}}{\|\boldsymbol{g_{n-1}^w}\|_{\Omega_D}^2}. \tag{4.61}$$

4.2.7.6 Determination of the weights α^w and α^χ for minimizing the cost functional

Now that the update directions are determined, the next step is to derive the weights α^w and α^χ that will minimize the cost functional F in the given update directions. First the following relations between the residuals at step n and at step $n-1$ are required

$$\boldsymbol{f_n} = \boldsymbol{f_{n-1}} - \alpha_n^w \boldsymbol{v}_n + \alpha^w \chi_{n-1} \boldsymbol{\mathcal{L}}_{\Omega_D} \boldsymbol{v}_n, \tag{4.62}$$

$$\boldsymbol{\rho_n} = \boldsymbol{\rho}_{n-1} - \alpha^w \boldsymbol{\mathcal{L}}_{\Omega_D} \boldsymbol{v}_n. \tag{4.63}$$

Substituting eqs. (4.62) and (4.63) into eq. (4.46) gives

$$F_n = \alpha_n^w \left[\eta_{D,n-1} \langle \boldsymbol{f_n}, -\boldsymbol{v}_n + \chi_{n-1} \boldsymbol{\mathcal{L}}_{\Omega_D} \boldsymbol{v}_n \rangle_{\Omega_D} + \eta_S \langle \boldsymbol{\rho_n}, -\boldsymbol{\mathcal{L}}_{\Omega_D} \boldsymbol{v}_n \rangle_{\Gamma_S} \right], \tag{4.64}$$

Then, using eq. (4.62) and eq. (4.63) and equating $F_n = 0$ gives

$$\begin{aligned} &[\eta_{D,n-1} \langle \boldsymbol{f_{n-1}}, -\boldsymbol{v}_n + \chi_{n-1} \boldsymbol{\mathcal{L}}_{\Omega_D} \boldsymbol{v}_n \rangle_{\Omega_D} + \eta_S \langle \boldsymbol{\rho_{n-1}}, -\boldsymbol{\mathcal{L}}_{\Omega_D} \boldsymbol{v}_n \rangle_{\Gamma_S}] \\ &\qquad = \alpha_n^w \left[\eta_{D,n-1} \|\boldsymbol{v}_n - \chi_{n-1} \boldsymbol{\mathcal{L}}_{\Omega_D} \boldsymbol{v}_n\|_{\Omega_D}^2 + \eta_S \|\boldsymbol{\mathcal{L}}_{\Omega_D} \boldsymbol{v}_n\|_{\Gamma_S}^2 \right]. \end{aligned} \tag{4.65}$$

Inserting the gradient $\boldsymbol{g_n^w}$ from eq. (4.52) in eq. (4.65), the resulting weight for the update of the contrast current that minimizes the cost functional reads

$$\alpha_n^w = \frac{\langle \boldsymbol{g_n^w}, \boldsymbol{v_n} \rangle_{\Omega_D}}{\eta_{D,n-1} \|\boldsymbol{v}_n - \chi_{n-1} \boldsymbol{\mathcal{L}}_{\Omega_D} \boldsymbol{v}_n\|_{\Omega_D}^2 + \eta_S \|\boldsymbol{\mathcal{L}}_{\Omega_D} \boldsymbol{v}_n\|_{\Gamma_S}^2}. \tag{4.66}$$

Next, the appropriate weight α^{χ} is obtained with a procedure slightly different from the one that was used to determine α^{w}. $F_{\text{state},n-1}$ is minimized by substituting χ_n by its expression in eq. (4.45) as follows

$$F_{\text{state},n-1}(\chi_{n-1}+\alpha_n^{\chi}d_n,\boldsymbol{w_n}) = \frac{\|(\chi_{n-1}+\alpha_n^{\chi}d_n)\boldsymbol{E_n}-\boldsymbol{w_n}\|^2_{\Omega_D}}{\|(\chi_{n-1}+\alpha_n^{\chi}d_n)\boldsymbol{E_i}\|^2_{\Omega_D}}. \tag{4.67}$$

The numerator of eq. (4.67) can be expanded as

$$\begin{aligned}\|\chi_{n-1}\boldsymbol{E_n}-\boldsymbol{w_n}+\alpha_n^{\chi}d_n\boldsymbol{E_n}\|^2_{\Omega_D} = \|\chi_{n-1}\boldsymbol{E_n}-\boldsymbol{w_n}\|^2_{\Omega_D} + (\alpha_n^{\chi})^2\|d_n\boldsymbol{E_n}\|^2_{\Omega_D} \\ + 2\text{Re}\,\langle\chi_{n-1}\boldsymbol{E_n}-\boldsymbol{w_n},\alpha_n^{\chi}d_n\boldsymbol{E_n}\rangle,\end{aligned} \tag{4.68}$$

and its denominator as

$$\begin{aligned}\|\chi_{n-1}\boldsymbol{E_i}+\alpha_n^{\chi}d_n\boldsymbol{E_i}\|^2_{\Omega_D} = \|\chi_{n-1}\boldsymbol{E_i}\|^2_{\Omega_D} + (\alpha_n^{\chi})^2\|d_n\boldsymbol{E_i}\|^2_{\Omega_D} \\ + 2\alpha_n^{\chi}\text{Re}\,\langle\chi_{n-1}\boldsymbol{E_i},d_n\boldsymbol{E_i}\rangle.\end{aligned} \tag{4.69}$$

Finally, $F_{\text{state},n-1}$ can be rewritten as

$$F_D(\chi_{n-1}+\alpha_n^{\chi}d_n) = \frac{a(\alpha_n^{\chi})^2+2b\alpha_n^{\chi}+c}{A(\alpha_n^{\chi})^2+2B\alpha_n^{\chi}+C}, \tag{4.70}$$

in which $a = \|d_n\boldsymbol{E_n}\|^2_{\Omega_D}$, $b = \text{Re}\,\langle\chi_{n-1}\boldsymbol{E_n}-\boldsymbol{w_n},\alpha_n^{\chi}d_n\boldsymbol{E_n}\rangle$, $c = \|\chi_{n-1}\boldsymbol{E_n}-\boldsymbol{w_n}+\alpha_n^{\chi}d_n\boldsymbol{E_n}\|^2_{\Omega_D}$, $A = \|d_n\boldsymbol{E_i}\|^2_{\Omega_D}$, $B = \text{Re}\,\langle\chi_{n-1}\boldsymbol{E_n}-\boldsymbol{w_n},\alpha_n^{\chi}d_n\boldsymbol{E_n}\rangle$, and $C = \|\chi_{n-1}\boldsymbol{E_i}\|^2_{\Omega_D}$.

This cost functional can be minimized by taking its derivative equal to 0, this gives a second order polynomial that has to be solved for α_n^{χ}

$$(-2bA+2aB)(\alpha_n^{\chi})^2+(2aC-2Ac)\alpha_n^{\chi}+(2bC-2Bc)=0 \tag{4.71}$$

which gives

$$\alpha_n^{\chi} = \frac{-(aC-Ac)+\sqrt{(aC-Ac)^2-4(-bA+aB)(bC-Bc)}}{2(-bA+aB)}. \tag{4.72}$$

In CSI, a simpler way to minimize the cost functional for χ without the need for the computation of the gradient and the weight is to minimize directly $\boldsymbol{f_n'}$ in eq. (4.53). The updated susceptibility can be obtained as follows from the knowledge of the electric field and the contrast source at step n [11]

$$\chi_n = \frac{\boldsymbol{E_n}\cdot\bar{\boldsymbol{w}}_{\boldsymbol{n}}}{|\boldsymbol{E_n}|^2}. \tag{4.73}$$

However, this update does not hold if regularization terms depending on χ are added to the standard CSI cost functional.

4.2.7.7 Initialization of the susceptibility and contrast current

Now that all the update procedure has been defined, the starting values for the CSI algorithm should be chosen. In general, the contrast source is initialized first and then the susceptibility is initialized from it. The initialization of the contrast current is equivalent to an inverse source problem in which only the data equation eq. (4.40) is employed, i.e. find $\boldsymbol{w_0}$ such that F_{data} is minimized. The minimization can be achieved via back propagation [62]. The resulting initial contrast source reads

$$\boldsymbol{w_0} = \frac{\|\boldsymbol{\mathcal{L}}^{\star}_{\Omega_D} \boldsymbol{E}_s\|^2_{\Omega_D}}{\|\boldsymbol{\mathcal{L}}_{\Omega_D} \boldsymbol{\mathcal{L}}^{\star}_{\Omega_D} \boldsymbol{E}_s\|^2_{\Omega_D}}, \tag{4.74}$$

and the resulting initial total field is

$$\boldsymbol{E_0} = \boldsymbol{E}_i + \boldsymbol{\mathcal{L}}_{\Omega_D} \boldsymbol{w_0}. \tag{4.75}$$

Finally the susceptibility at step $n = 0$ can be obtained from eq. (4.73). The overall CSI algorithm is provided in Algorithm 3.

Algorithm 3: Contrast Source Inversion

```
n = 0;
Init w_0 with eq. (4.74);
Init E_0 with eq. (4.75);
Init χ_0 with eq. (4.73);
Init F_0;
Update η_{D,0};
while F_n > tolerance do
    n=n+1;
    Compute the gradients g_n^χ and g_n^w using eq. (4.52) and eq. (4.55);
    Compute the update directions d_n and v_n from eq. (4.56) and eq. (4.59);
    Compute the weights α_n^χ and α_n^w using eq. (4.66) and eq. (4.72);
    Update the contrast source as w_n = w_{n-1} + α^w v_n ;
    Update the susceptibility as χ_n = χ_{n-1} + α^χ d_n;
    Update the residuals f_n and ρ_n using eq. (4.41) and eq. (4.42);
    Update η_{D,n};
    Update F_n;
end
```

4.2.7.8 Discretization of the J-VIE based CSI

This CSI algorithm is based on the J-VIE, of which the discretization is given in section 2.3.3.

4.3 A New D-VIE-Based Inverse Scattering Scheme

In this section we present a new inverse scattering scheme based on the electric flux volume integral equation. In this inverse scattering problem, the unknown quantities are the electric flux and the dielectric contrast κ. This algorithm pertains to the family of the gradient based methods as the CSI method, which is presented in section 4.2.7.

4.3.1 Data and State Equations

Since $\boldsymbol{D}$ and κ are the unknowns of this inverse scattering problem, the first step is to rewrite the state and data equations as a function of these unknowns

$$\boldsymbol{E_i}(\boldsymbol{r}) + \boldsymbol{\mathcal{L}}_{\kappa}^{\Omega_D}(\boldsymbol{D}) = \frac{1-\kappa(\boldsymbol{r})}{\epsilon_0}\boldsymbol{D}(\boldsymbol{r}) \quad \boldsymbol{r} \in \Omega_D, \tag{4.76}$$

$$\boldsymbol{E_s}(\boldsymbol{r}) = \boldsymbol{\mathcal{L}}_{\kappa}^{\Omega_D}(\boldsymbol{D}) \quad \boldsymbol{r} \in \Gamma_S, \tag{4.77}$$

where $\boldsymbol{\mathcal{L}}_{\kappa}^{\Omega_D}$ is defined in section 2.2.4.2 and the dielectric contrast $\kappa = (\epsilon_r - 1)/\epsilon_r$. To simplify the following derivations, the operator $\boldsymbol{\mathcal{M}}_{\kappa}^{\Omega_D} = \frac{1-\kappa}{\epsilon_0}\boldsymbol{\mathcal{I}} - \boldsymbol{\mathcal{L}}_{\kappa}^{\Omega_D}$ is introduced. With this operator, eq. (4.76) simplifies to $\boldsymbol{\mathcal{M}}_{\kappa}^{\Omega_D}(\boldsymbol{D}) = \boldsymbol{E}_i$.

4.3.2 Residuals and Cost Functional

A cost functional enforcing simultaneously the state and data equations should then be defined

$$\begin{aligned} F(\kappa, \boldsymbol{D}) &= F_{\text{data}}(\kappa, \boldsymbol{D}) + F_{\text{state}}(\kappa, \boldsymbol{D}) \\ &= \eta_S \|\boldsymbol{E}_s - \boldsymbol{\mathcal{L}}_{\kappa}^{\Omega_D}(\boldsymbol{D})\|_{\Gamma_S}^2 + \eta_D \|\boldsymbol{E}_i + \boldsymbol{\mathcal{L}}_{\kappa}^{\Omega_D}\boldsymbol{D} - \frac{1-\kappa}{\epsilon_0}\boldsymbol{D}\|_{\Omega_D}^2, \end{aligned} \tag{4.78}$$

where η_S and η_D are used for normalization as in the CSI method. Here we define $\eta_S = 1/\|\boldsymbol{E}_s\|_{\Gamma_S}^2$ and $\eta_D = 1/\|\boldsymbol{E}_i\|_{\Omega_D}^2$. The residual errors of the data and state equations are defined as follows

$$\begin{aligned} \boldsymbol{\rho} &= \boldsymbol{E_s} - \boldsymbol{\mathcal{L}}_{\kappa}^{\Omega_D}\boldsymbol{D} \\ \boldsymbol{f} &= \boldsymbol{E_i} + \boldsymbol{\mathcal{L}}_{\kappa}^{\Omega_D}\boldsymbol{D} - \frac{1-\kappa}{\epsilon_0}\boldsymbol{D} \\ &= \boldsymbol{E_i} - \boldsymbol{\mathcal{M}}_{\kappa}^{\Omega_D}\boldsymbol{D} \end{aligned} \tag{4.79}$$

To minimize F in eq. (4.78), the two unknowns are updated iteratively as follows

$$\boldsymbol{D_n} = \boldsymbol{D_{n-1}} + \alpha^D \boldsymbol{v_n} \tag{4.80}$$

$$\kappa_n = \kappa_{n-1} + \alpha^{\kappa} w_n \tag{4.81}$$

in which $\boldsymbol{v_n}$ and w_n are the update directions given by the gradients of the cost functional with respect to $\boldsymbol{D}$ and κ at step n, respectively, and α^D and α^χ are coefficients obtained through line minimization of F along the update directions. At each iteration $\boldsymbol{v_n}$, w_n, α^D, and α^κ should be determined. The cost functional at step n can then be defined as

$$\begin{aligned} F(\kappa_n, \boldsymbol{D_n}) &= F_{\text{data}}(\kappa_n, \boldsymbol{D_n}) + F_{\text{state}}(\kappa_n, \boldsymbol{D_n}) \\ &= \eta_S \|\boldsymbol{E}_s - \boldsymbol{\mathcal{L}}_{\kappa_n}^{\Omega_D} \boldsymbol{D_n}\|_{\Gamma_S}^2 + \eta_D \|\boldsymbol{E}_i + \boldsymbol{\mathcal{L}}_{\kappa_n}^{\Omega_D} \boldsymbol{D_n} - \frac{1-\kappa_n}{\epsilon_0} \boldsymbol{D_n}\|_{\Omega_D}^2. \end{aligned} \tag{4.82}$$

4.3.3 Gradients of the Cost Functional

4.3.3.1 Gradient of the cost functional with respect to $\boldsymbol{D}$

As for the CSI method, the gradient of the cost functional F with respect to $\boldsymbol{D}$ at step n can be obtained by deriving the Fréchet derivative at step $n-1$. For the the data equation, it reads

$$\begin{aligned} \partial F_{\text{data},n-1}/\partial \boldsymbol{D_{n-1}} &= \lim_{\epsilon \to 0} \left(F_{\text{data},n-1}(\kappa_{n-1}, \boldsymbol{D_{n-1}} + \epsilon \boldsymbol{v_n}) - F_{\text{data},n-1}(\kappa_{n-1}, \boldsymbol{D_{n-1}})\right)/\epsilon \\ &= \lim_{\epsilon \to 0} \frac{\eta_S}{\epsilon} \Big[-\epsilon \langle \boldsymbol{E}_s, \boldsymbol{\mathcal{L}}_{\kappa_{n-1}}^{\Omega_D}(\boldsymbol{v_n}) \rangle \; -\epsilon \langle \boldsymbol{\mathcal{L}}_{\kappa_{n-1}}^{\Omega_D}(\boldsymbol{v_n}), \boldsymbol{E}_s \rangle \\ &\quad + \epsilon \langle \boldsymbol{\mathcal{L}}_{\kappa_{n-1}}^{\Omega_D}(\boldsymbol{D_{n-1}}), \boldsymbol{\mathcal{L}}_{\kappa_{n-1}}^{\Omega_D}(\boldsymbol{v_n}) \rangle \; + \epsilon \langle \boldsymbol{\mathcal{L}}_{\kappa_{n-1}}^{\Omega_D}(\boldsymbol{v_n}), \boldsymbol{\mathcal{L}}_{\kappa_{n-1}}^{\Omega_D}(\boldsymbol{D_{n-1}}) \rangle \Big] \\ &= -\eta_S \langle {\boldsymbol{\mathcal{L}}_{\kappa_{n-1}}^{\Omega_D}}^\star(\boldsymbol{\rho_{n-1}}), \boldsymbol{v_n} \rangle - \eta_S \langle \boldsymbol{v_n}, {\boldsymbol{\mathcal{L}}_{\kappa_{n-1}}^{\Omega_D}}^\star(\boldsymbol{\rho_{n-1}}) \rangle \\ &= -2\eta_S \text{Re} \, \langle {\boldsymbol{\mathcal{L}}_{\kappa_{n-1}}^{\Omega_D}}^\star(\boldsymbol{\rho_{n-1}}), \boldsymbol{v_n} \rangle, \end{aligned} \tag{4.83}$$

and for the state equation we have

$$\begin{aligned} \partial F_{\text{state},n-1}/\partial \boldsymbol{D_{n-1}} &= \lim_{\epsilon \to 0} \left(F_{\text{state},n-1}(\kappa_{n-1}, \boldsymbol{D_{n-1}} + \epsilon \boldsymbol{v_n}) - F_{\text{state},n-1}(\kappa_{n-1}, \boldsymbol{D_{n-1}})\right)/\epsilon \\ &= -2\eta_D \text{Re} \left(\langle {\boldsymbol{\mathcal{M}}_{\kappa_{n-1}}^{\Omega_D}}^\star(\boldsymbol{f_{n-1}}), \boldsymbol{v_n} \rangle \right). \end{aligned} \tag{4.84}$$

Finally, the gradient of F at step n with respect to $\boldsymbol{D}$ deduced from eq. (4.83) and eq. (4.84) is

$$\boldsymbol{g_n^D} = \eta_S {\boldsymbol{\mathcal{L}}_{\kappa_{n-1}}^{\Omega_D}}^\star(\boldsymbol{\rho_{n-1}}) + \eta_D {\boldsymbol{\mathcal{M}}_{\kappa_{n-1}}^{\Omega_D}}^\star(\boldsymbol{f_{n-1}}). \tag{4.85}$$

4.3.3.2 Gradient of the cost functional with respect to κ

Unlike for the CSI, the contrast is also present in the data equation, thus both the state and the data cost functionals should be differentiated. Moreover, since κ pertains to the definition of the D-VIE operator ($\boldsymbol{\mathcal{L}}_\kappa^{\Omega_D}$), the operator $\boldsymbol{\mathcal{L}}_{\boldsymbol{D}}^{\Omega_D}$ introduced in eq. (2.62) should be used to be able to Fréchet differentiate F with respect

to κ. With this operator, the residual errors of the object and data equations can be rewritten as

$$\begin{aligned} \boldsymbol{\rho} &= \boldsymbol{E_s} - \boldsymbol{\mathcal{L}}_{\boldsymbol{D}}^{\Omega_D}(\kappa) \\ \boldsymbol{f} &= \boldsymbol{E}_i - \frac{\boldsymbol{D}}{\epsilon_0} + \boldsymbol{\mathcal{L}}_{\boldsymbol{D}}^{\Omega_D}(\kappa) + \frac{\boldsymbol{D}}{\epsilon_0}\kappa. \end{aligned} \tag{4.86}$$

The Frechet derivative of F_{data} with respect to κ can be expanded as follows

$$\begin{aligned} \partial F_{\text{data},n-1}/\partial \kappa_{n-1} &= \lim_{\epsilon\to 0} \left(F_{\text{data},n-1}(\kappa_{n-1}+\epsilon w_n, \boldsymbol{D_{n-1}}) - F_{\text{data},n-1}(\kappa_{n-1}, \boldsymbol{D_{n-1}})\right)/\epsilon \\ &= \eta_S \langle \boldsymbol{\rho_{n-1}}, \boldsymbol{\mathcal{L}}_{\boldsymbol{D_{n-1}}}^{\Omega_D}(w_n)\rangle + \eta_S \langle \boldsymbol{\mathcal{L}}_{\boldsymbol{D_{n-1}}}^{\Omega_D}(w_n), \boldsymbol{\rho_{n-1}}\rangle \\ &= \eta_S \langle \boldsymbol{\mathcal{L}}_{\boldsymbol{D_{n-1}}}^{\Omega_D\ \star}(\rho_{n-1}), w_n\rangle + \eta_S \langle w_n, \boldsymbol{\mathcal{L}}_{\boldsymbol{D_{n-1}}}^{\Omega_D\ \star}(\rho_{n-1})\rangle \\ &= 2\eta_S \text{Re}\ \langle \boldsymbol{\mathcal{L}}_{\boldsymbol{D_{n-1}}}^{\Omega_D\ \star}(\rho_{n-1}), w_n\rangle. \end{aligned} \tag{4.87}$$

Next the expansion of the Fréchet derivative of the cost functional of the state equation with respect to κ gives

$$\begin{aligned} \partial F_{\text{state}_{n-1}}/\partial \kappa_{n-1} &= \lim_{\epsilon\to 0} \left(F_{\text{state},n-1}(\kappa_{n-1}+\epsilon w_n, \boldsymbol{D_{n-1}}) - F_{\text{state},n-1}(\kappa_{n-1}, \boldsymbol{D_{n-1}})\right)/\epsilon \\ &= \eta_D \langle \boldsymbol{f_{n-1}}, \boldsymbol{\mathcal{L}}_{\boldsymbol{D_{n-1}}}^{\Omega_D}(w_n)\rangle + \eta_D \langle \boldsymbol{\mathcal{L}}_{\boldsymbol{D_{n-1}}}^{\Omega_D}(w_n), \boldsymbol{f_{n-1}}\rangle \\ &- \eta_D \langle \boldsymbol{f_{n-1}}, \frac{1}{\epsilon_0}\boldsymbol{D_{n-1}} w_n\rangle - \eta_D \langle \frac{1}{\epsilon_0}\boldsymbol{D_{n-1}} w_n, \boldsymbol{f_{n-1}}\rangle \\ &= 2\eta_D \text{Re}\ \langle \boldsymbol{\mathcal{L}}_{\boldsymbol{D_{n-1}}}^{\Omega_D\ \star}(\boldsymbol{f_{n-1}}), w_n\rangle - 2\frac{\eta_D}{\epsilon_0}\text{Re}\ \langle \bar{\boldsymbol{D}}_{\boldsymbol{n-1}} \cdot \boldsymbol{f_{n-1}}, w_n\rangle. \end{aligned} \tag{4.88}$$

The resulting gradient of F at step n with respect to κ reads

$$g_n^\kappa = -\eta_S \boldsymbol{\mathcal{L}}_{\boldsymbol{D_{n-1}}}^{\Omega_D\ \star}(\boldsymbol{\rho_{n-1}}) - \eta_D \left(\boldsymbol{\mathcal{L}}_{\boldsymbol{D_{n-1}}}^{\Omega_D\ \star}(\boldsymbol{f_{n-1}}) - \frac{1}{\epsilon_0}\bar{\boldsymbol{D}}_{\boldsymbol{n-1}} \cdot \boldsymbol{f_{n-1}}\right). \tag{4.89}$$

As in the CSI, the update directions can be improved by choosing a Polak-Ribière update scheme (section 4.2.7.5).

4.3.3.3 Polak-Ribière Update

The new update direction w_n for the dielectric contrast can be expressed as

$$w_1 = g_1^\kappa, \quad n = 1 \tag{4.90}$$

$$w_n = g_n^\kappa + \gamma_n^\kappa w_{n-1}, \quad n \geq 2 \tag{4.91}$$

in which

$$\gamma_n^\kappa = \frac{\langle g_n^\kappa, g_{n-1}^\kappa\rangle_{\Omega_D}}{\|g_{n-1}^\kappa\|_{\Omega_D}^2}. \tag{4.92}$$

The update direction for the electric flux reads

$$\boldsymbol{v_1} = \boldsymbol{g_1^D}, \quad n = 1 \tag{4.93}$$

$$\boldsymbol{v_n} = \boldsymbol{g_n^D} + \gamma_n^D \boldsymbol{v_{n-1}}, \quad n \geq 2 \tag{4.94}$$

in which

$$\gamma_n^D = \frac{\langle \boldsymbol{g_n^D}, \boldsymbol{g_{n-1}^D} \rangle_{\Omega_D}}{\|\boldsymbol{g_{n-1}^D}\|_{\Omega_D}^2}. \tag{4.95}$$

4.3.4 Determination of the Weights

Now that the update directions are determined, the next step is to derive the weights $\alpha^{\boldsymbol{D}}$ and α^{κ} that minimize the cost functional F in the given update directions. At each iteration, κ and $\boldsymbol{D}$ are updated as follows

$$\boldsymbol{D_n} = \boldsymbol{D_{n-1}} + \alpha_n^D \boldsymbol{v_n} \tag{4.96}$$

$$\kappa_n = \kappa_{n-1} + \alpha_n^{\kappa} w_n, \tag{4.97}$$

where w_n and $\boldsymbol{v_n}$ are given in eq. (4.91) and eq. (4.94), respectively. Substituting eq. (4.96) and eq. (4.97) into the residual errors gives the following relations between the residual errors at step n and at step $n-1$

$$\boldsymbol{\rho_n} = \boldsymbol{\rho_{n-1}} - \alpha_n^D \boldsymbol{\mathcal{L}}_{\kappa_{n-1}}^{\Omega_D}(\boldsymbol{v_n}) - \alpha_n^{\kappa}\alpha_n^D \boldsymbol{\mathcal{L}}_{w_n}^{\Omega_D}(\boldsymbol{v_n}) - \alpha_n^{\kappa} \boldsymbol{\mathcal{L}}_{w_n}^{\Omega_D} \boldsymbol{D_{n-1}}, \tag{4.98}$$

for the data equation and

$$\begin{aligned} \boldsymbol{f_n} = \boldsymbol{f_{n-1}} &+ \alpha_n^D (\boldsymbol{\mathcal{L}}_{\kappa_{n-1}}^{\Omega_D}(\boldsymbol{v_n}) - \frac{\boldsymbol{v_n}}{\epsilon_0} + \frac{\kappa_{n-1}}{\epsilon_0}\boldsymbol{v_n}) \\ &+ \alpha_n^{\kappa} (\boldsymbol{\mathcal{L}}_{w_n}^{\Omega_D}(\boldsymbol{D_{n-1}}) + \frac{w_n}{\epsilon_0}\boldsymbol{D_{n-1}}) + \alpha_n^D \alpha_n^{\kappa} (\boldsymbol{\mathcal{L}}_{w_n}^{\Omega_D}(\boldsymbol{v_n}) + \frac{w_n}{\epsilon_0}\boldsymbol{v_n}), \end{aligned} \tag{4.99}$$

for the state equation.

The next step is to replace eq. (4.98) and eq. (4.99) into the cost functional (4.78)

$$F_n = F_{n,\text{data}}(\kappa_n, \boldsymbol{D_n}) + F_{n,\text{state}}(\kappa_n, \boldsymbol{D_n}) = \eta_S \|\boldsymbol{\rho_n}\|_{\Gamma_S}^2 + \eta_D \|\boldsymbol{f_n}\|_{\Omega_D}^2. \tag{4.100}$$

The expansion of the data cost functional at step n gives

$$\begin{aligned} F_{n,\text{data}}(\kappa_n, \boldsymbol{D_n}) = \eta_S \Big[&\alpha_n^D a + \alpha_n^{\kappa} b + \alpha_n^D \alpha_n^{\kappa} c + (\alpha_n^D)^2 A + (\alpha_n^{\kappa})^2 B \\ &+ (\alpha_n^D \alpha_n^{\kappa})^2 C + D + \alpha_n^D (\alpha_n^{\kappa})^2 E + (\alpha_n^D)^2 \alpha_n^{\kappa} F \Big], \end{aligned} \tag{4.101}$$

where $a, b, c, A, B, C, D, E, F$ are defined as follows

$$\begin{cases} a = \eta_S \left[-2\mathrm{Re}\, \langle \boldsymbol{\rho_{n-1}}, \boldsymbol{\mathcal{L}}^{\Omega_D}_{\kappa_{n-1}}(\boldsymbol{v_n}) \rangle_{\Gamma_S} \right] \\ b = \eta_S \left[-2\mathrm{Re}\, \langle \boldsymbol{\rho_{n-1}}, \boldsymbol{\mathcal{L}}^{\Omega_D}_{w_n}(\boldsymbol{D_{n-1}}) \rangle_{\Gamma_S} \right] \\ c = \eta_S \left[2\mathrm{Re}\, \langle \boldsymbol{\mathcal{L}}^{\Omega_D}_{\kappa_{n-1}}(\boldsymbol{v_n}), \boldsymbol{\mathcal{L}}^{\Omega_D}_{w_n}(\boldsymbol{D_{n-1}}) \rangle_{\Gamma_S} - 2\mathrm{Re}\, \langle \boldsymbol{\rho_{n-1}}, \boldsymbol{\mathcal{L}}^{\Omega_D}_{w_n}(\boldsymbol{v_n}) \rangle_{\Gamma_S} \right] \\ A = \eta_S \| \boldsymbol{\mathcal{L}}^{\Omega_D}_{\kappa_{n-1}}(\boldsymbol{v_n}) \|^2_{\Gamma_S} \\ B = \eta_S \| \boldsymbol{\mathcal{L}}^{\Omega_D}_{w_n}(\boldsymbol{D_{n-1}}) \|^2_{\Gamma_S} \\ C = \eta_S \| \boldsymbol{\mathcal{L}}^{\Omega_D}_{w_n}(\boldsymbol{v_n}) \|^2_{\Gamma_S} \\ D = \eta_D \| \boldsymbol{\rho_{n-1}} \|^2_{\Gamma_S} \\ E = \eta_S \left[2\mathrm{Re}\, \langle \boldsymbol{\mathcal{L}}^{\Omega_D}_{w_n}(\boldsymbol{v_n}), \boldsymbol{\mathcal{L}}^{\Omega_D}_{w_n}(\boldsymbol{D_{n-1}}) \rangle_{\Gamma_S} \right] \\ F = \eta_S \left[2\mathrm{Re}\, \langle \boldsymbol{\mathcal{L}}^{\Omega_D}_{\kappa_{n-1}}(\boldsymbol{v_n}), \boldsymbol{\mathcal{L}}^{\Omega_D}_{w_n}(\boldsymbol{v_n}) \rangle_{\Gamma_S} \right]. \end{cases} \tag{4.102}$$

Similarly the cost functional of the state equation has the following form when expanded

$$\begin{aligned} F_{n,\mathrm{state}}(\kappa_n, \boldsymbol{D_{n-1}}) = \eta_D \Big[& \alpha_n^D a' + \alpha_n^\kappa b' + \alpha_n^D \alpha_n^\kappa c' + (\alpha_n^D)^2 A' \\ & + (\alpha_n^\kappa)^2 B' + (\alpha_n^D \alpha_n^\kappa)^2 C' + D' + \alpha_n^D (\alpha_n^\kappa)^2 E' + (\alpha_n^D)^2 \alpha_n^\kappa F' \Big], \end{aligned} \tag{4.103}$$

where $a', b', c', A', B', C', D', E', F'$ are defined as

$$\begin{cases} a' = \eta_D(-\frac{2}{\epsilon_0}\langle \boldsymbol{v_n}, \boldsymbol{f_{n-1}} \rangle_{\Omega_D} + \frac{2}{\epsilon_0}\mathrm{Re}\, \langle \kappa_{n-1}\boldsymbol{v_n}, \boldsymbol{f_{n-1}} \rangle_{\Omega_D} + 2\mathrm{Re}\, \langle \boldsymbol{f_{n-1}}, \boldsymbol{\mathcal{L}}^{\Omega_D}_{\kappa_{n-1}}(\boldsymbol{v_n}) \rangle_{\Omega_D}) \\ b' = \eta_D(\frac{2}{\epsilon_0}\mathrm{Re}\, \langle w_n \boldsymbol{D_{n-1}}, \boldsymbol{f_{n-1}} \rangle_{\Omega_D} + 2\mathrm{Re}\, \langle \boldsymbol{f_{n-1}}, \boldsymbol{\mathcal{L}}^{\Omega_D}_{w_n}(\boldsymbol{D_{n-1}}) \rangle_{\Omega_D}) \\ c' = \eta_D(-\frac{2}{\epsilon_0^2}\mathrm{Re}\, \langle \boldsymbol{v_n}, w_n \boldsymbol{D_{n-1}} \rangle_{\Omega_D} + \frac{2}{\epsilon_0^2}\mathrm{Re}\, \langle \kappa_{n-1}\boldsymbol{v_n}, w_n \boldsymbol{D_{n-1}} \rangle_{\Omega_D} \\ + \frac{2}{\epsilon_0^2}\langle w_n \boldsymbol{v_n}, \boldsymbol{f_{n-1}} \rangle_{\Omega_D} + \frac{2}{\epsilon_0}\mathrm{Re}\, \langle w_n \boldsymbol{D_{n-1}}, \boldsymbol{\mathcal{L}}^{\Omega_D}_{\kappa_{n-1}}(\boldsymbol{v_n}) \rangle_{\Omega_D} \\ - \frac{2}{\epsilon_0}\mathrm{Re}\, \langle \boldsymbol{v_n}, \boldsymbol{\mathcal{L}}^{\Omega_D}_{w_n}(\boldsymbol{D_{n-1}}) \rangle_{\Omega_D} + \frac{2}{\epsilon_0}\mathrm{Re}\, \langle \kappa_{n-1}\boldsymbol{v_n}, \boldsymbol{\mathcal{L}}^{\Omega_D}_{w_n}(\boldsymbol{D_{n-1}}) \rangle_{\Omega_D} \\ + 2\mathrm{Re}\, \langle \boldsymbol{\mathcal{L}}^{\Omega_D}_{\kappa_{n-1}}(\boldsymbol{v_n}), \boldsymbol{\mathcal{L}}^{\Omega_D}_{w_n}(\boldsymbol{D_{n-1}}) \rangle_{\Omega_D} + 2\langle \boldsymbol{f_{n-1}}, \boldsymbol{\mathcal{L}}^{\Omega_D}_{w_n}(\boldsymbol{v_n}) \rangle_{\Omega_D}) \\ A' = \eta_D(\frac{1}{\epsilon_0^2}\|\boldsymbol{v_n}\|^2_{\Omega_D} - \frac{2}{\epsilon_0^2}\langle \boldsymbol{v_n}, \kappa_{n-1}\boldsymbol{v_n} \rangle_{\Omega_D} + \frac{1}{\epsilon_0^2}\|\kappa_{n-1}\boldsymbol{v_n}\|^2_{\Omega_D} - \frac{2}{\epsilon_0}\langle \boldsymbol{v_n}, \boldsymbol{\mathcal{L}}^{\Omega_D}_{\kappa_{n-1}}(\boldsymbol{v_n}) \rangle_{\Omega_D} \\ + \frac{2}{\epsilon_0}\mathrm{Re}\, \langle \kappa_{n-1}\boldsymbol{v}, \boldsymbol{\mathcal{L}}^{\Omega_D}_{\kappa_{n-1}}(\boldsymbol{v_n}) \rangle_{\Omega_D} + \|\boldsymbol{\mathcal{L}}^{\Omega_D}_{\kappa_{n-1}}(\boldsymbol{v_n})\|^2_{\Omega_D}) \\ B' = \eta_D(\frac{1}{\epsilon_0^2}\|w_n \boldsymbol{D_{n-1}}\|^2_{\Omega_D} + \frac{2}{\epsilon_0}\mathrm{Re}\, \langle w_n \boldsymbol{D_{n-1}}, \boldsymbol{\mathcal{L}}^{\Omega_D}_{w_n}(\boldsymbol{D_{n-1}}) \rangle_{\Omega_D} + \|\boldsymbol{\mathcal{L}}^{\Omega_D}_{w_n}(\boldsymbol{D_{n-1}})\|^2_{\Omega_D}) \\ C' = \eta_D(\frac{1}{\epsilon_0^2}\|w_n \boldsymbol{v_n}\|^2_{\Omega_D} + \frac{2}{\epsilon_0}\mathrm{Re}\, \langle w_n \boldsymbol{v_n}, \boldsymbol{\mathcal{L}}^{\Omega_D}_{w_n}(\boldsymbol{v_n}) \rangle_{\Omega_D} + \|\boldsymbol{\mathcal{L}}^{\Omega_D}_{w_n}(\boldsymbol{v_n})\|^2_{\Omega_D}) \\ D' = \eta_D \|\boldsymbol{f_{n-1}}\|^2_{\Omega_D} \\ E' = \eta_D(\frac{2}{\epsilon_0^2}\langle w_n \boldsymbol{D_{n-1}}, w_n \boldsymbol{v_n} \rangle_{\Omega_D} + \frac{2}{\epsilon_0}\langle w_n \boldsymbol{v_n}, \boldsymbol{\mathcal{L}}^{\Omega_D}_{w_n}(\boldsymbol{D_{n-1}}) \rangle_{\Omega_D} \\ + \frac{2}{\epsilon_0}\mathrm{Re}\, \langle w_n \boldsymbol{D_{n-1}}, \boldsymbol{\mathcal{L}}^{\Omega_D}_{w_n}(\boldsymbol{v_n}) \rangle_{\Omega_D} + 2\mathrm{Re}\, \langle \boldsymbol{\mathcal{L}}^{\Omega_D}_{w_n}(\boldsymbol{D_{n-1}}), \boldsymbol{\mathcal{L}}^{\Omega_D}_{w_n}(\boldsymbol{v_n}) \rangle_{\Omega_D}) \\ F' = \eta_D(-\frac{2}{\epsilon_0^2}\mathrm{Re}\, \langle \boldsymbol{v_n}, w_n \boldsymbol{v_n} \rangle_{\Omega_D} + \frac{2}{\epsilon_0^2}\langle \kappa_{n-1}\boldsymbol{v_{n-1}}, w_n \boldsymbol{v} \rangle_{\Omega_D} \\ + \frac{2}{\epsilon_0}\mathrm{Re}\, \langle w_n \boldsymbol{v_n}, \boldsymbol{\mathcal{L}}^{\Omega_D}_{\kappa_{n-1}}(\boldsymbol{v_n}) \rangle_{\Omega_D} - \frac{2}{\epsilon_0}\mathrm{Re}\, \langle \boldsymbol{v_n}, \boldsymbol{\mathcal{L}}^{\Omega_D}_{w_n}(\boldsymbol{v_n}) \rangle_{\Omega_D} \\ + \frac{2}{\epsilon_0}\mathrm{Re}\, \langle \kappa_{n-1}\boldsymbol{v_{n-1}}, \boldsymbol{\mathcal{L}}^{\Omega_D}_{w_n}(\boldsymbol{v_n}) \rangle_{\Omega_D} + 2\mathrm{Re}\, \langle \boldsymbol{\mathcal{L}}^{\Omega_D}_{\kappa_{n-1}}(\boldsymbol{v_n}), \boldsymbol{\mathcal{L}}^{\Omega_D}_{w_n}(\boldsymbol{v_n}) \rangle_{\Omega_D}). \end{cases} \tag{4.104}$$

The two above-mentioned equations (eq. (4.101) and eq. (4.103)) in α_n^D and α_n^κ should be simultaneously minimized to obtain α_n^D and α_n^κ. This system is nonlinear, not as in the CSI method (eq. (4.71)). However, since the equations are scalar, the system can be solved using a standard nonlinear conjugate gradient method.

4.3.5 Initialization of the Electric Flux Inversion Method

The EFI is initialized similarly to the D-VIE based Born iterative method (section 4.2.5) and the DVIE-based Newton-Kantorovich method (section 4.2.6).

4.3.6 Summary of the Algorithm

The overall electric flux inversion algorithm is provided in Algorithm 4.

Algorithm 4: Electric Flux Inversion

n = 0;
Compute η_D and η_S ;
Assume that the unknown dielectric contrast κ is small enough so that $\boldsymbol{D_0} \approx \epsilon_0 \boldsymbol{E}_i$ for $\boldsymbol{r} \in \Omega_D$;
Solve $\boldsymbol{E_s}(\boldsymbol{r}) = \boldsymbol{\mathcal{L}}_{\boldsymbol{D_0}}^{\Omega_D}(\kappa_0)$ for κ_0;
Init F_0;
while $F_n > tolerance$ **do**
    n=n+1;
    Compute the gradients g_n^κ and $\boldsymbol{g_n^D}$ using eq. (4.89) and eq. (4.85);
    Compute the update directions w_n and $\boldsymbol{v_n}$ from eq. (4.91) and eq. (4.94);
    Compute the weights α^κ and α^D by simultenaously solving eq. (4.101) and eq. (4.103) ;
    Update the electric flux as $\boldsymbol{D_n} = \boldsymbol{D_{n-1}} + \alpha^D \boldsymbol{v_n}$;
    Update the dielectric contrast as $\kappa_n = \kappa_{n-1} + \alpha^\kappa w_n$;
    Update the residuals $\boldsymbol{f_n}$ and $\boldsymbol{\rho_n}$ using eq. (4.99) and eq. (4.98);
    Update F_n;
end

4.3.7 Discretization of the EFI

The EFI follows the same discretization procedure as the Born iterative method, which is presented in section 4.2.5.1.

4.4 Numerical Results

This section provides a numerical comparison of the new EFI with the other inverse scattering algorithms introduced above.

In this numerical example, the inverse scattering scheme should localize a cube in an unknown domain. The domain is of size 0.67λ by 0.67λ by 0.67λ and is divided into 216 cubes as shown in fig. 4.2. Each cube is made of 6 tetrahedra since the formulations used in the inverse scattering schemes (J-VIE and D-VIE) are here discretized on a tetrahedral mesh. The total number of tetrahedra in the mesh used in the inverse schemes is 1296. The cube to localize has a size of 0.22λ by 0.22λ by 0.22λ and a relative permittivity 1.5 and is illustrated in fig. 4.3. The unknown domain is illuminated by 100 antennas (point dipoles) emitting in two orthogonal directions tangent to Γ_S. The antennas are also acting as receivers. The measured data (scattered electric field) is synthetic, is generated by the forward solver associated to the inverse scheme: the D-VIE for the BIM, NKM, and EFI schemes and the J-VIE for the CSI scheme. In the first experiment the mesh used to generate the data is the same as the mesh used in the inverse scattering scheme. Note that this way of generating data, commonly referred to as inverse crime [58], is too optimistic when testing an inverse scattering scheme. In the following we provide additional numerical results in which this problem is avoided by using a different mesh to generate the data.

From fig. 4.4a and fig. 4.4b we can see that the permittivity profile of the reconstructed domain is close to the one of the real one, i.e. the target object is correctly localized. Figure 4.5 provides the convergence of the data and the state cost functionals (errors) of the EFI inverse scheme. We observe that the convergence is smooth and that as expected both the data equation and the state equation errors are minimized simultaneously. Now that the proper behavior of the EFI has been presented, we compare its convergence to the other inverse scattering schemes (BIM, NKM, and CSI). Figure 4.6 shows the relative error on the permittivity profile of the reconstructed object with respect to the number of iterations for all the methods. Note that the relative error between the reconstructed permittivity ϵ_n at step n and the target permittivity ϵ_{target} is calculated as

$$E_{\epsilon,n} = \frac{\|\epsilon_n - \epsilon_{\text{target}}\|}{\|\epsilon_{\text{target}}\|}, \tag{4.105}$$

and that the relative error tolerance is set to 0.03. It can be observed that the algorithms are all converging to this tolerance but not at the same speed.

To illustrate the performance of the algorithms in a scenario which does not correspond to an inverse crime, another numerical test was performed using different discretized geometries to generate the synthetic data. The convergence of the IS methods in that case is illustrated in fig. 4.7. While the convergence of the gradient based methods (EFI and CSI) is weakly affected by these "noisy" data,

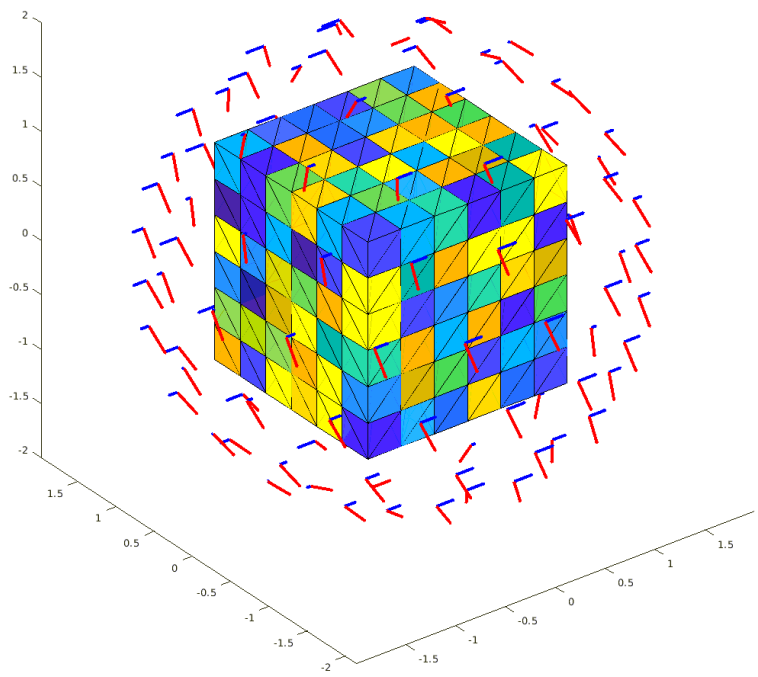

Figure 4.2: Domain to be imaged (Ω_D) surrounded by 100 antennas (point dipoles) tangent to Γ_S located at 0.8λ from the origin.

the Born iterative methods were significantly perturbed and could not converge to the tolerance.

Subsequently, it should be noted that since the computational complexity of one iteration differs depending on the inverse scattering scheme employed, the convergence of the different algorithms provided in fig. 4.6 and fig. 4.7 does not reflect accurately the computational efficiency of the schemes. To make a comparison that is more fair, the total number of matrix-vector products (MVP) between the discretized operators and the unknowns quantities of the state equation are compared in the following. Here only the MVPs with the state equation operators are considered since they represent the highest computational cost in all the IS problems. Also, note that the MVPs with Gram matrices are not counted since the Gram matrix is naturally sparse and represents a negligible cost. The BIM and the NKM require solving 1 and 2 forward problems per iteration, respectively. The forward problem is solved with a linear iterative method, here the conjugate gradient (CG) method, that has to perform MVPs to reach the desired error tolerance. This number of iterations depends on the condition number (see section 2.4) and the tolerance. In the numerical experiments that led to those results, it was observed that the average number of iterations to reach a relative error tolerance of 10^{-6} was around 20. Thus in the following, the number of MVPs per iteration in the

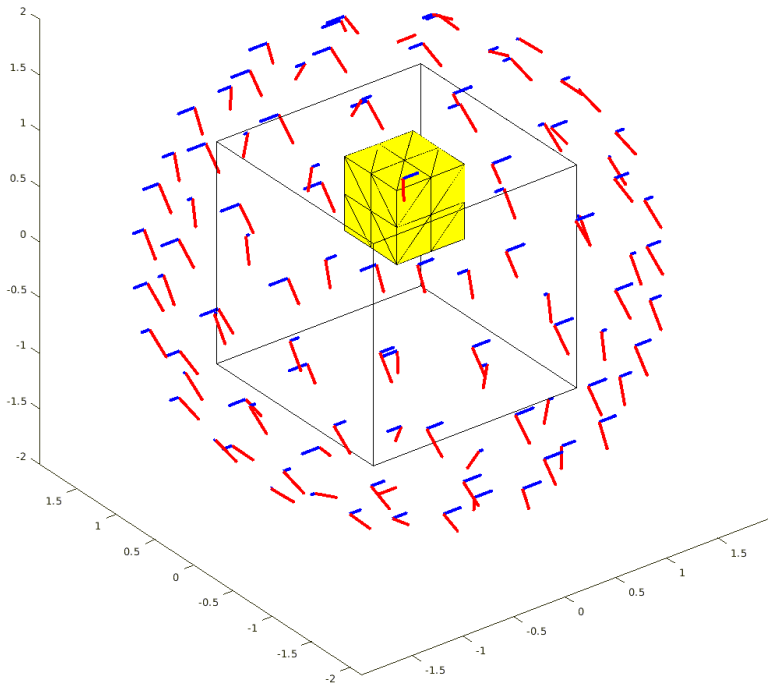

Figure 4.3: Object of relative permittivity 1.5 and size 0.22λ by 0.22λ by 0.22λ and located in Ω_D to be imaged.

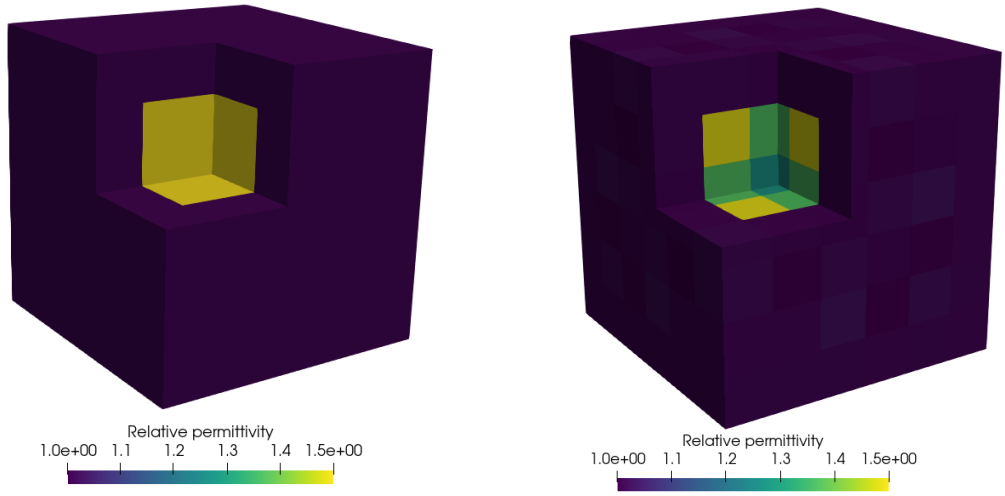

(a) (b)

Figure 4.4: (a)Target permittivity profile. (b) Reconstructed permittivity profile with the EFI.

BIM and NKM are respectively 20 and 40. In the case of the EFI, there are 6

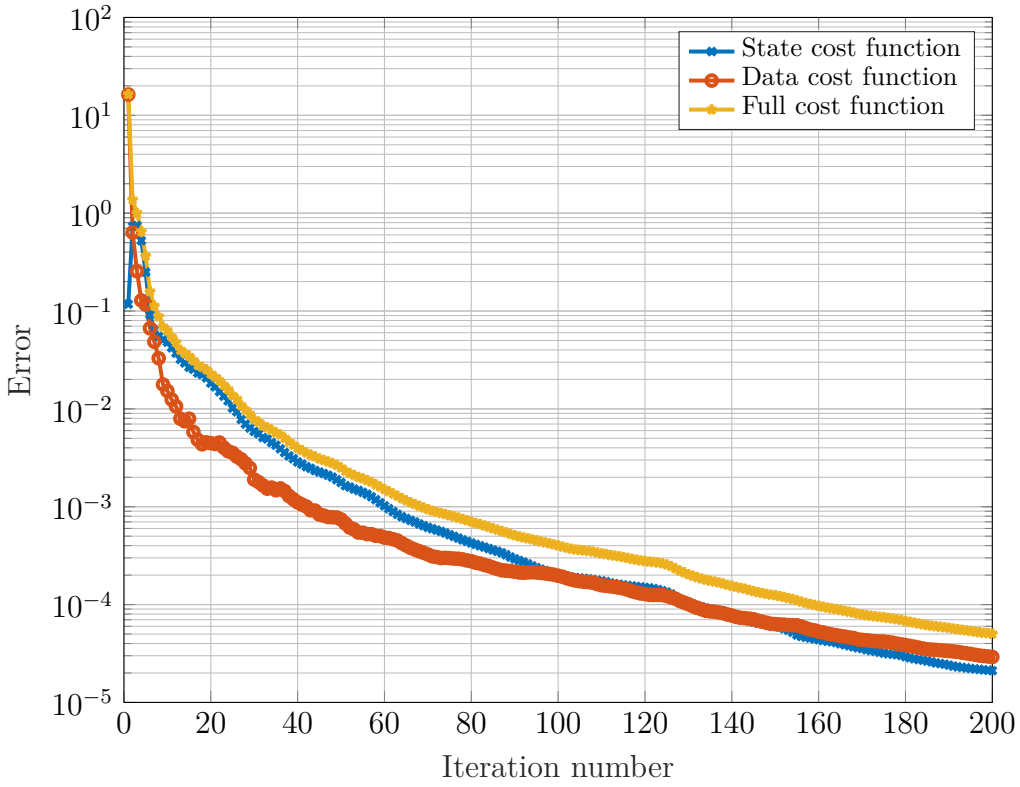

Figure 4.5: Convergence of the data and state equations in the EFI.

MVPs per iteration that are required to compute the gradients and the weights. They arise from the following mappings ($\boldsymbol{\mathcal{L}}^{\Omega_D}_{\kappa_{n-1}}\boldsymbol{D_{n-1}}$, $\boldsymbol{\mathcal{L}}^{\Omega_D}_{\kappa_{n-1}}\boldsymbol{v_n}$, $\boldsymbol{\mathcal{L}}^{\Omega_D}_{w_n}\boldsymbol{D_{n-1}}$, $\boldsymbol{\mathcal{L}}^{\Omega_D}_{w_n}\boldsymbol{v_n}$, $\boldsymbol{\mathcal{L}}^{\Omega_D}_{\boldsymbol{D_{n-1}}}{}^{\star}\boldsymbol{f_{n-1}}$, $\boldsymbol{\mathcal{L}}^{\Omega_D}_{\kappa_{n-1}}{}^{\star}\boldsymbol{f_{n-1}}$). In CSI, there are only two MVPs needed per iterations, they originate from $\boldsymbol{\mathcal{L}}^{\star}_{\Omega_D}\boldsymbol{f_{n-1}}$ and $\boldsymbol{\mathcal{L}}_{\Omega_D}\boldsymbol{v_n}$. The resulting number of MVPs to reach the desired tolerance in the numerical results provided in fig. 4.6 and fig. 4.7 are reported in table 4.1. It can be observed that the EFI method compares to the other methods in terms of efficiency when the same mesh is employed to generate the data and that its convergence (in this scenario) is not deteriorated when a different mesh is used. Note that, while giving the total number of MVPs is more accurate than simply observing the number of iterations, some other considerations should be taken to provide a better estimate for the computational efficiency of these algorithms (e.g. number of unknowns, time for one MVP).

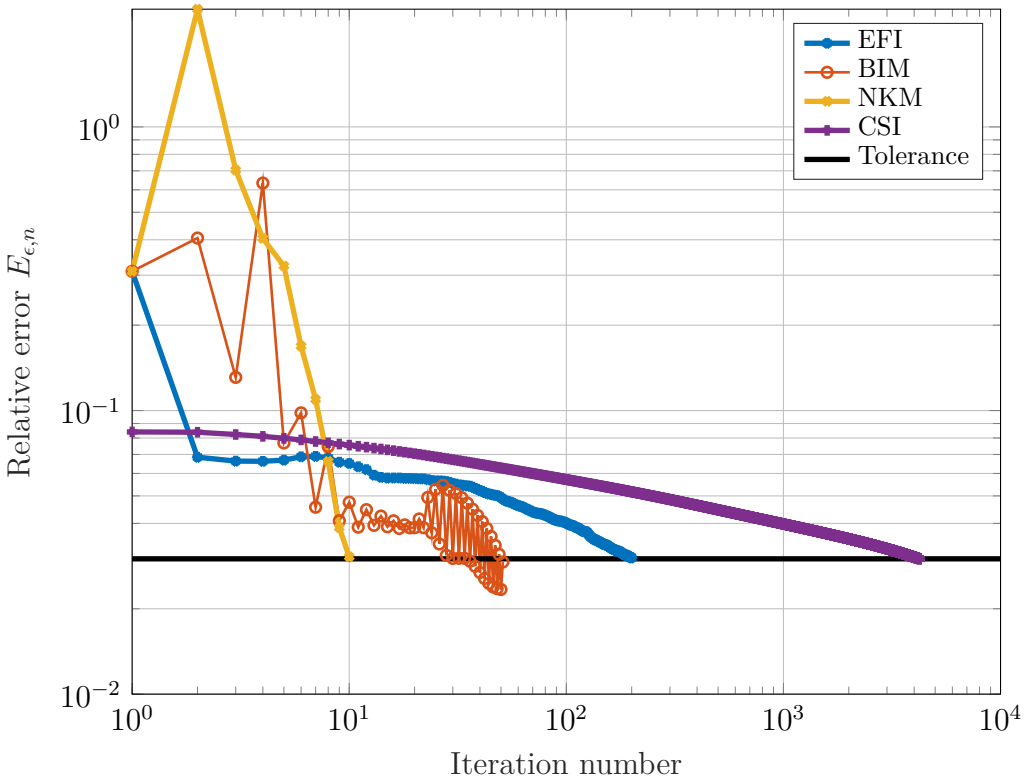

Figure 4.6: Relative error between the permittivity obtained and the target permittivity versus the number of iterations for the electric flux inversion (EFI), the Born iterative method (BIM), the Newton-Kantorovich method (NKM), and the contrast source inversion (CSI). Case in which the same mesh is employed to generate the synthetic data (inverse crime).

Table 4.1: Comparison of the total number of matrix vector products (MVP) required for the convergence of EFI, CSI, BIM, and NKM using the same mesh to generate the synthetic data ($\boldsymbol{E_s}$) and using a different mesh ($\tilde{\boldsymbol{E}}_{\boldsymbol{s}}$).

Method	Num. of MVPs/iter.	Num. of iter. ($\boldsymbol{E_s}$,$\tilde{\boldsymbol{E}}_{\boldsymbol{s}}$)	Tot. num. of MVPs ($\boldsymbol{E_s}$,$\tilde{\boldsymbol{E}}_{\boldsymbol{s}}$)
EFI	6	(200,213)	(1200,1278)
CSI	2	(4122,4928)	(8244,9856)
BIM	20	(51,no convergence)	(1020,no convergence)
NKM	40	(10,no convergence)	(400,no convergence)

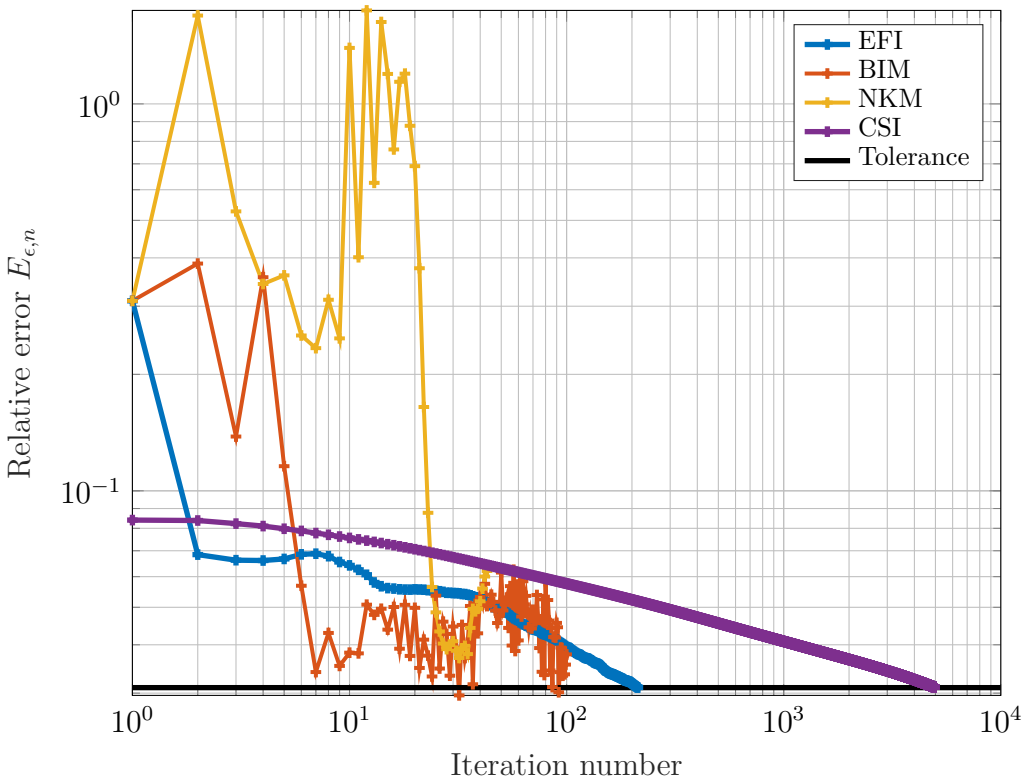

Figure 4.7: Relative error between the permittivity obtained and the target permittivity versus the number of iterations for the electric flux inverse (EFI), the Born iterative method (BIM), the Newton-Kantorovich method (NKM), and the contrast source inversion (CSI). The synthetic data was generated with a different mesh in that case.

4.5 Conclusion and Future Work

A new D-VIE inverse scattering scheme has been introduced for imaging unknown objects in the frequency domain. It was compared to existing standard inverse scattering techniques such as the Born iterative method, the Newton-Kantorovich method, and the contrast source inversion method. In the two numercal scenarios, the EFI method successfully reconstructed the permittivity profile. Further research is needed to theoretically determine the convergence rate of this algorithm and apply it to more challenging bioelectromagnetic scenarios. The latter can be done by accelerating the discretized D-VIE with the fast multipole method (FMM) or the adaptive cross approximation (ACA) and by adding regularization techniques to the electric flux inversion method that are specifically tailored for the application it is applied to.

Chapter 5

Inverse Design of a Lensed Antenna Enabling EEG Recordings in the Presence of a RF Source

Inverse electromagnetic design is the process that consists in determining some geometric and electromagnetic properties of a source so that it radiates the desired field. This chapter presents a new scheme for the inverse synthesis of a lensed antenna enabling the reconstruction of the field radiated by a phone in the the presence of electroencephalography (EEG) caps. The source obtained from this procedure paves the way to a more realistic study of the impact of a radio frequency (RF) source on brain activity.

5.1 Introduction

From telecommunication to medical devices, sources radiating electromagnetic waves extensively spread in society. It is thus important to understand precisely their effect on human health. One field of study that received a lot of attention with the spreading of mobile phones is the quantification of the penetration of electromagnetic waves in the human brain, which enables a better evaluation of the risk of ionization in human tissues. The electromagnetic power due to electromagnetic sources in a given area is quantified with the specific absorption rate (SAR). When conceiving a radiating device meant to be used in the vicinity of persons, the antenna should be designed so that the SAR remains below a certain limit. A comprehensive study on these limitations was performed by the international commission on non-ionizing radiation protection (ICNIRP) providing guidelines for devices operating in various frequency ranges (below 100 kHz [66] and up to

300 GHz [75]).

A less covered aspect about radio frequency (RF) sources is their possible impact on brain activity. Apart from ionization, other phenomena could occur in the brain and yield a perturbation of brain activity. The experimental research on this topic has reached conflicting conclusions. Some of the studies showed that there is an influence of RF devices on cerebral activity [29, 28, 102], while some others disagree [50, 52]. This clearly shows that that the topic is still an active field of research with several open research questions. Among them, we will address in this chapter the potential problem of electromagnetic disturbance occurring between the RF device and the system used for recording brain activity, which has been raised in [38].

As explained in the numerical results of chapter 3, the measurement of brain activity is generally done with an electroencephalography (EEG) setup which requires placing electrode caps on the scalp of the patient. Since they are metallic, the EEG caps have a shielding effect on the field radiated by the source. For this reason, a solution should be found to allow the recording of electrical signals in the brain from an EEG device, in the presence of an RF source. In this way, the impact of an RF source on the cerebral activity could be better investigated.

In this chapter, a new type of source is designed for the reconstruction of the original field distribution radiated by the RF source in the brain while recording the brain activity with an EEG setup. In other words, the goal is to synthesize a source able to radiate a pre-deformed field that compensates for the interference between the EEG caps and the head. Inverse design algorithms are particularly suitable for solving problems involving field reconstruction [81, 80, 56]. For this reason, this field reconstruction problem is reformulated as an inverse scattering problem, thus allowing the use of the new IS algorithm presented in chapter 4 as a basis for a synthesis framework that optimizes both the dielectric properties of a lens and the coefficients of an array of dipoles.

The chapter is divided as follows: the general framework for computational modeling of the lens, the dipole array, the head, and the EEG caps is first introduced in section 5.2. Then, section 5.3 presents the new inverse synthesis algorithm employed for the reconstruction of the field in the presence of the EEG electrodes. Finally the new framework is tested in a canonical numerical scenario section 5.4.

5.2 Background and Notations

5.2.1 Modeling of the EEG caps, the Head, and the Lens

This section provides the modeling of the head covered with EEG caps and the lens used in the reconstruction together with the mutual interactions occurring between them. The requirements for the solver are to model the metallic EEG

caps and the head, which can be considered as PEC surfaces and as an inhomogeneous lossy dielectric material, respectively. The solver chosen is based on a hybrid volume-surface integral equation (HVSIE). It combines a surface integral equation (EFIE) to model the PEC objects and a volume integral equation (D-VIE) to model inhomogeneous bodies. Note that the lens is also modeled using the D-VIE. To avoid reconstructing the field too near the EEG caps where the reconstruction would be too cumbersome due to the shielding of the electrodes, the head volume is divided into two parts: a part where the field should be reconstructed $\Omega_{\tilde{H}}$ in the presence of the electrodes and a complementary part in the head where the reconstruction is not needed Ω_H (see fig. 5.1). Following section 2.2.5 and the notations provided in fig. 5.1 for the unknowns and the domains, the system composed of the head, the lens, and the EEG caps can be described with the following equations.

5.2.1.1 Integral formulation describing the whole system

The volume integral equation in Ω_H can be expressed as

$$\frac{\boldsymbol{J}_v(\boldsymbol{r})}{j\omega\epsilon_h(\boldsymbol{r})} = \boldsymbol{E}_s^l(\boldsymbol{D}_l) + \boldsymbol{E}_s^v(\boldsymbol{J}_v) + \boldsymbol{E}_s^{\tilde{v}}(\boldsymbol{J}_{\tilde{v}}) + \boldsymbol{E}_s^s(\boldsymbol{J}_s) + \boldsymbol{E}_i(\boldsymbol{J}_i), \quad \boldsymbol{r} \in \Omega_H \tag{5.1}$$

in which ϵ_h is the permittivity of the head and $\boldsymbol{E}_i$ is the field radiated by the array of dipoles. The volume integral equation in $\Omega_{\tilde{H}}$ can be expressed as

$$\frac{\boldsymbol{J}_{\tilde{v}}(\boldsymbol{r})}{j\omega\epsilon_h(\boldsymbol{r})} = \boldsymbol{E}_s^l(\boldsymbol{D}_l) + \boldsymbol{E}_s^v(\boldsymbol{J}_v) + \boldsymbol{E}_s^{\tilde{v}}(\boldsymbol{J}_{\tilde{v}}) + \boldsymbol{E}_s^s(\boldsymbol{J}_s) + \boldsymbol{E}_i(\boldsymbol{J}_i), \quad \boldsymbol{r} \in \Omega_{\tilde{H}}. \tag{5.2}$$

The surface integral equation on Γ_C can be expressed as

$$\begin{aligned} -\hat{\boldsymbol{n}} \times \boldsymbol{E}_i(\boldsymbol{J}_i) = \hat{\boldsymbol{n}} \times \boldsymbol{E}_s^l(\boldsymbol{D}_l) + \hat{\boldsymbol{n}} \times \boldsymbol{E}_s^v(\boldsymbol{J}_v) \\ + \hat{\boldsymbol{n}} \times \boldsymbol{E}_s^{\tilde{v}}(\boldsymbol{J}_{\tilde{v}}) + \hat{\boldsymbol{n}} \times \boldsymbol{E}_s^s(\boldsymbol{J}_s), \quad \boldsymbol{r} \in \Gamma_C. \end{aligned} \tag{5.3}$$

The volume integral equation in Ω_L can be expressed as

$$\frac{\boldsymbol{D}_l(\boldsymbol{r})}{\epsilon_l(\boldsymbol{r})} = \boldsymbol{E}_s^l(\boldsymbol{D}_l) + \boldsymbol{E}_s^v(\boldsymbol{J}_v) + \boldsymbol{E}_s^{\tilde{v}}(\boldsymbol{J}_{\tilde{v}}) + \boldsymbol{E}_s^s(\boldsymbol{J}_s) + \boldsymbol{E}_i(\boldsymbol{J}_i), \quad \boldsymbol{r} \in \Omega_L \tag{5.4}$$

in which ϵ_l is the permittivity of the lens. The scattered fields used in eq. (5.1), eq. (5.2), eq. (5.3), and eq. (5.4) are defined as

$$\boldsymbol{E}_s^v(\boldsymbol{J}_v(\boldsymbol{r}')) = -jk_0\eta_0\boldsymbol{\mathcal{T}}_A^{\kappa,\Omega_H}(\boldsymbol{J}_v(\boldsymbol{r}')) + \frac{\eta_0}{jk_0}\boldsymbol{\mathcal{T}}_\Phi^{\kappa,\Omega_H}(\boldsymbol{J}_v(\boldsymbol{r}')) = \frac{\eta_0}{jk_0}\boldsymbol{\mathcal{L}}_\kappa^{\Omega_H}(\boldsymbol{J}_v(\boldsymbol{r}')), \tag{5.5}$$

$$\boldsymbol{E}_s^{\tilde{v}}(\boldsymbol{J}_{\tilde{v}}(\boldsymbol{r}')) = -jk_0\eta_0\boldsymbol{\mathcal{T}}_A^{\kappa,\Omega_{\tilde{H}}}(\boldsymbol{J}_{\tilde{v}}(\boldsymbol{r}')) + \frac{\eta_0}{jk_0}\boldsymbol{\mathcal{T}}_\Phi^{\kappa,\Omega_{\tilde{H}}}(\boldsymbol{J}_{\tilde{v}}(\boldsymbol{r}')) = \frac{\eta_0}{jk_0}\boldsymbol{\mathcal{L}}_\kappa^{\Omega_{\tilde{H}}}(\boldsymbol{J}_{\tilde{v}}(\boldsymbol{r}')), \tag{5.6}$$

$$\boldsymbol{E}_s^s(\boldsymbol{J}_s(\boldsymbol{r}')) = -j\eta_0 k_0 \left(\boldsymbol{\mathcal{T}}_A^{\Gamma_C}\boldsymbol{J}_s(\boldsymbol{r}')\right) + \frac{\eta_0}{jk_0}\left(\boldsymbol{\mathcal{T}}_\Phi^{\Gamma_C}\boldsymbol{J}_s(\boldsymbol{r}')\right) = \frac{\eta_0}{jk_0}\boldsymbol{\mathcal{L}}_{\Gamma_C}(\boldsymbol{J}_s(\boldsymbol{r}')), \tag{5.7}$$

$$\boldsymbol{E}_s^l(\boldsymbol{D}_l(\boldsymbol{r}')) = \frac{k_0^2}{\epsilon_0}\boldsymbol{\mathcal{T}}_A^{\kappa,\Omega_L}(\boldsymbol{D}_l(\boldsymbol{r}')) + \frac{1}{\epsilon_0}\boldsymbol{\mathcal{T}}_\Phi^{\kappa,\Omega_L}(\boldsymbol{D}_l(\boldsymbol{r}')) = \boldsymbol{\mathcal{L}}_\kappa^{\Omega_L}(\boldsymbol{D}_l(\boldsymbol{r}')). \tag{5.8}$$

in which $\boldsymbol{r}'$ lies in Ω_H, $\Omega_{\tilde{H}}$, Γ_C, and Ω_L, respectively.

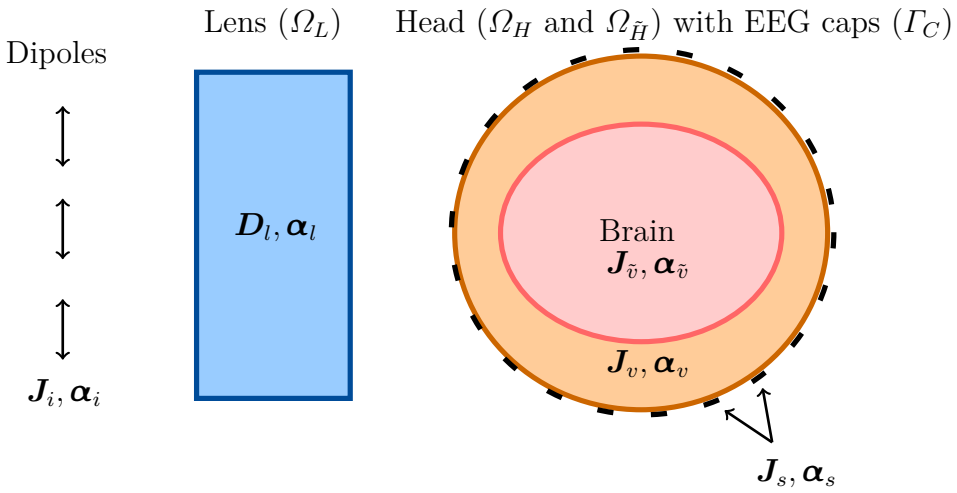

Figure 5.1: Volume and surface definitions, continuous ($\boldsymbol{J}_i$, $\boldsymbol{D}_l$, $\boldsymbol{J}_v$, and $\boldsymbol{J}_s$) and discretized ($\boldsymbol{\alpha}_i$, $\boldsymbol{\alpha}_l$, $\boldsymbol{\alpha}_v$, and $\boldsymbol{\alpha}_s$) unknowns and continuous ($\boldsymbol{J}_{\tilde{v}}$) and discretized ($\boldsymbol{\alpha}_{\tilde{v}}$) known quantities (zone where the field is reconstructed).

5.2.1.2 Field Radiated by an Array of Dipoles

Electric point dipoles are employed for the field reconstruction. The field radiated by such a dipole at position $\boldsymbol{r}$ in free space reads

$$\boldsymbol{E}_{\boldsymbol{i},\mathrm{dip}}(\boldsymbol{r}) = \left(\boldsymbol{\mathcal{T}}_i \boldsymbol{J}_{\boldsymbol{i},\mathrm{dip}}\right)(\boldsymbol{r}) = \left(\boldsymbol{\mathcal{T}}'_{\Phi} \boldsymbol{J}_{\boldsymbol{i},\mathrm{dip}}\right)(\boldsymbol{r}) + \left(\boldsymbol{\mathcal{T}}'_{A} \boldsymbol{J}_{\boldsymbol{i},\mathrm{dip}}\right)(\boldsymbol{r}), \tag{5.9}$$

where $\boldsymbol{\mathcal{T}}_i = \boldsymbol{\mathcal{T}}'_A + \boldsymbol{\mathcal{T}}'_{\Phi}$, with

$$\boldsymbol{\mathcal{T}}'_A \boldsymbol{J}_{\boldsymbol{i},\mathrm{dip}} = -jk_0\eta_0 \int_{\Omega} G_0(\boldsymbol{r},\boldsymbol{r}') \boldsymbol{J}_{\boldsymbol{i},\mathrm{dip}}(\boldsymbol{r}',\boldsymbol{r}_0)\,\mathrm{d}v', \tag{5.10}$$

$$\boldsymbol{\mathcal{T}}'_{\Phi} \boldsymbol{J}_{\boldsymbol{i},\mathrm{dip}} = \frac{\eta_0}{jk_0} \nabla \int_{\Omega} G_0(\boldsymbol{r},\boldsymbol{r}') \nabla' \cdot \boldsymbol{J}_{\boldsymbol{i},\mathrm{dip}}(\boldsymbol{r}',\boldsymbol{r}_0)\,\mathrm{d}v', \tag{5.11}$$

$\boldsymbol{r}' \in \mathbb{R}^3$, and $\boldsymbol{J}_{i,\mathrm{dip}}(\boldsymbol{r}',\boldsymbol{r}_0) = j\omega\delta^{(3)}(\boldsymbol{r}'-\boldsymbol{r}_0)\boldsymbol{p}$ is the current dipole with $\delta^{(3)}$, $\boldsymbol{p}$, and $\boldsymbol{r_0}$ being the Dirac delta function, the dipole moment, and the dipole position, respectively. The total current of an array of N dipoles is defined as $\boldsymbol{J}_i(\boldsymbol{r}) = \sum_{m=1}^{N} [\boldsymbol{\alpha}_i]_m \boldsymbol{f}^i_{\boldsymbol{m}}(\boldsymbol{r})$ in which $[\boldsymbol{\alpha}_i]_m$ is the coefficient of dipole m and $\boldsymbol{f}^i_{\boldsymbol{m}}(\boldsymbol{r}) = j\omega\delta^{(3)}(\boldsymbol{r}-\boldsymbol{r}_{0,m})\boldsymbol{p_m}$ with $\boldsymbol{r}_{0,m}$ and $\boldsymbol{p_m}$ being the position and moment of dipole m, respectively. Then, the total electric field radiated by the dipole array reads

$$\boldsymbol{E}_i(\boldsymbol{r}) = \boldsymbol{\mathcal{T}}_i(\boldsymbol{J}_i(\boldsymbol{r}')) = \sum_{m=1}^{N} [\boldsymbol{\alpha}_i]_m \boldsymbol{\mathcal{T}}_i(\boldsymbol{f}^i_{\boldsymbol{m}}(\boldsymbol{r}')). \tag{5.12}$$

In the following this incident field operator will be tested with the basis functions defined in Ω_L, Ω_H, $\Omega_{\tilde{H}}$, and Γ_C.

5.2.1.3 Discretization of the equations

This section provides the discretization of the operators introduced above. The currents in the lens, the EEG caps, and the head are expanded as

$$\boldsymbol{D}_l(\boldsymbol{r}) \approx \sum_{m=1}^{N_l} [\boldsymbol{\alpha}_l]_m \boldsymbol{f}_{\boldsymbol{m}}^l(\boldsymbol{r}), \tag{5.13}$$

$$\boldsymbol{J}_s(\boldsymbol{r}) \approx \sum_{m=1}^{N_{mh}} [\boldsymbol{\alpha}_s]_m \boldsymbol{f}_{\boldsymbol{m}}^s(\boldsymbol{r}), \tag{5.14}$$

$$\boldsymbol{J}_v(\boldsymbol{r}) \approx \sum_{m=1}^{N_{vh}} [\boldsymbol{\alpha}_v]_m \boldsymbol{f}_{\boldsymbol{m}}^v(\boldsymbol{r}), \tag{5.15}$$

$$\boldsymbol{J}_{\tilde{v}}(\boldsymbol{r}) \approx \sum_{m=1}^{N_{\tilde{v}h}} [\boldsymbol{\alpha}_{\tilde{v}}]_m \boldsymbol{f}_{\boldsymbol{m}}^{\tilde{v}}(\boldsymbol{r}), \tag{5.16}$$

in which $\{\boldsymbol{f}_{\boldsymbol{m}}^l\}$, $\{\boldsymbol{f}_{\boldsymbol{m}}^v\}$, and $\{\boldsymbol{f}_{\boldsymbol{m}}^{\tilde{v}}\}$ are SWG basis functions defined in Ω_L, Ω_H, and $\Omega_{\tilde{H}}$, respectively, $\{\boldsymbol{f}_{\boldsymbol{m}}^s\}$ are RWG basis functions defined on Γ_C, and N_l, N_{vh}, $N_{\tilde{v}h}$, and N_{mh} are the corresponding numbers of basis functions. The discretization of the operators modeling the scattering in the head together with the EEG caps corresponds to the discretization of the hybrid VSIE introduced in section 2.3.5. It yields the following linear system

$$\boldsymbol{Z}_{\boldsymbol{H}} = \begin{bmatrix} \boldsymbol{Z}_{ss} & \boldsymbol{Z}_{vs} & \boldsymbol{Z}_{\tilde{v}s} \\ \boldsymbol{Z}_{sv} & \boldsymbol{Z}_{vv} & \boldsymbol{Z}_{\tilde{v}v} \\ \boldsymbol{Z}_{s\tilde{v}} & \boldsymbol{Z}_{v\tilde{v}} & \boldsymbol{Z}_{\tilde{v}\tilde{v}} \end{bmatrix} \begin{bmatrix} \boldsymbol{\alpha}_s \\ \boldsymbol{\alpha}_v \\ \boldsymbol{\alpha}_{\tilde{v}} \end{bmatrix} = \begin{bmatrix} \boldsymbol{v}_s \\ \boldsymbol{v}_v \\ \boldsymbol{v}_{\tilde{v}} \end{bmatrix}, \tag{5.17}$$

in which the nine blocks of $\boldsymbol{Z}_{\boldsymbol{H}}$ correspond to the interaction matrices between Ω_H, $\Omega_{\tilde{H}}$, and Γ_C and $\boldsymbol{v}_s$, $\boldsymbol{v}_v$, and $\boldsymbol{v}_{\tilde{v}}$ denote the tested incident field on Γ_C, Ω_H, and $\Omega_{\tilde{H}}$, respectively. The discretization procedure for the operators defined in the lens (Ω_L) corresponds to the non-symmetric discretization of the D-VIE formulation, which is presented in section 2.3.4. The resulting matrix is

$$[\boldsymbol{Z}_{\boldsymbol{L}}]_{nm} = \langle \boldsymbol{f}_{\boldsymbol{n}}^l, \epsilon_l^{-1} \boldsymbol{f}_{\boldsymbol{m}}^l \rangle_{\Omega_L} - \langle \boldsymbol{f}_{\boldsymbol{n}}^l, \boldsymbol{\mathcal{L}}_\kappa^{\Omega_L} \boldsymbol{f}_{\boldsymbol{m}}^l \rangle_{\Omega_L}. \tag{5.18}$$

Next the following discretized operators are introduced to describe the mutual coupling between the lens and the head covered with caps

$$[\boldsymbol{Z}_{\boldsymbol{L}s}]_{nm} = \langle \hat{\boldsymbol{n}} \times \boldsymbol{f}_{\boldsymbol{n}}^{s}, \boldsymbol{\mathcal{L}}_{\kappa}^{\Omega_L} \boldsymbol{f}_{\boldsymbol{m}}^{l} \rangle_{\Gamma_C} \tag{5.19}$$

$$[\boldsymbol{Z}_{\boldsymbol{L}v}]_{nm} = \langle \kappa \boldsymbol{f}_{\boldsymbol{n}}^{v}, \boldsymbol{\mathcal{L}}_{\kappa}^{\Omega_L} \boldsymbol{f}_{\boldsymbol{m}}^{l} \rangle_{\Omega_H} \tag{5.20}$$

$$[\boldsymbol{Z}_{\boldsymbol{L}\tilde{v}}]_{nm} = \langle \kappa \boldsymbol{f}_{\boldsymbol{n}}^{\tilde{v}}, \boldsymbol{\mathcal{L}}_{\kappa}^{\Omega_L} \boldsymbol{f}_{\boldsymbol{m}}^{l} \rangle_{\Omega_{\tilde{H}}} \tag{5.21}$$

$$[\boldsymbol{H}_{s}]_{nm} = \frac{\eta_0}{jk_0} \langle \boldsymbol{f}_{\boldsymbol{n}}^{l}, \boldsymbol{\mathcal{L}}_{\Gamma_C} \boldsymbol{f}_{\boldsymbol{m}}^{s} \rangle_{\Omega_L} \tag{5.22}$$

$$[\boldsymbol{H}_{v}]_{nm} = \frac{\eta_0}{jk_0} \langle \boldsymbol{f}_{\boldsymbol{n}}^{l}, \boldsymbol{\mathcal{L}}_{\kappa}^{\Omega_H} \boldsymbol{f}_{\boldsymbol{m}}^{v} \rangle_{\Omega_L} \tag{5.23}$$

$$[\boldsymbol{H}_{\tilde{v}}]_{nm} = \frac{\eta_0}{jk_0} \langle \boldsymbol{f}_{\boldsymbol{n}}^{l}, \boldsymbol{\mathcal{L}}_{\kappa}^{\Omega_{\tilde{H}}} \boldsymbol{f}_{\boldsymbol{m}}^{\tilde{v}} \rangle_{\Omega_L}. \tag{5.24}$$

Finally, the following matrices giving the incident field scattered by the dipole array should also be defined

$$[\boldsymbol{Z}_{\boldsymbol{I}s}]_{nm} = \langle \hat{\boldsymbol{n}} \times \boldsymbol{f}_{\boldsymbol{n}}^{s}, \boldsymbol{\mathcal{T}}_i \boldsymbol{f}_{\boldsymbol{m}}^{i} \rangle_{\Gamma_C} \tag{5.25}$$

$$[\boldsymbol{Z}_{\boldsymbol{I}v}]_{nm} = \langle \kappa \boldsymbol{f}_{\boldsymbol{n}}^{v}, \boldsymbol{\mathcal{T}}_i \boldsymbol{f}_{\boldsymbol{m}}^{i} \rangle_{\Omega_H} \tag{5.26}$$

$$[\boldsymbol{Z}_{\boldsymbol{I}\tilde{v}}]_{nm} = \langle \kappa \boldsymbol{f}_{\boldsymbol{n}}^{\tilde{v}}, \boldsymbol{\mathcal{T}}_i \boldsymbol{f}_{\boldsymbol{m}}^{i} \rangle_{\Omega_{\tilde{H}}} \tag{5.27}$$

$$[\boldsymbol{Z}_{\boldsymbol{I}l}]_{nm} = \langle \kappa \boldsymbol{f}_{\boldsymbol{n}}^{\tilde{v}}, \boldsymbol{\mathcal{T}}_i \boldsymbol{f}_{\boldsymbol{m}}^{i} \rangle_{\Omega_L}. \tag{5.28}$$

5.3 Proposed Algorithm for Field Reconstruction

In this section a new framework for the design of a lensed antenna for the reconstruction of the field radiated by an RF source in the head in the presence of EEG caps is presented. The main goal is to reduce the reconstruction error with the addition of the lens and the array of dipoles. The flowchart shown in fig. 5.2 summarizes the main steps of this scheme, which correspond to the different parts of this section.

5.3.1 Obtain the Target Field from the Initial Source

The aim of this step is to retrieve the target electric field in $\Omega_{\tilde{H}}$, that is the field radiated by the initial source in the head without EEG caps ($\Gamma_C = \varnothing$). This field should subsequently be reconstructed with the dipoles and the lens in the presence of the EEG caps. It can be obtained from eq. (5.17) by solving the following linear system

$$\begin{bmatrix} \boldsymbol{Z}_{vv} & \boldsymbol{Z}_{\tilde{v}v} \\ \boldsymbol{Z}_{v\tilde{v}} & \boldsymbol{Z}_{\tilde{v}\tilde{v}} \end{bmatrix} \begin{bmatrix} \boldsymbol{\alpha}_v \\ \boldsymbol{\alpha}_{\tilde{v}} \end{bmatrix} = \begin{bmatrix} \boldsymbol{v}_v \\ \boldsymbol{v}_{\tilde{v}} \end{bmatrix}, \tag{5.29}$$

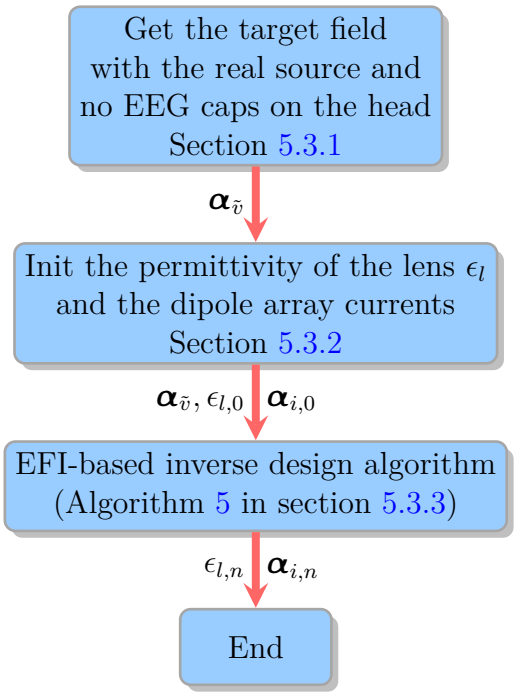

Figure 5.2: Flowchart representing the main steps to design the lens for field reconstruction.

for $\boldsymbol{\alpha}_{\tilde{v}}$. The right hand side $[\boldsymbol{v}_v,\ \boldsymbol{v}_{\tilde{v}}]^{\mathrm{T}}$ is obtained by testing the field radiated by the real source with the functions $\{\kappa \boldsymbol{f}_n^v\}$ and $\{\kappa \boldsymbol{f}_n^{\tilde{v}}\}$. Note that $\boldsymbol{\alpha}_{\tilde{v}}$ corresponds to the coefficients of the expansion of the dielectric current in $\Omega_{\tilde{H}}$, which is directly proportional to the total electric field. For this reason, $\boldsymbol{\alpha}_{\tilde{v}}$ is sometimes referred to as target field in the following.

5.3.2 Initialization of the Permittivity of the Lens and the Dipole Array Currents

The permittivity of the lens should be initialized at the beginning of the optimization procedure. One solution is to set the initial relative permittivity at 1 in all the lens, which would enable the use of the Born approximation (section 4.2.3). However, after numerical experimentation, it was observed that this initialization choice does not lead to satisfying results for the design of the lens. Instead, the starting permittivity should be determined through numerical experiments.

Next the coefficients of the dipole array should be initialized so that the error between the reconstructed field and the target field is minimized. In a first approach, it is assumed that the scattering of the head does not influence the field in the lens ($\boldsymbol{H}_s = \boldsymbol{0}$, $\boldsymbol{H}_v = \boldsymbol{0}$, and $\boldsymbol{H}_{\tilde{v}} = \boldsymbol{0}$). However, the interactions in the head and with the EEG caps are considered. The dipole coefficients $\boldsymbol{\alpha}_i$ should be then

determined such that the following matrix equation holds

$$\left[\begin{array}{ccc|c} \boldsymbol{Z}_{L} & \boldsymbol{0} & \boldsymbol{0} & \boldsymbol{0} \\ \boldsymbol{Z}_{Ls} & \boldsymbol{Z}_{ss} & \boldsymbol{Z}_{vs} & \boldsymbol{Z}_{\tilde{v}s} \\ -\boldsymbol{Z}_{Lv} & \boldsymbol{Z}_{sv} & \boldsymbol{Z}_{vv} & \boldsymbol{Z}_{\tilde{v}v} \\ \hline -\boldsymbol{Z}_{L\tilde{v}} & \boldsymbol{Z}_{s\tilde{v}} & \boldsymbol{Z}_{v\tilde{v}} & \boldsymbol{Z}_{\tilde{v}\tilde{v}} \end{array}\right] \left[\begin{array}{c} \boldsymbol{\alpha}_{l} \\ \boldsymbol{\alpha}_{s} \\ \boldsymbol{\alpha}_{v} \\ \hline \boldsymbol{\alpha}_{\tilde{v}} \end{array}\right] = \left[\begin{array}{ccc|c} & \multicolumn{2}{c}{} & \boldsymbol{0} \\ & \multicolumn{2}{c}{\boldsymbol{A}} & \boldsymbol{Z}_{\tilde{v}s} \\ & \multicolumn{2}{c}{} & \boldsymbol{Z}_{\tilde{v}v} \\ \hline -\boldsymbol{Z}_{L\tilde{v}} & \boldsymbol{Z}_{s\tilde{v}} & \boldsymbol{Z}_{v\tilde{v}} & \boldsymbol{Z}_{\tilde{v}\tilde{v}} \end{array}\right] \left[\begin{array}{c} \boldsymbol{\alpha}_{l} \\ \boldsymbol{\alpha}_{s} \\ \boldsymbol{\alpha}_{v} \\ \hline \boldsymbol{\alpha}_{\tilde{v}} \end{array}\right] = \left[\begin{array}{c} \boldsymbol{Z}_{Il}\boldsymbol{\alpha}_{i} \\ -\boldsymbol{Z}_{Is}\boldsymbol{\alpha}_{i} \\ \boldsymbol{Z}_{Iv}\boldsymbol{\alpha}_{i} \\ \hline \boldsymbol{Z}_{I\tilde{v}}\boldsymbol{\alpha}_{i} \end{array}\right]. \tag{5.30}$$

This matrix equation models scattering in the head, the EEG caps, the lens, and their mutual coupling (partly neglected here) under the excitation of the dipole array (right hand side of eq. (5.30)). The goal is to find a relation between the known target field $\boldsymbol{\alpha}_{\tilde{v}}$ and the unknown dipole coefficients $\boldsymbol{\alpha}_{i}$ which does not depend on the other unknowns ($\boldsymbol{\alpha}_{l}$, $\boldsymbol{\alpha}_{s}$, and $\boldsymbol{\alpha}_{v}$) and then specify $\boldsymbol{\alpha}_{l}$, $\boldsymbol{\alpha}_{s}$, and $\boldsymbol{\alpha}_{v}$ from the knowledge of $\boldsymbol{\alpha}_{i}$. This can be done by splitting the system matrix into a 2-by-2 block matrix as suggested in eq. (5.30). Applying the Schur complement formulas [46] on those blocks, the following relation between $\boldsymbol{\alpha}_{\tilde{v}}$ and $\boldsymbol{\alpha}_{i}$ is obtained

$$\boldsymbol{B}_{21}\begin{bmatrix} \boldsymbol{Z}_{Il} \\ \boldsymbol{Z}_{Is} \\ \boldsymbol{Z}_{Iv} \end{bmatrix}\boldsymbol{\alpha}_{i} + \boldsymbol{B}_{22}\boldsymbol{Z}_{I\tilde{v}}\boldsymbol{\alpha}_{i} = \boldsymbol{\alpha}_{\tilde{v}}, \tag{5.31}$$

in which

$$\boldsymbol{B}_{21} = -\boldsymbol{Z}_{\tilde{v}\tilde{v}}^{-1}\begin{bmatrix} -\boldsymbol{Z}_{L\tilde{v}} & \boldsymbol{Z}_{s\tilde{v}} & \boldsymbol{Z}_{v\tilde{v}} \end{bmatrix}\left(\boldsymbol{A} - \begin{bmatrix} \boldsymbol{0} \\ \boldsymbol{Z}_{\tilde{v}s} \\ \boldsymbol{Z}_{\tilde{v}v} \end{bmatrix}\boldsymbol{Z}_{\tilde{v}\tilde{v}}^{-1}\begin{bmatrix} -\boldsymbol{Z}_{L\tilde{v}} & \boldsymbol{Z}_{s\tilde{v}} & \boldsymbol{Z}_{v\tilde{v}} \end{bmatrix}\right)^{-1} \tag{5.32}$$

$$\boldsymbol{B}_{22} = \left(\boldsymbol{Z}_{\tilde{v}\tilde{v}} - \begin{bmatrix} -\boldsymbol{Z}_{L\tilde{v}} & \boldsymbol{Z}_{s\tilde{v}} & \boldsymbol{Z}_{v\tilde{v}} \end{bmatrix}\boldsymbol{A}^{-1}\begin{bmatrix} \boldsymbol{0} \\ \boldsymbol{Z}_{\tilde{v}s} \\ \boldsymbol{Z}_{\tilde{v}v} \end{bmatrix}\right)^{-1}. \tag{5.33}$$

The resulting equation (eq. (5.31)) is independent of the unknowns $\boldsymbol{\alpha}_{l}$, $\boldsymbol{\alpha}_{s}$, and $\boldsymbol{\alpha}_{v}$ and can be solved from the knowledge of the permittivity of the lens ϵ_{l} and the target field. Now that the method to initialize the permittivity of the lens and the coefficients of the dipole array is described, the next step is to introduce the scheme for reconstructing the field by simultaneously optimizing for $\boldsymbol{\alpha}_{i}$, $\boldsymbol{\alpha}_{l}$, and ϵ_{l}.

5.3.3 A New Scheme for the Design of a Lensed Antenna

In this section, the inverse scattering scheme employed for field reconstruction is presented. This iterative procedure aims at minimizing the error between the reconstructed field and the target field by simultaneously updating the dipole array coefficients and the permittivity of the lens. Here, the goal is to perform inverse scattering for a design purpose, so falling into a local minimum would not be too problematic since there is no true solution, unlike in microwave imaging (chapter 4). Note that the following derivation is performed with the continuous equations, not the discretized ones.

5.3.3.1 Data and State Equations

For this specific application, the standard inverse scattering setup presented in chapter 4 requires additional degrees of freedom that correspond to the currents in the dipole array and the unknown currents in the head. The data equation ($\boldsymbol{r} \in \Omega_{\tilde{H}}$) obtained from eq. (5.2) reads

$$\boldsymbol{E}_{\tilde{v}}(\boldsymbol{r}) = \boldsymbol{\mathcal{L}}_{\kappa}^{\Omega_L}(\boldsymbol{D}_l) + \frac{\eta_0}{jk_0}\boldsymbol{\mathcal{L}}_{\kappa}^{\Omega_H}(\boldsymbol{J}_v) + \frac{\eta_0}{jk_0}\boldsymbol{\mathcal{L}}_{\kappa}^{\Omega_H}(\boldsymbol{J}_{\tilde{v}}) + \frac{\eta_0}{jk_0}\boldsymbol{\mathcal{L}}_{\Gamma_S}(\boldsymbol{J}_s) + \boldsymbol{\mathcal{T}}_i(\boldsymbol{J}_i), \quad \boldsymbol{r} \in \Omega_{\tilde{H}} \tag{5.34}$$

in which $\boldsymbol{E}_{\tilde{v}} = \boldsymbol{J}_{\tilde{v}}/(j\omega\epsilon_h)$ is the target electric field in $\Omega_{\tilde{H}}$ and $\boldsymbol{J}_v$, $\boldsymbol{J}_s$, $\boldsymbol{J}_i$, κ (for $\boldsymbol{r} \in \Omega_L$), and $\boldsymbol{D}_l$ are the unknowns. Note that here the data equation is not be solved for the currents $\boldsymbol{J}_v$ and $\boldsymbol{J}_s$ in the head. These currents are supposed to be defined from the knowledge of $\boldsymbol{J}_i$ and $\boldsymbol{D}_l$. This idea originates from the fact that algebraically the data and the state equations in $\Omega_{\tilde{H}}$ and Ω_L can be solved for the unknowns $\boldsymbol{\alpha}_i$ and $\boldsymbol{\alpha}_l$ and then the unknown current coefficients $\boldsymbol{\alpha}_s$ and $\boldsymbol{\alpha}_v$ can simply be obtained using $\boldsymbol{\alpha}_i$, $\boldsymbol{\alpha}_l$, and the discretized equations in Ω_H and Γ_C. For instance, a similar procedure was employed to determine the dipole array coefficients in section 5.3.2. For this reason, the data equation is redefined as

$$\boldsymbol{E}_{\tilde{v}}(\boldsymbol{r}) = \tilde{\boldsymbol{\mathcal{L}}}_{\kappa}^{\Omega_L}(\boldsymbol{D}_l) + \frac{\eta_0}{jk_0}\boldsymbol{\mathcal{L}}_{\kappa}^{\Omega_H}(\boldsymbol{J}_{\tilde{v}}) + \tilde{\boldsymbol{\mathcal{T}}}_i(\boldsymbol{J}_i), \quad \boldsymbol{r} \in \Omega_{\tilde{H}} \tag{5.35}$$

in which $\tilde{\boldsymbol{\mathcal{L}}}_{\kappa}^{\Omega_L}$ and $\tilde{\boldsymbol{\mathcal{T}}}_i$ are the new operators implicitly taking into account the currents $\boldsymbol{J}_v$ and $\boldsymbol{J}_s$.

Then since fields radiated by $\boldsymbol{J}_v$, $\boldsymbol{J}_{\tilde{v}}$, and $\boldsymbol{J}_s$ in Ω_L are neglected in this chapter (as a first approach), the state equation ($\boldsymbol{r} \in \Omega_L$) can be expressed in Ω_L using eq. (5.4) as

$$\boldsymbol{\mathcal{T}}_i(\boldsymbol{J}_i) + \boldsymbol{\mathcal{L}}_{\kappa}^{\Omega_L}(\boldsymbol{D}_l) = \frac{1-\kappa}{\epsilon_0}\boldsymbol{D}_l(\boldsymbol{r}), \quad \boldsymbol{r} \in \Omega_L. \tag{5.36}$$

5.3.3.2 Residual Errors and Cost Functional

Equations (5.35) and (5.36) are solved iteratively for the unknowns $\boldsymbol{J}_i$, κ, and $\boldsymbol{D}_l$, which are updated as follows

$$\boldsymbol{D}_{\boldsymbol{l,n}} = \boldsymbol{D}_{\boldsymbol{l,n-1}} + \alpha^D \boldsymbol{v}_{\boldsymbol{n}}, \tag{5.37}$$

$$\kappa_n = \kappa_{n-1} + \alpha^{\kappa} d_n, \tag{5.38}$$

$$\boldsymbol{J}_{i,n} = \boldsymbol{J}_{\boldsymbol{i,n-1}} + \alpha^J \boldsymbol{z}_{\boldsymbol{n}}, \tag{5.39}$$

in which $\boldsymbol{v}_{\boldsymbol{n}}$, $\boldsymbol{z}_{\boldsymbol{n}}$, and d_n are the update directions derived from the gradients of the cost functional F with respect to $\boldsymbol{D}_l$, $\boldsymbol{J}_i$, and κ at step n, respectively, and α^D, α^J,

and α_κ are coefficients obtained through line minimization of F along the update directions. The goal at each iteration is to determine $\boldsymbol{v_n}$, $\boldsymbol{z_n}$, d_n, α^D, α^J, and α_κ.

To quantify the errors of the state equation (eq. (5.36)) and the data equation (eq. (5.35)) at step n, the following residual errors are defined in symbolic form

$$\boldsymbol{f_n} = \boldsymbol{\mathcal{T}}_i(\boldsymbol{J}_{i,n}) + \boldsymbol{\mathcal{L}}_{\kappa_n}^{\Omega_L}(\boldsymbol{D}_{l,n}) - \frac{1-\kappa_n}{\epsilon_0}\boldsymbol{D}_{l,n}, \tag{5.40}$$

$$\boldsymbol{\rho_n} = \boldsymbol{E}_{\tilde{v}} - \frac{\eta_0}{jk_0}\boldsymbol{\mathcal{L}}_{\kappa}^{\Omega_H}(\boldsymbol{J}_{\tilde{v}}) - \tilde{\boldsymbol{\mathcal{L}}}_{\kappa_n}^{\Omega_L}(\boldsymbol{D}_{l,n}) - \tilde{\boldsymbol{\mathcal{T}}}_i(\boldsymbol{J}_{i,n}), \tag{5.41}$$

and the resulting cost functional at step n reads

$$\begin{aligned} F_n(\kappa_n, \boldsymbol{D}_{l,n}, \boldsymbol{J}_{i,n}) &= F_{\text{data},n}(\kappa, \boldsymbol{D}_l, \boldsymbol{J}_i) + F_{\text{state},n}(\kappa, \boldsymbol{D}_l, \boldsymbol{J}_i) \\ &= \eta_S \|\boldsymbol{\rho_n}\|_{\Omega_D}^2 + \eta_D \|\boldsymbol{f_n}\|_{\Omega_L}^2, \end{aligned} \tag{5.42}$$

in which the normalization factors $\eta_{D,n}$ and η_S are defined as follows

$$\eta_{D,n} = \|\boldsymbol{\mathcal{T}}_i(\boldsymbol{J}_{i,n})\|_{\Omega_L} \tag{5.43}$$

$$\eta_S = \|\boldsymbol{E}_{\tilde{v}} - \frac{\eta_0}{jk_0}\boldsymbol{\mathcal{L}}_{\kappa}^{\Omega_H}(\boldsymbol{J}_{\tilde{v}})\|_{\Omega_{\tilde{H}}}. \tag{5.44}$$

5.3.3.3 Gradient of the Cost Functional with respect to $\boldsymbol{D}_l$, κ, and $\boldsymbol{J}_i$

The gradient of the cost functional F with respect to the electric flux $\boldsymbol{D}_l$ at step n has the same form as in eq. (4.85), it reads

$$\boldsymbol{g_n^D} = \eta_S \tilde{\boldsymbol{\mathcal{L}}}_{\kappa_{n-1}}^{\Omega_L\ \star}\boldsymbol{\rho_{n-1}} + \eta_{D,n-1}\boldsymbol{\mathcal{M}}_{\kappa_{n-1}}^{\Omega_L\ \star}\boldsymbol{f_{n-1}}, \tag{5.45}$$

in which $\boldsymbol{\mathcal{M}}_{\kappa}^{\Omega_L}\boldsymbol{D}_l = -\boldsymbol{\mathcal{L}}_{\kappa}^{\Omega_L}\boldsymbol{D}_l + \frac{1-\kappa}{\epsilon_0}\boldsymbol{D}_l$. The gradient of F with respect to κ is equal to the gradient obtained in eq. (4.89). This leads to

$$g_n^\kappa = \eta_S \tilde{\boldsymbol{\mathcal{L}}}_{\boldsymbol{D_{l,n-1}}}^{\Omega_L\ \star}(\boldsymbol{\rho_{n-1}}) - \eta_{D,n-1}\left(\boldsymbol{\mathcal{L}}_{\boldsymbol{D_{l,n-1}}}^{\Omega_L\ \star}(\boldsymbol{f_{n-1}}) - \frac{1}{\epsilon_0}\bar{\boldsymbol{D}}_{\boldsymbol{l,n-1}} \cdot \boldsymbol{f_{n-1}}\right) \tag{5.46}$$

in which $(\cdot)$ denotes the dot product between two vector functions. The gradient of F with respect to the dipole currents $\boldsymbol{J}_i$ can be obtained leveraging a Fréchet derivative of the cost functional, which gives

$$\begin{aligned} \partial F_{n-1}/\partial \boldsymbol{J}_{i,n-1} &= \lim_{\epsilon\to 0}(F(\boldsymbol{J_{i,n-1}} + \epsilon \boldsymbol{z_n}) - F(\boldsymbol{J_{i,n-1}}))/\epsilon \\ &= -2\eta_S \text{Re}\,\langle \boldsymbol{\mathcal{T}}_i^\star \boldsymbol{\rho_{n-1}}, \boldsymbol{z_n}\rangle_{\Omega_L} - 2\eta_{D,n-1}\text{Re}\,\langle \boldsymbol{\mathcal{T}}_i^\star \boldsymbol{f_{n-1}}, \boldsymbol{z_n}\rangle_{\Omega_L}. \end{aligned} \tag{5.47}$$

Note that the dependence of the normalization coefficient $\eta_{D,n-1}$ with respect to $\boldsymbol{J}_i$ was neglected in this derivation. The resulting expression for the gradient at step n is

$$\boldsymbol{g_n^J} = \eta_S \tilde{\boldsymbol{\mathcal{T}}}_i^{\ \star}\boldsymbol{\rho_{n-1}} + \eta_{D,n-1}\boldsymbol{\mathcal{T}}_i^\star \boldsymbol{f_{n-1}}. \tag{5.48}$$

5.3.3.4 Polak-Ribière Update

The new update direction w_n for the dielectric contrast is defined as

$$w_1 = g_1^\kappa, \quad n = 1 \tag{5.49}$$
$$w_n = g_n^\kappa + \gamma_n^\kappa w_{n-1}, \quad n \geq 2 \tag{5.50}$$

in which

$$\gamma_n^\kappa = \frac{\langle g_n^\kappa, g_{n-1}^\kappa \rangle_{\Omega_L}}{\|g_{n-1}^\kappa\|_{\Omega_L}^2}. \tag{5.51}$$

The update direction for the electric flux reads

$$\boldsymbol{v_1} = \boldsymbol{g_1^D}, \quad n = 1 \tag{5.52}$$
$$\boldsymbol{v_n} = \boldsymbol{g_n^D} + \gamma_n^D \boldsymbol{v_{n-1}}, \quad n \geq 2 \tag{5.53}$$

in which

$$\gamma_n^D = \frac{\langle \boldsymbol{g_n^D}, \boldsymbol{g_{n-1}^D} \rangle_{\Omega_L}}{\|\boldsymbol{g_{n-1}^D}\|_{\Omega_L}^2}, \tag{5.54}$$

and the update direction for the dipole array currents is

$$\boldsymbol{z_1} = \boldsymbol{g_1^D}, \quad n = 1 \tag{5.55}$$
$$\boldsymbol{z_n} = \boldsymbol{g_n^D} + \gamma_n^D \boldsymbol{z_{n-1}}, \quad n \geq 2 \tag{5.56}$$

in which

$$\gamma_n^J = \frac{\langle \boldsymbol{g_n^J}, \boldsymbol{g_{n-1}^J} \rangle}{\|\boldsymbol{g_{n-1}^J}\|^2}. \tag{5.57}$$

5.3.3.5 Determination of the Weights for the Minimization

In this section, the weights α^D, α^κ, and α^J are determined to minimize the cost functional at each iteration when updating the electric flux, the dielectric contrast, and dipole array coefficients. As in section 4.3.4, the first step is to expand residual errors using the expressions of $\boldsymbol{D}_{l,n}$, κ_n, and $\boldsymbol{J}_{i,n}$ (eq. (5.37), eq. (5.38), and eq. (5.39)). This results in

$$\begin{aligned}
\boldsymbol{\rho_n} &= \boldsymbol{E}_t - \tilde{\boldsymbol{\mathcal{L}}}_{\kappa_n}^{\Omega_L} \boldsymbol{D_{l,n}} - \tilde{\boldsymbol{\mathcal{T}}}_i \boldsymbol{J}_{i,n} \\
&= \boldsymbol{E}_t - (\tilde{\boldsymbol{\mathcal{L}}}_{\kappa_{n-1}}^{\Omega_L} + \alpha^\kappa \tilde{\boldsymbol{\mathcal{L}}}_{w_n}^{\Omega_L})(\boldsymbol{D_{l,n-1}} + \alpha_n^D \boldsymbol{v_n}) - \tilde{\boldsymbol{\mathcal{T}}}_i(\boldsymbol{J_{i,n-1}} + \alpha_n^J \boldsymbol{z_n}) \\
&= \boldsymbol{\rho_{n-1}} - \alpha_n^D \tilde{\boldsymbol{\mathcal{L}}}_{\kappa_{n-1}}^{\Omega_L} \boldsymbol{v_n} - \alpha_n^\kappa \tilde{\boldsymbol{\mathcal{L}}}_{w_n}^{\Omega_L} \boldsymbol{D_{l,n-1}} - \alpha_n^D \alpha_n^\kappa \tilde{\boldsymbol{\mathcal{L}}}_{w_n}^{\Omega_L} \boldsymbol{v_n} - \alpha_n^J \tilde{\boldsymbol{\mathcal{T}}}_i \boldsymbol{z_n},
\end{aligned} \tag{5.58}$$

in which $\boldsymbol{E}_t = \boldsymbol{E}_{\tilde{v}} - \frac{\eta_0}{jk_0}\boldsymbol{\mathcal{L}}_{\kappa}^{\Omega_H}(\boldsymbol{J}_{\tilde{v}})$ for the data equation and

$$\begin{aligned}
\boldsymbol{f_n} &= \boldsymbol{\mathcal{T}}_i\boldsymbol{J}_{i,n} - \frac{\eta_0}{jk_0}(\boldsymbol{\mathcal{L}}_{\kappa}^{\Omega_H}(\boldsymbol{J}_v) + \boldsymbol{\mathcal{L}}_{\kappa}^{\Omega_H}(\boldsymbol{J}_{\tilde{v}}) + \boldsymbol{\mathcal{L}}_{\Gamma_S}(\boldsymbol{J}_s)) + \boldsymbol{\mathcal{L}}_{\kappa_n}^{\Omega_L}\boldsymbol{D}_l - \frac{1-\kappa_n}{\epsilon_0}\boldsymbol{D}_l \\
&= \boldsymbol{\mathcal{T}}_i(\boldsymbol{J_{i,n-1}} + \alpha_n^J\boldsymbol{z_n}) + (\boldsymbol{\mathcal{L}}_{\kappa_{n-1}}^{\Omega_L} + \alpha^{\kappa}\boldsymbol{\mathcal{L}}_{w_n}^{\Omega_L})(\boldsymbol{D_{l,n-1}} + \alpha_n^D\boldsymbol{v_n}) \\
&- \frac{1-(\kappa_{n-1}+\alpha_n^{\kappa}w_n)}{\epsilon_0}(\boldsymbol{D_{l,n-1}} + \alpha_n^D\boldsymbol{v_n}) \\
&= \boldsymbol{f_{n-1}} + \alpha_n^J\boldsymbol{\mathcal{T}}_i\boldsymbol{z_n} + \alpha_n^D\boldsymbol{\mathcal{L}}_{\kappa_{n-1}}^{\Omega_L}\boldsymbol{v_n} + \alpha_n^{\kappa}\boldsymbol{\mathcal{L}}_{w_n}^{\Omega_L}\boldsymbol{D_{l,n-1}} + \alpha_n^{\kappa}\alpha_n^D\boldsymbol{\mathcal{L}}_{w_n}^{\Omega_L}\boldsymbol{v_n} \\
&- \frac{\alpha_n^D}{\epsilon_0}\boldsymbol{v_n} + \frac{\alpha_n^D}{\epsilon_0}\kappa_{n-1}\boldsymbol{v_n} + \frac{\alpha_n^{\kappa}}{\epsilon_0}w_n\boldsymbol{D_{l,n-1}} + \frac{\alpha_n^{\kappa}\alpha_n^D}{\epsilon_0}w_n\boldsymbol{v_n},
\end{aligned} \tag{5.59}$$

for the state equation. The next step is to substitute eq. (5.58) and eq. (5.59) into the cost functional eq. (5.42)

$$\begin{aligned}
F_n &= F_{n,\text{data}}(\kappa_n, \boldsymbol{D}_{l,n}, \boldsymbol{J}_{i,n}) + F_{n,\text{state}}(\kappa_n, \boldsymbol{D_{l,n}}, \boldsymbol{J}_{i,n}) \\
&= \eta_S\|\boldsymbol{\rho_n}\|_{\Omega_{\tilde{H}}}^2 + \eta_{D,n-1}\|\boldsymbol{f_n}\|_{\Omega_L}^2.
\end{aligned} \tag{5.60}$$

The cost functional $F_{n,\text{data}}(\kappa_n, \boldsymbol{D}_{l,n}, \boldsymbol{J}_{i,n})$ can be rearranged as

$$\begin{aligned}
F_{n,\text{data}}(\kappa_n, \boldsymbol{D}_{l,n}, \boldsymbol{J}_{i,n}) = \eta_S \Big[&\alpha_n^D a + \alpha_n^{\kappa} b + \alpha_n^u c + \alpha_n^D\alpha_n^{\kappa} d + \alpha_n^u\alpha_n^{\kappa} e + \alpha_n^u\alpha_n^D f \\
&+\alpha_n^u\alpha_n^{\kappa}\alpha_n^D g + (\alpha_n^D)^2 A + (\alpha_n^{\kappa})^2 B + (\alpha_n^u)^2 C \\
&+(\alpha_n^D\alpha_n^{\kappa})^2 D + E + \alpha_n^D(\alpha_n^{\kappa})^2 F + (\alpha_n^D)^2\alpha_n^{\kappa} G\Big],
\end{aligned} \tag{5.61}$$

where the scalar coefficients $a, b, c, d, e, f, g, A, B, C, D, E, F$, and G are provided in appendix D. Similarly the cost functional of the state equation is written as

$$\begin{aligned}
F_{n,\text{state}}(\kappa_n, \boldsymbol{D}_{l,n}, \boldsymbol{J}_{i,n}) = \eta_{D,n-1} \Big[&\alpha_n^D a' + \alpha_n^{\kappa} b' + \alpha_n^u c' + \alpha_n^D\alpha_n^{\kappa} d' + \alpha_n^u\alpha_n^{\kappa} e' + \alpha_n^u\alpha_n^D f' \\
&+\alpha_n^u\alpha_n^{\kappa}\alpha_n^D g' + (\alpha_n^D)^2 A' + (\alpha_n^{\kappa})^2 B' + (\alpha_n^u)^2 C' + (\alpha_n^D\alpha_n^{\kappa})^2 D' + E' \\
&+\alpha_n^D(\alpha_n^{\kappa})^2 F' + (\alpha_n^D)^2\alpha_n^{\kappa} G'\Big],
\end{aligned} \tag{5.62}$$

where $a', b', c', d', e', f', g', A', B', C', D', E', F'$, and G' are also given in appendix D.

Finally, the weights α^D, α^{κ}, and α^J can be obtained through the line minimization of eq. (5.61) and eq. (5.62). This system of scalar equations is nonlinear, it can be solved using a standard nonlinear conjugate gradient method. This synthesis algorithm is delineated in Algorithm 5.

5.3.4 Discretization of the EFI-Based Inverse Algorithm

This algorithm follows the same discretization procedure as the Born iterative method (section 4.2.5.1). Note that a discretized version of the operators $\tilde{\boldsymbol{\mathcal{L}}}_{\kappa}^{\Omega_L}$ and

Algorithm 5: EFI-based Inverse Design Algorithm

n=0 ;
Init $\boldsymbol{J}_{i,0}$ and $\epsilon_{l,0}$ following the algebraic procedure described in section 5.3.2;
Init $\boldsymbol{D}_{l,0}$ accordingly (eq. (5.30)) ;
Init the residuals $\boldsymbol{f_0}$ and $\boldsymbol{\rho_0}$ using eq. (5.40) and eq. (5.41);
Init $\eta_{D,0}$ and η_S using eq. (5.43) and eq. (5.44);
Init F_0;
while $F_n >$ *tolerance* **do**
    Compute the gradients g_n^κ, $\boldsymbol{g_n^D}$, and $\boldsymbol{g_n^J}$ using eq. (5.46), eq. (5.45), and eq. (5.48) ;
    Compute the Polak-Ribière update directions w_n, $\boldsymbol{v_n}$, and $\boldsymbol{z_n}$ from eq. (5.49), eq. (5.52), eq. (5.55);
    Compute the weights α_n^D, α_n^κ, and α_n^J by simultaneously minimizing eq. (5.62) and eq. (5.61);
    Update $\boldsymbol{D_{l,n}}$, κ_n, and $\boldsymbol{J}_{i,n}$ using eq. (5.37), eq. (5.38), and eq. (5.39);
    Update the residuals $\boldsymbol{f_n}$ and $\boldsymbol{\rho_n}$ using eq. (5.40) and eq. (5.41);
    Update $\eta_{D,n}$ using eq. (5.43);
    Update F_n;
    n=n+1;
end

$\tilde{\boldsymbol{\mathcal{T}}}_i$ introduced in eq. (5.35) can be obtained by leveraging the Schur complement formulas on eq. (5.30), as performed in section 5.3.2 to obtain a relation between the coefficients of the target field and the coefficients of the currents in the dipole array.

5.4 Numerical Results

The numerical results regarding the reconstruction of the electric field in the brain in the presence of EEG electrodes are provided in this section. The geometrical model employed for testing the algorithm is a homogeneous sphere of radius 10 cm and relative permittivity $40 - 15j$. The domains Ω_v and $\Omega_{\tilde{v}}$ which are introduced in section 5.2 are depicted in fig. 5.3a. The sphere is discretized with 1069 tetrahedra (see fig. 5.3a and fig. 5.3b) and is covered with 18 EEG caps that are made of triangles of the surface of the tetrahedral mesh (as shown in fig. 5.3b). The frequency used in the simulation for the real source and the reconstruction source is 0.1 GHz. The real source is a point dipole with dipole moment $\hat{\boldsymbol{z}}$ placed at 10 cm from the left side of the head. Regarding the reconstruction setup, an array of 18 dipoles is placed at 9 positions on the same plane as the real source (at each point there is a $\hat{\boldsymbol{y}}-$oriented dipole and $\hat{\boldsymbol{z}}-$oriented dipole). The lens is placed between the dipole array and the head and is discretized with 1536 tetrahedra forming 256 cubes, each cube possibly having a different permittivity. The relative permittivity of the lens is initialized at 8. The reconstruction source composed of the array of dipoles and the lens is illustrated in fig. 5.4a. In the reconstruction algorithm, the coefficients of the 18 dipoles and the permittivities of the 256 cubes are optimized to get the minimum error as possible with respect to the field originally radiated by the real source (i.e. minimum F_n in eq. (5.60)).

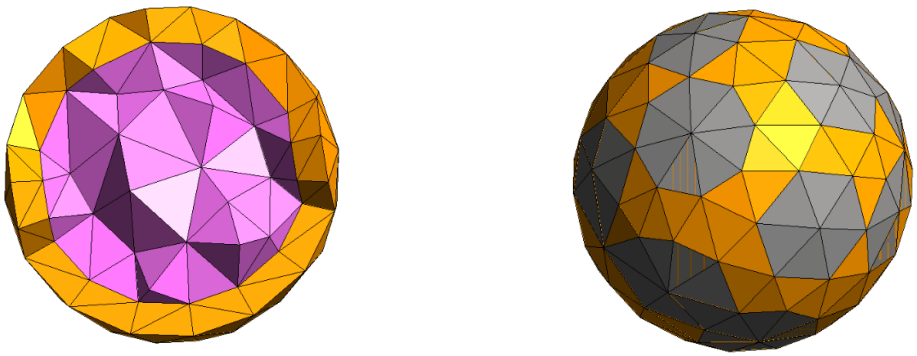

(a) (b)

Figure 5.3: (a) Cut view of the sphere showing the two layers Ω_v (orange) and $\Omega_{\tilde{v}}$ (pink). (b) 3D view of the discretized sphere covered with discretized EEG caps.

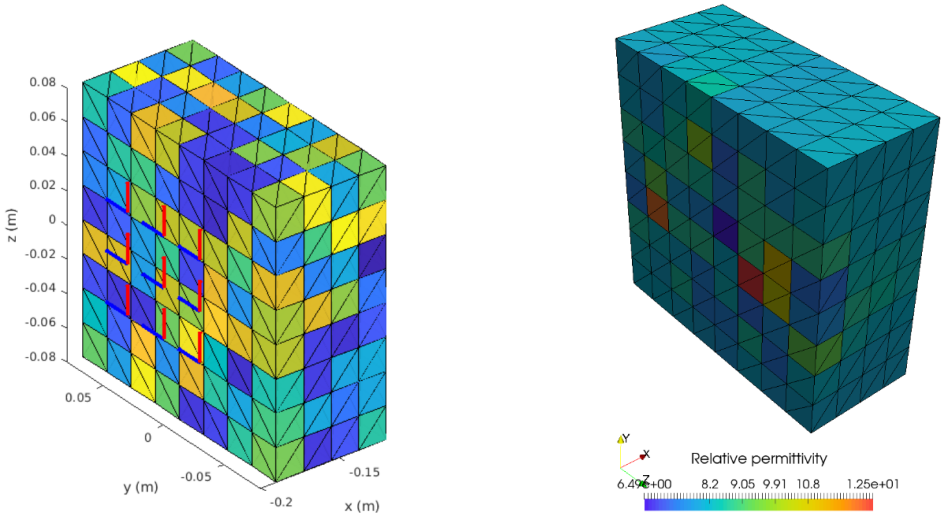

(a) (b)

Figure 5.4: (a) 3D visualization of the discretized lens and the array of 18 dipoles. (b) Permittivity profile of the synthesized lens.

The convergence of the reconstruction algorithm for the system dipole array and lens (lensed antenna) is provided (in blue) in fig. 5.6. The black horizontal line corresponds to the error on the field when no reconstruction is performed, it represents how perturbed the field is. The red line corresponds to the reconstruction error using only the dipole array. It results that the reconstruction error for the lensed antenna is converging below the errors mentioned above (black and red lines). In that case, the addition of the lens to the array of dipoles enables lowering the reconstruction error. The resulting permittivity profile of the synthesized lens is displayed in fig. 5.4b.

Finally, the relative errors between the norm of the target electric field and the norm of the fields without and with reconstruction as a function of the position in the reconstruction region are shown in figs. 5.5a and 5.5b, respectively. The proper reconstruction of the field can be clearly visualized in fig. 5.5b, especially in the region that is on the same side as the lensed antenna (i.e. left hand side).

5.5 Conclusion and Future Work

A synthesis method has been introduced for the design of a lensed antenna enabling the reconstruction of the electric field radiated by a source in the head in the presence of EEG electrodes on the scalp. This was achieved by leveraging a hybrid volume surface integral equation method together with an inverse scattering scheme applied in the context of material and source synthesis. The remaining tasks

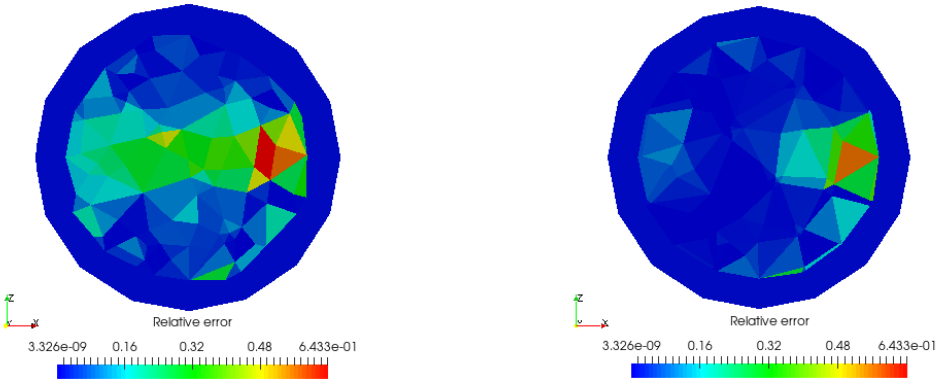

(a) (b)

Figure 5.5: Cut view of the sphere showing the relative error between the norm of the target electric field and the norm of the field obtained (a) without reconstruction and (b) with reconstruction.

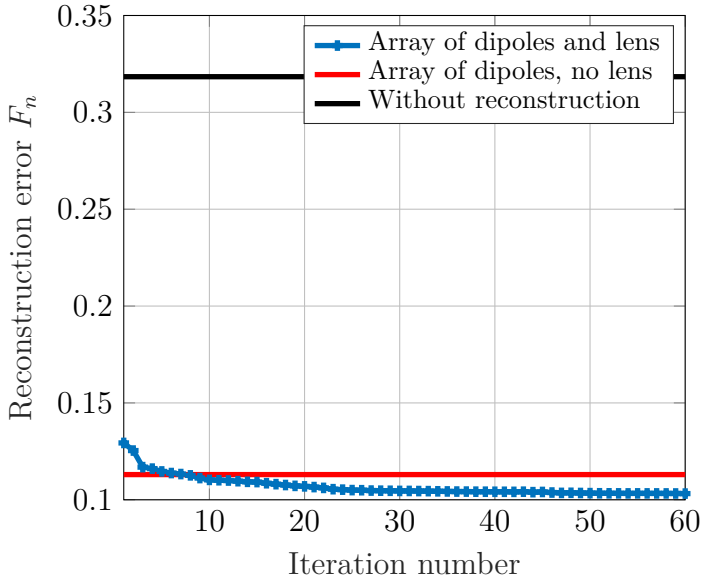

Figure 5.6: Convergence of the reconstruction error F_n.

to further improve the reconstruction and make it more realistic are the following

- Use a more realistic source for the modeling of the phone,
- Use a realistic head model (i.e. specific anthropomorphic mannequin (SAM) head [54] shown in fig. 5.7),

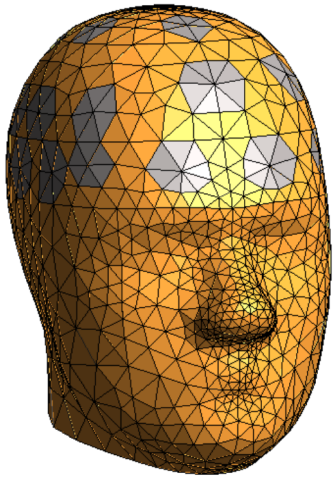

Figure 5.7: 3D view of the discretized SAM head model covered with discretized EEG caps.

- Constrain the algorithm to get a permittivity profile that can be manufactured,
- Consider the coupling between the head and the lens in the source design,
- Perform the experimental validation of the reconstruction source.

Chapter 6

Conclusion and Future Work

In this dissertation the following techniques based on volume integral equations were introduced for the improvement of the forward modeling and the resolution of inverse problems in bioelectromagnetics

- **Regularized D-VIE for bioelectromagnetic forward modeling** Leveraging a new set of volume quasi-Helmholtz projectors, the D-VIE was regularized at low frequencies in lossy dielectric objects, making it a formulation of choice when the full-wave electromagnetic modeling of biological tissues is needed,
- **D-VIE based inverse scheme for microwave imaging** An inverse scattering scheme in the family of gradient based methods has been introduced for the D-VIE formulation. It successfully reconstructed three-dimensional permittivity profiles in a microwave imaging setting,
- **Design of a lensed antenna for field reconstruction in a head with EEG caps** An inverse synthesis technique for the design of a source composed of a dipole array and a dielectric lens was presented. This source is specifically tailored to pre-deform a field so that the resulting field distribution in the head is not perturbed by the EEG electrodes placed on it.

The techniques introduced in this work can be further improved and pave the way to some new research lines.

- **Acceleration of the D-VIE formulation** The acceleration of the D-VIE formulation would benefit to the three contributions above-mentioned. Some existing acceleration techniques (e.g. the FMM, the ACA, or the adaptive integral method (AIM)) could be applied to the D-VIE to enable fast matrix-vector products, which is a property highly desired in iterative methods such as the inverse scattering schemes presented in this thesis,

- **Benefit from the regularized D-VIE in deep brain stimulation** In this thesis, the preconditioned formulation was applied to the problem of EEG source localization. While it proves that the formulation behaves correctly in the quasi-static regime, this application does not fully exploit its potential. In deep brain stimulation, pulses beyond the kilohertz regime are injected in the brain to treat pathologies. For this reason, the regularized D-VIE could be employed instead of Poisson-based solvers to better capture the frequency effects occurring,

- **Add a sparsity constraint in the cost functional of the inverse design algorithm** In the scheme employed to optimize the coefficients of the array of dipoles and the permittivity of the lens, the dipoles were placed at a (reasonable) number of discrete positions on a grid. A better solution would be to use a dense grid of possible positions for the dipoles and at the same time to enforce that the coefficients of the dipoles on that grid must be sparse. This constraint would possibly increase the number of degrees of freedom for a given number of dipoles,

- **Tackle the high internal contrast limitation of the D-VIE** While the regularized D-VIE introduced in this thesis cures the high-contrast problem between lossy dielectric objects and their background, the limitations caused by the internal contrasts between the different parts of the inhomogeneous object cannot be solved with the proposed preconditioner. A further theoretical analysis around the new set of volume quasi-Helmholtz projectors should be performed to show that they can cure the high internal contrast problem in the D-VIE with proper re-scaling.

Appendix A

Complementarity of the Scaled Projectors

In this appendix, it is shown that eq. (3.19) is valid, i.e., the sum of the two scaled projectors is equal to the identity matrix. We first prove that any SWG coefficient vector $\boldsymbol{\alpha}$ can be uniquely decomposed with the scaled loop-star decomposition

$$\boldsymbol{\alpha} = \boldsymbol{A}\boldsymbol{\Sigma}\tilde{\boldsymbol{s}} + \boldsymbol{\Lambda}\tilde{\boldsymbol{l}}, \tag{A.1}$$

where $\boldsymbol{A} \in \mathbb{C}^{N_F \times N_F}$ is an invertible complex symmetric matrix with one of the (potentially many different) square root matrices denoted by $\boldsymbol{A}^{\frac{1}{2}}$ and $\tilde{\boldsymbol{l}}$ and $\tilde{\boldsymbol{s}}$ are the coefficient vectors of the solenoidal and non-solenoidal basis functions in this new decomposition. Equation eq. (A.1) is equivalent to say that the column vectors of $\boldsymbol{\Lambda}$ and $\boldsymbol{A}\boldsymbol{\Sigma}$ form complementary subspaces in $\mathbb{C}^{N_F}$ and also equivalent to say that the matrix $[\boldsymbol{A}\boldsymbol{\Sigma} \;\; \boldsymbol{\Lambda}]$ is invertible.

To prove eq. (A.1) we show that $\boldsymbol{A}^{-\frac{1}{2}}\boldsymbol{\alpha}$ can be orthogonally decomposed as

$$\boldsymbol{A}^{-\frac{1}{2}}\boldsymbol{\alpha} = \boldsymbol{A}^{-\frac{1}{2}}\boldsymbol{\Lambda}\tilde{\boldsymbol{l}} + \boldsymbol{A}^{\frac{1}{2}}\boldsymbol{\Sigma}\tilde{\boldsymbol{s}}, \tag{A.2}$$

the existence (and unicity) of which is equivalent to the existence (and unicity) of eq. (A.1) since $\boldsymbol{A}^{\frac{1}{2}}$ is invertible. Since $\left(\boldsymbol{A}^{-\frac{1}{2}}\boldsymbol{\Lambda}\right)^{\mathrm{T}} \boldsymbol{A}^{\frac{1}{2}}\boldsymbol{\Sigma} = \boldsymbol{0}$, the decomposition is an orthogonal one and these two scaled transformation matrices have linearly independent column vectors. Then we need to show that the rank of the sum of $\boldsymbol{A}^{-\frac{1}{2}}\boldsymbol{\Lambda}$ and $\boldsymbol{A}^{\frac{1}{2}}\boldsymbol{\Sigma}$ is equal to the number of SWG basis functions N_F. Since $\operatorname{rank}(\boldsymbol{A}^{-\frac{1}{2}}\boldsymbol{\Lambda}) = \operatorname{rank}(\boldsymbol{\Lambda})$ ($\boldsymbol{A}^{\frac{1}{2}}$ is invertible), $\operatorname{rank}(\boldsymbol{A}^{\frac{1}{2}}\boldsymbol{\Sigma}) = \operatorname{rank}(\boldsymbol{\Sigma})$, $\operatorname{rank}([\boldsymbol{\Sigma} \;\; \boldsymbol{\Lambda}]) = N_F$, and $\boldsymbol{A}^{-\frac{1}{2}}\boldsymbol{\Lambda}$ and $\boldsymbol{A}^{\frac{1}{2}}\boldsymbol{\Sigma}$ have their column vectors linearly independent, we have

$$\begin{aligned} \operatorname{rank}\left(\left[\boldsymbol{A}^{\frac{1}{2}}\boldsymbol{\Sigma} \;\; \boldsymbol{A}^{-\frac{1}{2}}\boldsymbol{\Lambda}\right]\right) &= \operatorname{rank}(\boldsymbol{A}^{\frac{1}{2}}\boldsymbol{\Sigma}) + \operatorname{rank}(\boldsymbol{A}^{-\frac{1}{2}}\boldsymbol{\Lambda}) \\ &= \operatorname{rank}(\boldsymbol{\Sigma}) + \operatorname{rank}(\boldsymbol{\Lambda}) = N_F. \end{aligned} \tag{A.3}$$

for which it follows the invertibility of $\left[\boldsymbol{A}^{\frac{1}{2}}\boldsymbol{\Sigma} \;\; \boldsymbol{A}^{-\frac{1}{2}}\boldsymbol{\Lambda}\right]$ and thus of $[\boldsymbol{A}\boldsymbol{\Sigma} \;\; \boldsymbol{\Lambda}]$ which proves eq. (A.1).

Then, from eq. (A.1), we want to show that eq. (3.19) is true. To this aim, we first multiply eq. (A.1) by $\boldsymbol{\Lambda}^{\mathrm{T}}\boldsymbol{A}^{-1}$ and $\boldsymbol{\Sigma}^{\mathrm{T}}$, and we obtain the following equations

$$\boldsymbol{\Lambda}^{\mathrm{T}}\boldsymbol{A}^{-1}\boldsymbol{\alpha} = \boldsymbol{\Lambda}^{\mathrm{T}}\boldsymbol{A}^{-1}\boldsymbol{\Lambda}\tilde{\boldsymbol{l}} \tag{A.4}$$

$$\boldsymbol{\Sigma}^{\mathrm{T}}\boldsymbol{\alpha} = \boldsymbol{\Sigma}^{\mathrm{T}}\boldsymbol{A}\boldsymbol{\Sigma}\tilde{\boldsymbol{s}}, \tag{A.5}$$

in which we used the properties that $\boldsymbol{\Lambda}^{\mathrm{T}}\boldsymbol{A}^{-1}\boldsymbol{A}\boldsymbol{\Sigma} = \boldsymbol{0}$ and $\boldsymbol{\Sigma}^{\mathrm{T}}\boldsymbol{\Lambda} = \boldsymbol{0}$. From eq. (A.4) and eq. (A.5), we can now express the coefficients of the loop and star basis functions from the coefficients of the SWG basis functions

$$\tilde{\boldsymbol{l}} = (\boldsymbol{\Lambda}^{\mathrm{T}}\boldsymbol{A}^{-1}\boldsymbol{\Lambda})^{+}\boldsymbol{\Lambda}^{\mathrm{T}}\boldsymbol{A}^{-1}\boldsymbol{\alpha} \tag{A.6}$$

$$\tilde{\boldsymbol{s}} = (\boldsymbol{\Sigma}^{\mathrm{T}}\boldsymbol{A}\boldsymbol{\Sigma})^{+}\boldsymbol{\Sigma}^{\mathrm{T}}\boldsymbol{\alpha}. \tag{A.7}$$

The next step is to obtain the solenoidal and non-solenoidal parts of $\boldsymbol{\alpha}$ ($\boldsymbol{\alpha}_{\boldsymbol{l}}$ and $\boldsymbol{\alpha}_{\boldsymbol{s}}$) in terms of $\boldsymbol{\alpha}$ by applying $\boldsymbol{\Lambda}$ and $\boldsymbol{A}\boldsymbol{\Sigma}$ to equations eqs. (A.6) and (A.7)

$$\boldsymbol{\alpha}_{\boldsymbol{l}} = \boldsymbol{\Lambda}\tilde{\boldsymbol{l}} = \boldsymbol{\Lambda}(\boldsymbol{\Lambda}^{\mathrm{T}}\boldsymbol{A}^{-1}\boldsymbol{\Lambda})^{+}\boldsymbol{\Lambda}^{\mathrm{T}}\boldsymbol{A}^{-1}\boldsymbol{f} = \boldsymbol{P}^{\boldsymbol{\Lambda}}_{\boldsymbol{A}^{-1}}\boldsymbol{\alpha} \tag{A.8}$$

$$\boldsymbol{\alpha}_{\boldsymbol{s}} = \boldsymbol{A}\boldsymbol{\Sigma}\tilde{\boldsymbol{s}} = \boldsymbol{A}\boldsymbol{\Sigma}(\boldsymbol{\Sigma}^{\mathrm{T}}\boldsymbol{A}\boldsymbol{\Sigma})^{+}\boldsymbol{\Sigma}^{\mathrm{T}}\boldsymbol{f} = \boldsymbol{P}^{\boldsymbol{\Sigma}}_{\boldsymbol{A}^{-1}}\boldsymbol{\alpha}, \tag{A.9}$$

where

$$\boldsymbol{P}^{\boldsymbol{\Sigma}}_{\boldsymbol{A}^{-1}} = \boldsymbol{A}\boldsymbol{\Sigma}\left(\boldsymbol{\Sigma}^{\mathrm{T}}\boldsymbol{A}\boldsymbol{\Sigma}\right)^{+}\boldsymbol{\Sigma}^{\mathrm{T}} \tag{A.10}$$

$$\boldsymbol{P}^{\boldsymbol{\Lambda}}_{\boldsymbol{A}^{-1}} = \boldsymbol{\Lambda}\left(\boldsymbol{\Lambda}^{\mathrm{T}}\boldsymbol{A}^{-1}\boldsymbol{\Lambda}\right)^{+}\boldsymbol{\Lambda}^{\mathrm{T}}\boldsymbol{A}^{-1}. \tag{A.11}$$

Finally, $\boldsymbol{\alpha} = \boldsymbol{\alpha}_{\boldsymbol{l}} + \boldsymbol{\alpha}_{\boldsymbol{s}}$ yields $\boldsymbol{\alpha} = (\boldsymbol{P}^{\boldsymbol{\Lambda}}_{\boldsymbol{A}^{-1}} + \boldsymbol{P}^{\boldsymbol{\Sigma}}_{\boldsymbol{A}^{-1}})\boldsymbol{\alpha}$, and thus $\boldsymbol{P}^{\boldsymbol{\Lambda}}_{\boldsymbol{A}^{-1}} + \boldsymbol{P}^{\boldsymbol{\Sigma}}_{\boldsymbol{A}^{-1}} = \mathbf{I}$.

Appendix B

Cancellation of the Surface Terms with the Loop-to-SWG Mapping Matrix

We show in this appendix that $\boldsymbol{Z}_{\boldsymbol{\phi},\mathbf{11}}\boldsymbol{\Lambda} = \mathbf{0}$. To this aim, we first decompose $\boldsymbol{Z}_{\boldsymbol{\phi},\mathbf{11}}$ as

$$\boldsymbol{Z}_{\boldsymbol{\phi},\mathbf{11}} = \boldsymbol{Z}^{\text{full}}_{\boldsymbol{\phi},\mathbf{11}} + \boldsymbol{Z}^{\text{hbf}}_{\boldsymbol{\phi},\mathbf{11}}, \tag{B.1}$$

where

$$\begin{aligned}
&[\boldsymbol{Z}^{\text{full}}_{\boldsymbol{\phi},\mathbf{11}}]_{nm_1} = \\
&\epsilon_0^{-1}\left[\int_\Omega \nabla\cdot\boldsymbol{f_n}(\boldsymbol{r})\int_\Omega G_0(\boldsymbol{r},\boldsymbol{r'})\kappa(\boldsymbol{r'})\nabla\cdot\boldsymbol{f_{m_1}}(\boldsymbol{r'})\,\mathrm{d}v'\,\mathrm{d}v\right. \\
&\left.-\int_{\partial\Omega}\hat{\boldsymbol{n}}_n\cdot\boldsymbol{f_n}(\boldsymbol{r})\int_\Omega G_0(\boldsymbol{r},\boldsymbol{r'})\kappa(\boldsymbol{r'})\nabla\cdot\boldsymbol{f_{m_1}}(\boldsymbol{r'})\,\mathrm{d}v'\,\mathrm{d}s\right],
\end{aligned} \tag{B.2}$$

and

$$\begin{aligned}
&[\boldsymbol{Z}^{\text{hbf}}_{\boldsymbol{\phi},\mathbf{11}}]_{nm_2} = \\
&\epsilon_0^{-1}\left[\int_\Omega \nabla\cdot\boldsymbol{f_n}(\boldsymbol{r})\int_\Omega G_0(\boldsymbol{r},\boldsymbol{r'})\kappa(\boldsymbol{r'})\nabla\cdot\boldsymbol{f_{m_2}}(\boldsymbol{r'})\,\mathrm{d}v'\,\mathrm{d}v\right. \\
&-\int_\Omega \nabla\cdot\boldsymbol{f_n}(\boldsymbol{r})\int_{\partial\Omega} G_0(\boldsymbol{r},\boldsymbol{r'})\kappa^+_{m2}\hat{\boldsymbol{n}}_{m2}\cdot\boldsymbol{f_{m_2}}(\boldsymbol{r'})\,\mathrm{d}s'\,\mathrm{d}v \\
&-\int_{\partial\Omega}\hat{\boldsymbol{n}}_n\cdot\boldsymbol{f_n}(\boldsymbol{r})\int_\Omega G_0(\boldsymbol{r},\boldsymbol{r'})\kappa(\boldsymbol{r'})\nabla\cdot\boldsymbol{f_{m_2}}(\boldsymbol{r'})\,\mathrm{d}v'\,\mathrm{d}s \\
&\left.+\int_{\partial\Omega}\hat{\boldsymbol{n}}_n\cdot\boldsymbol{f_n}(\boldsymbol{r})\int_{\partial\Omega} G_0(\boldsymbol{r},\boldsymbol{r'})\kappa^+_{m2}\hat{\boldsymbol{n}}_{m2}\cdot\boldsymbol{f_{m_2}}(\boldsymbol{r'})\,\mathrm{d}s'\,\mathrm{d}s\right],
\end{aligned} \tag{B.3}$$

in which $\{\boldsymbol{f_{m1}}\}$ and $\{\boldsymbol{f_{m2}}\}$ are the sets of SWG basis functions defined on two tetrahedra and the half SWG basis functions, respectively and the indices m_1 and m_2 are the indices of these basis functions in the original set of SWG basis functions. The total number of SWG basis functions N_F is the sum of the cardinality of $\{\boldsymbol{f_{m1}}\}$

and the cardinality of $\{\boldsymbol{f_{m2}}\}$. Note that the matrix entries of $\boldsymbol{Z}^{\text{full}}_{\boldsymbol{\Phi},\mathbf{11}}$ and $\boldsymbol{Z}^{\text{hbf}}_{\boldsymbol{\Phi},\mathbf{11}}$ that are not filled in eqs. (B.2) and (B.3) are filled with zeros, that is $[\boldsymbol{Z}^{\text{full}}_{\boldsymbol{\Phi},\mathbf{11}}]_{nm_2} = 0$ and $[\boldsymbol{Z}^{\text{hbf}}_{\boldsymbol{\Phi},\mathbf{11}}]_{nm_1} = 0$.

The property $\boldsymbol{Z}^{\text{full}}_{\boldsymbol{\Phi},\mathbf{11}}\boldsymbol{\Lambda} = \mathbf{0}$ can be verified trivially. However, we need a further analysis to show that $\boldsymbol{Z}^{\text{hbf}}_{\boldsymbol{\Phi},\mathbf{11}}\boldsymbol{\Lambda} = \mathbf{0}$. Instead of directly proving that $\boldsymbol{Z}^{\text{hbf}}_{\boldsymbol{\Phi},\mathbf{11}}\boldsymbol{\Lambda} = \mathbf{0}$, we will show that $\boldsymbol{Z}^{\text{hbf}}_{\boldsymbol{\Phi},\mathbf{11}}\boldsymbol{P}^{\boldsymbol{\Lambda}}_{\boldsymbol{A}^{-1}} = \mathbf{0}$, which implies that $\boldsymbol{Z}^{\text{hbf}}_{\boldsymbol{\Phi},\mathbf{11}}\boldsymbol{\Lambda} = \mathbf{0}$ ($\boldsymbol{\Lambda}$ being a full column rank matrix). Recalling that the basis functions in $\boldsymbol{Z}^{\text{hbf}}_{\boldsymbol{\Phi},\mathbf{11}}$ can be reordered such that

$$\boldsymbol{Z}^{\text{hbf}}_{\boldsymbol{\Phi},\mathbf{11}} = \begin{bmatrix}\mathbf{0} & \boldsymbol{H}\end{bmatrix}, \tag{B.4}$$

in which $\boldsymbol{H} \in \mathbb{C}^{N_F \times N_{eF}}$ contains all the matrix entries defined in eq. (B.3) (i.e. columns of $\boldsymbol{Z}^{\text{hbf}}_{\boldsymbol{\Phi},\mathbf{11}}$ that are not zero) and that $\boldsymbol{\Sigma_s}^{\mathrm{T}}$ can be rearranged as $[\mathbf{0} \ -\mathbf{I}]$ following its definition in eq. (3.15). Using the above-mentioned definitions of $\boldsymbol{Z}^{\text{hbf}}_{\boldsymbol{\Phi},\mathbf{11}}$ and $\boldsymbol{\Sigma_s}^{\mathrm{T}}$, we can expand $\boldsymbol{Z}^{\text{hbf}}_{\boldsymbol{\Phi},\mathbf{11}}\boldsymbol{P}^{\boldsymbol{\Lambda}}_{\boldsymbol{A}^{-1}}$ as

$$\begin{aligned}
\boldsymbol{Z}^{\text{hbf}}_{\boldsymbol{\Phi},\mathbf{11}}\boldsymbol{P}^{\boldsymbol{\Lambda}}_{\boldsymbol{A}^{-1}} &= \left[\mathbf{0} \mid \boldsymbol{H}\right] \left[\begin{array}{c|c}\mathbf{I} & \mathbf{0} \\ \hline \mathbf{0} & \mathbf{I}\end{array}\right] \boldsymbol{P}^{\boldsymbol{\Lambda}}_{\boldsymbol{A}^{-1}} \\
&= \left[\mathbf{0} \mid \boldsymbol{H}\right] \left[\begin{array}{c|c}\mathbf{I} & \mathbf{0} \\ \hline -\boldsymbol{\Sigma_s}^{\mathrm{T}} & \end{array}\right] \boldsymbol{P}^{\boldsymbol{\Lambda}}_{\boldsymbol{A}^{-1}} \\
&= -\boldsymbol{H}\boldsymbol{\Sigma_s}^{\mathrm{T}}\boldsymbol{P}^{\boldsymbol{\Lambda}}_{\boldsymbol{A}^{-1}}.
\end{aligned} \tag{B.5}$$

Therefore, $\boldsymbol{\Sigma_s}^{\mathrm{T}}\boldsymbol{P}^{\boldsymbol{\Lambda}}_{\boldsymbol{A}^{-1}} = \mathbf{0}$ leads to $\boldsymbol{Z}^{\text{hbf}}_{\boldsymbol{\Phi},\mathbf{11}}\boldsymbol{P}^{\boldsymbol{\Lambda}}_{\boldsymbol{A}^{-1}} = \mathbf{0}$. Given that the expansion of $\boldsymbol{\Sigma}^{\mathrm{T}}\boldsymbol{P}^{\boldsymbol{\Lambda}}_{\boldsymbol{A}^{-1}}$ results in

$$\begin{aligned}
\boldsymbol{\Sigma}^{\mathrm{T}}\boldsymbol{P}^{\boldsymbol{\Lambda}}_{\boldsymbol{A}^{-1}} &= \boldsymbol{\Sigma}^{\mathrm{T}}\left(\mathbf{I} - \boldsymbol{P}^{\boldsymbol{\Sigma}}_{\boldsymbol{A}^{-1}}\right) \\
&= \boldsymbol{\Sigma}^{\mathrm{T}}\left(\mathbf{I} - \boldsymbol{A}\boldsymbol{\Sigma}\left(\boldsymbol{\Sigma}^{\mathrm{T}}\boldsymbol{A}\boldsymbol{\Sigma}\right)^{+}\boldsymbol{\Sigma}^{\mathrm{T}}\right) \\
&= \boldsymbol{\Sigma}^{\mathrm{T}} - \boldsymbol{\Sigma}^{\mathrm{T}}\boldsymbol{A}\boldsymbol{\Sigma}\left(\boldsymbol{\Sigma}^{\mathrm{T}}\boldsymbol{A}\boldsymbol{\Sigma}\right)^{+}\boldsymbol{\Sigma}^{\mathrm{T}} \\
&= \boldsymbol{\Sigma}^{\mathrm{T}} - \boldsymbol{\Sigma}^{\mathrm{T}} \\
&= \mathbf{0},
\end{aligned} \tag{B.6}$$

and that the property $\boldsymbol{\Sigma}^{\mathrm{T}}\boldsymbol{P}^{\boldsymbol{\Lambda}}_{\boldsymbol{A}^{-1}} = [\boldsymbol{\Sigma_v} \ \boldsymbol{\Sigma_s}]^{\mathrm{T}}\boldsymbol{P}^{\boldsymbol{\Lambda}}_{\boldsymbol{A}^{-1}} = \mathbf{0}$ implies that $\boldsymbol{\Sigma_s}^{\mathrm{T}}\boldsymbol{P}^{\boldsymbol{\Lambda}}_{\boldsymbol{A}^{-1}} = \mathbf{0}$ since $\boldsymbol{\Sigma_s}^{\mathrm{T}}$ is of the form $[\mathbf{0} \ -\mathbf{I}]$, we obtain that $\boldsymbol{\Sigma_s}^{\mathrm{T}}\boldsymbol{P}^{\boldsymbol{\Lambda}}_{\boldsymbol{A}^{-1}} = \mathbf{0}$. Finally, leveraging eq. (B.5), it results that $\boldsymbol{Z}^{\text{hbf}}_{\boldsymbol{\Phi},\mathbf{11}}\boldsymbol{P}^{\boldsymbol{\Lambda}}_{\boldsymbol{A}^{-1}} = \mathbf{0}$, which in turn gives $\boldsymbol{Z}_{\boldsymbol{\Phi},\mathbf{11}}\boldsymbol{\Lambda} = \mathbf{0}$.

Appendix C

Non-Singularity of the Normalized Loop-Star Decomposition Matrix

In this appendix, we show that the normalized loop/star-to-SWG decomposition matrix introduced in eq. (3.26) is non-singular, and hence can be employed to investigate the conditioning behavior of the discretized D-VIE in section 3.4. To this aim, we first expand $\boldsymbol{M_{LS}} = \boldsymbol{B}_{\boldsymbol{\Lambda\Sigma}}^{\tilde{\boldsymbol{G}}_\epsilon\,\mathrm{T}} \boldsymbol{B}_{\boldsymbol{\Lambda\Sigma}}^{\tilde{\boldsymbol{G}}_\epsilon}$ to study the singular values of $\boldsymbol{B}_{\boldsymbol{\Lambda\Sigma}}^{\tilde{\boldsymbol{G}}_\epsilon}$

$$\begin{aligned} \boldsymbol{M_{LS}} &= \boldsymbol{B}_{\boldsymbol{\Lambda\Sigma}}^{\tilde{\boldsymbol{G}}_\epsilon\,\mathrm{T}} \boldsymbol{B}_{\boldsymbol{\Lambda\Sigma}}^{\tilde{\boldsymbol{G}}_\epsilon} \\ &= \begin{bmatrix} \overline{\overline{\boldsymbol{\Lambda}}}^{\mathrm{T}}\overline{\overline{\boldsymbol{\Lambda}}} & \overline{\overline{\boldsymbol{\Lambda}}}^{\mathrm{T}}\overline{\overline{\boldsymbol{\Sigma}}} \\ \overline{\overline{\boldsymbol{\Sigma}}}^{\mathrm{T}}\overline{\overline{\boldsymbol{\Lambda}}} & \overline{\overline{\boldsymbol{\Sigma}}}^{\mathrm{T}}\overline{\overline{\boldsymbol{\Sigma}}} \end{bmatrix} \\ &= \begin{bmatrix} \mathbf{I} & \boldsymbol{O} \\ \boldsymbol{O}^{\mathrm{T}} & \mathbf{I} \end{bmatrix}. \end{aligned} \tag{C.1}$$

in which

$$\boldsymbol{O} = (\boldsymbol{\Lambda}^{\mathrm{T}}\boldsymbol{\Lambda})^{-\frac{1}{2}}\boldsymbol{\Lambda}^{\mathrm{T}}\tilde{\boldsymbol{G}}_\epsilon{}^{-1}\boldsymbol{\Sigma}(\boldsymbol{\Sigma}^{\mathrm{T}}\tilde{\boldsymbol{G}}_\epsilon{}^{-2}\boldsymbol{\Sigma})^{-\frac{1}{2}}. \tag{C.2}$$

From eq. (C.1), it results that $\boldsymbol{B}_{\boldsymbol{\Lambda\Sigma}}^{\tilde{\boldsymbol{G}}_\epsilon}$ has no singular value at 0 if the norm of the off-diagonal block $\boldsymbol{O}$ is strictly lower than 1. To show that this condition is fulfilled, some properties regarding the angle between complementary subspaces [94, 55] are employed in the following. Here the angle of interest is the angle between the subspaces $\mathcal{R}$ and $\mathcal{N}$ in $\mathbb{C}^{N_F}$, associated to the orthonormal bases formed by the column vectors of $\overline{\overline{\boldsymbol{\Sigma}}}$ and $\overline{\overline{\boldsymbol{\Lambda}}}$, respectively. By introducing the following orthogonal (symmetric) projectors onto $\mathcal{R}$ and $\mathcal{N}$

$$\boldsymbol{P}^{\mathcal{R}} = \overline{\overline{\boldsymbol{\Sigma}\boldsymbol{\Sigma}}}^{\mathrm{T}} = \tilde{\boldsymbol{G}}_\epsilon{}^{-1}\boldsymbol{\Sigma}(\boldsymbol{\Sigma}^{\mathrm{T}}\tilde{\boldsymbol{G}}_\epsilon{}^{-2}\boldsymbol{\Sigma})^{-1}\boldsymbol{\Sigma}^{\mathrm{T}}\tilde{\boldsymbol{G}}_\epsilon{}^{-1} \tag{C.3}$$

$$\boldsymbol{P}^{\mathcal{N}} = \overline{\overline{\boldsymbol{\Lambda}\boldsymbol{\Lambda}}}^{\mathrm{T}} = \boldsymbol{\Lambda}(\boldsymbol{\Lambda}^{\mathrm{T}}\boldsymbol{\Lambda})^{-1}\boldsymbol{\Lambda}^{\mathrm{T}}, \tag{C.4}$$

the cosine of the minimal angle θ ($0 \leq \theta \leq \pi/2$) between $\mathcal{R}$ and $\mathcal{N}$ can be defined as [94, 55]

$$\cos\theta = \|\boldsymbol{P}^{\mathcal{N}}\boldsymbol{P}^{\mathcal{R}}\| = \|\boldsymbol{P}^{\mathcal{R}}\boldsymbol{P}^{\mathcal{N}}\|. \tag{C.5}$$

Then, using the fact that $\overline{\overline{\boldsymbol{\Lambda}}}^{\mathrm{T}}\overline{\overline{\boldsymbol{\Lambda}}} = \mathbf{I}$ and $\overline{\overline{\boldsymbol{\Sigma}}}^{\mathrm{T}}\overline{\overline{\boldsymbol{\Sigma}}} = \mathbf{I}$ yields the following inequalities

$$\|\boldsymbol{P}^{\mathcal{N}}\boldsymbol{P}^{\mathcal{R}}\| = \|\overline{\overline{\boldsymbol{\Lambda}\boldsymbol{\Lambda}}}^{\mathrm{T}}\overline{\overline{\boldsymbol{\Sigma}\boldsymbol{\Sigma}}}^{\mathrm{T}}\| \leq \|\overline{\overline{\boldsymbol{\Lambda}}}^{\mathrm{T}}\overline{\overline{\boldsymbol{\Sigma}}}\| \tag{C.6}$$

$$\|\overline{\overline{\boldsymbol{\Lambda}}}^{\mathrm{T}}\overline{\overline{\boldsymbol{\Sigma}}}\| = \|\overline{\overline{\boldsymbol{\Lambda}}}^{\mathrm{T}}\overline{\overline{\boldsymbol{\Lambda}\boldsymbol{\Lambda}}}^{\mathrm{T}}\overline{\overline{\boldsymbol{\Sigma}\boldsymbol{\Sigma}}}^{\mathrm{T}}\overline{\overline{\boldsymbol{\Sigma}}}\| = \|\overline{\overline{\boldsymbol{\Lambda}}}^{\mathrm{T}}\boldsymbol{P}^{\mathcal{N}}\boldsymbol{P}^{\mathcal{R}}\overline{\overline{\boldsymbol{\Sigma}}}\| \leq \|\boldsymbol{P}^{\mathcal{N}}\boldsymbol{P}^{\mathcal{R}}\|, \tag{C.7}$$

which shows that $\|\boldsymbol{P}^{\mathcal{N}}\boldsymbol{P}^{\mathcal{R}}\| = \|\overline{\overline{\boldsymbol{\Lambda}}}^{\mathrm{T}}\overline{\overline{\boldsymbol{\Sigma}}}\|$. From eq. (C.5), it follows that

$$\cos\theta = \|\overline{\overline{\boldsymbol{\Lambda}}}^{\mathrm{T}}\overline{\overline{\boldsymbol{\Sigma}}}\|. \tag{C.8}$$

Then, recalling the fact that $\mathcal{R}$ and $\mathcal{N}$ are complementary subspaces in $\mathbb{C}^{N_F}$ (see Appendix A), we have $\cos\theta < 1$ [94, 55]. Finally, leveraging eq. (C.8), it results that $\boldsymbol{B}^{\tilde{\boldsymbol{G}}_\epsilon}_{\boldsymbol{\Lambda}\boldsymbol{\Sigma}}$ is non-singular.

Appendix D

Estimation of the Update Weights in the EFI-Based Inverse Design Algorithm

The coefficients of the nonlinear systems which solved for the weights α_n^D, α_n^κ, and α_n^J are given in the following. The cost functional $F_{n,\mathrm{data}}(\kappa_n, \boldsymbol{D}_{l,n}, \boldsymbol{J}_{i,n})$ can be rearranged as

$$\begin{aligned} F_{n,\mathrm{data}}(\kappa_n, \boldsymbol{D}_{l,n}, \boldsymbol{J}_{i,n}) = \eta_S \big[&\alpha_n^D a + \alpha_n^\kappa b + \alpha_n^u c + \alpha_n^D \alpha_n^\kappa d + \alpha_n^u \alpha_n^\kappa e + \alpha_n^u \alpha_n^D f + \alpha_n^u \alpha_n^\kappa \alpha_n^D g \\ &+(\alpha_n^D)^2 A + (\alpha_n^\kappa)^2 B + (\alpha_n^u)^2 C + (\alpha_n^D \alpha_n^\kappa)^2 D + E \\ &+\alpha_n^D (\alpha_n^\kappa)^2 F + (\alpha_n^D)^2 \alpha_n^\kappa G \big] \end{aligned} \tag{D.1}$$

in which the coefficients $a, b, c, d, e, f, g, A, B, C, D, E, F$, and G read

$$\begin{cases} a = -2\mathrm{Re}\,\langle \boldsymbol{\rho_{n-1}}, \tilde{\boldsymbol{\mathcal{L}}}^{\Omega_L}_{\kappa_{n-1}} \boldsymbol{v_n} \rangle_{\Omega_{\tilde{H}}} \\ b = -2\mathrm{Re}\,\langle \boldsymbol{\rho_{n-1}}, \tilde{\boldsymbol{\mathcal{L}}}^{\Omega_L}_{w_n} \boldsymbol{D_{l,n-1}} \rangle_{\Omega_{\tilde{H}}} \\ c = -2\mathrm{Re}\,\langle \boldsymbol{\rho_{n-1}}, \tilde{\boldsymbol{\mathcal{T}}}_i \boldsymbol{z_n} \rangle_{\Omega_{\tilde{H}}} \\ d = 2\mathrm{Re}\,\langle \tilde{\boldsymbol{\mathcal{L}}}^{\Omega_L}_{\kappa_{n-1}} \boldsymbol{v_n}, \tilde{\boldsymbol{\mathcal{L}}}^{\Omega_L}_{w_n} \boldsymbol{D_{l,n-1}} \rangle_{\Omega_{\tilde{H}}} - 2\mathrm{Re}\,\langle \boldsymbol{\rho_{n-1}}, \tilde{\boldsymbol{\mathcal{L}}}^{\Omega_L}_{w_n} \boldsymbol{v_n} \rangle_{\Omega_{\tilde{H}}} \\ e = 2\mathrm{Re}\,\langle \tilde{\boldsymbol{\mathcal{T}}}_i \boldsymbol{z_n}, \tilde{\boldsymbol{\mathcal{L}}}^{\Omega_L}_{w_n} \boldsymbol{D_{l,n-1}} \rangle_{\Omega_{\tilde{H}}} \\ f = 2\mathrm{Re}\,\langle \tilde{\boldsymbol{\mathcal{T}}}_i \boldsymbol{z_n}, \tilde{\boldsymbol{\mathcal{L}}}^{\Omega_L}_{\kappa_{n-1}} \boldsymbol{v_n} \rangle_{\Omega_{\tilde{H}}} \\ g = 2\mathrm{Re}\,\langle \tilde{\boldsymbol{\mathcal{T}}}_i \boldsymbol{z_n}, \tilde{\boldsymbol{\mathcal{L}}}^{\Omega_L}_{w_n} \boldsymbol{v_n} \rangle_{\Omega_{\tilde{H}}} \\ A = \| \tilde{\boldsymbol{\mathcal{L}}}^{\Omega_L}_{\kappa_{n-1}} \boldsymbol{v_n} \|^2_{\Omega_{\tilde{H}}} \\ B = \| \tilde{\boldsymbol{\mathcal{L}}}^{\Omega_L}_{w_n} \boldsymbol{D_{l,n-1}} \|^2_{\Omega_{\tilde{H}}} \\ C = \| \tilde{\boldsymbol{\mathcal{T}}}_i \boldsymbol{z_n} \|^2_{\Omega_{\tilde{H}}} \\ D = \| \tilde{\boldsymbol{\mathcal{L}}}^{\Omega_L}_{w_n} \boldsymbol{v_n} \|^2_{\Omega_{\tilde{H}}} \\ E = \| \boldsymbol{\rho_{n-1}} \|^2_{\Omega_{\tilde{H}}} \\ F = 2\mathrm{Re}\,\langle \tilde{\boldsymbol{\mathcal{L}}}^{\Omega_L}_{w_n} \boldsymbol{D_{l,n-1}}, \tilde{\boldsymbol{\mathcal{L}}}^{\Omega_L}_{w_n} \boldsymbol{v_n} \rangle_{\Omega_{\tilde{H}}} \\ G = 2\mathrm{Re}\,\langle \tilde{\boldsymbol{\mathcal{L}}}^{\Omega_L}_{\kappa_{n-1}} \boldsymbol{v_n}, \tilde{\boldsymbol{\mathcal{L}}}^{\Omega_L}_{w_n} \boldsymbol{v_n} \rangle_{\Omega_{\tilde{H}}}. \end{cases} \tag{D.2}$$

and the cost functional of the state equation can be rewritten as

$$\begin{aligned} F_{n,\mathrm{state}}(\kappa_n, \boldsymbol{D}_{l,n}, \boldsymbol{J}_{i,n}) = \eta_{D,n-1} \big[&\alpha_n^D a' + \alpha_n^\kappa b' + \alpha_n^u c' + \alpha_n^D \alpha_n^\kappa d' + \alpha_n^u \alpha_n^\kappa e' + \alpha_n^u \alpha_n^D f' + \alpha_n^u \alpha_n^\kappa \alpha_n^D g' \\ &+(\alpha_n^D)^2 A' + (\alpha_n^\kappa)^2 B' + (\alpha_n^u)^2 C' + (\alpha_n^D \alpha_n^\kappa)^2 D' + E' \\ &+\alpha_n^D (\alpha_n^\kappa)^2 F' + (\alpha_n^D)^2 \alpha_n^\kappa G' \big], \end{aligned} \tag{D.3}$$

in which $a', b', c', d', e', f', g', A', B', C', D', E', F'$, and G' are defined as

$$
\begin{cases}
a' = 2\mathrm{Re}\,\langle \boldsymbol{f_{n-1}}, \boldsymbol{\mathcal{L}}_{\kappa_{n-1}}^{\Omega_L} \boldsymbol{v_n}\rangle_{\Omega_L} - \frac{2}{\epsilon_0}\mathrm{Re}\,\langle \boldsymbol{v_n}, \boldsymbol{f_{n-1}}\rangle_{\Omega_L} + \frac{2}{\epsilon_0}\mathrm{Re}\,\langle \kappa_{n-1}\boldsymbol{v_n}, \boldsymbol{f_{n-1}}\rangle_{\Omega_L} \\
b' = 2\mathrm{Re}\,\langle \boldsymbol{f_{n-1}}, \boldsymbol{\mathcal{L}}_{w_n}^{\Omega_L} \boldsymbol{D_{l,n-1}}\rangle_{\Omega_L} + \frac{2}{\epsilon_0}\mathrm{Re}\,\langle w_n \boldsymbol{D_{l,n-1}}, \boldsymbol{f_{n-1}}\rangle_{\Omega_L} \\
c' = 2\mathrm{Re}\,\langle \boldsymbol{f_{n-1}}, \boldsymbol{\mathcal{T}}_i \boldsymbol{z_n}\rangle_{\Omega_L} \\
d' = -\frac{2}{{\epsilon_0}^2}\mathrm{Re}\,\langle \boldsymbol{v_n}, w_n \boldsymbol{D_{l,n-1}}\rangle_{\Omega_L} + \frac{2}{\epsilon_0^2}\mathrm{Re}\,\langle \kappa_{n-1}\boldsymbol{v_n}, w_n \boldsymbol{D_{l,n-1}}\rangle_{\Omega_L} + \frac{2}{\epsilon_0}\mathrm{Re}\,\langle w_n \boldsymbol{v_n}, \boldsymbol{f_{n-1}}\rangle_{\Omega_L} \\
+\frac{2}{\epsilon_0}\mathrm{Re}\,\langle w_n \boldsymbol{D_{l,n-1}}, \boldsymbol{\mathcal{L}}_{\kappa_{n-1}}^{\Omega_L} \boldsymbol{v_n}\rangle_{\Omega_L} - \frac{2}{\epsilon_0}\mathrm{Re}\,\langle \boldsymbol{v_n}, \boldsymbol{\mathcal{L}}_{w_n}^{\Omega_L} \boldsymbol{D_{l,n-1}}\rangle_{\Omega_L} + \frac{2}{\epsilon_0}\mathrm{Re}\,\langle \kappa_{n-1}\boldsymbol{v_n}, \boldsymbol{\mathcal{L}}_{w_n}^{\Omega_L} \boldsymbol{D_{l,n-1}}\rangle_{\Omega_L} \\
+2\mathrm{Re}\,\langle \boldsymbol{\mathcal{L}}_{\kappa_{n-1}}^{\Omega_L} \boldsymbol{v_n}, \boldsymbol{\mathcal{L}}_{w_n}^{\Omega_L} \boldsymbol{D_{l,n-1}}\rangle_{\Omega_L} + 2\mathrm{Re}\,\langle \boldsymbol{f_{n-1}}, \boldsymbol{\mathcal{L}}_{w_n}^{\Omega_L} \boldsymbol{v_n}\rangle_{\Omega_L} \\
e' = \frac{2}{\epsilon_0}\mathrm{Re}\,\langle w_n \boldsymbol{D_{l,n-1}}, \boldsymbol{\mathcal{T}}_i \boldsymbol{z_n}\rangle_{\Omega_L} + 2\mathrm{Re}\,\langle \boldsymbol{\mathcal{L}}_{w_n}^{\Omega_L} \boldsymbol{D_{l,n-1}}, \boldsymbol{\mathcal{T}}_i \boldsymbol{z_n}\rangle_{\Omega_L} \\
f' = -\frac{2}{\epsilon_0}\mathrm{Re}\,\langle \boldsymbol{v_n}, \boldsymbol{\mathcal{T}}_i \boldsymbol{z_n}\rangle_{\Omega_L} + \frac{2}{\epsilon_0}\mathrm{Re}\,\langle \kappa_{n-1}\boldsymbol{v_n}, \boldsymbol{\mathcal{T}}_i \boldsymbol{z_n}\rangle_{\Omega_L} + 2\mathrm{Re}\,\langle \boldsymbol{\mathcal{L}}_{\kappa_{n-1}}^{\Omega_L} \boldsymbol{v_n}, \boldsymbol{\mathcal{T}}_i \boldsymbol{z_n}\rangle_{\Omega_L} \\
g' = \frac{2}{\epsilon_0}\mathrm{Re}\,\langle w_n \boldsymbol{v_n}, \boldsymbol{Z_l} \boldsymbol{z_n}\rangle_{\Omega_L} + 2\mathrm{Re}\,\langle \boldsymbol{\mathcal{L}}_{w_n}^{\Omega_L} \boldsymbol{v_n}, \boldsymbol{Z_l} \boldsymbol{z_n}\rangle_{\Omega_L} \\
A' = \frac{1}{\epsilon_0}\|\boldsymbol{v_n}\|_{\Omega_L}^2 + \frac{1}{\epsilon_0}\|\kappa_{n-1}\boldsymbol{v_n}\|_{\Omega_L}^2 + \|\boldsymbol{\mathcal{L}}_{\kappa_{n-1}}^{\Omega_L} \boldsymbol{v_n}\|_{\Omega_L}^2 + \frac{2}{{\epsilon_0}^2}\mathrm{Re}\,\langle \boldsymbol{v_n}, \kappa_{n-1}\boldsymbol{v_n}\rangle_{\Omega_L} \\
-\frac{2}{\epsilon_0}\mathrm{Re}\,\langle \boldsymbol{v_n}, \boldsymbol{\mathcal{L}}_{\kappa_{n-1}}^{\Omega_L} \boldsymbol{v_n}\rangle_{\Omega_L} + \frac{2}{\epsilon_0}\mathrm{Re}\,\langle \kappa_{n-1}\boldsymbol{v_n}, \boldsymbol{\mathcal{L}}_{\kappa_{n-1}}^{\Omega_L} \boldsymbol{v_n}\rangle_{\Omega_L} \\
B' = \frac{1}{\epsilon_0}\|w_n \boldsymbol{D_{l,n-1}}\|_{\Omega_L}^2 + \|\boldsymbol{\mathcal{L}}_{w_n}^{\Omega_L} \boldsymbol{D_{l,n-1}}\|_{\Omega_L}^2 + \frac{2}{\epsilon_0}\mathrm{Re}\,\langle w_n \boldsymbol{D_{l,n-1}}, \boldsymbol{\mathcal{L}}_{w_n}^{\Omega_L} \boldsymbol{D_{l,n-1}}\rangle_{\Omega_L} \\
C' = \|\boldsymbol{\mathcal{T}}_i \boldsymbol{z_n}\|_{\Omega_L}^2 \\
D' = \frac{1}{\epsilon_0}\|w_n \boldsymbol{v_n}\|_{\Omega_L}^2 + \|\boldsymbol{\mathcal{L}}_{w_n}^{\Omega_L} \boldsymbol{v_n}\|_{\Omega_L}^2 + \frac{2}{\epsilon_0}\mathrm{Re}\,\langle w_n \boldsymbol{v_n}, \boldsymbol{\mathcal{L}}_{w_n}^{\Omega_L} \boldsymbol{v_n}\rangle_{\Omega_L} \\
E' = \|\boldsymbol{f_{n-1}}\|_{\Omega_L}^2 \\
F' = \frac{2}{{\epsilon_0}^2}\mathrm{Re}\,\langle w_n \boldsymbol{D_{l,n-1}}, w_n \boldsymbol{v_n}\rangle_{\Omega_L} + \frac{2}{\epsilon_0}\mathrm{Re}\,\langle w_n \boldsymbol{v_n}, \boldsymbol{\mathcal{L}}_{w_n}^{\Omega_L} \boldsymbol{D_{l,n-1}}\rangle_{\Omega_L} \\
+\frac{2}{\epsilon_0}\mathrm{Re}\,\langle w_n \boldsymbol{D_{l,n-1}}, \boldsymbol{\mathcal{L}}_{w_n}^{\Omega_L} \boldsymbol{v_n}\rangle_{\Omega_L} + 2\mathrm{Re}\,\langle \boldsymbol{\mathcal{L}}_{w_n}^{\Omega_L} \boldsymbol{D_{l,n-1}}, \boldsymbol{\mathcal{L}}_{w_n}^{\Omega_L} \boldsymbol{v_n}\rangle_{\Omega_L} \\
G' = -\frac{2}{{\epsilon_0}^2}\mathrm{Re}\,\langle \boldsymbol{v_n}, w_n \boldsymbol{v_n}\rangle_{\Omega_L} + \frac{2}{{\epsilon_0}^2}\mathrm{Re}\,\langle \kappa_{n-1}\boldsymbol{v_n}, w_n \boldsymbol{v_n}\rangle_{\Omega_L} + \frac{2}{\epsilon_0}\mathrm{Re}\,\langle w_n \boldsymbol{v_n}, \boldsymbol{\mathcal{L}}_{\kappa_{n-1}}^{\Omega_L} \boldsymbol{v_n}\rangle_{\Omega_L} \\
-\frac{2}{\epsilon_0}\mathrm{Re}\,\langle \boldsymbol{v_n}, \boldsymbol{\mathcal{L}}_{w_n}^{\Omega_L} \boldsymbol{v_n}\rangle_{\Omega_L} + \frac{2}{\epsilon_0}\mathrm{Re}\,\langle \kappa_{n-1}\boldsymbol{v_n}, \boldsymbol{\mathcal{L}}_{w_n}^{\Omega_L} \boldsymbol{v_n}\rangle_{\Omega_L} + 2\mathrm{Re}\,\langle \boldsymbol{\mathcal{L}}_{\kappa_{n-1}}^{\Omega_L} \boldsymbol{v_n}, \boldsymbol{\mathcal{L}}_{w_n}^{\Omega_L} \boldsymbol{v_n}\rangle_{\Omega_L}.
\end{cases}
\tag{D.4}
$$

Nomenclature

Acronyms

ACA	Adaptive cross approximation
BIM	Born iterative method
CEM	Computational electromagnetics
D-VIE	Electric flux volume integral equation
EEG	Electroencephalography
EFI	Electric flux inversion
EFIE	Electric field integral equation
FDM	Finite difference method
FEM	Finite element method
FMM	Fast multipole method
HVSIE	Hybrid volume-surface integral equation
ICNIRP	International commission on non-ionizing radiation protection
IE	Integral equation
IS	Inverse scattering
J-VIE	Current volume integral equation
MGM	Modified gradient method
MoM	Method of moments
MVP	Matrix-vector product
MWI	Microwave imaging

NKM	Newton Kantorovich method
PEC	Perfect electric conductor
RCS	Radar cross section
RF	Radio frequency
RWG	Rao-Wilton-Glisson
SAR	Specific absorption rate
SEP	Surface equivalence principle
SIE	Surface integral equation
SWG	Schaubert-Wilton-Glisson
VEP	Volume equivalence principle
VIE	Volume integral equation

Notations

$\arg\min$	Argument of the minimum
ϵ_r	Relative permittivity
$\mathbf{I}$	Identity matrix
$\mathcal{O}$	Big O Bachmann–Landau symbol
$\boldsymbol{A}^*$	Conjugate transpose of $\boldsymbol{A}$
$\boldsymbol{A}^+$	Moore-Penrose pseudo inverse of $\boldsymbol{A}$
$\mathrm{cond}(\boldsymbol{Z})$	Condition number of $\boldsymbol{Z}$
$\boldsymbol{u}^{\mathrm{T}}$	Transpose of $\boldsymbol{u}$
$\hat{\boldsymbol{n}}(\boldsymbol{r})$	Unit normal to the boundary of the domain at position $\boldsymbol{r}$
$\boldsymbol{\mathcal{A}}^\star$	Adjoint of $\boldsymbol{\mathcal{A}}$
$\boldsymbol{\gamma}_{\boldsymbol{r}}$	Rotated tangential trace operator
$s_{\max}(\boldsymbol{Z})$	Maximum singular value of $\boldsymbol{Z}$
$s_{\min}(\boldsymbol{Z})$	Minimum singular value of $\boldsymbol{Z}$

Physical Quantities

ϵ_0 ($\mathrm{F\,m^{-1}}$)	Permittivity of vacuum
μ_0 ($\mathrm{H\,m^{-1}}$)	Permeability of free space
ω ($\mathrm{rad\,s^{-1}}$)	Angular frequency
ρ ($\mathrm{C\,m^{-3}}$)	Electric charge density
φ (V)	Electric scalar potential
$\boldsymbol{r}, \boldsymbol{r'}$	Position vectors
$\boldsymbol{A}$ ($\mathrm{V\,s\,m^{-1}}$)	Magnetic vector potential
$\boldsymbol{B}$ (T)	Magnetic flux density
$\boldsymbol{D}$ ($\mathrm{C\,m^{-2}}$)	Electric flux density
$\boldsymbol{E}$ ($\mathrm{A\,m^{-1}}$)	Electric field
$\boldsymbol{H}$ ($\mathrm{A\,m^{-1}}$)	Magnetic field
$\boldsymbol{J}$ ($\mathrm{A\,m^{-2}}$)	Electric current density
$\boldsymbol{M}$ ($\mathrm{V/m^2}$)	Magnetic current density
c_0 ($\mathrm{m\,s^{-1}}$)	Speed of light in vacuum
$G_0(\boldsymbol{r}, \boldsymbol{r'})$	3D Green's function in vacuum
k_0	Wave number in vacuum

Publications

Journal Publications

- Xi Cheng, Clément Henry, Francesco P. Andriulli, Christian Person, and Joe Wiart. "A Surrogate Model Based on Artificial Neural Network for RF Radiation Modelling with High-Dimensional Data". In: *International Journal of Environmental Research and Public Health* 17.7 (2020)

- Jade Martínez-Llinàs, Clément Henry, Daniel Andrén, Ruggero Verre, Mikael Käll, and Philippe Tassin. "A Gaussian reflective metasurface for advanced wavefront manipulation". In: *Opt. Express* 27.15 (July 2019), pp. 21069–21082

Publications in Preparation

- Clément Henry, Adrien Merlini, Lyes Rahmouni, and Francesco P. Andriulli. "On a Low-Frequency and Contrast Stabilized Full-Wave Volume Integral Equation Solver for Lossy Media". 2021

Conference Contributions

- Clément Henry, Adrien Merlini, Lyes Rahmouni, and Francesco P. Andriulli. "A Regularized Electric Flux Volume Integral Equation for Brain Imaging". In: *2020 IEEE International Symposium on Antennas and Propagation and North American Radio Science Meeting*. 2020, pp. 1025–1026

- Clément Henry, Adrien Merlini, Lyes Rahmouni, and Francesco P. Andriulli. "On the Use of a Full-Wave Solver in the Solution of the Electroencephalography Forward Problem". In: *2019 IEEE International Symposium on Antennas and Propagation & USNC/URSI National Radio Science Meeting*. July 2019, Abstract and presentation

Bibliography

[1] Aria Abubakar and Peter M van den Berg. "Iterative forward and inverse algorithms based on domain integral equations for three-dimensional electric and magnetic objects". In: *Journal of computational physics* 195.1 (2004), pp. 236–262.

[2] A. Afsari, A. M. Abbosh, and Y. Rahmat-Samii. "A Rapid Medical Microwave Tomography Based on Partial Differential Equations". In: *IEEE Transactions on Antennas and Propagation* 66.10 (Oct. 2018), pp. 5521–5535.

[3] Erik Aguirre Gallego et al. "Evaluation of electromagnetic dosimetry of wireless systems in complex indoor scenarios with human body interaction". In: *Progress In Electromagnetics Research B, Vol. 43, 189-209, 2012.* (2012).

[4] F. P. Andriulli. "Loop-Star and Loop-Tree Decompositions: Analysis and Efficient Algorithms". In: *IEEE Transactions on Antennas and Propagation* 60.5 (May 2012), pp. 2347–2356.

[5] F. P. Andriulli et al. "On a Well-Conditioned Electric Field Integral Operator for Multiply Connected Geometries". In: *IEEE Transactions on Antennas and Propagation* 61.4 (Apr. 2013), pp. 2077–2087.

[6] M. Azghani and F. Marvasti. "L2-Regularized Iterative Weighted Algorithm for Inverse Scattering". In: *IEEE Transactions on Antennas and Propagation* 64.6 (June 2016), pp. 2293–2300.

[7] S. Baillet, J. C. Mosher, and R. M. Leahy. "Electromagnetic brain mapping". In: *IEEE Signal Processing Magazine* 18.6 (2001), pp. 14–30.

[8] Anthony T Barker, Reza Jalinous, and Ian L Freeston. "Non-invasive magnetic stimulation of human motor cortex". In: *The Lancet* 325.8437 (1985), pp. 1106–1107.

[9] Mario Bebendorf. "Approximation of boundary element matrices". In: *Numerische Mathematik* 86.4 (2000), pp. 565–589.

[10] Yves Beghein et al. "On a low-frequency and refinement stable PMCHWT integral equation leveraging the quasi-Helmholtz projectors". In: *IEEE Transactions on Antennas and Propagation* 65.10 (2017), pp. 5365–5375.

[11] P. M. van den Berg and A. Abubakar. "Contrast Source Inversion Method: State of Art". In: *Progress In Electromagnetics Research* 34 (2001), pp. 189–218.

[12] Peter M van den Berg, AL Van Broekhoven, and Aria Abubakar. "Extended contrast source inversion". In: *Inverse problems* 15.5 (1999), p. 1325.

[13] Max Born. "Quantenmechanik der stoßvorgänge". In: *Zeitschrift für Physik* 38.11-12 (1926), pp. 803–827.

[14] A Bossavit. "Computational electromagnetism and geometry: Building a finite-dimensional "Maxwell's house"". In: *Journal of Japanese Society of Applied Electromagnetics and Mechanics* 7 (1999), pp. 150–159.

[15] Chad A Bossetti, Merrill J Birdno, and Warren M Grill. "Analysis of the quasi-static approximation for calculating potentials generated by neural stimulation". In: *Journal of Neural Engineering* 5.1 (Dec. 2007), pp. 44–53.

[16] Matthys M. Botha. "Solving the volume integral equations of electromagnetic scattering". In: *Journal of Computational Physics* 218.1 (2006), pp. 141–158.

[17] Neil V. Budko and Alexander B. Samokhin. "Spectrum of the Volume Integral Operator of Electromagnetic Scattering". In: *SIAM Journal on Scientific Computing* 28.2 (2006), pp. 682–700.

[18] Augustin Cauchy et al. "Méthode générale pour la résolution des systemes d'équations simultanées". In: *Comp. Rend. Sci. Paris* 25.1847 (1847), pp. 536–538.

[19] Michel Cessenat. *Mathematical methods in electromagnetism: linear theory and applications*. Vol. 41. World scientific, 1996.

[20] Margaret Cheney, David Isaacson, and Jonathan C. Newell. "Electrical Impedance Tomography". In: *SIAM Review* 41.1 (1999), pp. 85–101.

[21] Xi Cheng et al. "A Surrogate Model Based on Artificial Neural Network for RF Radiation Modelling with High-Dimensional Data". In: *International Journal of Environmental Research and Public Health* 17.7 (2020).

[22] W. C. Chew and Y. M. Wang. "Reconstruction of two-dimensional permittivity distribution using the distorted Born iterative method". In: *IEEE Transactions on Medical Imaging* 9.2 (June 1990), pp. 218–225.

[23] I.-T. Chiang and W.-C. Chew. "New Formulation and Iterative Solution for Low-Frequency Volume Integral Equation". In: *Journal of Electromagnetic Waves and Applications* 19.3 (2005), pp. 289–306.

[24] Febo Cincotti et al. "High-resolution EEG techniques for brain–computer interface applications". In: *Journal of Neuroscience Methods* 167.1 (2008), pp. 31–42.

[25] J. Claassen et al. “Continuous EEG monitoring and midazolam infusion for refractory nonconvulsive status epilepticus”. In: *Neurology* 57.6 (2001), pp. 1036–1042.

[26] David L Colton, Rainer Kress, and Rainer Kress. *Inverse acoustic and electromagnetic scattering theory*. Vol. 93. Springer, 1998.

[27] Martin Costabel, Eric Darrigrand, and Hamdi Sakly. “The essential spectrum of the volume integral operator in electromagnetic scattering by a homogeneous body”. In: *Comptes Rendus Mathematique* 350.3 (2012), pp. 193–197.

[28] RJ Croft et al. “The effect of mobile phone electromagnetic fields on the alpha rhythm of human electroencephalogram”. In: *Bioelectromagnetics: Journal of the Bioelectromagnetics Society, The Society for Physical Regulation in Biology and Medicine, The European Bioelectromagnetics Association* 29.1 (2008), pp. 1–10.

[29] G Curcio et al. “Is the brain influenced by a phone call?: an EEG study of resting wakefulness”. In: *Neuroscience research* 53.3 (2005), pp. 265–270.

[30] M. Cvetković, D. Poljak, and J. Haueisen. “Analysis of Transcranial Magnetic Stimulation Based on the Surface Integral Equation Formulation”. In: *IEEE Transactions on Biomedical Engineering* 62.6 (2015), pp. 1535–1545.

[31] J. C. de Munck, B. W. van Dijk, and H. Spekreijse. “Mathematical dipoles are adequate to describe realistic generators of human brain activity”. In: *IEEE Transactions on Biomedical Engineering* 35.11 (Nov. 1988), pp. 960–966.

[32] S. Depatla, C. R. Karanam, and Y. Mostofi. “Robotic Through-Wall Imaging: Radio-Frequency Imaging Possibilities with Unmanned Vehicles.” In: *IEEE Antennas and Propagation Magazine* 59.5 (2017), pp. 47–60.

[33] D. Dobbelaere et al. “A Calderón multiplicative preconditioner for the electromagnetic Poincaré–Steklov operator of a heterogeneous domain with scattering applications”. In: *Journal of Computational Physics* 303 (2015), pp. 355–371.

[34] Marián Fabian et al. *Functional analysis and infinite-dimensional geometry*. Springer Science & Business Media, 2013.

[35] Elise C Fear et al. “Microwave breast imaging with a monostatic radar-based system: A study of application to patients”. In: *IEEE transactions on microwave theory and techniques* 61.5 (2013), pp. 2119–2128.

[36] C. Forestiere et al. “A Frequency Stable Volume Integral Equation Method for Anisotropic Scatterers”. In: *IEEE Transactions on Antennas and Propagation* 65.3 (Mar. 2017), pp. 1224–1235.

[37] S Gabriel, R W Lau, and C Gabriel. "The dielectric properties of biological tissues: III. Parametric models for the dielectric spectrum of tissues". In: *Physics in Medicine and Biology* 41.11 (Nov. 1996), pp. 2271–2293.

[38] Rania Ghosn et al. "Effets des radiofréquences sur le système nerveux central chez l'homme: EEG, sommeil, cognition, vascularisation". In: *Comptes Rendus Physique* 14.5 (2013), pp. 395–401.

[39] C. Gilmore, P. Mojabi, and J. LoVetri. "Comparison of an Enhanced Distorted Born Iterative Method and the Multiplicative-Regularized Contrast Source Inversion method". In: *IEEE Transactions on Antennas and Propagation* 57.8 (Aug. 2009), pp. 2341–2351.

[40] L. J. Gomez, A. C. Yücel, and E. Michielssen. "Low-Frequency Stable Internally Combined Volume-Surface Integral Equation for High-Contrast Scatterers". In: *IEEE Antennas and Wireless Propagation Letters* 14 (2015), pp. 1423–1426.

[41] L. J. Gomez, A. C. Yücel, and E. Michielssen. "The ICVSIE: A General Purpose Integral Equation Method for Bio-Electromagnetic Analysis". In: *IEEE Transactions on Biomedical Engineering* 65.3 (Mar. 2018), pp. 565–574.

[42] M. Gossye et al. "A Calderón Preconditioner for High Dielectric Contrast Media". In: *IEEE Transactions on Antennas and Propagation* 66.2 (Feb. 2018), pp. 808–818.

[43] L. Greengard and V. Rokhlin. "A Fast Algorithm for Particle Simulations". In: *Journal of Computational Physics* 135.2 (1997), pp. 280–292.

[44] Stefan Gumhold, Stefan Guthe, and Wolfgang Straundefineder. "Tetrahedral Mesh Compression with the Cut-Border Machine". In: *Proceedings of the Conference on Visualization '99: Celebrating Ten Years*. San Francisco, California, USA: IEEE Computer Society Press, 1999, pp. 51–58.

[45] Per Christian Hansen. *Rank-deficient and discrete ill-posed problems: numerical aspects of linear inversion*. SIAM, 1998.

[46] Harold V Henderson and Shayle R Searle. "On deriving the inverse of a sum of matrices". In: *Siam Review* 23.1 (1981), pp. 53–60.

[47] Clément Henry et al. "A Regularized Electric Flux Volume Integral Equation for Brain Imaging". In: *2020 IEEE International Symposium on Antennas and Propagation and North American Radio Science Meeting*. 2020, pp. 1025–1026.

[48] Clément Henry et al. "On a Low-Frequency and Contrast Stabilized Full-Wave Volume Integral Equation Solver for Lossy Media". 2021.

[49] Clément Henry et al. "On the Use of a Full-Wave Solver in the Solution of the Electroencephalography Forward Problem". In: *2019 IEEE International Symposium on Antennas and Propagation & USNC/URSI National Radio Science Meeting*. July 2019, Abstract and presentation.

[50] Maila Hietanen, Tero Kovala, and Anna-Maija Hämäläinen. "Human brain activity during exposure to radiofrequency fields emitted by cellular phones". In: *Scandinavian journal of work, environment & health* (2000), pp. 87–92.

[51] Desmond J Higham. "Condition numbers and their condition numbers". In: *Linear Algebra and its Applications* 214 (1995), pp. 193–213.

[52] K.-A. Hossmann and D.M. Hermann. "Effects of electromagnetic radiation of mobile phones on the central nervous system". In: *Bioelectromagnetics* 24.1 (2003), pp. 49–62.

[53] Bryan Howell, Leonel E Medina, and Warren M Grill. "Effects of frequency-dependent membrane capacitance on neural excitability". In: *Journal of neural engineering* 12.5 (2015), p. 056015.

[54] "IEEE Recommended Practice for Determining the Peak Spatial-Average Specific Absorption Rate (SAR) in the Human Head from Wireless Communications Devices: Measurement Techniques". In: *IEEE Std 1528-2013 (Revision of IEEE Std 1528-2003)* (2013), pp. 1–246.

[55] Ilse CF Ipsen and Carl D Meyer. "The angle between complementary subspaces". In: *The American mathematical monthly* 102.10 (1995), pp. 904–911.

[56] T. Isernia et al. "Inverse scattering and compressive sensing as advanced e.m. design tools". In: *2017 IEEE International Symposium on Antennas and Propagation USNC/URSI National Radio Science Meeting*. 2017 IEEE International Symposium on Antennas and Propagation USNC/URSI National Radio Science Meeting. July 2017, pp. 433–434.

[57] Jian-Ming Jin. *Theory and computation of electromagnetic fields*. John Wiley & Sons, 2011.

[58] Jari Kaipio and Erkki Somersalo. *Statistical and computational inverse problems*. Vol. 160. Springer Science & Business Media, 2006.

[59] R. E. Kleinman and P. M. Van den Berg. "A modified gradient method for two-dimensional problems in tomography". In: *Journal of Computational and Applied Mathematics* 42.1 (1992), pp. 17–35.

[60] Ralph Ellis Kleinman and PM Van den Berg. "An extended range-modified gradient technique for profile inversion". In: *Radio Science* 28.5 (1993), pp. 877–884.

[61] Ralph Ellis Kleinman and PM Van den Berg. "Iterative methods for solving integral equations". In: *Radio Science* 26.1 (1991), pp. 175–181.

[62] RE Kleinman and PM Van den Berg. "Two-dimensional location and shape reconstruction". In: *Radio Science* 29.4 (1994), pp. 1157–1169.

[63] J. Kornprobst, J. Knapp, and T. F. Eibert. "Approximate Inverse of the Rao-Wilton-Glisson Basis Functions Gram Matrix via Monopolar Representation". In: *2019 IEEE International Symposium on Antennas and Propagation and USNC-URSI Radio Science Meeting*. 2019, pp. 795–796.

[64] Alexis M. Kuncel and Warren M. Grill. "Selection of stimulus parameters for deep brain stimulation". In: *Clinical Neurophysiology* 115.11 (2004), pp. 2431–2441.

[65] Maokun Li and Weng Cho Chew. "Applying divergence-free condition in solving the volume integral equation". In: *Progress In Electromagnetics Research* 57 (2006), pp. 311–333.

[66] J. Lin et al. "ICNIRP Guidelines for limiting exposure to time-varying electric and magnetic fields (1 Hz to 100 kHz)." In: *Health Physics* 99 (2010), pp. 818–836.

[67] P. M. van den Berg. "Chapter 1.3.3 - Nonlinear Scalar Inverse Scattering: Algorithms and Applications". In: *Scattering*. Ed. by Roy Pike and Pierre Sabatier. London: Academic Press, 2002, pp. 142–161.

[68] J. Markkanen. "Discrete Helmholtz Decomposition for Electric Current Volume Integral Equation Formulation". In: *IEEE Transactions on Antennas and Propagation* 62.12 (Dec. 2014), pp. 6282–6289.

[69] J. Markkanen et al. "Analysis of Volume Integral Equation Formulations for Scattering by High-Contrast Penetrable Objects". In: *IEEE Transactions on Antennas and Propagation* 60.5 (May 2012), pp. 2367–2374.

[70] Johannes Markkanen and Pasi Ylä-Oijala. "Numerical comparison of spectral properties of volume-integral-equation formulations". In: *Journal of Quantitative Spectroscopy and Radiative Transfer* 178 (2016), pp. 269–275.

[71] Jade Martínez-Llinàs et al. "A Gaussian reflective metasurface for advanced wavefront manipulation". In: *Opt. Express* 27.15 (July 2019), pp. 21069–21082.

[72] L. S. Mendes and S. A. Carvalho. "Scattering of EM waves by homogeneous dielectrics with the use of the method of moments and 3D solenoidal basis functions". In: *Microwave and Optical Technology Letters* 12.6 (1996), pp. 327–331.

[73] Rajendra Mitharwal. "Innovative Computational Paradigms for Invisible Radio Frequency Devices". PhD thesis. Télécom Bretagne, 2015.

[74] K. Niino and N. Nishimura. "Calderón preconditioning approaches for PMCHWT formulations for Maxwell's equations". In: *International Journal of Numerical Modelling: Electronic Networks, Devices and Fields* 25.5-6 (2012), pp. 558–572.

[75] International Commission on Non-Ionizing Radiation Protection. "ICNIRP Guidelines for limiting exposure to time-varying electric, magnetic and electromagnetic fields (up to 300 GHz)." In: *Health Physics* 97 (2009), pp. 257–258.

[76] Yvan Notay. "AGMG software and documentation". In: *see http://agmg.eu* ().

[77] Yvan Notay. "An aggregation-based algebraic multigrid method". In: *Electronic transactions on numerical analysis* 37.6 (2010), pp. 123–146.

[78] T. F. Oostendorp, J. Delbeke, and D. F. Stegeman. "The conductivity of the human skull: results of in vivo and in vitro measurements". In: *IEEE Transactions on Biomedical Engineering* 47.11 (2000), pp. 1487–1492.

[79] Robert Oostenveld et al. "FieldTrip: open source software for advanced analysis of MEG, EEG, and invasive electrophysiological data". In: *Computational intelligence and neuroscience* 2011 (2011), p. 1.

[80] R. Palmeri et al. "Design of Artificial-Material-Based Antennas Using Inverse Scattering Techniques". In: *IEEE Transactions on Antennas and Propagation* 66.12 (Dec. 2018), pp. 7076–7090.

[81] Roberta Palmeri and Tommaso Isernia. "Inverse Design of Artificial Materials Based Lens Antennas through the Scattering Matrix Method". In: *Electronics* 9.4 (Mar. 27, 2020), p. 559.

[82] Robert Plonsey and Dennis B Heppner. "Considerations of quasi-stationarity in electrophysiological systems". In: *The Bulletin of mathematical biophysics* 29.4 (1967), pp. 657–664.

[83] A.G. Polimeridis et al. "Stable FFT-JVIE solvers for fast analysis of highly inhomogeneous dielectric objects". In: *Journal of Computational Physics* 269 (2014), pp. 280–296.

[84] Z. Qian and W. C. Chew. "Enhanced A-EFIE With Perturbation Method". In: *IEEE Transactions on Antennas and Propagation* 58.10 (2010), pp. 3256–3264.

[85] Zhi Guo Qian and Weng Cho Chew. "A quantitative study on the low frequency breakdown of EFIE". In: *Microwave and Optical Technology Letters* 50.5 (2008), pp. 1159–1162.

[86] Sadasiva Rao, D Wilton, and Allen Glisson. "Electromagnetic scattering by surfaces of arbitrary shape". In: *IEEE Transactions on antennas and propagation* 30.3 (1982), pp. 409–418.

[87] André Roger. "Newton-Kantorovitch algorithm applied to an electromagnetic inverse problem". In: *IEEE Transactions on Antennas and Propagation* 29.2 (1981), pp. 232–238.

[88] G. Rubinacci and A. Tamburrino. "A Broadband Volume Integral Formulation Based on Edge-Elements for Full-Wave Analysis of Lossy Interconnects". In: *IEEE Transactions on Antennas and Propagation* 54.10 (2006), pp. 2977–2989.

[89] D. Schaubert, D. Wilton, and A. Glisson. "A tetrahedral modeling method for electromagnetic scattering by arbitrarily shaped inhomogeneous dielectric bodies". In: *IEEE Transactions on Antennas and Propagation* 32.1 (Jan. 1984), pp. 77–85.

[90] Jonathan Richard Shewchuk et al. *An introduction to the conjugate gradient method without the agonizing pain*. 1994.

[91] Arnold Sommerfeld. *Partial differential equations in physics*. Academic press, 1949.

[92] Julius Adams Stratton. *Electromagnetic theory*. Vol. 33. John Wiley & Sons, 2007.

[93] LE Sun and Weng Cho Chew. "A novel formulation of the volume integral equation for electromagnetic scattering". In: *Waves in Random and Complex Media* 19.1 (2009), pp. 162–180.

[94] Daniel B Szyld. "The many proofs of an identity on the norm of oblique projections". In: *Numerical Algorithms* 42.3-4 (2006), pp. 309–323.

[95] Andrei Nikolaevich Tikhonov. "Regularization of incorrectly posed problems". In: Soviet Mathematics Doklady. 1963.

[96] J. A. Tobon Vasquez et al. "Noninvasive Inline Food Inspection via Microwave Imaging Technology: An Application Example in the Food Industry". In: *IEEE Antennas and Propagation Magazine* 62.5 (2020), pp. 18–32.

[97] Eduard Ubeda and Juan M Rius. "Monopolar divergence-conforming and curl-conforming low-order basis functions for the electromagnetic scattering analysis". In: *Microwave and Optical Technology Letters* 46.3 (2005), pp. 237–241.

[98] MC Van Beurden and SJL Van Eijndhoven. "Well-posedness of domain integral equations for a dielectric object in homogeneous background". In: *Journal of Engineering Mathematics* 62.3 (2008), pp. 289–302.

[99] P. M. Van Den Berg et al. "A Computational Model of the Electromagnetic Heating of Biological Tissue with Application to Hyperthermic Cancer Therapy". In: *IEEE Transactions on Biomedical Engineering* BME-30.12 (1983), pp. 797–805.

[100] Peter M Van Den Berg and Ralph E Kleinman. "A contrast source inversion method". In: *Inverse problems* 13.6 (1997), p. 1607.

[101] G. Vecchi. "Loop-star decomposition of basis functions in the discretization of the EFIE". In: *IEEE Transactions on Antennas and Propagation* 47.2 (Feb. 1999), pp. 339–346.

[102] Zsuzsanna Vecsei et al. "Short-term radiofrequency exposure from new generation mobile phones reduces EEG alpha power with no effects on cognitive performance". In: *Scientific reports* 8.1 (2018), pp. 1–12.

[103] Y. M. Wang and W. C. Chew. "An iterative solution of the two-dimensional electromagnetic inverse scattering problem". In: *International Journal of Imaging Systems and Technology* 1.1 (1989), pp. 100–108.

[104] Zhipeng Wu and Haigang Wang. "Microwave Tomography for Industrial Process Imaging: Example Applications and Experimental Results." In: *IEEE Antennas and Propagation Magazine* 59.5 (2017), pp. 61–71.

[105] Pasi Yla-Oijala et al. "Surface and volume integral equation methods for time-harmonic solutions of Maxwell's equations". In: *Progress in electromagnetics Research* 149 (2014), pp. 15–44.

[106] Amer Zakaria, Colin Gilmore, and Joe LoVetri. "Finite-element contrast source inversion method for microwave imaging". In: *Inverse Problems* 26.11 (2010), p. 115010.

[107] Grigorios P. Zouros and Neil V. Budko. "Transverse Electric Scattering on Inhomogeneous Objects: Spectrum of Integral Operator and Preconditioning". In: *SIAM Journal on Scientific Computing* 34.3 (2012), B226–B246.